Advanced Modulation Techniques for Next-Generation Wireless Communications

by

Ali Tugberk Dogukan

A Dissertation Submitted to the
Graduate School of Sciences and Engineering
in Partial Fulfillment of the Requirements for
the Degree of

Doctor of Philosophy

in

Electrical and Electronics Engineering

KOÇ ÜNİVERSİTESİ

January 15, 2025

Advanced Modulation Techniques for Next-Generation Wireless Communications

Koç University

Graduate School of Sciences and Engineering

This is to certify that I have examined this copy of a doctoral dissertation by

Ali Tugberk Dogukan

and have found that it is complete and satisfactory in all respects,

and that any and all revisions required by the final

examining committee have been made.

Committee Members:

Prof. Dr. Ertuğrul Başar (Advisor)

Prof. Sinem Çöleri

Assoc. Prof. Murat Kuşçu

Prof. Hüseyin Arslan

Prof. Ali Emre Pusane

Date:

To my beloved wife, Sebile Serranur Tümer Doğukan, whose unwavering love, support, and patience have been my guiding light throughout this journey. And to my family, Mürüvvet Doğukan, Ayhan Doğukan, Ahmet Tuğşad, Ceyhun Emre, and Mehmet Orhun, for their endless encouragement, sacrifices, and belief in me.

ABSTRACT

Advanced Modulation Techniques for Next-Generation Wireless Communications
Ali Tugberk Dogukan
Doctor of Philosophy in Electrical and Electronics Engineering
January 15, 2025

The rapid advancement of wireless communication networks towards 6G and beyond necessitates innovative approaches to enhance spectrum efficiency, reduce complexity, and improve reliability. This thesis investigates the combination of index modulation (IM) and reconfigurable intelligent surfaces (RIS) with technologies such as orthogonal frequency division multiplexing (OFDM) and non-orthogonal multiple access (NOMA) to improve bit error rate (BER), spectral efficiency, and system reliability, while ensuring low complexity for practical implementation. In Chapter 2, a coordinate interleaved OFDM with in-phase/quadrature IM (CI-OFDM-IQIM) scheme is proposed to integrate OFDM with IM, achieving enhanced error performance and spectrum efficiency by reducing decoding complexity and transmitting real and imaginary components through subblock clustering. Chapter 3 introduces the RIS-aided enhanced receive spatial modulation (RIS-ERSM) scheme, which enhances spectrum efficiency and reliability by utilizing receive antenna indices in a clever manner and M-ary modulation, while Chapter 4 presents the RIS code IM with quadrature RSM (RIS-CIM-QRSM) scheme that integrates QRSM with CIM to improve error performance and energy efficiency. Chapter 5 proposes two hybrid-RIS-enabled enhanced reflection modulation (Hyb-ERM) schemes that enhance BER performance and spectrum efficiency, while Chapter 6 introduces the enhanced over-the-air RIS-IM (E-OTA-RIS-IM) system, leveraging RIS partitioning for OTA transmission of additional IM bits, leading to improved spectral efficiency. Finally, Chapter 7 presents a novel downlink NOMA system with passive RIS that eliminates successive interference cancellation (SIC) to reduce complexity and improve efficiency. This thesis demonstrates the potential of these innovative communication schemes to meet the stringent requirements of 6G and beyond, including

higher spectral efficiency, low complexity, and enhanced system reliability.

ÖZETÇE

Yeni Nesil Kablosuz İletişim için Gelişmiş Modülasyon Teknikleri
Ali Tugberk Dogukan
Elektrik ve Elektronik Mühendisliği, Doktora
15 Ocak 2025

Kablosuz iletişim ağlarının 6G ve ötesine doğru hızla ilerlemesi, spektrum verimliliğini artırmak, karmaşıklığı azaltmak ve güvenilirliği iyileştirmek için yenilikçi yaklaşımları gerekli kılmaktadır. Bu tez, bit hata oranını (BER), spektral verimliliği ve sistem güvenilirliğini iyileştirmek ve pratik uygulamalar için düşük karmaşıklık sunmak için indis modülasyonu (IM) ve yeniden yapılandırılabilir akıllı yüzeylerin (RIS) dik frekans bölmeli çoğullama (OFDM) ve dik olmayan çoklu erişim (NOMA) gibi teknolojilerle birleştirilmesini araştırmaktadır. Bölüm 2'de, OFDM'yi IM ile entegre etmek, kod çözme karmaşıklığını azaltarak ve gerçek ve sanal bileşenleri alt blok kümelemesi yoluyla ileterek gelişmiş hata performansı ve spektrum verimliliği elde etmek için eş fazlı/kare IM (CI-OFDM-IQIM) şemasına sahip koordinatlı iç içe geçmiş OFDM önerilmektedir. Bölüm 3, alıcı anten indislerini akıllıca bir şekilde ve M-ary modülasyonu kullanarak spektrum verimliliğini ve güvenilirliğini artıran RIS destekli gelişmiş alıcı uzaysal modülasyon (RIS-ERSM) şemasını tanıtırken, Bölüm 4, hata performansını ve enerji verimliliğini iyileştirmek için QRSM'yi CIM ile entegre eden karesel RSM'li RIS kod IM'yi (RIS-CIM-QRSM) sunar. Bölüm 5, BER performansını ve spektrum verimliliğini artıran iki hibrit-RIS etkin gelişmiş yansıma modülasyonu (Hyb-ERM) şemasını önerirken, Bölüm 6, ek IM bitlerinin OTA iletimi için RIS bölümlendirmesinden yararlanan ve gelişmiş spektral verimliliğe yol açan gelişmiş havadan RIS-IM (E-OTA-RIS-IM) sistemini tanıtır. Son olarak, Bölüm 7, karmaşıklığı azaltmak ve verimliliği iyileştirmek için ardışık girişim iptalini (SIC) ortadan kaldıran pasif RIS'li yeni bir aşağı bağlantı NOMA sistemi sunar. Bu tez, daha yüksek spektral verimlilik, düşük gecikme karmaşıklık ve gelişmiş sistem güvenilirliği de dahil olmak üzere 6G ve ötesinin katı gereksinimlerini karşılamak için bu yenilikçi iletişim şemalarının potansiyelini göstermektedir.

ACKNOWLEDGMENTS

I would like to begin by expressing my deepest gratitude to my advisor, Prof. Ertuğrul Başar, for his unwavering support, guidance, and encouragement throughout my academic journey. His mentorship has profoundly shaped my research in wireless communication, instilled a love for innovation, and provided life lessons that extend far beyond academia.

I am deeply grateful to my parents, Mürüvvet Doğukan and Ayhan Doğukan, for their sacrifices, unconditional love, and unwavering belief in me. Their support has been the foundation of my achievements and my greatest source of motivation.

My heartfelt thanks go to my wife, Sebile Serranur Tümer Doğukan, for her endless patience and unwavering support. She has been my anchor and constant source of encouragement, reminding me that I am never alone on this challenging road. Her love and understanding have been invaluable in helping me persevere.

To my brothers, Ahmet Tuğşad, Ceyhun Emre, and Mehmet Orhun, thank you for your support. You have been a source of strength and joy throughout this journey, and I am lucky to have you by my side.

I am also sincerely thankful to Emre Arslan and Fatih Kılınç, who are more than friends, they are brothers to me. Your support and encouragement have made a meaningful difference in my life, and I am truly grateful for your presence.

I extend my gratitude to Prof. Sinem Çöleri and Prof. Ali Emre Pusane for their invaluable feedback and guidance as thesis committee members. Their insights greatly enhanced the quality of this work.

Lastly, I also want to thank The Scientific and Technological Research Council of Turkey (TUBITAK) for supporting me during my PhD study through 2211-A National Scholarship Programme.

TABLE OF CONTENTS

LIST OF TABLES

LIST OF FIGURES

ABBREVIATIONS

ABEP	Average Bit Error Probability
AP	Access Point
APM	Amplitude And Phase Modulation
APSK	Amplitude Phase Shift Keying
AR	Augmented Reality
AWGN	Additive White Gaussian Noise
BEP	Bit Error Probability
BER	Bit Error Rate
BPCU	Bits Per Channel Use
BPSK	Binary Phase Shift Keying
BS	Base Station
CDF	Cumulative Distribution Function
CI	Coordinate Interleaving
CIM	Code Index Modulation
CIR	Channel Impulse Response
CLT	Central Limit Theorem
CP	Cyclic Prefix
CPEP	Conditional Pairwise Error Probability
CSI	Channel State Information
DL	Downlink
eMBB	Enhanced Mobile Broadband
FFT	Fast Fourier Transform
IFFT	Inverse Fast Fourier Transform
IM	Index Modulation
IoT	Internet-of-Things

IQ	In-phase/Quadrature
KPI	Key Performance Indicator
LLR	Log-Likelihood Ratio
LOS	Line-of-Sight
MAP	Mode Activation Pattern
MDS	Maximum-Distance Separable
MGF	Moment-Generating Function
MIMO	Multiple-Input Multiple-Output
mMTC	Massive Machine-Type Communications
ML	Maximum-Likelihood
NLOS	Non-Line-of-Sight
NOMA	Non-Orthogonal Multiple Access
OFDM	Orthogonal Frequency Division Multiplexing
OMA	Orthogonal Multiple Access
OTA	Over-The-Air
PAM	Pulse Amplitude Modulation
PDF	Probability Distribution Function
PSK	Phase Shift Keying
P/S	Parallel-to-Serial
QAM	Quadrature Amplitude Modulation
QoS	Quality of Service
QPSK	Quadrature Phase Shift Keying
RIS	Reconfigurable Intelligent Surface
RM	Reflection Modulation
RV	Random Variable
SAP	Subcarrier Activation Pattern
SEP	Symbol Error Probability
SIC	Successive Interference Cancellation
SIMO	Single-Input Multiple-Output

SINR	Signal-to-Interference-plus-Noise Ratio
SISO	Single-Input Single-Output
SM	Spatial Modulation
SNR	Signal-to-Noise Ratio
SSK	Space Shift Keying
TDMA	Time Division Multiple Access
UAV	Unmanned Aerial Vehicle
UE	User Equipment
UPEP	Unconditioned Pairwise Error Probability
URLLC	Ultra-Reliable Low-Latency Communications
VR	Virtual Reality
3GPP	Third Generation Partnership Project
5G	Fifth-Generation Wireless
6G	Sixth-Generation Wireless

Chapter 1

INTRODUCTION

Wireless communication has profoundly transformed modern life, enabling seamless information transmission and global connectivity. Starting with Marconi's wireless telegraph in the late 19th century, advancing to the development of cellular networks in the 20th century, and ending in the groundbreaking digital advancements of the 21st century, wireless technology has undergone significant growth [Sarkar et al., 2006]. Over the past two decades, wireless connectivity has experienced significant progress, driven by the rapid proliferation of mobile devices, the Internet of Things, and the continuous demand for high-speed data transmission. Global mobile subscriptions have exceeded 8 billion, with mobile internet accounting for over 70% of worldwide internet traffic [Department, 2023, Topics, 2023]. Every generational progression in wireless technology, from the analog 1G networks of the 1980s to the current 5G systems, has enhanced data transmission speeds and expanded the spectrum of supported applications, ranging from fundamental phone calls to immersive augmented and virtual reality environments [Sharma, 2013].

Currently, wireless communication plays an essential role across various industries, driving technological advancements and facilitating numerous consumer and industrial applications. The implementation of 5G networks has introduced groundbreaking capabilities, including eMBB, URLLC, and mMTC. These developments enable diverse applications such as autonomous vehicles, telemedicine, industrial automation, and real-time streaming of immersive AR/VR content [Vannithamby and Talwar, 2017]. For instance, autonomous vehicles rely on low-latency 5G networks to process large volumes of sensor data in real time, ensuring safe and efficient navigation [Hakak et al., 2023]. Similarly, telemedicine utilizes high-speed, reliable networks to perform remote surgeries and diagnostics, significantly improving healthcare accessibility [Valdez et al., 2021]. Fig. 1.1 illustrates the progression of KPIs from IMT-Advanced (4G) to IMT-2020 (5G), emphasizing the substantial advancements achieved with 5G technology [Electronics, 2015]. Each axis represents critical KPIs, including peak data rates, latency, connection density, spectrum efficiency, energy efficiency, and mobility. These improvements demonstrate the transformative potential of 5G, which is establishing the groundwork for the forthcoming generation of wireless communication technologies.

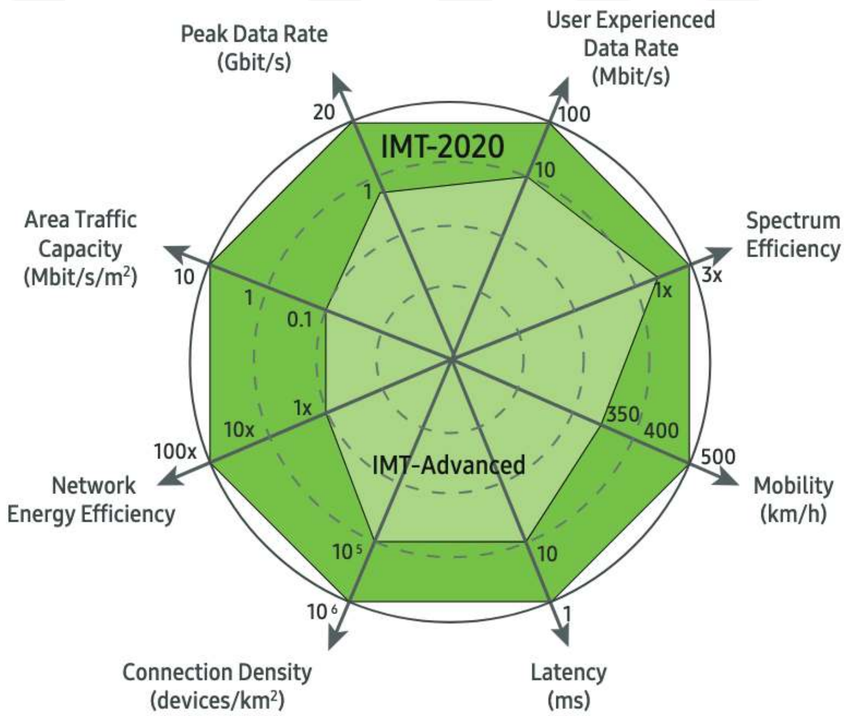

Figure 1.1: 5G KPIs [Electronics, 2015].

Despite these developments, the current wireless landscape encounters considerable challenges. The lack of spectrum, challenges over energy efficiency, and the increasing demand for seamless-connectivity among billions of devices highlight the constraints of current technologies. Moreover, as vertical applications such as smart cities, industrial IoT, and intelligent transportation systems expand, the demand for new solutions to overcome these restrictions increases [Giordani et al., 2020].

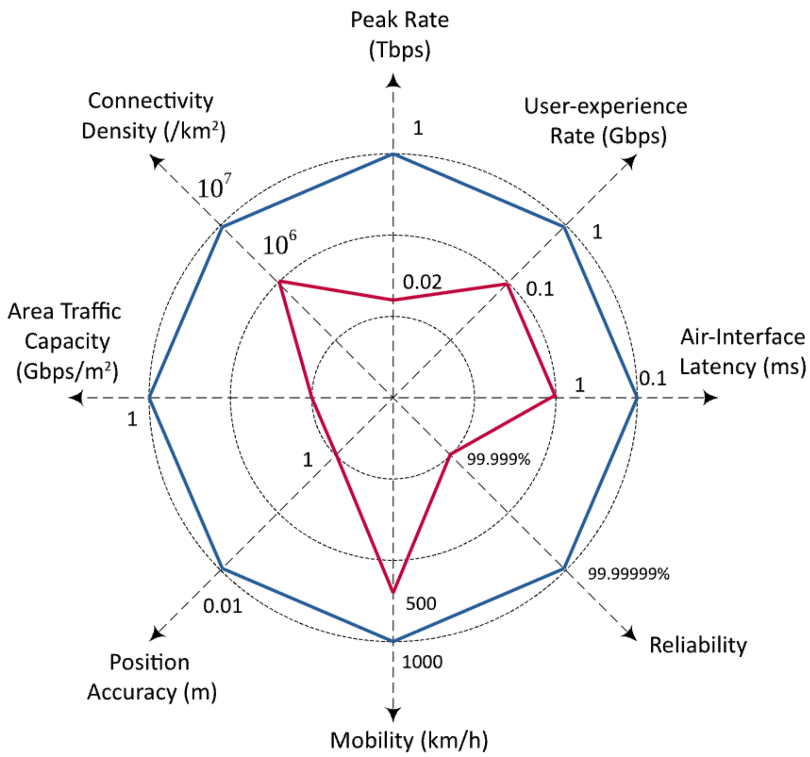

Figure 1.2: 6G KPIs [Jiang et al., 2021].

Looking ahead, the emergence of 6G networks represents the next frontier in wireless communication. Envisioned as a paradigm shift, 6G aims to address the shortcomings of 5G while unlocking unprecedented possibilities [Viswanathan and Mogensen, 2020]. Unlike its predecessor, 6G is expected to operate in higher frequency spectrum, enabling extreme data rates, ultra-low latency, and near-instantaneous connectivity. However, achieving these ambitious goals comes with significant challenges. The wireless channel, characterized by its inherent randomness and fading, poses a fundamental limitation. Additionally, the energy demands of 6G networks, coupled with the need for ultra-reliable performance, present formidable engineering obstacles.

KPIs for 6G include spectral efficiency, latency, reliability, energy efficiency, scalability and more. Fig. 1.2 presents the hexagonal requirement diagram for 6G, which highlights the dramatic improvements required across several critical metrics compared to 5G systems [Jiang et al., 2021]. The outer boundary of the hexagon

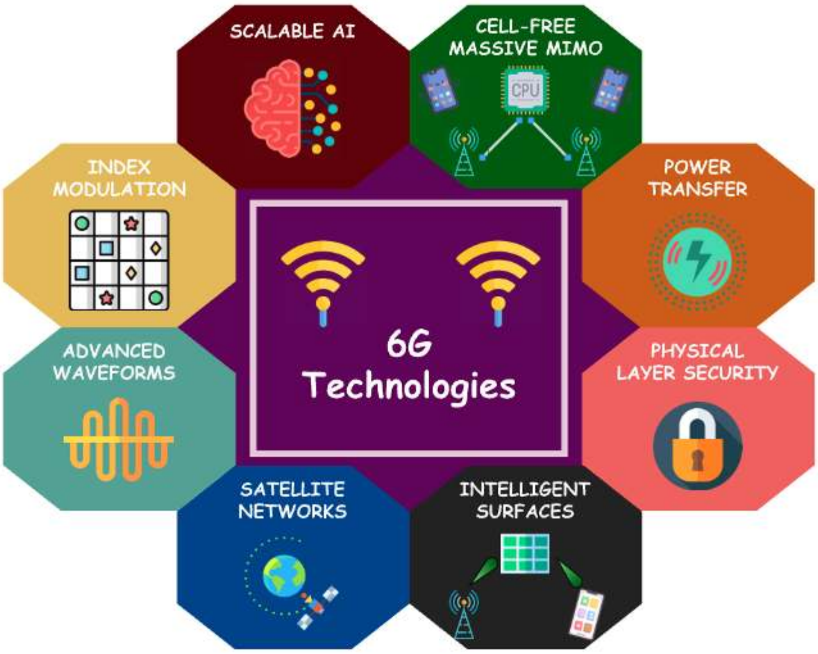

Figure 1.3: An overview of emerging PHY techniques that can shape the 6G era [Ozpoyraz et al., 2022].

represents the target capabilities of 6G, showcasing the significant advancements over current technologies. Fig. 1.2 visually underscores the gap between 5G and 6G capabilities, indicating the scale of improvements required. Each axis of the diagram encapsulates a KPI, with the larger hexagon representing 6G targets and the smaller inner hexagon denoting current 5G capabilities. This stark contrast highlights the extensive research and development efforts necessary to bridge the gap, laying the groundwork for innovative solutions to meet the unprecedented demands of the future. To achieve the extreme requirements envisioned for 6G, significant innovations in spectrum utilization, advanced signal processing techniques, and novel system architectures are necessary.

The physical layer serves as the backbone of wireless communication systems, and its advancements are critical for meeting 6G requirements. Emerging technologies as seen in Fig. 1.3, offer promising solutions to the challenges faced by 6G and are possible candidates as 6G enablers [Ozpoyraz et al., 2022]. These technologies aim to enhance key metrics, including spectral efficiency, BER, and energy efficiency. Among these innovations, three concepts have recieved significant attention in recent literature: IM, RIS, and NOMA. Each of these technologies brings unique advantages, addressing critical aspects of wireless communication such as spectrum utilization, channel control, and resource sharing.

1.1 Research Motivation

This research is primarily motivated by the necessity to improve the efficiency, robustness, and capacity of next-generation wireless communication networks, specifically regarding 6G. Conventional wireless communication systems frequently encounter restrictions regarding spectrum efficiency, energy efficiency, and interference management. Advanced technologies like IM, RIS, OFDM, and NOMA are being investigated to tackle these difficulties while preserving low system complexity.

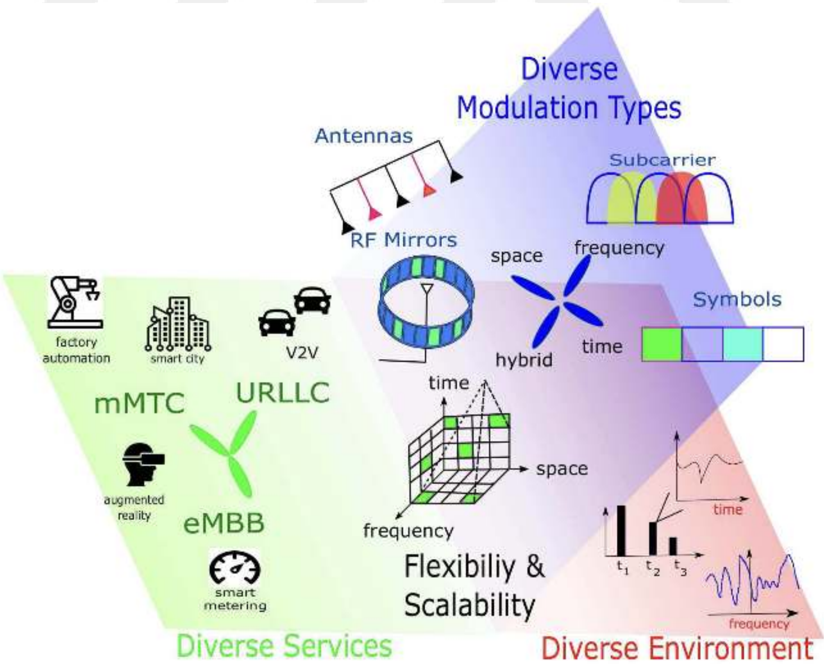

Figure 1.4: Diverse IM variants for various services and channel conditions [Tusha et al., 2020b].

IM is a transformative approach in wireless communication that encodes information into the indices of resources, such as subcarriers, antennas, or time slots, rather than solely relying on conventional modulation dimensions like amplitude, phase, or frequency [Basar et al., 2017]. By leveraging these indices as an additional degree of freedom, IM offers significant improvements in spectral efficiency, energy efficiency, and robustness against fading. Unlike traditional systems, which activate all available resources, IM selectively activates a subset of these resources, encoding information in their indices. This selective activation reduces power consumption and enhances resilience to fading, as the information encoded in the indices is less susceptible to signal degradation. Fig. 1.4 illustrates the versatility of IM in adapting to diverse services, modulation types, and environments [Tusha et al., 2020b]. IM supports a wide range of applications such as mMTC, URLLC, and eMBB, encompassing use cases like smart cities, augmented reality, and vehicle-to-vehicle (V2V) communication. Additionally, IM's adaptability to hybrid and multidimensional setups, combining space, time, and frequency domains, demonstrates its scalability and robustness. This flexibility ensures IM remains a robust solution for future wireless systems, capable of meeting the stringent demands of 6G networks.

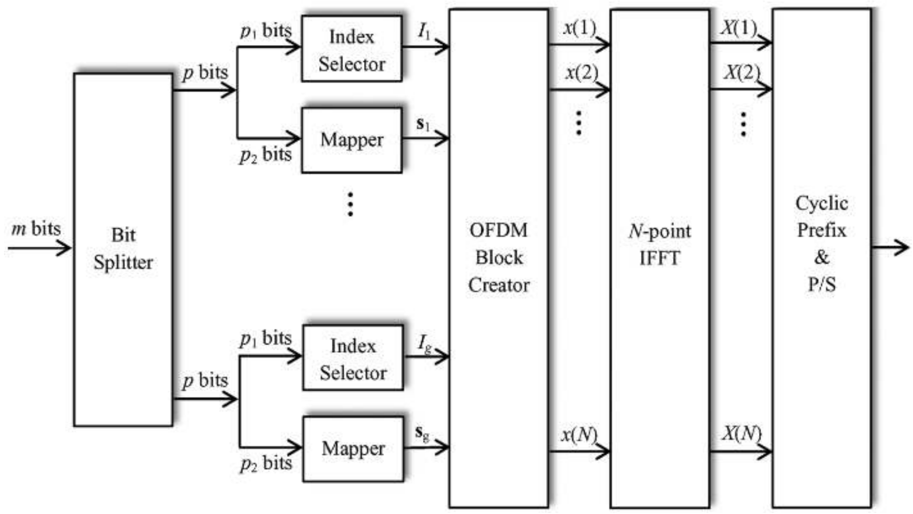

Figure 1.5: Block diagram of the OFDM-IM transmitter [Başar et al., 2013].

For example, OFDM-IM, with its transmitter structure illustrated in Fig. 1.5, is a foundational IM technique where the available subcarriers are divided into subblocks, with a predefined number of subcarriers activated in each subblock [Başar et al., 2013]. The indices of the active subcarriers encode part of the information, while the remaining bits are modulated onto symbols transmitted over these active subcarriers.

A critical advantage of IM is its ability to achieve a balance between complexity and performance. By reducing the number of active transmission elements, IM not only conserves power but also simplifies hardware design. The spectral efficiency of OFDM-IM can be mathematically expressed as,

$$\eta = \frac{\log_2 \binom{N}{K} + \log_2(M)}{N}, \tag{1.1}$$

where N is the number of subcarriers in a subblock, K is the number of active subcarriers per subblock, and M represents the modulation order. This equation highlights how IM supplements traditional symbol-based modulation with an additional layer of information encoding.

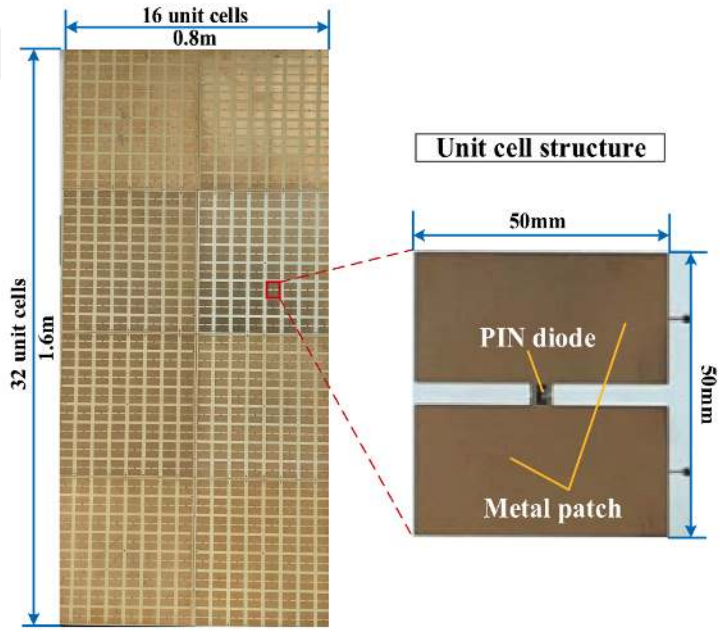

Figure 1.6: Fabricated PIN-diode based RIS wall [Wang et al., 2024a].

RISs are a revolutionary technology poised to redefine the wireless communication landscape by introducing control over the wireless propagation environment [Basar et al., 2019]. Composed of a large array of programmable meta-material elements, an RIS dynamically adjusts the phase, amplitude, or polarization of incident electromagnetic waves to optimize signal reflection. This capability allows RIS to overcome one of the fundamental challenges in wireless communication: the randomness of the wireless channel. Unlike conventional channels, which are influenced by uncontrollable factors such as reflection, scattering, and diffraction, RIS introduces an additional degree of freedom, enabling dynamic channel reconfiguration. This not only enhances signal quality but also mitigates interference, extends coverage, and reduces energy consumption.

As illustrated in Fig. 1.6, a real-world PIN-diode-based RIS prototype highlights the practicality of this technology. This metasurface, operating at 2.6 GHz, consists of a 1.6 m $\times$ 0.8 m structure with 32 $\times$ 16 independently regulated unit cells, each measuring 50 mm $\times$ 50 mm. Such prototypes demonstrate the feasibility of dynamically programming phase shifts for optimizing wireless channels, further solidifying RIS as a cornerstone of next-generation wireless systems.

The operation of an RIS can be described as follows: a signal transmitted from a source impinges on the RIS, where each element applies a programmable phase shift to the incident wave. The reflected waves are then constructively combined at the receiver to maximize the received signal strength. Mathematically, the received signal for an RIS-aided SISO system can be simply modeled as

$$y = x\left[f + \sum_{i=1}^{N} g_i\theta_i h_i\right] + n, \tag{1.2}$$

where f denotes the channel coefficient of the direct link between the transmitter and receiver, while g_i and h_i are channel coefficients corresponding to the ith RIS element for the links between the transmitter and RIS, and between RIS and receiver, respectively. Moreover, x, θ_i, N, and n represent the transmitted signal, the phase configuration of the ith RIS element, the total number of RIS elements, and the noise sample, respectively. By enabling precise control over signal propagation, RIS has the potential to significantly improve spectral efficiency, energy efficiency, and network reliability.

RIS technology is not merely a theoretical concept but has garnered significant interest from industry leaders, with prototypes and field tests demonstrating its feasibility. Companies such as Huawei [Technologies, 2023] and Ericsson [Wang et al., 2024b] have developed RIS prototypes capable of enhancing signal strength in urban environments. Despite its promise, RIS faces challenges such as optimizing phase shifts for large-scale implementations and integrating with other advanced technologies such as IM and NOMA. However, its potential to provide energy-efficient solutions for next-generation networks makes it a cornerstone of future wireless systems.

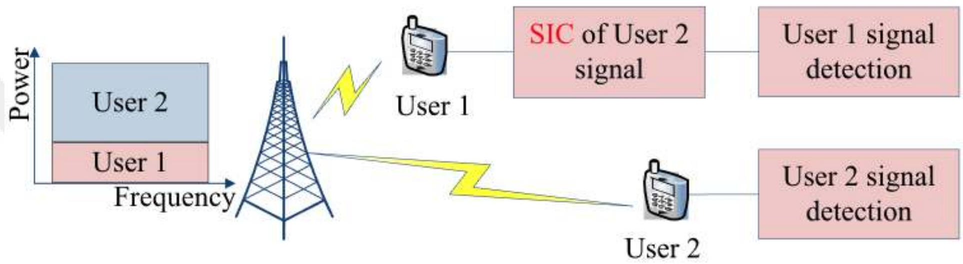

Figure 1.7: Basic power-domain NOMA relying on a SIC receiver [Dai et al., 2018].

NOMA is an innovative approach to resource allocation that departs from the traditional orthogonal paradigm by allowing multiple users to share the same time, frequency, or spatial resources [Dai et al., 2018]. In contrast to OMA, which assigns distinct resources to each user, NOMA enables simultaneous resource sharing, differentiating users through power or code domains. This results in significantly improved spectral efficiency and massive connectivity, which are critical for supporting the growing number of devices in the IoT era. As shown in Fig. 1.7, in power-domain NOMA, users are assigned different power levels based on their channel conditions, with weaker users receiving higher power to ensure fairness. The received signal is then processed using SIC, which decodes and subtracts the stronger user's signal to retrieve the weaker user's data.

The mathematical model for a power-domain NOMA system is expressed as

$$y = h_1\sqrt{P_1}x_1 + h_2\sqrt{P_2}x_2 + n, \tag{1.3}$$

where P_1 and P_2 are the power levels allocated to users 1 and 2, x_1 and x_2 are the transmitted signals, h_1 and h_2 are the respective channel coefficients, and n is the noise. By leveraging SIC, the receiver can effectively decode overlapping signals, ensuring reliable communication for all users. NOMA's ability to accommodate diverse QoS requirements makes it particularly suitable for dense user scenarios, such as smart cities and industrial IoT applications.

However, NOMA introduces challenges related to interference management and computational complexity, particularly in systems with a large number of users. Recent research has focused on integrating NOMA with technologies like RIS and IM to address these challenges. For example, combining NOMA with RIS enhances channel control, while incorporating IM provides additional spectral efficiency, creating a synergistic system capable of meeting 6G performance requirements.

While IM, RIS, and NOMA each offer significant benefits individually, their integration has the potential to revolutionize wireless communication by combining their respective strengths. IM enhances spectral and energy efficiency, RIS provides unprecedented control over the wireless channel, and NOMA optimizes resource sharing among multiple users. Together, these technologies address critical challenges such as spectrum scarcity, energy efficiency, and massive connectivity, positioning them as key enablers for 6G networks. However, combining these technologies also introduces complexities, such as parameter conflicts and increased computational demands. This thesis tackles these challenges by proposing innovative solutions that ensure low complexity and superior performance. By leveraging the synergistic potential of IM, RIS, and NOMA, this work aims to pave the way for scalable and efficient next-generation wireless systems.

1.2 Research Objectives and Contributions

The main objective of this thesis is to explore and propose novel modulation schemes which exploit IM, OFDM, RIS, and NOMA to improve the performance of future wireless communication systems. The research findings include the following two major improvements in system design:

- Improving spectral efficiency and error performance: This thesis develops novel wireless communication schemes that significantly improve both spectral efficiency and BER performance under various conditions, such as imperfect CSI.

- Low-complexity system design: The proposed schemes aim to enhance performance while maintaining low computational complexity, ensuring practical implementation feasibility.

1.3 Overview of Thesis Structure

The following chapters form the structure of this thesis:

Chapter 2: This chapter presents OFDM-IM and explores several developments in IM techniques. We propose a novel scheme, CI-OFDM-IQIM, which offers additional diversity gain and low-complexity detection. The chapter investigates the diversity order and presents an optimal rotation angle selection technique to enhance the performance of the proposed method under both perfect and imperfect CSI.

Chapter 3: This chapter explores the combination of IM with RIS, focusing on the development of RIS-assisted enhanced receive SM (RIS-ERSM). This technique divides the RIS into distinct groups, modifying the phases of each group to transmit additional IM bits. The chapter illustrates how RIS can significantly enhance the amount of IM bits while preserving signal power, resulting in improved performance for spectral efficiency and BER.

Chapter 4 presents RIS-CIM with quadrature RSM (RIS-CIM-QRSM), a new RIS-assisted wireless communication method that expands on the concept of RIS-aided communication. By integrating M-PAM, spreading codes, and receive antennas, this system improves error performance. We split the RIS into two parts to handle in-phase and quadrature components independently. Additionally, the chapter introduces a low-complexity detector and shows how effectively RIS-CIM-QRSM performs in terms of error when compared to benchmark schemes.

Chapter 5: This chapter explores the integration of hybrid RIS technology with IM techniques for 6G systems. Two novel schemes, Hyb-ERM-I and Hyb-ERM-II, are introduced, where a hybrid RIS, which is partitioned into multiple groups, is exploited. Each group can switch between active and passive modes based on the IM bits. Both of these schemes present a signal constellation that increases the minimum squared Euclidean distance, improves error performance, reduces power consumption, and improves the received SNR.

Chapter 6 proposes a novel enhanced OTA RIS-IM (E-OTA-RIS-IM) technique that leverages RIS to operate in different modes, thereby enhancing spectral efficiency and BER performance. This technique utilizes a hybrid RIS configuration with multiple groups, where each group can switch between active, passive, and absorption modes based on the IM bits, further advancing the concept of RIS-assisted IM systems.

Chapter 7: The final chapter of this thesis proposes a novel DL OTA NOMA scheme using RIS. This scheme generates the required power difference OTA at the RIS, reducing system complexity and improving efficiency, unlike conventional NOMA systems that enable the power difference at the BS. The chapter presents a thorough system model, theoretical analysis of outage probability and error probability, and extensive simulation results that demonstrate the superior performance of the proposed scheme compared to conventional RIS-based OMA systems.

1.4 Summary

This thesis offers an in-depth investigation of cutting-edge communication techniques that improve wireless system performance by utilizing RIS, OFDM, IM, and NOMA. The proposed approaches advance next-generation wireless networks, especially in the context of 6G, by tackling important issues including spectrum efficiency, BER, and system complexity. Combining these effective technologies provides a scalable and effective solution to satisfy the demanding needs of future applications.

Chapter 2

COORDINATE INTERLEAVED OFDM WITH REPEATED IN-PHASE / QUADRATURE INDEX MODULATION

2.1 Introduction

OFDM-IM [Başar et al., 2013] is a promising OFDM-based multicarrier transmission scheme that conveys additional information bits via the indices of activated subcarriers. This approach improves error performance compared to conventional OFDM because the information bits transmitted by IM are more resistant to fading than those transmitted using traditional M-ary PSK or QAM modulation. Furthermore, OFDM-IM has garnered significant attention in the literature due to its advantages, including high flexibility and simplicity of implementation.

To further enhance flexibility, OFDM with generalized IM (OFDM-GIM) has been proposed in [Fan et al., 2014]. Unlike traditional OFDM-IM, OFDM-GIM does not mandate a fixed number of active subcarriers within a subblock. Additionally, OFDM-IQ-IM [Zheng et al., 2015, Wen et al., 2017c] has been developed to enhance the spectral efficiency of OFDM-IM by separately applying IM to in-phase and quadrature components, therefore doubling the amount of IM bits. Similarly, OFDM with subcarrier number modulation (OFDM-SNM) [Jaradat et al., 2018] determines the number of active subcarriers in each subblock based on the incoming data bits, further enhancing spectral efficiency. Other techniques include layered OFDM-IM [Li et al., 2019], where SAPs are chosen across multiple layers to increase the number of IM bits, and subcarrier-level block interleaving [Xiao et al., 2014], which improves error performance. To eliminate the need for CSI at the receiver, rectangular differential coding was applied to OFDM-IM in [Xiao et al., 2021].

The flexibility of IM has also been leveraged to address the diverse requirements of 5G services, including improved reliability, higher spectral and energy efficiency, and low complexity. For example, OFDM with hybrid number and IM (OFDM-HNIM) [Jaradat et al., 2020] and sparse-encoded codebook IM (SE-CBIM) [Arslan et al., 2020c] have been introduced to support applications such as mMTC and URLLC. Due to its simple and adaptable structure, OFDM-IM can be integrated with emerging wireless communication systems, including MIMO [Basar, 2016b, Lu et al., 2018, Chen and Zheng, 2018, Wang, 2021], NOMA [Tusha et al., 2020a, Chen et al., 2020, Doğan et al., 2019, Arslan et al., 2020a, Şahin and Arslan, 2020], joint radar-communication [Şahin et al., 2021], and optical communication systems [Başar and Panayırcı, 2015, Azim et al., 2020].

OFDM-IM encounters difficulties in achieving increased spectral efficiency because of its idle subcarriers. To overcome this issue, dual mode aided OFDM (DM-OFDM) has been introduced in [Mao et al., 2016b], wherein null subcarriers are modulated with a secondary and distinct constellation to convey additional data symbols. The generalization of this approach is presented in [Mao et al., 2016a], where the number of subcarriers modulated by the identical mode can change. In order to further augment the number of bits transmitted by IM, multiple-mode OFDM-IM (MM-OFDM-IM) has been introduced in [Wen et al., 2017a]. This method uses multiple signal constellations and their full permutations to realize IM. In [Wen et al., 2018], MM-OFDM-IM was generalized by permitting the constellations to vary in size while maintaining the same number of bits transmitted via IM. An advanced variant, $\mathcal{Q}$-ary multiple mode OFDM-IM($\mathcal{Q}$-MM-OFDM-IM), was proposed in [Yarkin and Coon, 2020a]. Here, each subcarrier is modulated by $\mathcal{Q}$ disjoint M-ary constellations repeatedly, with a MDS code applied to the constellation indices. This results in a greater number of index symbols and higher spectral efficiency. Further innovations include OFDM implementations with MDS-APM and MDS-IQM, as discussed in [Yarkin and Coon, 2022]. Super-mode OFDM-IM (SuM-OFDM-IM) [Dogukan and Basar, 2020b], which jointly optimizes MAPs and SAPs, was proposed to further increase the number of information bits transmitted by IM. Another technique, OFDM with set partitioning modulation (OFDM-SPM), proposed in [Yarkin and Coon, 2020b], uses distinguishable constellations to differentiate subsets within a set partition, achieving better error performance. Additionally, OFDM with transmit diversity (OFDM-TD) [Zheng and Chen, 2017] activates null subcarriers to convey redundant information using multiple constellations, enhancing reliability. Since all subcarriers are active in these schemes, they achieve higher spectral efficiency compared to traditional OFDM-IM. As a result, these methods are strong candidates for future eMBB services, including applications such as AR and VR.

Many OFDM-IM-based techniques, which provide additional diversity advantages, have been presented in the literature to reduce multipath fading and improve reliability in wireless communication systems. One such scheme is repeated IM-OFDM (ReMO) [Van Luong et al., 2018], which achieves transmit diversity by transmitting the same data symbol over activated subcarriers. Similarly, coded OFDM-IM incorporates a simple transmit diversity scheme to enhance the error performance of OFDM-IM [Choi, 2017]. Coordinate interleaved OFDM-IM (CI-OFDM-IM) [Başar, 2015] improves reliability by transmitting the real and imaginary parts of data symbols over different subcarriers and achieves a diversity order of two. Another novel scheme, OFDM with power distribution IM (OFDM-PIM) [Dogukan and Basar, 2020a], provides additional diversity gain by transmitting data symbols through two subcarriers with different power levels (high and low). Building on this concept, CI-OFDM-PIM [Dogukan et al., 2022] combines CI with power distribution, ensuring a diversity gain equal to the subblock size by distributing coordinate-interleaved data symbols across two subcarriers with high and low power levels. To further enhance error performance, Repeated IM-OFDM with CI (RIM-OFDM-CI) was introduced in [Thanh et al., 2018]. This scheme transmits coordinate-interleaved data symbols using identical subcarrier indices across different clusters, enabling improved detection of index bits. It has been demonstrated that RIM-OFDM-CI outperforms both OFDM-IM and CI-OFDM-IM in terms of error performance while maintaining the same spectral efficiency. The work in [Thanh et al., 2018] was later extended in [Le et al., 2021] by optimizing the signal constellation rotation angle and developing low-complexity detectors to reduce receiver complexity. A comprehensive survey of OFDM-IM-based schemes is presented in [Mao et al., 2018], highlighting the advancements and challenges in the field. Despite these notable improvements, there remains a pressing need for OFDM-IM-based waveform designs that deliver superior error performance without sacrificing spectral efficiency. In this context, our focus is on increasing the number of additional data bits transmitted by IM while maintaining robust diversity gain.

In this chapter, a novel OFDM-IM-based transmission scheme called *coordinate interleaved OFDM with IQ IM (CI-OFDM-IQIM)*, which provides additional diversity gain compared to conventional OFDM-IM, is proposed. In contrast to CI-OFDM-IM, in CI-OFDM-IQIM, all subblocks are separated into two clusters with equal number of subcarriers. In CI-OFDM-IQIM, four distinct SAPs are determined by the incoming data bits to transmit the real and imaginary parts of the first and second halves of data symbol vector. Since the real and imaginary parts of each data symbol are conveyed over two different subcarriers, a diversity order of two is ensured. Additionally, a low-complexity detector is designed to decode CI-OFDM-IQIM subblocks, where IM bits and data symbols are decoded by LLR-based technique and single symbol detection, respectively. We have derived an upper bound on the ABEP. Moreover, diversity order of the proposed scheme is analyzed, and an optimum rotation angle selection strategy is presented. Finally, error performance comparisons between the proposed and benchmark schemes are presented through comprehensive computer simulations under perfect and imperfect CSI.

2.2 System Model

CI-OFDM-IQIM is an OFDM-based transmission system, which consists of N_F subcarriers. As shown in Fig. 2.1, the system begins with B input bits, which are separated into G groups of b bits each, where $b = B/G$. Each group of b bits is used to generate a CI-OFDM-IQIM subblock of size $N_S = N_F/G$, with N_S being an even number greater than 2. Each subblock is further divided into two clusters of length

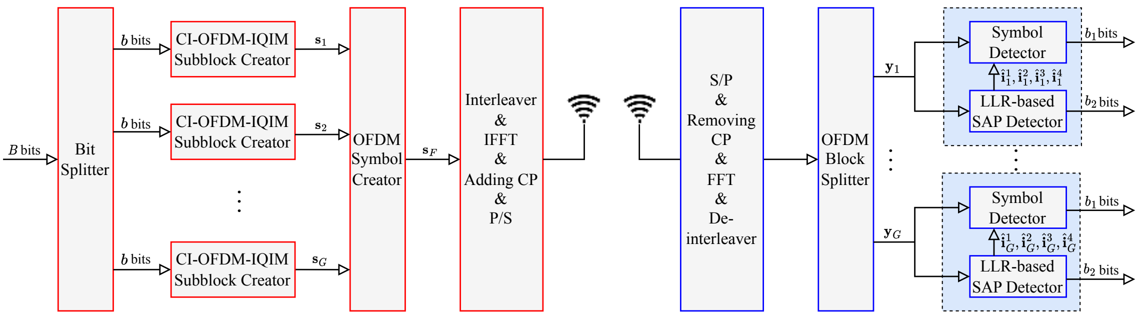

Figure 2.1: Transceiver architecture of CI-OFDM-IQIM.

$N_C = N_S/2$.

The process for forming a CI-OFDM-IQIM subblock can be demonstrated by considering only the ξ^{th} subblock $\mathbf{s}_\xi$, since the same steps are applied to all subblocks, where $\xi = 1, \cdots, G$. To construct $\mathbf{s}_\xi$, the b bits are split into two groups containing b_1 and b_2 bits, respectively. First, $b_1 = 2K \log_2 M$ bits are used to determine the ξ^{th} data symbol vector $\mathbf{x}_\xi = [x_{\xi,1}, \cdots, x_{\xi,2K}]^{\text{T}}$, where $x_{\xi,\kappa} \in \mathcal{M}^\theta$ for $\kappa = 1, \cdots, 2K$. Here, K represents the number of active subcarriers in a cluster, and $\mathcal{M}^\theta$ denotes an M-ary constellation rotated by an angle θ. Note that constellation rotation is essential to exploit diversity in CI-based schemes [Khan and Rajan, 2006]. Then, $\mathbf{x}_\xi$ is split into two parts: $\mathbf{x}_\xi^1 = [x_{\xi,1}, \cdots, x_{\xi,K}]^{\text{T}}$ and $\mathbf{x}_\xi^2 = [x_{\xi,K+1}, \cdots, x_{\xi,2K}]^{\text{T}}$, $\mathbf{x}_\xi = [(\mathbf{x}_\xi^1)^{\text{T}}, (\mathbf{x}_\xi^2)^{\text{T}}]^{\text{T}}$ and the real and imaginary parts of these vectors are obtained as $\mathbf{x}_\xi^1 = \mathbf{x}_\xi^{(1,\mathfrak{R})} + j\mathbf{x}_\xi^{(1,\mathfrak{I})}$ and $\mathbf{x}_\xi^2 = \mathbf{x}_\xi^{(2,\mathfrak{R})} + j\mathbf{x}_\xi^{(2,\mathfrak{I})}$. Moreover, $b_2 = 4\lfloor \log_2 \binom{N_C}{K} \rfloor$ bits are separated into four groups, each group of $b_2/4$ bits determines an SAP $\mathbf{i}_\xi^\nu = [i_{\xi,1}^\nu, \cdots, i_{\xi,K}^\nu]^{\text{T}}$, $i_{\xi,k}^\nu \in \{1, \cdots, N\}$, $k = 1, \cdots, K$, $\nu = 1, \cdots, 4$. The entries of $\mathbf{x}_\xi^{(1,\mathfrak{R})}$ and $\mathbf{x}_\xi^{(2,\mathfrak{I})}$ are placed into the first cluster $\mathbf{c}_\xi^1$ with the entries of $\mathbf{i}_\xi^1$ and $\mathbf{i}_\xi^4$, respectively. Moreover, the entries of $\mathbf{x}_\xi^{(2,\mathfrak{R})}$ and $\mathbf{x}_\xi^{(1,\mathfrak{I})}$ are placed into the second cluster $\mathbf{c}_\xi^2$ with the entries of $\mathbf{i}_\xi^3$ and $\mathbf{i}_\xi^2$, respectively. Hence, the ξ^{th} subblock is obtained as $\mathbf{s}_\xi = [(\mathbf{c}_\xi^1)^{\text{T}}, (\mathbf{c}_\xi^2)^{\text{T}}]^{\text{T}}$. The number of bits transmitted by a single CI-OFDM-IQIM subblock is given by

$$b = 2K \log_2 M + 4 \left\lfloor \log_2 \binom{N_C}{K} \right\rfloor. \tag{2.1}$$

Finally, by concatenating all subblocks, the overall transmitted OFDM symbol in the frequency domain is expressed as $\mathbf{s}_F = [\mathbf{s}_1^{\mathrm{T}}, \cdots, \mathbf{s}_G^{\mathrm{T}}]^{\mathrm{T}}$. Unlike the scheme in [Başar, 2015], where CI is directly applied to the data symbols, this scheme applies CI selectively. Specifically, after placing the data symbols into the subblocks, some of the data symbols may be coordinate interleaved.

For simplicity, we provide an example that demonstrates the creation of a CI-OFDM-IQIM subblock. We remove the subscript ξ for the ease of presentation.

Example: Assume that $N_C = 4$, $K = 2$, $\mathbf{i}^1 = [1, 3]^T$, $\mathbf{i}^2 = [1, 4]^T$, $\mathbf{i}^3 = [2, 3]^T$, and $\mathbf{i}^4 = [2, 3]^T$. With these parameters, an example subblock is obtained as:

$$\mathbf{s} = \left[x_1^{\Re}, jx_3^{\Im}, x_2^{\Re} + jx_4^{\Im}, 0 \,|\, jx_1^{\Im}, x_3^{\Re}, x_4^{\Re}, jx_2^{\Im}\right]^{\mathrm{T}}. \tag{2.2}$$

After constructing the overall OFDM symbol by repeating the same procedure for all subblocks, a block-type interleaver, as used in [Başar, 2015], is applied. The time-domain signal is then obtained by performing an IFFT. A CP of length L is added to the beginning of the OFDM frame. Following this, P/S conversion and digital-to-analog transformation are performed, preparing the signal for transmission.

The time-domain OFDM signal is transmitted through a T-tap frequency-selective Rayleigh fading channel. The channel is characterized by CIR coefficients:

$$\mathbf{h}_t = [h_t(1) \cdots h_t(T)]^{\mathrm{T}}, \tag{2.3}$$

where $h_t(\beta), \beta = 1, \cdots, T$ are circularly symmetric complex Gaussian RVs with distribution $\mathcal{CN}(0, 1/T)$.

At the receiver, the signal is first processed by removing the CP. Subsequently, a FFT is applied to convert the signal to the frequency domain, followed by a deinterleaving operation. The resulting equivalent input-output relationship for ξ^{th} subblock in the frequency domain can then be expressed as:

$$\mathbf{y}_\xi = \mathbf{S}_\xi \mathbf{h}_\xi + \mathbf{n}_\xi, \tag{2.4}$$

where $\mathbf{S}_\xi = \mathrm{diag}(\mathbf{s}_\xi)$ represents the transmitted signal, while $\mathbf{y}_\xi$, $\mathbf{h}_\xi$, and $\mathbf{n}_\xi$ denote the received signal vector, channel coefficients, and noise samples vector for the ξ^{th} subblock, respectively. The elements of $\mathbf{n}_\xi$ and $\mathbf{h}_\xi$ are distributed as $\mathcal{CN}(0, N_0)$ and

$\mathcal{CN}(0, 1)$, respectively, where N_0 denotes the noise variance. By neglecting the effect of the CP, the spectral efficiency of the system is given by: $\eta = B/N_F$.

ML detection for the ξ^{th} subblock can be performed using the set:

$$\mathcal{S} = \{\mathbf{s}(1), \mathbf{s}(2), \cdots, \mathbf{s}(2^b)\}, \tag{2.5}$$

which includes all possible realizations of the subblock. The aim is to detect the transmitted subblock $\mathbf{s}_\xi$ by comparing the received signal with every possible candidate in the set $\mathcal{S}$.

$$\hat{\mathbf{s}}_\xi = \arg \min_{\mathbf{s}_\xi \in \mathcal{S}} \|\mathbf{y}_\xi - \mathbf{S}_\xi \mathbf{h}_\xi\|^2. \tag{2.6}$$

The ML detector performs an exhaustive search over all possible SAPs and data symbols, making it computationally infeasible for larger values of N_S, K, and M. To address this limitation and reduce detection complexity, we propose a LLR-based detector for CI-OFDM-IQIM.

2.2.1 Low-Complexity LLR Detector For CI-OFDM-IQIM

Algorithm 1 Low-Complexity LLR-Based SAP Detector for CI-OFDM-IQIM

Input: $\bar{\mathbf{y}}$, N_0, $\mathcal{M}^{(\theta,\mathfrak{R})}$, $\mathcal{M}^{(\theta,\mathfrak{I})}$, $\mathcal{I}$

Output: $\hat{\mathbf{i}}^1$, $\hat{\mathbf{i}}^2$, $\hat{\mathbf{i}}^3$, $\hat{\mathbf{i}}^4$

for $c = 1$ **to** N_C **do**
  for $\chi = 1$ **to** M **do**
    $\Delta^{\mathfrak{R}}_{(1,1)} = -\frac{|h(c)|^2}{N_0}|\bar{y}^{\mathfrak{R}}(c) - \mathcal{M}^{(\theta,\mathfrak{R})}(\chi)|^2$
    $\Delta^{\mathfrak{R}}_{(1,2)} = -\frac{|h(c)|^2}{N_0}|\bar{y}^{\mathfrak{R}}(c)|^2$
    $\Delta^{\mathfrak{R}}_{(2,1)} = -\frac{|h(N_C+c)|^2}{N_0}|\bar{y}^{\mathfrak{R}}(N_C+c) - \mathcal{M}^{(\theta,\mathfrak{R})}(\chi)|^2$
    $\Delta^{\mathfrak{R}}_{(2,2)} = -\frac{|h(N_C+c)|^2}{N_0}|\bar{y}^{\mathfrak{R}}(N_C+c)|^2$
    $\Delta^{\mathfrak{I}}_{(1,1)} = -\frac{|h(c)|^2}{N_0}|\bar{y}^{\mathfrak{I}}(c) - \mathcal{M}^{(\theta,\mathfrak{I})}(\chi)|^2$
    $\Delta^{\mathfrak{I}}_{(1,2)} = -\frac{|h(c)|^2}{N_0}|\bar{y}^{\mathfrak{I}}(c)|^2$
    $\Delta^{\mathfrak{I}}_{(2,1)} = -\frac{|h(N_C+c)|^2}{N_0}|\bar{y}^{\mathfrak{I}}(N_C+c) - \mathcal{M}^{(\theta,\mathfrak{I})}(\chi)|^2$
    $\Delta^{\mathfrak{I}}_{(2,2)} = -\frac{|h(N_C+c)|^2}{N_0}|\bar{y}^{\mathfrak{I}}(N_C+c)|^2$
    $\mathbf{\Lambda}^{\mathfrak{R}}_1(\chi,c) = \Delta^{\mathfrak{R}}_{(1,1)} - \Delta^{\mathfrak{R}}_{(1,2)} + \log(\frac{K}{N_C-K})$
    $\mathbf{\Lambda}^{\mathfrak{R}}_2(\chi,c) = \Delta^{\mathfrak{R}}_{(2,1)} - \Delta^{\mathfrak{R}}_{(2,2)} + \log(\frac{K}{N_C-K})$
    $\mathbf{\Lambda}^{\mathfrak{I}}_1(\chi,c) = \Delta^{\mathfrak{I}}_{(1,1)} - \Delta^{\mathfrak{I}}_{(1,2)} + \log(\frac{K}{N_C-K})$
    $\mathbf{\Lambda}^{\mathfrak{I}}_2(\chi,c) = \Delta^{\mathfrak{I}}_{(2,1)} - \Delta^{\mathfrak{I}}_{(2,2)} + \log(\frac{K}{N_C-K})$
  end for
  $\Xi^{\mathfrak{R}}_1 = \mathbf{\Lambda}^{\mathfrak{R}}_1(1,c)$
  $\Xi^{\mathfrak{R}}_2 = \mathbf{\Lambda}^{\mathfrak{R}}_2(1,c)$
  $\Xi^{\mathfrak{I}}_1 = \mathbf{\Lambda}^{\mathfrak{I}}_1(1,c)$
  $\Xi^{\mathfrak{I}}_2 = \mathbf{\Lambda}^{\mathfrak{I}}_2(1,c)$
  for $\chi = 2$ **to** M **do**
    $\psi^{\mathfrak{R}}_1 = \log(1+\exp(-|\Xi^{\mathfrak{R}}_1 - \mathbf{\Lambda}^{\mathfrak{R}}_1(\chi,c)|))$
    $\psi^{\mathfrak{R}}_2 = \log(1+\exp(-|\Xi^{\mathfrak{R}}_2 - \mathbf{\Lambda}^{\mathfrak{R}}_2(\chi,c)|))$
    $\psi^{\mathfrak{I}}_1 = \log(1+\exp(-|\Xi^{\mathfrak{I}}_1 - \mathbf{\Lambda}^{\mathfrak{I}}_1(\chi,c)|))$
    $\psi^{\mathfrak{I}}_2 = \log(1+\exp(-|\Xi^{\mathfrak{I}}_2 - \mathbf{\Lambda}^{\mathfrak{I}}_2(\chi,c)|))$
    $T^{\mathfrak{R}}_1 = \max(\Xi^{\mathfrak{R}}_1, \mathbf{\Lambda}^{\mathfrak{R}}_1(\chi,c)) + \psi^{\mathfrak{R}}_1$
    $T^{\mathfrak{R}}_2 = \max(\Xi^{\mathfrak{R}}_2, \mathbf{\Lambda}^{\mathfrak{R}}_2(\chi,c)) + \psi^{\mathfrak{R}}_2$
    $T^{\mathfrak{I}}_1 = \max(\Xi^{\mathfrak{I}}_1, \mathbf{\Lambda}^{\mathfrak{I}}_1(\chi,c)) + \psi^{\mathfrak{I}}_1$
    $T^{\mathfrak{I}}_2 = \max(\Xi^{\mathfrak{I}}_2, \mathbf{\Lambda}^{\mathfrak{I}}_2(\chi,c)) + \psi^{\mathfrak{I}}_2$
    $\Xi^{\mathfrak{R}}_1 = T^{\mathfrak{R}}_1$
    $\Xi^{\mathfrak{R}}_2 = T^{\mathfrak{R}}_2$
    $\Xi^{\mathfrak{I}}_1 = T^{\mathfrak{I}}_1$
    $\Xi^{\mathfrak{I}}_2 = T^{\mathfrak{I}}_2$
  end for
  $\Omega^{\mathfrak{R}}_1(c) = \Xi^{\mathfrak{R}}_1$
  $\Omega^{\mathfrak{R}}_2(c) = \Xi^{\mathfrak{R}}_2$
  $\Omega^{\mathfrak{I}}_1(c) = \Xi^{\mathfrak{I}}_1$
  $\Omega^{\mathfrak{I}}_2(c) = \Xi^{\mathfrak{I}}_2$
end for
for $\beta = 1$ **to** $2^{b_2/2}$ **do**
  $\breve{\Omega}^{\mathfrak{R}}_1(\beta) = \sum_k \Omega^{\mathfrak{R}}_1(\mathcal{I}_\beta(k))$
  $\breve{\Omega}^{\mathfrak{R}}_2(\beta) = \sum_k \Omega^{\mathfrak{R}}_2(\mathcal{I}_\beta(k))$
  $\breve{\Omega}^{\mathfrak{I}}_1(\beta) = \sum_k \Omega^{\mathfrak{I}}_1(\mathcal{I}_\beta(k))$
  $\breve{\Omega}^{\mathfrak{I}}_2(\beta) = \sum_k \Omega^{\mathfrak{I}}_2(\mathcal{I}_\beta(k))$
end for
$\hat{\mathbf{i}}^1 = \mathcal{I}_{\max(\breve{\Omega}^{\mathfrak{R}}_1)}$
$\hat{\mathbf{i}}^2 = \mathcal{I}_{\max(\breve{\Omega}^{\mathfrak{I}}_1)}$
$\hat{\mathbf{i}}^3 = \mathcal{I}_{\max(\breve{\Omega}^{\mathfrak{R}}_2)}$
$\hat{\mathbf{i}}^4 = \mathcal{I}_{\max(\breve{\Omega}^{\mathfrak{I}}_2)}$

The proposed LLR detector aims to detect the CI-OFDM-IQIM symbol subblock-by-subblock. For simplicity, we remove the subscript ξ.

The inputs of Algorithm 1 are given as follows:

- New received signal vector with zero-forcing (ZF) equalizer: $\bar{\mathbf{y}} = [\bar{y}_1, \cdots, \bar{y}_{N_S}]^{\mathrm{T}}$, $\bar{y}_\mu = y_\mu / h_\mu$, $\mu = 1, \cdots, N_S$.

- Two different constellation sets: $\mathcal{M}^{(\theta,\Re)}$, $\mathcal{M}^{(\theta,\Im)}$.

- A set including all legal SAPs: $\mathcal{I} = \{\mathbf{i}_1, \cdots, \mathbf{i}_{2^{b_2/2}}\}$

- Noise variance: N_0.

The major steps of Algorithm 1 are discussed below:

1. The LLR value of the c^{th} subcarrier is calculated between lines (1-38).

2. The LLR values are combined according to the legal SAPs between lines (39-44). Note that $\mathcal{I}_\beta(k)$ represents the k^{th} element of the β^{th} SAP.

3. The detected SAPs $(\hat{\mathbf{i}}^1, \hat{\mathbf{i}}^2, \hat{\mathbf{i}}^3, \hat{\mathbf{i}}^4)$ are provided between lines (45-48). Note that the function $\max(\breve{\Omega}_\lambda)$ gives the index of the maximum value of $\breve{\Omega}_\lambda$.

After obtaining $(\hat{\mathbf{i}}^1, \hat{\mathbf{i}}^2, \hat{\mathbf{i}}^3, \hat{\mathbf{i}}^4)$, the equivalent model is utilized to detect the k^{th} data symbol corresponding to the λ^{th} half of the data symbol vector $\mathbf{x}^\lambda$ as follows:

$$\hat{x}_k^\lambda = \min_{x \in \mathcal{M}^\theta} \|\breve{\mathbf{y}}_k^\lambda - \breve{\mathbf{H}}_k^\lambda [x^\Re \, x^\Im]^{\mathrm{T}}\|^2, \tag{2.7}$$

where $\breve{\mathbf{y}}_k^\lambda$ and $\breve{\mathbf{H}}_k^\lambda$ are given as follows:

$$\breve{\mathbf{y}}_k^1 = \begin{bmatrix} \mathbf{y}^\Re(\hat{\mathbf{i}}^1(k)) \\ \mathbf{y}^\Im(\hat{\mathbf{i}}^1(k)) \\ \mathbf{y}^\Re(\hat{\mathbf{i}}^2(k) + N_C) \\ \mathbf{y}^\Im(\hat{\mathbf{i}}^2(k) + N_C) \end{bmatrix}, \ \breve{\mathbf{y}}_k^2 = \begin{bmatrix} \mathbf{y}^\Re(\hat{\mathbf{i}}^4(k)) \\ \mathbf{y}^\Im(\hat{\mathbf{i}}^4(k)) \\ \mathbf{y}^\Re(\hat{\mathbf{i}}^3(k) + N_C) \\ \mathbf{y}^\Im(\hat{\mathbf{i}}^3(k) + N_C) \end{bmatrix}, \tag{2.8}$$

and

$$\breve{\mathbf{H}}_k^1 = \begin{bmatrix} \mathbf{h}^{\Re}(\hat{\mathbf{i}}^1(k)) & 0 \\ \mathbf{h}^{\Im}(\hat{\mathbf{i}}^1(k)) & 0 \\ 0 & -\mathbf{h}^{\Im}(\hat{\mathbf{i}}^2(k)+N_C) \\ 0 & \mathbf{h}^{\Re}(\hat{\mathbf{i}}^2(k)+N_C) \end{bmatrix}, \ \breve{\mathbf{H}}_k^2 = \begin{bmatrix} 0 & -\mathbf{h}^{\Im}(\hat{\mathbf{i}}^4(k)) \\ 0 & \mathbf{h}^{\Re}(\hat{\mathbf{i}}^4(k)) \\ \mathbf{h}^{\Re}(\hat{\mathbf{i}}^3(k)+N_C) & 0 \\ \mathbf{h}^{\Im}(\hat{\mathbf{i}}^3(k)+N_C) & 0 \end{bmatrix}, \tag{2.9}$$

respectively, for $\lambda = 1, 2$.

2.3 Performance Analysis

In this section, we derive the theoretical upper bound on the BEP for the proposed schemes and analyze their diversity order. Additionally, we present an optimization strategy for the θ parameter to minimize the BER, thereby enhancing error performance.

2.3.1 Theoretical Upper Bound on BEP

In this subsection, we derive an upper bound for the BEP of the proposed schemes using ML detection. By applying (6.5), the CPEP, which represents the probability of incorrectly detecting $\hat{\mathbf{S}}$ when $\mathbf{S}$ is transmitted, conditioned on $\mathbf{h}$, is expressed as follows:

$$\mathrm{P}(\mathbf{S} \to \hat{\mathbf{S}}|\mathbf{h}) = \mathrm{Q}\left(\sqrt{\frac{E_b}{2N_0}\left|\left|(\mathbf{S}-\hat{\mathbf{S}})\mathbf{h}\right|\right|^2}\right), \tag{2.10}$$

where E_b is the average transmitted energy per bit, defined as $E_b = \frac{N_F+T}{B}$. Next, by approximating the Q-function as $\mathrm{Q}(x) \approx \frac{e^{-2x^2/3}}{4} + \frac{e^{-x^2/2}}{12}$, the UPEP can be derived as shown in [Başar et al., 2013]:

$$\mathrm{P}(\mathbf{S} \to \hat{\mathbf{S}}) = E_{\mathbf{h}}\{\mathrm{P}(\mathbf{S} \to \hat{\mathbf{S}}|\mathbf{h})\} \approx \frac{1/4}{\det(\mathbf{I}_{N_S}+\phi_1\mathbf{A})} + \frac{1/12}{\det(\mathbf{I}_{N_S}+\phi_2\mathbf{A})}, \tag{2.11}$$

where $\phi_1 = \frac{1}{3N_0}$, $\phi_2 = \frac{1}{4N_0}$, and $\mathbf{A} = (\mathbf{S}-\hat{\mathbf{S}})^{\mathrm{H}}(\mathbf{S}-\hat{\mathbf{S}})$ represents the $N_s \times N_s$ difference matrix. The BER of CI-OFDM-RIQIM can then be upper bounded as follows:

$$P_b \leq \frac{1}{b2^b}\sum_{\mathbf{S}}\sum_{\hat{\mathbf{S}}} \mathrm{P}(\mathbf{S} \to \hat{\mathbf{S}})\mathrm{e}(\mathbf{S}, \hat{\mathbf{S}}), \tag{2.12}$$

where $\mathrm{e}(\mathbf{S}, \hat{\mathbf{S}})$ denotes the number of erroneous bits when $\mathbf{S}$ is transmitted but incorrectly detected as $\hat{\mathbf{S}}$.

2.3.2 Diversity Analysis

In this subsection, we investigate the diversity order of CI-OFDM-IQIM by considering two cases: (a) erroneous detection of index bits while data symbols are correctly decoded and (b) erroneous detection of single or multiple data symbols while index bits are correctly decoded. For case (a), assume that subblock $\mathbf{s}$ with the parameters $\mathbf{i}^1 = [1,3]^{\mathrm{T}}$, $\mathbf{i}^2 = [1,3]^{\mathrm{T}}$, $\mathbf{i}^3 = [1,3]^{\mathrm{T}}$, and $\mathbf{i}^4 = [1,3]^{\mathrm{T}}$, is transmitted; however, subblock $\hat{\mathbf{s}}$ with the parameters $\hat{\mathbf{i}}^1 = [1,3]^{\mathrm{T}}$, $\hat{\mathbf{i}}^2 = [1,3]^{\mathrm{T}}$, $\hat{\mathbf{i}}^3 = [1,4]^{\mathrm{T}}$, and $\hat{\mathbf{i}}^4 = [1,3]^{\mathrm{T}}$, is erroneously decoded for the given parameters $N_C = 4$ and $K = 2$ while data symbols are assumed to be correctly decoded. This error event can be expressed as:

In this subsection, we analyze the diversity order of CI-OFDM-IQIM by considering two scenarios: (a) erroneous detection of index bits while the data symbols are correctly decoded and (b) erroneous detection of one or more data symbols while the index bits are correctly decoded. For case (a), assume that subblock $\mathbf{s}$, with SAPs $\mathbf{i}^1 = [1,3]^{\mathrm{T}}$, $\mathbf{i}^2 = [1,3]^{\mathrm{T}}$, $\mathbf{i}^3 = [1,3]^{\mathrm{T}}$, and $\mathbf{i}^4 = [1,3]^{\mathrm{T}}$, is transmitted. However, the receiver erroneously decodes subblock $\hat{\mathbf{s}}$ with SAPs $\hat{\mathbf{i}}^1 = [1,3]^{\mathrm{T}}$, $\hat{\mathbf{i}}^2 = [1,3]^{\mathrm{T}}$, $\hat{\mathbf{i}}^3 = [1,4]^{\mathrm{T}}$, and $\hat{\mathbf{i}}^4 = [1,3]^{\mathrm{T}}$. This error occurs for the given parameters $N_C = 4$ and $K = 2$, while assuming the data symbols are correctly decoded. This error event can be mathematically expressed as:

$$\begin{aligned}\mathbf{s} \rightarrow \hat{\mathbf{s}} = &\left[x_1^{\Re} + jx_3^{\Im}, 0, x_2^{\Re} + jx_4^{\Im}, 0 \mid x_3^{\Re} + jx_1^{\Im}, 0, x_4^{\Re} + jx_2^{\Im}, 0\right]^{\mathrm{T}} \\ &\rightarrow \left[x_1^{\Re} + jx_3^{\Im}, 0, x_2^{\Re} + jx_4^{\Im}, 0 \mid x_3^{\Re} + jx_1^{\Im}, 0, jx_2^{\Im}, x_4^{\Re}\right]^{\mathrm{T}}.\end{aligned} \tag{2.13}$$

This specific example represents the worst-case scenario, which yields a diversity order of $\Gamma = 2$, where $\Gamma = \mathrm{rank}(\mathbf{A})$.

For case (b), assume that subblock $\mathbf{s}$, containing data symbols x_1, x_2, x_3, x_4, is transmitted. However, subblock $\hat{\mathbf{s}}$ is erroneously decoded with a single symbol error, specifically $\hat{x}_1$ instead of x_1, while the other symbols x_2, x_3, x_4 decoded accurately.

The SAPs $\mathbf{i}^1 = [1,3]^\mathrm{T}$, $\mathbf{i}^2 = [1,3]^\mathrm{T}$, $\mathbf{i}^3 = [1,3]^\mathrm{T}$, and $\mathbf{i}^4 = [1,4]^\mathrm{T}$ are assumed to be correctly detected. This example case considers other system parameters as $N_C = 4$ and $K = 2$. The error event can be expressed as follows:

$$\begin{aligned} \mathbf{s} \rightarrow \hat{\mathbf{s}} &= \left[x_1^{\Re} + jx_3^{\Im}, 0, x_2^{\Re} + jx_4^{\Im}, 0 \mid x_3^{\Re} + jx_1^{\Im}, 0, x_4^{\Re} + jx_2^{\Im}, 0\right]^\mathrm{T} \\ &\rightarrow \left[\hat{x}_1^{\Re} + jx_3^{\Im}, 0, x_2^{\Re} + jx_4^{\Im}, 0 \mid x_3^{\Re} + j\hat{x}_1^{\Im}, 0, x_4^{\Re} + jx_2^{\Im}, 0\right]^\mathrm{T}. \end{aligned} \tag{2.14}$$

As shown in (2.14), even the erroneous detection of a single data symbol results in errors over two distinct subcarriers. This ensures a diversity order of $\Gamma = 2$. Therefore, the proposed scheme guarantees that $\min_{\mathbf{s},\hat{\mathbf{s}}}(\Gamma) = 2$, which proves that the diversity order of CI-OFDM-IQIM is 2.

2.3.3 Optimization

In this subsection, we determine the optimum value of θ that minimizes the BER by searching over angles from 1° to 89° with increments of 1°. Since the QAM constellation repeats every 90°, the search is restricted to this range. The angle that results in the lowest BER for a given SNR is selected as the optimum rotation angle for the system. Additionally, the proposed LLR detector is exploited to identify the optimal rotation angle for higher modulation orders, as it is not feasible to perform this search using ML detection.

2.4 Simulation Results And Comparisons

In this section, CI-OFDM-IQIM is evaluated through computer simulations and compared with various OFDM-IM-based reference schemes. All simulations are conducted using the system parameters $N_F = 128$, $L = 16$, and a $T = 10$-tap Rayleigh fading channel.

For simplicity, the following naming conventions are adopted:

- "OFDM-IM (N_S, K, M)" refers to the OFDM-IM scheme.
- "OFDM-IQ-IM (N_S, K, M)" refers to the OFDM-IQ-IM scheme.

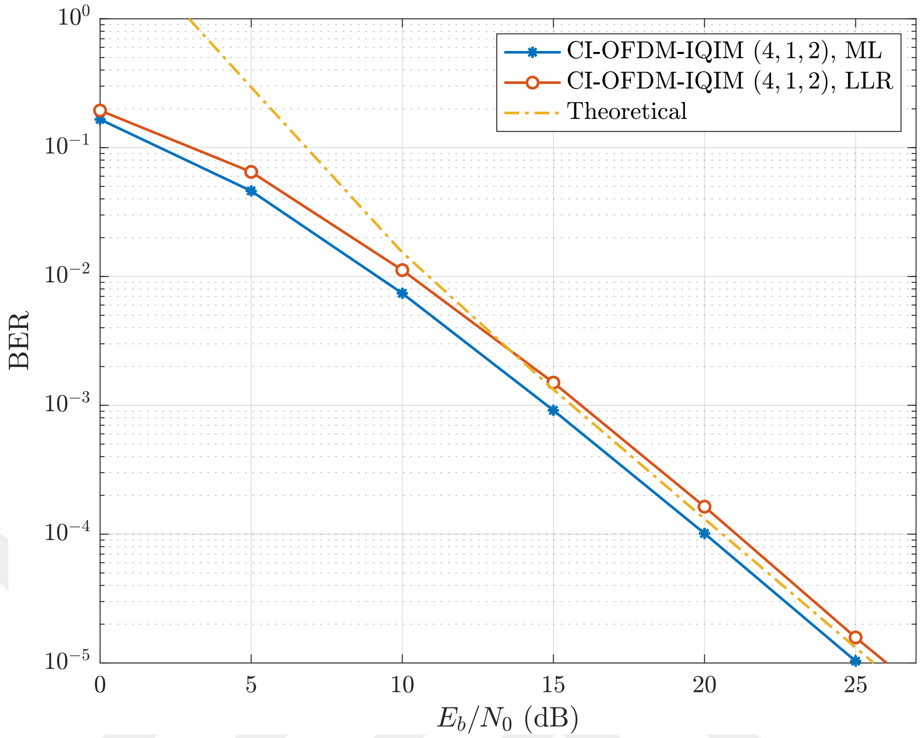

Figure 2.2: Error Performance of CI-OFDM-IQIM with ML and LLR Detectors at a Spectral Efficiency of 1.25 bps/Hz.

- "CI-OFDM-IM (N_S, K, M)" refers to the CI-OFDM-IM scheme.
- "ReMO (N_S, K, M)" refers to the ReMO scheme.

In these schemes, K out of N_S subcarriers are activated in each subblock, and M represents the modulation order.

Similarly, the following definitions are used for cluster-based schemes:

- "RIM-OFDM-CI (N_C, K, M)" refers to the RIM-OFDM-CI scheme.
- "CI-OFDM-RIQIM (N_C, K, M)" refers to the CI-OFDM-RIQIM scheme.
- "CI-OFDM-IQIM (N_C, K, M)" refers to the CI-OFDM-IQIM scheme.

In these cases, K subcarriers are active in each cluster of size N_C, and M denotes the modulation order. It is important to note that the optimum rotation angles used

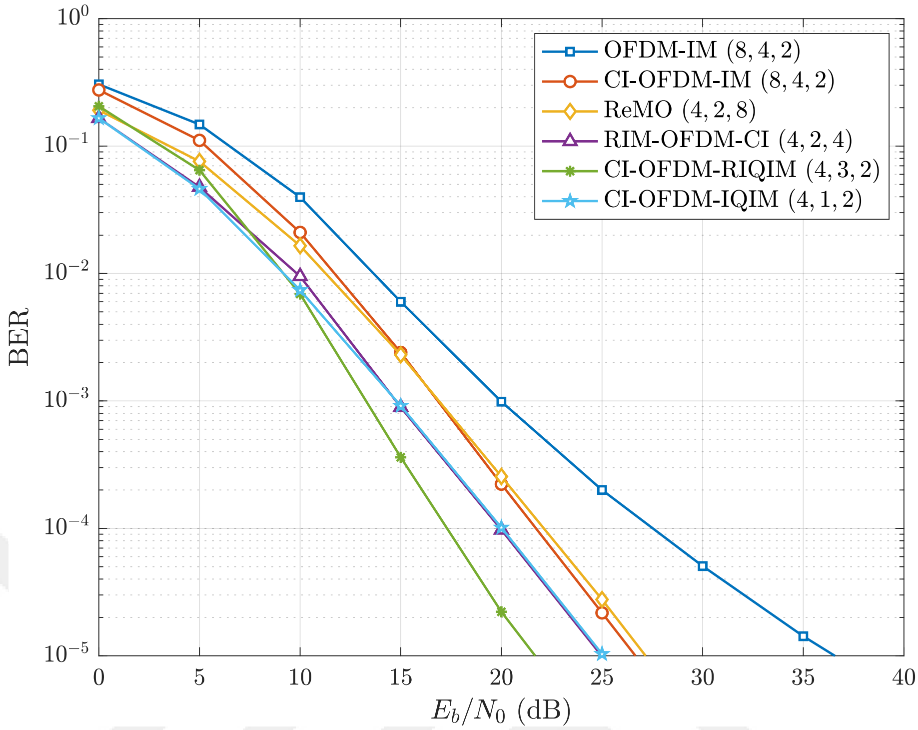

Figure 2.3: Error Performance Comparison of CI-OFDM-IQIM with Benchmark Schemes at a Spectral Efficiency of 1.25 bps/Hz.

in simulations for the proposed schemes are determined based on the optimization strategy outlined in Section 2.3.3.

As shown in Fig. 2.2, the theoretical BER curve obtained from (2.12) serves as an accurate upper bound for CI-OFDM-IQIM. Additionally, the proposed LLR detector demonstrates sub-optimal performance compared to the ML detector, as observed in Fig. 2.2.

In Fig. 2.3, the error performance of CI-OFDM-IQIM is compared with reference schemes at a spectral efficiency of 1.25 bps/Hz. The results demonstrate that CI-OFDM-RIQIM outperforms all benchmark schemes in terms of error performance. Notably, CI-OFDM-RIQIM achieves nearly a 4 dB gain over the nearest benchmark, despite utilizing a lower modulation order due to the doubled number of IM bits. Furthermore, CI-OFDM-IQIM achieves approximately the same error performance as RIM-OFDM-CI, while requiring a lower modulation order and fewer active subcarriers. This improvement is attributed to the quadrupling of the number

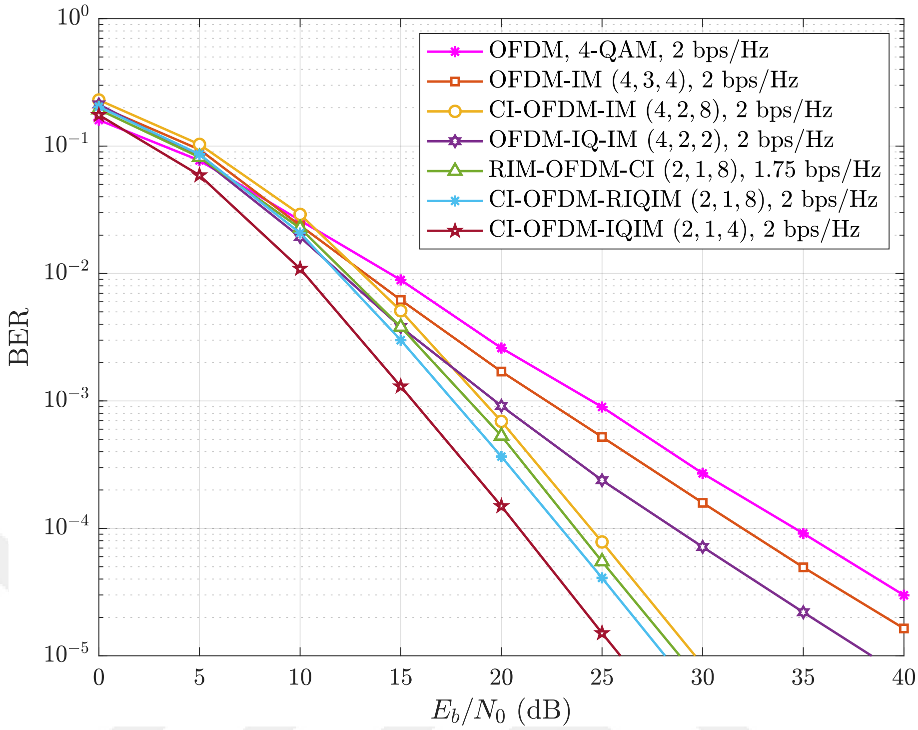

Figure 2.4: Error performance comparison of CI-OFDM-IQIM with benchmark schemes.

of transmitted IM bits.

Fig. 2.4 presents an error performance comparison between the proposed schemes and benchmark schemes, with a subblock size of 4. From Fig. 2.4, it can be observed that CI-OFDM-IQIM significantly outperforms both CI-OFDM-RIQIM and the benchmark schemes. This improvement is achieved because CI-OFDM-IQIM provides the same data rate with a lower modulation order, owing to the increased number of IM bits. Furthermore, CI-OFDM-IQIM demonstrates superior error performance compared to RIM-OFDM-CI, while achieving a 14.3% higher spectral efficiency.

In Fig. 2.5, CI-OFDM-IQIM is compared with benchmark schemes in terms of BER performance under the following conditions: spectral efficiency for the benchmark schemes is 2.75 bps/Hz, $N_S = 8$, and LLR detectors are employed in all simulations. The spectral efficiency values for CI-OFDM-IQIM are set to 2.5 and 3 bps/Hz. As observed in Fig. 2.5, CI-OFDM-IQIM with a spectral efficiency of

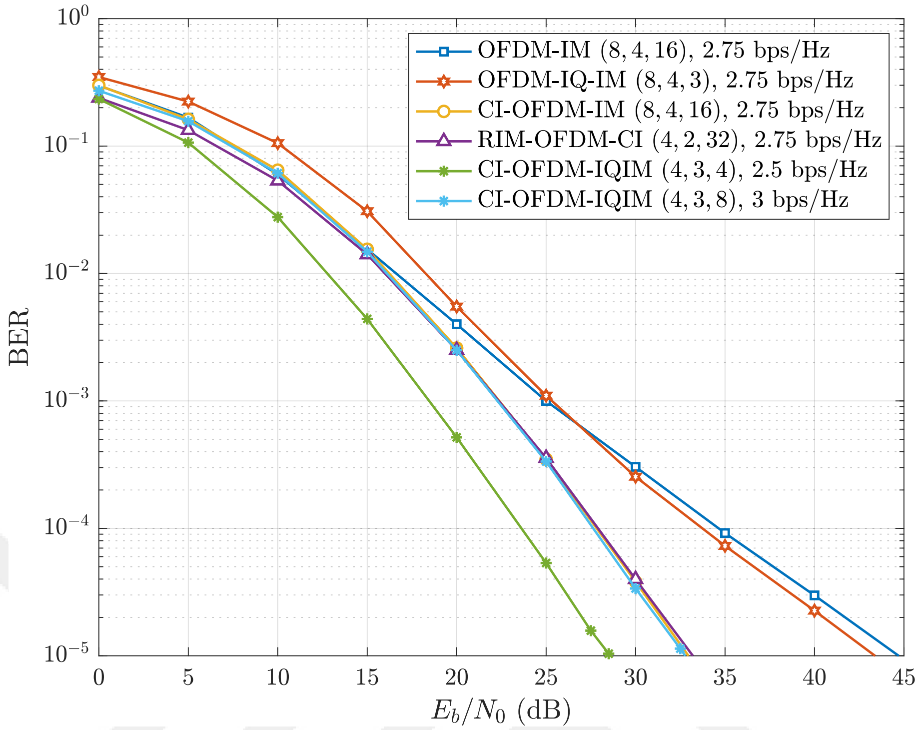

Figure 2.5: Error performance comparison of CI-OFDM-IQIM with benchmark schemes using LLR detectors.

2.5 bps/Hz outperforms the benchmark schemes in error performance, although it offers 9.1% less spectral efficiency. Additionally, CI-OFDM-IQIM with 3 bps/Hz achieves comparable error performance to its closest competitors, RIM-OFDM-CI and CI-OFDM-IM, while providing 9.1% higher spectral efficiency.

Fig. 2.6 illustrates the error performance of CI-OFDM-RIQIM and CI-OFDM-IQIM for varying cluster sizes, using LLR detectors, at a spectral efficiency of 2.5 bps/Hz. As the cluster size N_C increases, higher rank values are obtained more frequently. This explains why CI-OFDM-RIQIM with a larger subblock size outperforms other configurations, as observed in Fig. 2.6. In contrast, CI-OFDM-IQIM demonstrates similar error performance for the cases where $N_C = 4$ and $N_C = 8$.

While the previous simulation results assume perfect CSI, Fig. 2.7 compares the error performance of the proposed and existing schemes, both of which provide a diversity order of two, under imperfect CSI conditions. In this scenario, ML detection is performed using the estimated channel matrix $\hat{\mathbf{H}} = \mathrm{diag}([\hat{h}_1, \cdots, \hat{h}_{N_S}]^{\mathrm{T}})$ instead

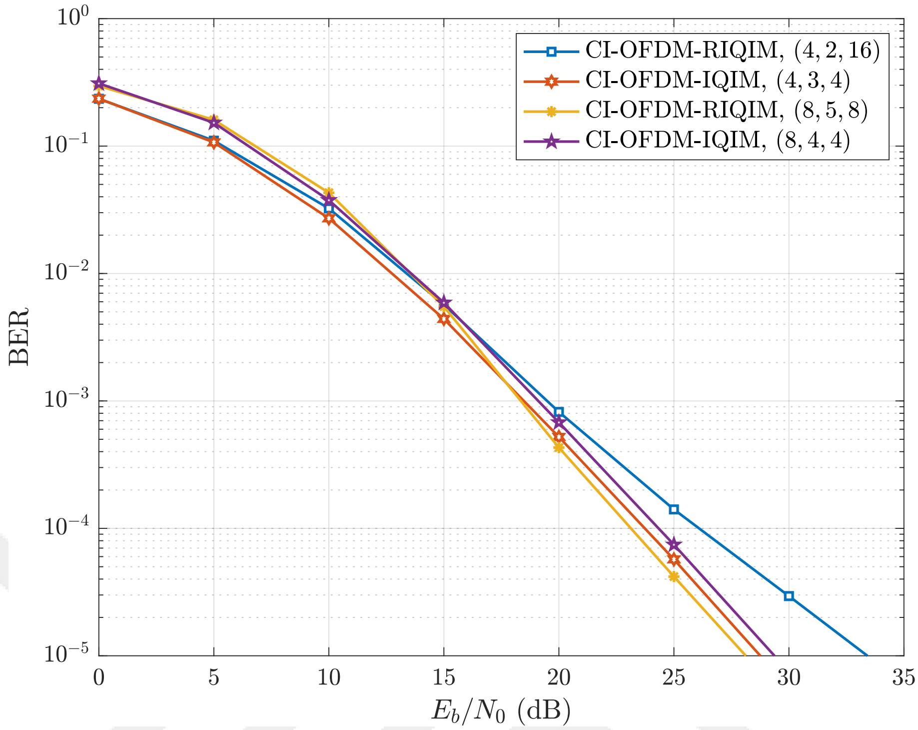

Figure 2.6: Error performance comparison of CI-OFDM-RIQIM and CI-OFDM-IQIM for different parameters at a spectral efficiency of 2.5 bps/Hz.

of the true channel matrix $\mathbf{H}$ from (2.4), following the approach in [Van Luong et al., 2018].

The channel is modeled as $\mathbf{H} = \hat{\mathbf{H}} + \mathbf{E}$, where $\mathbf{E} = \text{diag}([e_1, \cdots, e_{N_S}]^{\mathrm{T}})$ represents the channel estimation error matrix. Each element of $\mathbf{E}$ is distributed as $e_\alpha \sim \mathcal{CN}(0, \epsilon^2)$, for $\alpha = 1, \cdots, N_S$, where ϵ^2 denotes the error variance and satisfies $\epsilon^2 \in [0, 1)$. Consequently, the elements of $\hat{\mathbf{H}}$ follow the distribution $\hat{h}_\alpha \sim \mathcal{CN}(0, 1 - \epsilon^2)$.

Thus, the relationship for each sub-channel is expressed as $h_\alpha = \hat{h}_\alpha + e_\alpha$. The simulations in Fig. 2.7 are conducted under fixed CSI conditions with error variances of $\epsilon^2 = 0.05$ and $\epsilon^2 = 0.01$ As observed in Fig. 2.7, the proposed schemes consistently outperform the reference schemes. For example, at a BER value of 10^{-5} and $\epsilon^2 = 0.01$, CI-OFDM-IQIM achieves approximately 3 dB SNR gain over its closest competitor.

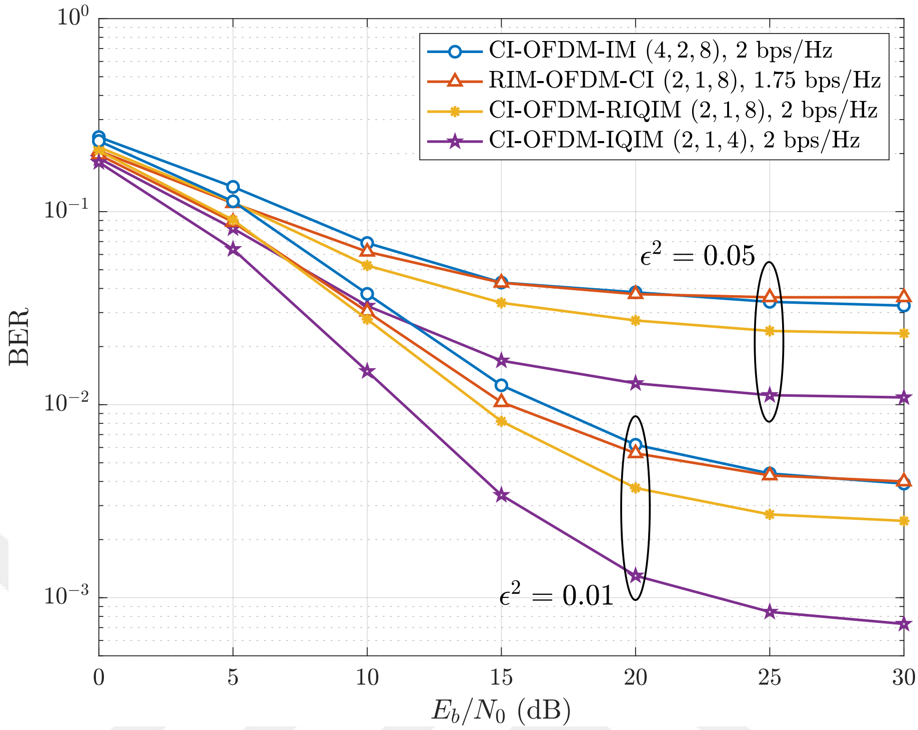

Figure 2.7: Error performance comparison of CI-OFDM-RIQIM and CI-OFDM-IQIM with benchmark schemes under imperfect CSI conditions for $\epsilon^2 = 0.05$ and $\epsilon^2 = 0.01$.

2.4.1 Complexity Analysis

In Table 2.1, the decoding complexity per subcarrier is compared for the proposed and benchmark schemes. As observed in Table 2.1, the decoding complexity order of CI-OFDM-IQIM is equivalent to that of classical OFDM and OFDM-IM, while offering improved error performance and additional diversity gain.

Additionally, the number of real multiplications required by the ML and LLR detectors is calculated to compare their decoding complexity in terms of real multiplications. The number of real multiplications required for the ML detector and the proposed LLR detector can be expressed as follows, respectively:

$$\mathfrak{C}^{\mathrm{ML}} = M^{2K} \times 2^{2\left\lfloor \log_2 \binom{N_C}{K} \right\rfloor} \times 6N_S, \tag{2.15}$$

$$\mathfrak{C}^{\mathrm{LLR}} = N_C \times (40M - 8) + 40M. \tag{2.16}$$

To provide a clearer understanding, we present a numerical example of the de-

Table 2.1: Decoding Complexity Comparison Per Subcarrier

System	**Detector**	**Complexity Order**
OFDM	ML	$\mathcal{O}(M)$
OFDM-IM	Red. Comp. ML	$\mathcal{O}(M)$
CI-OFDM-IM	Red. Comp. ML	$\mathcal{O}(M^2)$
OFDM-IQ-IM	Red. Comp. ML	$\mathcal{O}(M)$
RIM-OFDM-CI	Suboptimal	$\mathcal{O}(M^2)$
CI-OFDM-RIQIM	Suboptimal	$\mathcal{O}(M^2)$
CI-OFDM-IQIM	Suboptimal	$\mathcal{O}(M)$

coding complexity in terms of the number of real multiplications. Assuming $N_C = 4$, $K = 3$, and $M = 4$, the number of real multiplications required for the ML and LLR detectors are calculated as 3145728 and 768, respectively. This shows that the LLR detector achieves significantly lower decoding complexity compared to the ML detector in terms of real multiplications.

2.5 Conclusion

In this chapter, we proposed a novel diversity-achieving OFDM-IM-based transmission scheme called CI-OFDM-IQIM. The scheme divides all subblocks into two clusters, transmitting the real and imaginary parts of the data symbols over the active subcarriers in these clusters. Additionally, an LLR-based detector was designed to reduce the decoding complexity of CI-OFDM-IQIM subblocks. The error performance of the proposed scheme was extensively analyzed through computer simulations. Our findings demonstrate that CI-OFDM-IQIM achieves superior error performance, particularly at higher spectral efficiency values. This is attributed to the increased number of information bits transmitted through IM, enabling the system to achieve the same spectral efficiency with lower modulation orders. In conclusion, the diversity gain, remarkable error performance, and enhanced spectral efficiency of CI-OFDM-IQIM make it a promising candidate for next-generation communication services.

Chapter 3

RIS-AIDED ENHANCED RECEIVE SPATIAL MODULATION

3.1 Introduction

IM [Basar et al., 2017], which utilizes the indices of transmit entities such as antennas and time slots, has garnered considerable interest from researchers. This is due to its benefits over traditional communication systems, particularly in terms of reducing transceiver complexity and enhancing spectral and energy efficiency. Due to its highly flexible nature, IM has been applied in various domains such as frequency, time, code, and space, leading to numerous innovative designs presented in the literature. For example, different transmit entities such as subcarriers and transmit antennas have been exploited to realize IM in studies [Tugtekin et al., 2023] and [Kurt et al., 2023], respectively.

RIS [Basar et al., 2019] have also attracted immense interest from both academia and industries since they provide a solution to enhance wireless communication system. Through the use of programmable reflective elements, RISs can manipulate the manner through which electromagnetic waves are radiated, received, and reflected leading to enhanced signal quality, minimized interference, as well as spectral and energy efficiency [Basar et al., 2023]. RISs are unlike conventional reflectors, which can only change the direction of the impinging signal but cannot control its phase and amplitude, resulting in a smart and reconfigurable wireless environment. This flexibility makes RISs a powerful solution for dense urban areas with obstructions causing dead zones where signals cannot reach, as well as for implementing innovative technologies such as 5G.

Integrating IM with RIS has emerged as an intriguing research area due to its potential to significantly enhance the performance and efficiency of modern wireless communication systems. For the first time in [Basar, 2020], IM has been implemented in RIS-aided wireless systems, where RIS-SSK and RIS-SM schemes have been proposed. In these schemes, the index of the receive antenna is exploited to transmit information bits, with the phase values of RIS elements are adjusted based on the channel coefficients of the selected receive antenna. In [Yuan et al., 2021], to increase the number of information bits transmitted by IM in the receive antenna domain, a scheme called RIS-aided receive quadrature RM (RIS-RQRM) has been presented, where the RIS is split into two parts, each responsible for producing signals with only in-phase and quadrature components, respectively. In this study, since the RIS is partitioned into two groups, the number of RIS elements that specify each receive antenna is halved, leading to a degradation in received signal power in each specified antenna. To overcome this drawback, another receive antenna IM scheme, named RIS-assisted receive quadrature SSK (RIS-RQSSK) [Dinan et al., 2022], is proposed, where all RIS elements concurrently maximize the SNR for both the in-phase and quadrature components of the received signal at the chosen antennas. In [Zhang et al., 2022a], the RIS is amalgamated with the generalized SSK (GSSK) technique that employs the indices of more than one antenna to further increase the IM bits. RIS generalized SM (RIS-GSM) is another scheme introduced in [Zhang et al., 2021], where an enhanced antenna pattern and constellation design is provided. Moreover, RIS-assisted extended variable SM (RIS-EVSM) has been proposed in [Yue et al., 2024], where the RIS is partitioned into multiple parts to realize receive antenna IM. In RIS-EVSM, the number of receive antennas specified by the RIS parts is first determined, and then the antenna combination is selected based on additional information bits.

In this chapter, we propose a novel RIS-assisted receive antenna IM scheme called *RIS-aided enhanced receive SM (RIS-ERSM)*. In the proposed scheme, the number of receive antennas specified by the RIS is not fixed to enhance the number of IM bits. Instead, the RIS is split into multiple parts depending on the number of selected receive antennas. For each part of RIS to specify one of the selected

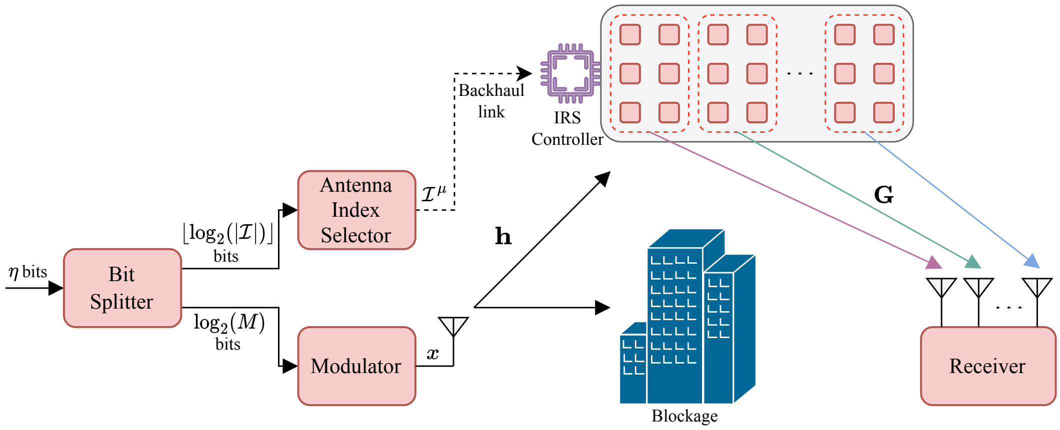

Figure 3.1: System model of the proposed RIS-ERSM scheme.

receive antenna, the phases of that RIS part are adjusted according to the channel coefficients corresponding to the selected receive antenna. RIS-ERSM introduces a clever receive antenna indexing technique that both increases the number of bits conveyed via the index/indices receive antennas and also maintains the received signal power obtained at each chosen receive antenna.

3.2 System Model

In this section, the system model of the proposed RIS-ERSM scheme is presented. As seen in Fig. 3.1, we consider a SIMO system with a single transmit antenna, N_r receive antennas and an RIS where the direct link between the transmitter and receiver is assumed to be blocked. Since there is no direct path between the transmitter and receiver, communication is enabled through the RIS which is configured by the transmitter through a backhaul link. The channel vector between the transmitter and RIS is indicated as $\mathbf{h} = [h_1, \cdots, h_N]^{\mathrm{T}}$, whereas the channel matrix between the RIS and receiver is given as $\mathbf{G} = [\mathbf{g}_1, \cdots, \mathbf{g}_{N_r}]^{\mathrm{T}} \in \mathbb{C}^{N_r \times N}$, $\mathbf{g}_r = [g_{r,1}, \cdots, g_{r,N}]^{\mathrm{T}}$, $r = 1, \cdots, N_r$, where N is the number of reflecting elements in RIS and $[\cdot]^{\mathrm{T}}$ denotes the transposition operator. The ith element of $\mathbf{h}$ and $\mathbf{g}_r$ follow complex Gaussian distribution with $h_i = \alpha_i e^{j\theta_i} \sim \mathcal{CN}(0, 1)$ and $g_{r,i} = \beta_{r,i} e^{j\phi_{r,i}} \sim \mathcal{CN}(0, 1)$ for $i = 1, \cdots, N$.

Table 3.1: Example of Mapping of B_2 Bits Into Antenna Combinations

B_2 bits	μ	$\mathcal{I}^{\mu}$	$\lvert\mathcal{I}^{\mu}\rvert$	$\bar{\mathcal{I}}^{\mu}$
$[0,0]$	1	$\{1\}$	1	$\{1,1\}$
$[0,1]$	2	$\{2\}$	1	$\{2,2\}$
$[1,0]$	3	$\{3\}$	1	$\{3,3\}$
$[1,1]$	4	$\{1,2\}$	2	$\{1,2\}$

3.2.1 RIS-ERSM Transmitter

In RIS-ERSM, the information bits are transmitted via both M-ary QAM/PSK modulated symbols and also the index/indices of receive antennas. As seen in Fig. 3.1, $B_1 = \log_2 M$ bits determine the M-ary modulated symbol x. Here, we define a set including all possible receive antenna combinations as $\mathcal{I} = \bigcup_{r=1}^{N_r} \mathcal{I}_r$, where $|\mathcal{I}| = \sum_{r=1}^{N_r} \binom{N_r}{r}$ and $|\cdot|$ is the cardinality of a set. Each $\mathcal{I}_r$ is a set containing all possible r-antenna combinations of N_r elements. Specifically, $\mathcal{I}_r$ can be expressed as:

$$\mathcal{I}_r = \{S \subseteq \{1, 2, \cdots, N_r\} \mid |S| = r\}. \tag{3.1}$$

In order to map information bits into a receive antenna combination, $B_2 = \lfloor \log_2 (|\mathcal{I}|) \rfloor$ number of bits are converted into a decimal value μ. The set $\mathcal{I}$ is considered as an ordered list, and the μ-th entity of $\mathcal{I}$, denoted as $\mathcal{I}^{\mu}$, is selected as the antenna combination. For simplicity, an example for mapping of B_2 information bits into antenna combinations is provided in Table 3.1 for $N_r = 3$. In this example, a total number of $|\mathcal{I}| = 7$ antenna combination can be generated: $\{1\}$, $\{2\}$, $\{3\}$, $\{1,2\}$, $\{1,3\}$, $\{2,3\}$, $\{1,2,3\}$; however, only $2^{\lfloor \log_2(7) \rfloor} = 4$ of them can be used to transmit information bits via the antenna combinations. The data rate of the RIS-ERSM for a given transmission interval can be given in terms of bpcu as:

$$\eta = \log_2 M + \lfloor \log_2(|\mathcal{I}|) \rfloor. \tag{3.2}$$

To maximize the instantaneous SNR on the selected receive antennas, the RIS is equally partitioned into $|\mathcal{I}^{\mu}|$ number of groups and the phase values of elements in the ζ-th RIS group are adjusted considering the channel coefficients from the RIS to the $\mathcal{I}^{\mu}[\zeta]$-th receive antenna, where ζ indicates the index within the combination, $\zeta = 1, \cdots, |\mathcal{I}^{\mu}|$. In each RIS group, there are $\bar{N} = N/|\mathcal{I}^{\mu}|$ elements and the reflection coefficient vector of the ζ-th RIS group is expressed as $\mathbf{\Psi}_{\zeta} = \text{diag}\left(\Psi_{\zeta}\right)$, $\Psi_{\zeta} = [e^{j\psi_{\zeta,1}}, \cdots, e^{j\psi_{\zeta,\bar{N}}}]^{\mathrm{T}}$, diag$(\cdot)$ is for diagonalization. For the RIS to specify the determined antenna combination, the phase value of the k-th element of the ζ-th RIS group is adjusted as:

$$\psi_{\zeta,k} = -\left(\theta_{(\zeta-1)\bar{N}+k} + \phi_{\mathcal{I}^{\mu}[\zeta],(\zeta-1)\bar{N}+k}\right), \tag{3.3}$$

where $k = 1, \cdots, \bar{N}$. Hence, the received signal $\mathbf{y} \in \mathbb{C}^{N_r \times 1}$ can be written as:

$$\mathbf{y} = \mathbf{G\Psi h}x + \mathbf{w} = \sum_{\zeta=1}^{|\mathcal{I}^{\mu}|} \mathbf{G}_{\zeta}\mathbf{\Psi}_{\zeta}\mathbf{h}_{\zeta} + \mathbf{w}, \tag{3.4}$$

where

$$\mathbf{G}_{\zeta} =[\bar{\mathbf{g}}_1, \cdots, \bar{\mathbf{g}}_{N_r}]^{\mathrm{T}}, \tag{3.5}$$

$$\bar{\mathbf{g}}_r =[g_{r,(\zeta-1)\bar{N}+1}, \cdots, g_{r,\zeta\bar{N}}]^{\mathrm{T}}, \tag{3.6}$$

$$\mathbf{h}_{\zeta} =[h_{(\zeta-1)\bar{N}+1}, \cdots, h_{\zeta\bar{N}}]^{\mathrm{T}}, \tag{3.7}$$

and $\mathbf{w} = [w_1, \cdots, w_{N_r}]^{\mathrm{T}}$ is the AWGN vector whose elements follow $\mathcal{CN}(0, N_0)$, N_0 is the noise variance, and $\mathbf{\Psi} = \text{diag}([\Psi_1^{\mathrm{T}}, \cdots, \Psi_{|\mathcal{I}^{\mu}|}^{\mathrm{T}}])$. Moreover, for simplicity, we split $\mathbf{\Psi}_{\zeta}$ into the product of two vectors as follows:

$$\begin{aligned}\mathbf{\Psi}_{\zeta} =&\mathbf{\Psi}_{\zeta 1} \times \mathbf{\Psi}_{\zeta 2},\\ =&\text{diag}\left(\left[e^{j\phi_{\mathcal{I}^{\mu}[\zeta],(\zeta-1)\bar{N}+1}}, e^{j\phi_{\mathcal{I}^{\mu}[\zeta],(\zeta-1)\bar{N}+2}}, \cdots, e^{j\phi_{\mathcal{I}^{\mu}[\zeta],\zeta\bar{N}}}\right]^{\mathrm{T}}\right) \times &(3.8)\\ &\text{diag}\left(\left[e^{j\theta_{(\zeta-1)\bar{N}+1}}, e^{j\theta_{(\zeta-1)\bar{N}+2}}, \cdots, e^{j\theta_{\zeta\bar{N}}}\right]^{\mathrm{T}}\right). &(3.9)\end{aligned}$$

Hence, assuming $\boldsymbol{\lambda}_{\zeta} = \mathbf{\Psi}_{\zeta 2}\mathbf{h}_{\zeta}$, (3.4) can be rewritten as

$$\mathbf{y} = \sum_{\zeta=1}^{|\mathcal{I}^{\mu}|} \mathbf{G}_{\zeta}\mathbf{\Psi}_{\zeta 1}\mathbf{\Psi}_{\zeta 2}\mathbf{h}_{\zeta}x + \mathbf{w} = \sum_{\zeta=1}^{|\mathcal{I}^{\mu}|} \mathbf{G}_{\zeta}\mathbf{\Psi}_{\zeta 1}\boldsymbol{\lambda}_{\zeta}x + \mathbf{w}. \tag{3.6}$$

3.2.2 RIS-ERSM Receiver

In this subsection, we propose an ML detector to decode the received signal, which can be given as:

$$\left[\hat{\boldsymbol{\Psi}}, \hat{x}, \hat{\mu}\right] = \underset{\boldsymbol{\Psi},x,\mu}{\operatorname{argmin}} \left\|\mathbf{y} - \sum\nolimits_{\zeta=1}^{|\mathcal{I}^{\mu}|} \mathbf{G}_{\zeta}\boldsymbol{\Psi}_{\zeta 1}\boldsymbol{\lambda}_{\zeta}x\right\|^2, \tag{3.7}$$

where $\hat{\boldsymbol{\Psi}}, \hat{x}$, and $\hat{\mu}$ are the estimated RIS reflection coefficient matrix, modulated symbol, and index of the antenna combination, respectively.

3.3 Performance Analysis

In this section, the theoretical BEP of the proposed ERSM scheme is examined utilizing ML detection. Here, we define a parameter $\Lambda = |\mathcal{I}^{\mu_{\max}}| \times (|\mathcal{I}^{\mu_{\max}}| - 1) \times \cdots \times 1$, where $\mu_{\max}$ is the index of the last antenna combination. For example, in Table 3.1, $\mu_{\max}$ is equal to 4 for $N_r = 3$ and Λ is obtained as $(|\mathcal{I}^{\mu_{\max}}| \times (|\mathcal{I}^{\mu_{\max}}| - 1)) = 2 \times 1 = 2$. Then, each $\mathcal{I}^{\mu}$ is converted into another set, which can be expressed as:

$$\bar{\mathcal{I}}^{\mu} = \bigcup_{k \in \mathcal{I}^{\mu}} \underbrace{\{k, k, \ldots, k\}}_{\varpi \text{ times}}, \tag{3.8}$$

where $\varpi = \Lambda / |\mathcal{I}^{\mu_{\max}}|$. In this case, $\bar{\mathcal{I}}^{\mu}$ is used instead of $\mathcal{I}^{\mu}$ and the number of RIS groups is fixed and equal to Λ. Hence, for given channel matrices $\mathbf{h}$ and $\mathbf{G}$, the CPEP can be written as

$$\begin{aligned}
&P\left(\boldsymbol{\Psi}, x, \mu \rightarrow \hat{\boldsymbol{\Psi}}, \hat{x}, \hat{\mu} | \mathbf{h}, \mathbf{G}\right), \\
=&P\left(\sqrt{\left\|\mathbf{y} - \sum_{\zeta=1}^{\Lambda} \mathbf{G}_{\zeta}\boldsymbol{\Psi}_{\zeta 1}\boldsymbol{\lambda}_{\zeta}x\right\|^2 > \left\|\mathbf{y} - \sum_{\zeta=1}^{\Lambda} \mathbf{G}_{\zeta}\hat{\boldsymbol{\Psi}}_{\zeta 1}\boldsymbol{\lambda}_{\zeta}\hat{x}\right\|^2}\right), \\
=&\mathcal{Q}\left(\sqrt{\frac{\left\|\sum_{\zeta=1}^{\Lambda} \mathbf{G}_{\zeta}\boldsymbol{\Psi}_{\zeta 1}\boldsymbol{\lambda}_{\zeta}x - \sum_{\zeta=1}^{\Lambda} \mathbf{G}_{\zeta}\hat{\boldsymbol{\Psi}}_{\zeta 1}\boldsymbol{\lambda}_{\zeta}\hat{x}\right\|^2}{2N_0}}\right), \\
=&\mathcal{Q}\left(\sqrt{\frac{\Omega}{2\rho}}\right),
\end{aligned} \tag{3.9}$$

where $\mathcal{Q}(\cdot)$ and $1/\rho$ are the Gaussian Q-function and instantaneous SNR, respectively, and Ω can be given as

$$\Omega = \left\| \left[\sum_{\zeta=1}^{\Lambda} \Omega_{\zeta 1}^{\Re} \quad \sum_{\zeta=1}^{\Lambda} \Omega_{\zeta 1}^{\Im} \quad \cdots \quad \sum_{\zeta=1}^{\Lambda} \Omega_{\zeta N_r}^{\Im} \right]^{\mathrm{T}} \right\|^2, \tag{3.10}$$

where $\Omega_{\zeta r}^{\Re}$ and $\Omega_{\zeta r}^{\Im}$ are defined respectively as

$$\Omega_{\zeta r}^{\Re} = \mathrm{Re}\left\{ \left[\mathbf{G}_\zeta \mathbf{\Psi}_{\zeta 1} \boldsymbol{\lambda}_\zeta x - \hat{\mathbf{\Psi}}_{\zeta 1} \boldsymbol{\lambda}_\zeta \hat{x} \right]_r \right\}, \tag{3.11}$$

$$\Omega_{\zeta r}^{\Im} = \mathrm{Im}\left\{ \left[\mathbf{G}_\zeta \mathbf{\Psi}_{\zeta 1} \boldsymbol{\lambda}_\zeta x - \hat{\mathbf{\Psi}}_{\zeta 1} \boldsymbol{\lambda}_\zeta \hat{x} \right]_r \right\}, \tag{3.12}$$

where $\mathrm{Re}\{\cdot\}$ and $\mathrm{Im}\{\cdot\}$ denote the real and imaginary parts of a scalar, respectively, and $[\mathbf{a}]_r$ is the r-th element of vector $\mathbf{a}$. By applying an upper bound technique for the Q-function [Chiani et al., 2003], the CPEP achieves a closed-form upper bound, which can be expressed as:

$$P\left(\mathbf{\Psi}, x, \mu \to \hat{\mathbf{\Psi}}, \hat{x}, \hat{\mu} | \mathbf{h}, \mathbf{G}\right) \leq \frac{1}{12}\left(2e^{-\frac{\Omega}{\rho}} + e^{-\frac{\Omega}{2\rho}} + 3e^{-\frac{\Omega}{4\rho}}\right). \tag{3.13}$$

Through this approach, the average PEP is determined as

$$\begin{aligned} &P\left(\mathbf{\Psi}, x, \mu \to \hat{\mathbf{\Psi}}, \hat{x}, \hat{\mu}\right) \\ &\quad = \mathrm{E}_\Omega\left\{ Q\left(\sqrt{\frac{\Omega}{\rho}}\right) \right\} \\ &\quad \leq \frac{2\mathrm{E}_\Omega\left\{e^{-\frac{\Omega}{\rho}}\right\} + \mathrm{E}_\Omega\left\{e^{-\frac{\Omega}{2\rho}}\right\} + 3\mathrm{E}_\Omega\left\{e^{-\frac{\Omega}{4\rho}}\right\}}{12} \\ &\quad = \frac{2\mathrm{M}_\Omega\left(-\frac{1}{\rho}\right) + \mathrm{M}_\Omega\left(-\frac{1}{2\rho}\right) + 3\mathrm{M}_\Omega\left(-\frac{1}{4\rho}\right)}{12}, \end{aligned} \tag{3.14}$$

where $\mathrm{E}_\Omega\{\cdot\}$ and $\mathrm{M}_\Omega(t) = \mathrm{E}_\Omega\{e^{t\Omega}\}$ denote the expectation value and MGF of Ω, respectively. Therefore, the MGF of Ω is required, which varies depending on whether the specified receive antenna of the ζ-th RIS group is detected correctly or erroneously. Let us define Ω_ζ as

$$\Omega_\zeta = \mathbf{G}_\zeta \mathbf{\Psi}_{\zeta 1} \boldsymbol{\lambda}_\zeta x - \mathbf{G}_\zeta \hat{\mathbf{\Psi}}_{\zeta 1} \boldsymbol{\lambda}_\zeta \hat{x} = \begin{bmatrix} \Omega_{\zeta 1}^{\Re} + j\Omega_{\zeta 1}^{\Im} \\ \Omega_{\zeta 2}^{\Re} + j\Omega_{\zeta 2}^{\Im} \\ \vdots \\ \Omega_{\zeta N_r}^{\Re} + j\Omega_{\zeta N_r}^{\Im} \end{bmatrix}. \tag{3.15}$$

Based on the distribution of Ω_ζ varying under different estimation conditions, we can categorize into two error scenarios: $\boldsymbol{\Psi}_{\zeta 1} = \hat{\boldsymbol{\Psi}}_{\zeta 1}$ and $\boldsymbol{\Psi}_{\zeta 1} \neq \hat{\boldsymbol{\Psi}}_{\zeta 1}$.

Scenario 1 ($\boldsymbol{\Psi}_{\zeta 1} = \hat{\boldsymbol{\Psi}}_{\zeta 1}$): Assuming that the ζ-th RIS group designates the κ-th receive antenna and the decision antenna, Ω_ζ can be represented as

$$\Omega_\zeta = \begin{bmatrix} (x-\hat{x})\sum_i \alpha_i \beta_{1,i} e^{j(\phi_{1,i}-\phi_{\kappa,i})} \\ \vdots \\ (x-\hat{x})\sum_i \alpha_i \beta_{\kappa,i} \\ \vdots \\ (x-\hat{x})\sum_i \alpha_i \beta_{N_r,i} e^{j\left(\phi_{N_r,i}-\phi_{\kappa,i}\right)} \end{bmatrix}. \tag{3.16}$$

As shown in (3.16), each row except the κ-th is independent of the others, and the real part of the κ-th row is also independent of its imaginary part. According to the CLT, $\Omega^{\Re}_{\zeta\nu}$ and $\Omega^{\Im}_{\zeta\nu}$ for $\nu \neq \kappa$, follow the same distribution of $\mathcal{N}\left(0, \frac{\tilde{N}}{2}|x-\hat{x}|^2\right)$, $\tilde{N} = N/\Lambda$. Even though $\Omega^{\Re}_{\kappa i}$ and $\Omega^{\Im}_{\kappa i}$ still follow a Gaussian distribution under the CLT, they are not independent of each other, where a mean vector and covariance matrix of $\mathbf{z}_1 = [\Omega^{\Re}_{\zeta i}, \Omega^{\Im}_{\zeta i}]^{\mathrm{T}}$ can be respectively given as

$$\mathbf{m}_{\mathbf{z}_1} = \frac{\tilde{N}\pi}{4}\left[\mathrm{Re}\{x-\hat{x}\} \quad \mathrm{Im}\{x-\hat{x}\}\right]^{\mathrm{T}}, \tag{3.17}$$

$$\mathbf{C}_{\mathbf{z}_1} = \frac{\tilde{N}\left(16-\pi^2\right)}{16}\begin{bmatrix} (\mathrm{Re}\{x-\hat{x}\})^2 & C_{12} \\ C_{21} & (\mathrm{Im}\{x-\hat{x}\})^2 \end{bmatrix}, \tag{3.18}$$

where $C_{12} = C_{21} = \mathrm{Re}\{x-\hat{x}\} \times \mathrm{Im}\{x-\hat{x}\}$.

Scenario 2 ($\boldsymbol{\Psi}_{\zeta 1} \neq \hat{\boldsymbol{\Psi}}_{\zeta 1}$): Assuming that the ζ-th RIS group designates the κ-th receive antenna; however, the $\hat{\kappa}$ is the decision antenna. Hence, Ω_ζ can be obtained as

$$\Omega_\zeta = \begin{bmatrix} \sum_i \alpha_i \beta_{1,i}(x e^{-j\phi_{\kappa,i}} - \hat{x} e^{-j\phi_{\hat{\kappa},i}}) \\ \vdots \\ \sum_i \alpha_i \beta_{\kappa,i}(x - \hat{x} e^{-j\phi_{\hat{\kappa},i}}) \\ \vdots \\ \sum_i \alpha_i \beta_{\hat{\kappa},i}(x e^{-j\phi_{\kappa,i}} - \hat{x}) \\ \vdots \\ \sum_i \alpha_i \beta_{N_r,i}(x e^{-j\phi_{\kappa,i}} - \hat{x} e^{-j\phi_{\hat{\kappa},i}}) \end{bmatrix}. \tag{3.19}$$

Likewise, according to CLT, for any row other than the κ-th and $\hat{\kappa}$-th, the real and imaginary components adhere to the same normal distribution as follows:

$$\mathcal{N}\left(0, \frac{\tilde{N}}{2}\left(|x|^2 + |\hat{x}|^2\right)\right). \tag{3.20}$$

The real and imaginary components of the κ-th and $\hat{\kappa}$-th rows of Ω_ζ follow Gaussian distribution but they are not independent. The mean vector of $\mathbf{z}_2 = [\Omega^{\Re}_{\zeta i}\, \Omega^{\Im}_{\zeta i}\, \Omega^{\Re}_{\hat{\zeta} i}\, \Omega^{\Im}_{\hat{\zeta} i}]^{\mathrm{T}}$ is given as

$$\mathbf{m}_{\mathbf{z}_2} = \frac{\tilde{N}\pi}{4}\left[\mathrm{Re}\{x\}\mathrm{Im}\{x\} - \mathrm{Re}\{\hat{x}\} - \mathrm{Im}\{\hat{x}\}\right]^{\mathrm{T}}, \tag{3.21}$$

and the covariance matrix of $\mathbf{z}_2$ can be obtained as follows:

$$\mathbf{C}_{\mathbf{z}_2} = \frac{\tilde{N}}{2}\begin{bmatrix} C_{1,1} & x^{\Re}x^{\Im}\left(\frac{16-\pi^2}{16}\right) & x^{\Re}\hat{x}^{\Re}\left(\frac{\pi^2-4\pi}{16}\right) & x^{\Re}\hat{x}^{\Im}\left(\frac{\pi^2-4\pi}{16}\right) \\ x^{\Re}x^{\Im}\left(\frac{16-\pi^2}{16}\right) & C_{2,2} & x^{\Im}\hat{x}^{\Re}\left(\frac{\pi^2-4\pi}{16}\right) & x^{\Im}\hat{x}^{\Im}\left(\frac{\pi^2-4\pi}{16}\right) \\ x^{\Re}\hat{x}^{\Re}\left(\frac{\pi^2-4\pi}{16}\right) & x^{\Im}\hat{x}^{\Re}\left(\frac{\pi^2-4\pi}{16}\right) & C_{3,3} & \hat{x}^{\Re}\hat{x}^{\Im}\left(\frac{16-\pi^2}{16}\right) \\ x^{\Re}\hat{x}^{\Im}\left(\frac{\pi^2-4\pi}{16}\right) & x^{\Im}\hat{x}^{\Im}\left(\frac{\pi^2-4\pi}{16}\right) & \hat{x}^{\Re}\hat{x}^{\Im}\left(\frac{16-\pi^2}{16}\right) & C_{4,4} \end{bmatrix}. \tag{3.22}$$

where $C_{1,1} = |\hat{x}|^2 + (x^{\Re})^2\left(\frac{16-\pi^2}{16}\right)$, $C_{2,2} = |\hat{x}|^2 + (x^{\Im})^2\left(\frac{16-\pi^2}{16}\right)$, $C_{3,3} = |x|^2 + (\hat{x}^{\Re})^2\left(\frac{16-\pi^2}{16}\right)$, $C_{4,4} = |x|^2 + (\hat{x}^{\Im})^2\left(\frac{16-\pi^2}{16}\right)$, $x^{\Re} = \mathrm{Re}\{x\}$, $x^{\Im} = \mathrm{Im}\{x\}$, $\hat{x}^{\Re} = \mathrm{Re}\{\hat{x}\}$, and $\hat{x}^{\Im} = \mathrm{Im}\{\hat{x}\}$.

Because each Ω_κ is independent, Ω follows a generalized non-central chi-square distribution with $2N_r$ degrees of freedom, and its MGF can be expressed as

$$\mathrm{M}_\Omega(s) = [\det(\mathbf{I} - 2s\mathbf{C}_\Omega)]^{0.5} e^{-0.5\mathbf{m}_\Omega^{\mathrm{T}}[\mathbf{I}-(\mathbf{I}-2s\mathbf{C}_\Omega)^{-1}]\mathbf{C}_\Omega^{-1}\mathbf{m}_\Omega}, \tag{3.23}$$

where

$$\mathbf{m}_\Omega = \left[\sum_{\zeta=1}^{\Lambda} m_{\Omega^{\Re}_{\zeta 1}} \quad \sum_{\zeta=1}^{\Lambda} m_{\Omega^{\Im}_{\zeta 1}} \quad \cdots \quad \sum_{\zeta=1}^{\Lambda} m_{\Omega^{\Im}_{\zeta N_r}}\right]^{\mathrm{T}}, \tag{3.24}$$

$$\mathbf{C}_\Omega = \begin{bmatrix} \sum_{\zeta=1}^{\Lambda} \sigma^2_{\Omega^{\Re}_{\zeta 1},\Omega^{\Re}_{\zeta 1}} & \cdots & \sum_{\zeta=1}^{\Lambda} \sigma^2_{\Omega^{\Re}_{\zeta 1},\Omega^{\Im}_{\zeta N_r}} \\ \vdots & \ddots & \vdots \\ \sum_{\zeta=1}^{\Lambda} \sigma^2_{\Omega^{\Im}_{\zeta N_r},\Omega^{\Re}_{\zeta 1}} & \cdots & \sum_{\zeta=1}^{\Lambda} \sigma^2_{\Omega^{\Im}_{\zeta N_r},\Omega^{\Im}_{\zeta N_r}} \end{bmatrix}. \tag{3.25}$$

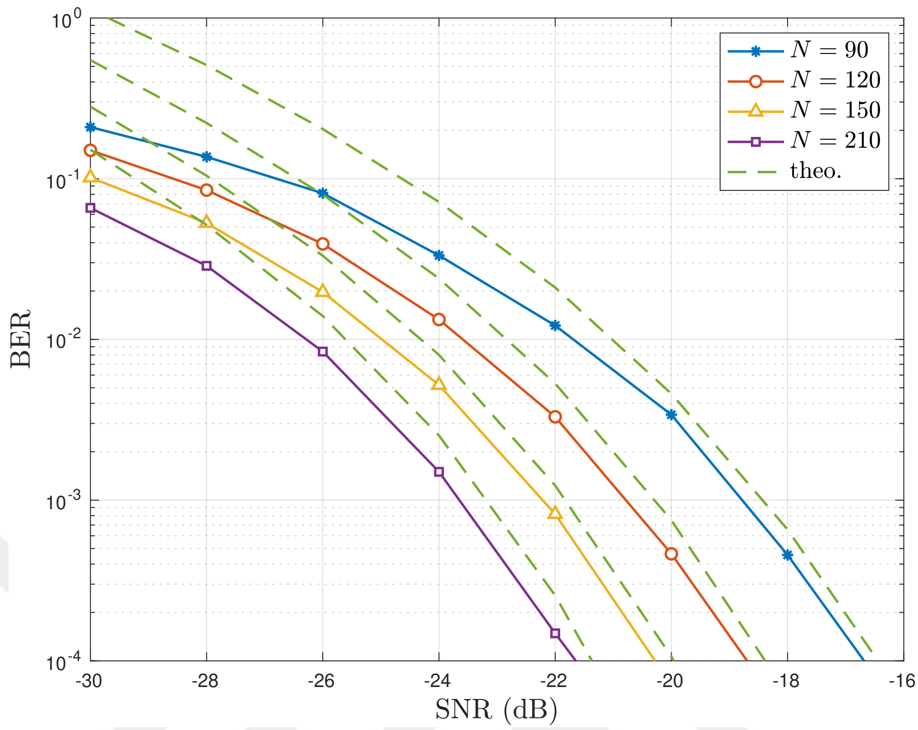

Figure 3.2: Theoretical upper bound of RIS-ERSM on BER with simulation results for $N_r = 6$, $M = 2$, $\eta = 6$ bpcu, and varying N values.

By taking both scenarios into account, an upper bound on ABER is obtained as

$$P_b \leq \frac{1}{\eta 2^{\eta}} \sum_{\mathbf{\Psi}} \sum_{x} \sum_{\mu} \sum_{\hat{\mathbf{\Psi}}} \sum_{\hat{x}} \sum_{\hat{\mu}} P\left(\mathbf{\Psi}, x, \mu \rightarrow \hat{\mathbf{\Psi}}, \hat{x}, \hat{\mu}\right) \times E\left(\mathbf{\Psi}, x, \mu \rightarrow \hat{\mathbf{\Psi}}, \hat{x}, \hat{\mu}\right), \tag{3.26}$$

where $E(\mathbf{\Psi}, x, \mu \rightarrow \hat{\mathbf{\Psi}}, \hat{x}, \hat{\mu})$ denotes the number of erroneous bits for the corresponding pairwise error event.

3.4 Simulation Results And Comparisons

In this section, we present theoretical and computer simulation results of the error performance for the proposed RIS-ERSM scheme with respect to SNR, defined as $1/N_0$, across various configurations. Moreover, it is compared to the benchmark schemes: RIS-RSM [Basar, 2020] and RIS-EVSM [Yue et al., 2024].

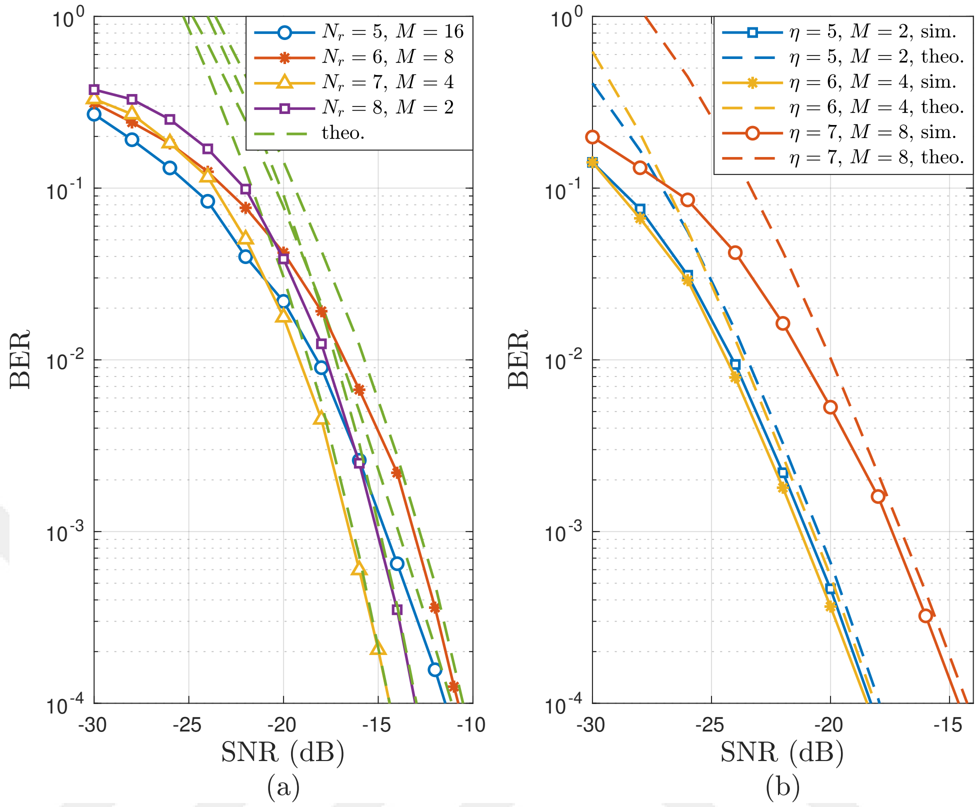

Figure 3.3: Theoretical upper bound of RIS-ERSM on BER with simulation results for $N = 96$, $\eta = 8$ bpcu, and varying M and N_r values (a) and $N = 120$, $N_r = 5$, and varying η and M values (b).

In Fig. 3.2, the theoretical and simulation results are illustrated for $N_r = 6$, $M = 2$, $\eta = 6$ bpcu, and varying number of RIS elements N. It can be seen in Fig. 3.2 that the theoretical curves obtained by (3.26) are highly consistent with simulated BER. Additionally, since the power of received signal per each antenna in the selected antenna combination is boosted with respect to the number of reflecting elements, the error performance of RIS-ERSM improves as N increases.

In Fig. 3.3(a), it can be seen that the theoretical curve obtained by (3.26) is an accurate upper bound on the BER for the proposed RIS-ERSM scheme for different configurations of M and N_r. As the number of receive antenna (N_r) increases, lower modulation order can be used for the same bpcu. Moreover, the configuration with $N_r = 7$ and $M = 4$ achieves the best error performance among all configurations. Similarly, in Fig. 3.3(b), it can observed that theoretical results serve as upper

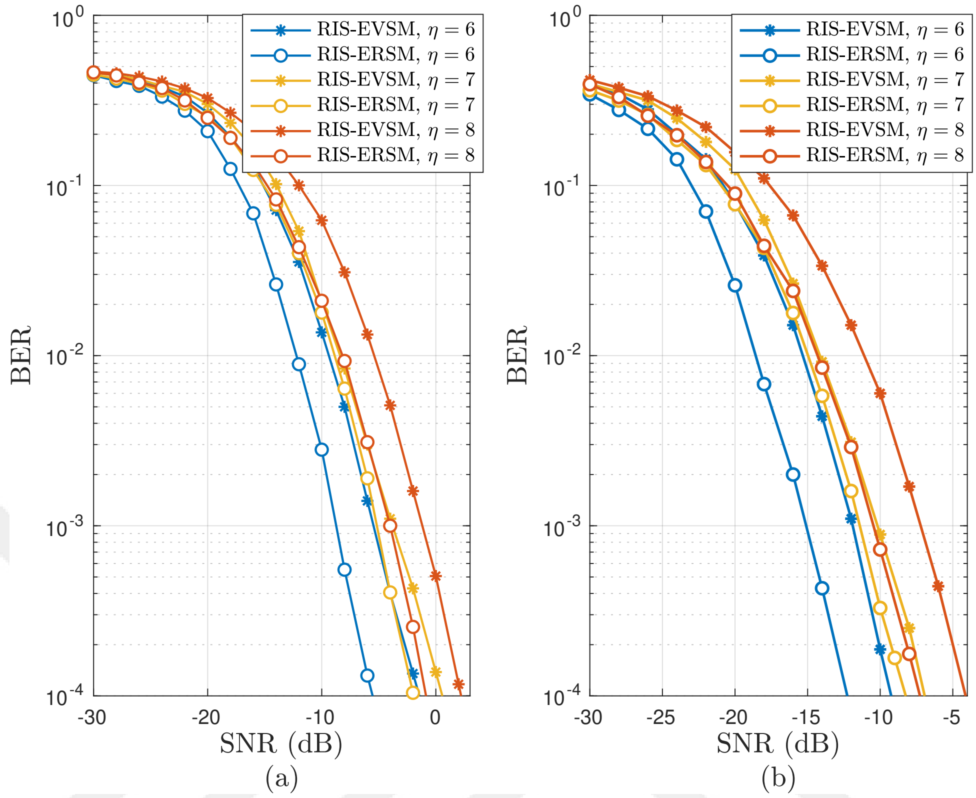

Figure 3.4: Error performance comparison of RIS-ERSM and RIS-EVSM for $N = 30$ (a) and $N = 60$ (b) with $N_r = 5$ and varying η values.

bounds on the BER curves for $N = 120$, $N_r = 5$, and varying η and M values. As η increases, the error performance of RIS-ERSM degrades.

The error performance of RIS-ERSM is compared to RIS-EVSM for $N = 30$ and $N = 60$ in Figs. 3.4(a) and 3.4(b), respectively, with $N_r = 5$ and varying η values. It can be seen that RIS-ERSM outperforms RIS-EVSM in terms of BER performance for each η values. The reason is that RIS-ERSM provides more clever information bits to receive antenna combination mapping leading to less number of RIS groups. As the number of RIS groups increases, the instantaneous SNR per each specified receive antenna decreases and this causes a degradation in the error performance. Another observation from Figs. 3.4(a) and 3.4(b) is that the error performance of both RIS-RSM and RIS-EVSM degrades as η increases due to higher modulation order.

Figs. 3.5(a) and 3.5(b) compare the error performance of RIS-ERSM and bench-

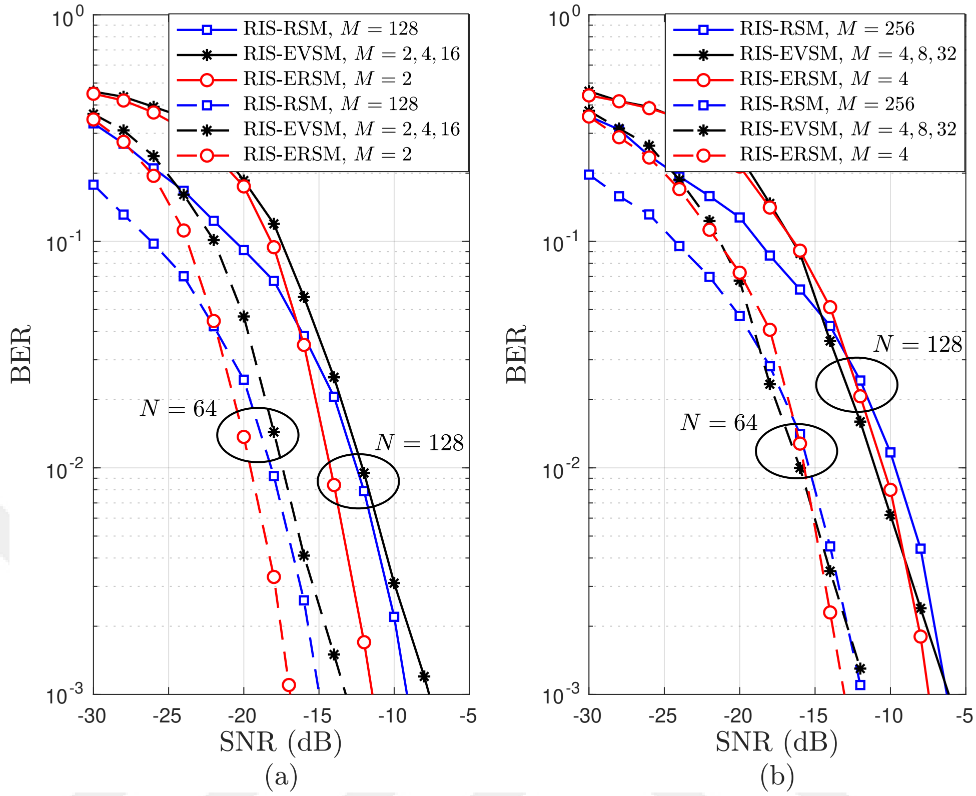

Figure 3.5: Error performance compariosn of RIS-ERSM and benchmark schemes for $\eta = 10$ (a) and $\eta = 11$ (b) bpcu when $N_r = 9$, $N = 64, 128$.

mark schemes for $\eta = 10$ and $\eta = 11$, respectively, with $N_r = 9$ and varying N values. As seen in Fig. 3.5, RIS-ERSM outperforms benchmark schemes in terms of error performance across different configurations. Since RIS-ERSM can transmit more IM bits compared to RIS-RSM by selecting more than one antenna at a transmission interval, it can leverage lower order modulation for the same bpcu values, resulting in an improved BER performance. Additionally, for the same configuration, due to enhanced antenna combination selection, higher number of RIS groups is less likely to occur in RIS-ERSM compared to RIS-EVSM, leading to higher received SNR values at specified receive antennas. Consequently, the higher SNR values obtained in RIS-ERSM than in RIS-EVSM result in better error performance.

3.5 Conclusion

In this chapter, we have proposed RIS-ERSM, an innovative RIS-assisted transmission scheme. By leveraging M-ary modulated data symbols and flexible receive antenna combinations, RIS-ERSM achieves high spectral efficiency and reliability. Simulation results demonstrate that RIS-ERSM outperforms benchmark schemes in error performance, making it a promising solution for future wireless communication systems.

Chapter 4

RECONFIGURABLE INTELLIGENT SURFACE CODE INDEX MODULATION WITH QUADRATURE RECEIVE SPATIAL MODULATION

4.1 Introduction

With the ever-increasing demand for higher data rates and more efficient use of wireless spectrum, innovative communication techniques are essential to meet the needs of modern wireless networks. IM [Basar, 2016a] is a promising wireless communication technique that enhances spectral and energy efficiency by encoding information not only in modulated symbols but also in indices of transmit entities across various domains such as time, frequency, code, and space. For example, subcarriers [Tugtekin et al., 2023] and antennas [Kurt et al., 2023] serve as transmit entities to embed information in the frequency and space domains, respectively. In [Kaddoum et al., 2014], code domain is used to perform IM, leading to the development of the code IM spread spectrum (CIM-SS) scheme. Moreover, in [Li et al., 2018], the CIM concept is applied within a multicarrier system and a scheme named index modulated OFDM SS (IM-OFDM-SS) scheme is presented, where the modulated symbols are spread over subcarriers using selected spreading codes based on index bits.

RIS technology, which has the capability to intelligently reconfigure the wireless channel, has emerged as a novel solution for enhancing wireless networks [Basar et al., 2019]. RIS-assisted communication has attracted significant interest from both academia and industry due to its strong potential for improving the performance of current and future wireless networks [Basar et al., 2023]. For example, RISs have been exploited for various purposes, including enhancing the sensing performance [Liu et al., 2023], enabling high-precision localization [Elzanaty et al., 2021], and improving the physical layer security [Khoshafa et al., 2024]. Additionally, RISs have been combined with IM, allowing researchers to propose numerous novel designs that levarage the highly flexible structure of IM. In [Basar, 2020], receive SM (RSM) and receive SSK (RSSK) schemes are implemented with the aid of an RIS, where receive antenna indices are selected according to IM bits. Furthermore, a generalized SSK scheme is realized with the help of an RIS in [**?**], where more than one receive antenna is specified by an RIS at the receiver side to increase the number of information bits transmitted by IM. In [Yuan et al., 2021], to enable the selection of two receive antennas, an RIS is divided into two parts, with the first and second RIS parts creating in-phase and quadrature components of signals at the specified antennas, respectively. In [Dogukan et al., 2024c], the number of specified receive antennas is strategically chosen and varied to both increase the data rate and enhance error performance. Moreover, in [Asmoro and Shin, 2022], a scheme called RIS grouping based IM (RGB-IM) is introduced, where the indices of RIS sub-groups are exploited to convey information bits. In [Arslan et al., 2024], the idea of RGB-IM is extended into a hybrid RIS structure, where all RIS elements are utilized to significantly increase the received instantaneous SNR while remaining capable of performing IM. In [Dogukan et al., 2024b], the number of active groups in a hybrid RIS is exploited to convey additional information bits, with further manipulation based on the IM bits to increase the minimum Euclidean distance, resulting in improved error performance.

In addition to these IM-based studies for RIS-aided wireless systems, CIM is integrated with RISs to leverage the benefits of both IM and spreading codes. In [Cogen et al., 2024], a CIM-RIS scheme is proposed for an RIS-aided SISO system, where CIM is performed at the transmitter, and the communication link between the transmitter and receiver is established through an RIS. Furthermore, a scheme called RIS-CIM, which performs CIM at the RIS, is presented in [Li et al., 2023]. In RIS-CIM, an RIS is configured at a rate faster than the symbol duration to enable spreading. For RIS-CIM signal, two low-complexity detectors that perform dispreading and demodulation separately have been designed in [Jin et al., 2023]. To further increase the number of IM bits, RIS-CIM-RSM [Ozden et al., 2024] is introduced for a SIMO system, combining RIS-CIM with RSM. Additionally, in [Jin et al., 2024], an active RIS structure is utilized to perform both CIM and SSK. Despite the existing studies combining RIS and CIM, there remains significant potential for further advancements in RIS-CIM-based schemes, particularly in enhancing error performance, designing low-complexity detectors, and achieving higher spectral and energy efficiency.

In this chapter, we propose a novel RIS-aided wireless communication scheme called *RIS-CIM with quadrature RSM (QRSM)*, or *RIS-CIM-QRSM*, to improve the error performance of RIS-aided IM schemes. In RIS-CIM-QRSM, in addition to M-PAM, information bits are conveyed through the indices of spreading codes and receive antennas. The RIS is divided into two parts, each dedicated to in-phase and quadrature domain operations. The considered RIS operates at a rate faster than the symbol period to spread the incoming signal, resulting in signals with a wider bandwidth and enabling CIM. The first and second RIS parts spread the incoming M-PAM modulated symbol with different spreading codes to increase the number of CIM bits. The second RIS part also introduces a $\pi/2$ phase shift to ensure orthogonality with the in-phase component. Additionally, the reflection coefficients of the first and second RIS parts are adjusted to specify the selected receive antennas. Since the two RIS parts reflect the incoming signal in an orthogonal manner, the spreading codes applied at each part can be distinguished even if the same receive antenna indices are selected. Moreover, a sub-optimal low-complexity detector is introduced for RIS-CIM-QRSM. The error performance and computational complexity of the low-complexity detector are compared to those of the optimal ML detector. A spectral efficiency analysis is also performed for RIS-CIM-QRSM and compared with benchmark schemes, RIS-CIM and RIS-CIM-RSM. Extensive computer simulations demonstrate the superior error performance of RIS-CIM-QRSM over benchmark schemes across various scenarios and system parameters.

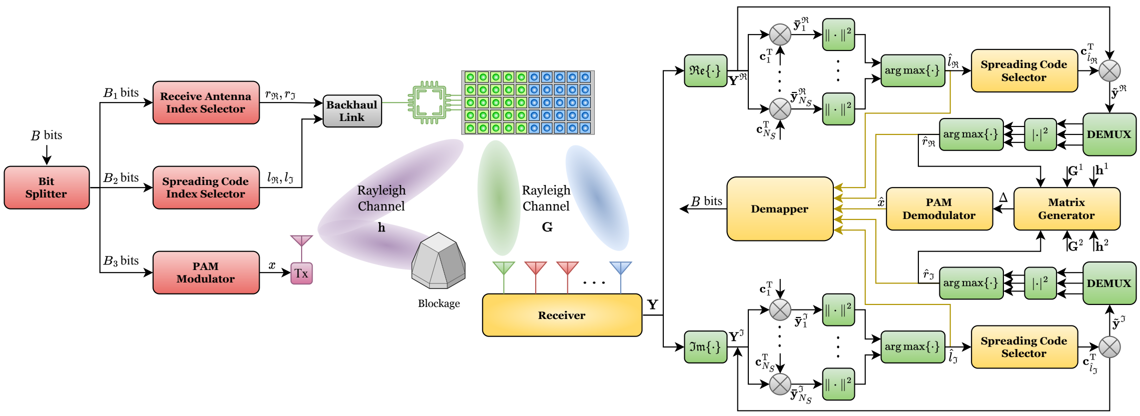

Figure 4.1: System model of the proposed RIS-CIM-QRSM scheme.

4.2 System Model

A SIMO system model for the proposed RIS-CIM-QRSM scheme, which involves a single-antenna transmitter and a receiver with N_r antennas, is shown in Fig. 4.1. The direct link between the transmitter and receiver is blocked, and communication is enabled through an RIS with N reflective elements. As shown in Fig. 4.1, a total of B bits are transmitted during each symbol duration T_s. These B bits are divided into three groups: symbol bits (B_1), spreading code index bits (B_2), and receive antenna index bits (B_3). Firstly, $B_1 = \log_2(M)$ bits determine the M-PAM modulated symbol $x \in \mathcal{M}$, where $\mathcal{M}$ represents the M-PAM constellation. Secondly, two bit sequences, each with $B_2/2 = \log_2(N_S)$ bits, are mapped to the indices of two spreading codes ($l_\Re$ and $l_\Im$), $l_\Re, l_\Im \in \{1, 2, \cdots, N_S\}$, where N_S is the total number of spreading codes. A set of Walsh codes is used and is expressed as $\mathcal{C} = \{\mathbf{c}_1, \mathbf{c}_2, \cdots, \mathbf{c}_{N_S}\}$, where $\mathbf{c}_k = [c_{k,1}, c_{k,2}, \cdots, c_{k,U}]$ represents the k^{th} Walsh-Hadamard spreading code. Here, U denotes the code length and the number of chips, with chip duration $T_c = T_s/U$ and $c_{k,u} \in \{-1, 1\}$, where $k = 1, \cdots, N_S$, $u = 1, \cdots, U$. The selected spreading codes are $\mathbf{c}_{l_\Re}$ and $\mathbf{c}_{l_\Im}$. In Table 4.1, an example of spreading code indices determination based on B_2 bits is provided for $N_S = 4$. Finally, each receive antenna index, $r_\Re$ and $r_\Im$, is selected based on $\log_2(N_r)$ bits, resulting in a total of $B_3 = 2\log_2(N_r)$ bits for both indices, where $(r_\Re, r_\Im) \in$

Table 4.1: An Example of Mapping B_2 Bits Into The Spreading Code Indices For $N_S = 4$.

First $B_2/2$ bits	$l_{\Re}$	Second $B_2/2$ bits	$l_{\Im}$
$\{0,0\}$	1	$\{0,0\}$	1
$\{0,1\}$	2	$\{0,1\}$	2
$\{1,0\}$	3	$\{1,0\}$	3
$\{1,1\}$	4	$\{1,1\}$	4

Table 4.2: An Example of Mapping B_3 Bits Into The Spreading Code Indices For $N_r = 4$.

First $B_3/2$ bits	$r_{\Re}$	Second $B_3/2$ bits	$r_{\Im}$
$\{0,0\}$	1	$\{0,0\}$	1
$\{0,1\}$	2	$\{0,1\}$	2
$\{1,0\}$	3	$\{1,0\}$	3
$\{1,1\}$	4	$\{1,1\}$	4

$\{1, 2, \cdots, N_r\}$. Table 4.2 provides an example of mapping B_3 bits to receive antenna indices. The total number of bits transmitted per channel use can be given by:

$$B = B_1 + B_2 + B_3 = \log_2(M) + 2\log_2(N_S) + 2\log_2(N_r). \tag{4.1}$$

As a result, the spectral efficiency of RIS-CIM-QRSM can be given as $\eta = B/N_S$ bits per second per Hertz (bps/Hz).

For the u^{th} chip signal, the Rayleigh fading channel matrices between the transmitter and the RIS, and the RIS and receiver, can be given as $\mathbf{h}_u = [h_{u,1}, \cdots, h_{u,N}]^{\mathrm{T}} \in \mathbb{C}^{N\times 1}$ and $\mathbf{G}_u = [\mathbf{g}_u^1, \cdots, \mathbf{g}_u^{N_r}]^{\mathrm{T}} \in \mathbb{C}^{N_r\times N}$, respectively. Here, $\mathbf{g}_u^r = [g_{u,1}^r, \cdots, g_{u,N}^r]^{\mathrm{T}} \in \mathbb{C}^{N\times 1}$, for $r = 1, \cdots, N_r$, with $h_{u,n} = \alpha_{u,i}e^{j\theta_{u,i}} \sim \mathcal{CN}(0,1)$ and $g_{u,i}^r = \beta_{u,i}^r e^{j\phi_{u,i}^r} \sim$

$\mathcal{CN}(0,1)$, for $i = 1, \cdots, N$.

As shown in Fig. 4.1, the selected M-PAM modulated symbol x is transmitted from the transmitter to the RIS during the symbol duration T_s. Assuming $\Gamma_{u,i} = e^{j\varpi_{u,i}}$ is the reflection coefficient of the i^{th} reflective element for the u^{th} chip signal, the received signal at the r^{th} received antenna for the u^{th} chip can be expressed as:

$$y_u^r = x\sum_{i=1}^{N} h_{u,i}e^{j\varpi_{u,i}}g_{u,i}^r + w_u^r = x\sum_{i=1}^{N}\alpha_{u,i}\beta_{u,i}^r e^{j(\varpi_{u,i}+\theta_{u,i}+\phi_{u,i}^r)} + w_u^r, \tag{4.2}$$

where w_u^r represents the AWGN sample at the r^{th} receive antenna for the u^{th} chip signal, distributed as $\mathcal{CN}(0, N_0)$, where N_0 is the noise variance. The RIS is divided into two parts, each consisting of $N/2$ elements. The first and second parts of RIS are associated with the in-phase and quadrature domain operations, respectively. For the u^{th} chip signal, the phase values of the first and second parts of the RIS elements are adjusted by utilizing the parameters $(l_{\Re,u}, r_{\Re})$ and $(l_{\Im,u}, r_{\Im})$, respectively, as follows:

$$\varpi_{u,i} = \begin{cases} -\theta_{u,i} - \phi_{u,i}^{r_{\Re}} + \angle c_{l_{\Re},u}, & \text{if } i \leq N/2 \\ -\theta_{u,i} - \phi_{u,i}^{r_{\Im}} + \angle c_{l_{\Im},u} + \frac{\pi}{2}, & \text{otherwise,} \end{cases} \tag{4.3}$$

where $\angle c_{l_{\Re},u}$ and $\angle c_{l_{\Im},u}$ represent the phase terms of $c_{l_{\Re},u}$ and $c_{l_{\Im},u}$, respectively, introduced by the RIS to perform CIM. By substituting (4.3) into (4.2), (4.2) can be rewritten as:

$$y_u^r = \frac{x}{\sqrt{U}}\left(c_{l_{\Re},u}\sum_{i=1}^{N/2}\alpha_{u,i}\beta_{u,i}^r e^{j(\phi_{u,i}^r-\phi_{u,i}^{r_{\Re}})} + jc_{l_{\Im},u}\sum_{i=N/2+1}^{N}\alpha_{u,i}\beta_{u,i}^r e^{j(\phi_{u,i}^r-\phi_{u,i}^{r_{\Im}})}\right) + w_u^r. \tag{4.4}$$

Additionally, for the u^{th} chip signal and $r_{\Re} \neq r_{\Im}$, the received signals at receive antennas $r_{\Re}$ and $r_{\Im}$ are respectively given as:

$$y_u^{r_{\Re}} = \frac{x}{\sqrt{U}}\left(c_{l_{\Re},u}\sum_{i=1}^{N/2}\alpha_{u,i}\beta_{u,i}^{r_{\Re}} + jc_{l_{\Im},u}\sum_{i=N/2+1}^{N}\alpha_{u,i}\beta_{u,i}^{r_{\Re}}e^{j\psi_{u,i}}\right) + w_u^{r_{\Re}}, \tag{4.5}$$

$$y_u^{r_{\Im}} = \frac{x}{\sqrt{U}}\left(c_{l_{\Re},u}\sum_{i=1}^{N/2}\alpha_{u,i}\beta_{u,i}^{r_{\Im}}e^{-j\psi_{u,i}} + jc_{l_{\Im},u}\sum_{i=N/2+1}^{N}\alpha_{u,i}\beta_{u,i}^{r_{\Im}}\right) + w_u^{r_{\Im}}, \tag{4.6}$$

where $\psi_{u,i} = \phi_{u,i}^{r_{\Re}} - \phi_{u,i}^{r_{\Im}}$. For $\bar{r} = r_{\Re} = r_{\Im}$, the received signal at $\bar{r}^{\text{th}}$ antenna can be given as:

$$y_u^{\bar{r}} = \frac{1}{\sqrt{U}} x \left(c_{l_{\Re},u} \sum_{i=1}^{N/2} \alpha_{u,i} \beta_{u,i}^{\bar{r}} + j c_{l_{\Im},u} \sum_{i=N/2+1}^{N} \alpha_{u,i} \beta_{u,i}^{\bar{r}} \right) + w_u^{\bar{r}}.$$

Slow fading channels are assumed, i.e., $\mathbf{h} = \mathbf{h}_1 = \cdots = \mathbf{h}_U$ and $\mathbf{G} = \mathbf{G}_1 = \cdots = \mathbf{G}_U$. Therefore, (4.4) can be rewritten in vector and matrix form as:

$$\mathbf{Y} = \frac{x}{\sqrt{U}} (\mathbf{G}^1 \mathbf{\Theta}^1 \mathbf{h}^1 \mathbf{c}_{l_{\Re}} + j \mathbf{G}^2 \mathbf{\Theta}^2 \mathbf{h}^2 \mathbf{c}_{l_{\Im}}) + \mathbf{W}, \tag{4.7}$$

where

$$\mathbf{h}^{\nu} = [h_{(\nu-1)N/2+1}, \cdots, h_{\nu N/2}]^{\text{T}}, \tag{4.8}$$

$$\mathbf{G}^{\nu} = [\mathbf{g}^{\nu,1}, \mathbf{g}^{\nu,2}, \cdots, \mathbf{g}^{\nu,N_r}]^{\text{T}}, \tag{4.9}$$

$$\mathbf{g}^{\nu,r} = [g_{(\nu-1)N/2+1}^{r}, \cdots, g_{\nu N/2}^{r}]^{\text{T}}, \tag{4.10}$$

for $\nu \in \{1, 2\}$. Additionally, $\mathbf{W} \in \mathbb{C}^{N_r \times U}$ is the noise matrix, where the $(r, u)^{\text{th}}$ element is the AWGN sample w_u^r. The matrices are given by

$$\mathbf{\Theta}^1 = \text{diag} \left([e^{j(-\theta_1 - \phi_1^{r_{\Re}})}, \cdots, e^{j(-\theta_{N/2} - \phi_{N/2}^{r_{\Re}})}]^{\text{T}} \right) \tag{4.11}$$

$$\mathbf{\Theta}^2 = \text{diag} \left([e^{j(-\theta_{N/2+1} - \phi_{N/2+1}^{r_{\Im}})}, \cdots, e^{j(-\theta_N - \phi_N^{r_{\Im}})}]^{\text{T}} \right), \tag{4.12}$$

and $\mathbf{Y} = [\mathbf{y}_1, \mathbf{y}_2, \cdots, \mathbf{y}_U]$, where $\mathbf{y}_u = [y_u^1, y_u^2, \cdots, y_u^{N_r}]^{\text{T}}$.

The SNR at the r^{th} receive antenna can be expressed as:

$$\gamma^r = \frac{|\mathbf{g}^{1,r} \mathbf{\Theta}^1 \mathbf{h}^1|^2 + |\mathbf{g}^{2,r} \mathbf{\Theta}^2 \mathbf{h}^2|^2}{N_0}. \tag{4.13}$$

For $r_{\Re} \neq r_{\Im}$, the SNR values at the receive antennas $r_{\Re}$ and $r_{\Im}$ are given as follows, respectively:

$$\gamma^{r_{\Re}} = \frac{(|\mathbf{g}^{1,r_{\Re}}||\mathbf{h}^1|)^2 + |\mathbf{g}^{2,r_{\Re}} \mathbf{\Theta}^2 \mathbf{h}^2|^2}{N_0}, \tag{4.14}$$

$$\gamma^{r_{\Im}} = \frac{|\mathbf{g}^{1,r_{\Im}} \mathbf{\Theta}^1 \mathbf{h}^1|^2 + (|\mathbf{g}^{2,r_{\Im}}||\mathbf{h}^2|)^2}{N_0}. \tag{4.15}$$

Additionally, for $\bar{r} = r_{\Re} = r_{\Im}$, the SNR at the receive antenna $\bar{r}$ is obtained as:

$$\gamma^{\bar{r}} = \frac{(|\mathbf{g}^{1,\bar{r}}||\mathbf{h}^1|)^2 + (|\mathbf{g}^{2,\bar{r}}||\mathbf{h}^2|)^2}{N_0}. \tag{4.16}$$

4.2.1 Detection

In this subsection, we first introduce the ML detector, followed by the low-complexity detector, which significantly reduces decoding complexity compared to the ML detector.

ML Detector

At the receiver side, after obtaining $\mathbf{Y}$, the ML detector considers all possible combinations for joint detection of the modulated symbol, spreading code indices, and receive antenna indices, achieving optimal performance. Therefore, the ML detection rule for RIS-CIM-QRSM is given as:

$$\left[\hat{x}, \hat{l}_{\Re}, \hat{l}_{\Im}, \hat{r}_{\Re}, \hat{r}_{\Im}\right] = \arg \min_{x, l_{\Re}, l_{\Im}, r_{\Re}, r_{\Im}} \left\| \mathbf{Y} - \frac{x}{\sqrt{U}}(\mathbf{G}^1 \mathbf{\Theta}^1 \mathbf{h}^1 \mathbf{c}_{l_{\Re}} + j\mathbf{G}^2 \mathbf{\Theta}^2 \mathbf{h}^2 \mathbf{c}_{l_{\Im}}) \right\|_{\mathrm{F}}^2, \tag{4.17}$$

Next, $\hat{x}$, $\hat{l}_{\Re}$, $\hat{l}_{\Im}$, $\hat{r}_{\Re}$, and $\hat{r}_{\Im}$ are used to obtain the decoded bits. Since the ML detector jointly detects the modulated symbol, spreading code indices, and receive antenna indices, the decoding complexity is substantially high and further increases with greater values of M, N_S, and N_r. To address this, we present a low-complexity detector to reduce the computational burden in the detection of RIS-CIM-QRSM signal.

Low-Complexity Detector

In contrast to the joint detection performed by the ML detector, the low-complexity detector decodes the transmitted entities one-by-one in order to reduce the decoding complexity. In the low-complexity detector, firstly, the real and imaginary parts of the received signal are obtained and can be expressed as:

$$\mathbf{Y}^{\Re} = \begin{bmatrix} \mathbf{y}_1^{\Re} & \mathbf{y}_2^{\Re} & \cdots & \mathbf{y}_U^{\Re} \end{bmatrix}, \tag{4.18}$$

$$\mathbf{Y}^{\Im} = \begin{bmatrix} \mathbf{y}_1^{\Im} & \mathbf{y}_2^{\Im} & \cdots & \mathbf{y}_U^{\Im} \end{bmatrix}, \tag{4.19}$$

where $\mathbf{y}_u^{\Re} = \mathfrak{Re}\{\mathbf{y}_u\}$ and $\mathbf{y}_u^{\Im} = \mathfrak{Im}\{\mathbf{y}_u\}$. Then, $\mathbf{Y}^{\Re}$ and $\mathbf{Y}^{\Im}$ are despreaded by multiplying with the l^{th} spreading code and summing over the symbol period T_s, as follows:

$$\bar{\mathbf{y}}_l^{\Re} = \mathbf{Y}^{\Re}\mathbf{c}_l^{\mathrm{T}} = \sum_{u=1}^{U} \mathbf{y}_u^{\Re} c_{l,u} = [\bar{y}^{\Re,1}, \cdots, \bar{y}^{\Re,N_r}]^{\mathrm{T}}, \tag{4.20}$$

$$\bar{\mathbf{y}}_l^{\Im} = \mathbf{Y}^{\Im}\mathbf{c}_l^{\mathrm{T}} = \sum_{u=1}^{U} \mathbf{y}_u^{\Re} c_{l,u} = [\bar{y}^{\Im,1}, \cdots, \bar{y}^{\Im,N_r}]^{\mathrm{T}}, \tag{4.21}$$

where $\bar{y}^{\Re,r} = \sum_{u=1}^{U} y_u^r c_{l,u}$. After despreading matrices $\mathbf{Y}^{\Re}$ and $\mathbf{Y}^{\Im}$ with each spreading code, two sets are obtained: $\{\|\bar{\mathbf{y}}_1^{\Re}\|^2, \cdots, \|\bar{\mathbf{y}}_{N_S}^{\Re}\|^2\}$ and $\{\|\bar{\mathbf{y}}_1^{\Im}\|^2, \cdots, \|\bar{\mathbf{y}}_{N_S}^{\Im}\|^2\}$. The detected spreading code indices can be obtained as follows:

$$\hat{l}_{\Re} = \arg \max_{l=1,\cdots,N_S} \|\bar{\mathbf{y}}_l^{\Re}\|^2, \tag{4.22}$$

$$\hat{l}_{\Im} = \arg \max_{l=1,\cdots,N_S} \|\bar{\mathbf{y}}_l^{\Im}\|^2. \tag{4.23}$$

The estimated spreading code indices $\hat{l}_{\Re}$ and $\hat{l}_{\Im}$ are used to despread $\mathbf{Y}^{\Re}$ and $\mathbf{Y}^{\Im}$, respectively, as $\tilde{\mathbf{y}}^{\Re} = \mathbf{Y}^{\Re}\mathbf{c}_{\hat{l}_{\Re}}^{\mathrm{T}} = [\tilde{y}_1^{\Re}, \cdots, \tilde{y}_{N_r}^{\Re}]^{\mathrm{T}}$ and $\tilde{\mathbf{y}}^{\Im} = \mathbf{Y}^{\Im}\mathbf{c}_{\hat{l}_{\Im}}^{\mathrm{T}} = [\tilde{y}_1^{\Im}, \cdots, \tilde{y}_{N_r}^{\Im}]^{\mathrm{T}}$. In the second step, an energy detection method is applied to decode the selected receive antenna indices as follows:

$$\hat{r}_{\Re} = \arg \max_{r=1,\cdots,N_r} |\tilde{y}_r^{\Re}|^2, \tag{4.24}$$

$$\hat{r}_{\Im} = \arg \max_{r=1,\cdots,N_r} |\tilde{y}_r^{\Im}|^2. \tag{4.25}$$

Finally, the modulated symbol can be decoded by using the parameters $\hat{l}_{\Re}$, $\hat{l}_{\Im}$, $\hat{r}_{\Re}$ and $\hat{r}_{\Im}$, as given:

$$\hat{x} = \arg \min_{x \in \mathcal{M}} \left|\tilde{y}_{\hat{r}_{\Re}}^{\Re} + j\tilde{y}_{\hat{r}_{\Im}}^{\Im} - \Delta x\right|^2, \tag{4.26}$$

where $\Delta = |\mathbf{g}^{1,\hat{r}_{\Re}}||\mathbf{h}^1| + j|\mathbf{g}^{2,\hat{r}_{\Im}}||\mathbf{h}^2|$.

4.3 Performance Analyses

In this section, the performance of RIS-CIM-QRSM is evaluated through analyses of detection complexity, spectral efficiency, and energy efficiency.

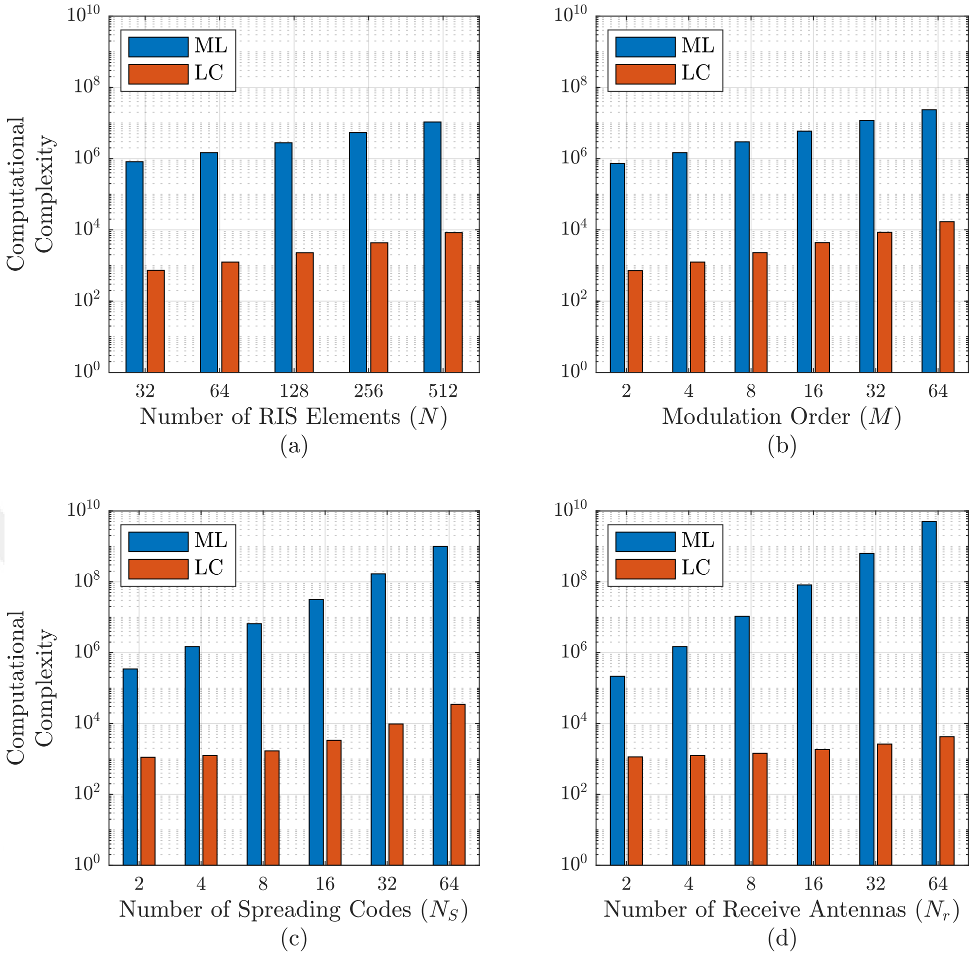

Figure 4.2: Computational complexity comparison of ML and LC detectors for the RIS-CIM-QRSM scheme for (a) varying the number of RIS elements (N), (b) varying the modulation order (M), (c) varying the number of spreading codes (N_S), (d) varying the number of receive antennas (N_r).

4.3.1 Detection Complexity Analysis

In this subsection, we analyze and compare the computational complexities of the ML and low-complexity detectors in terms of real multiplications. The ML detector relies on an exhaustive search, resulting in a computational complexity given by:

$$\mathfrak{C}^{\mathrm{ML}}_{\text{RIS-CIM-QRSM}} = (4N + 4N_r N + 4N_r N_S) M N_S^2 N_r^2. \tag{4.27}$$

This complexity is proportional to the modulation order M, the cube of the number of spreading codes N_S, and the cube of the number of receive antennas N_r. Consequently, decoding the RIS-CIM-QRSM signal with the ML detector can

Table 4.3: Parameters (M, N_S, N_r) for RIS-CIM, RIS-CIM-RSM, and RIS-CIM-QRSM schemes across four cases.

Cases / Schemes	**Case 1** $N = 256$	**Case 2** $N = 64$	**Case 3** $N = 64$	**Case 4** $N = 64$
RIS-CIM	$(256, 8, \varnothing)$	$(256, 8, \varnothing)$	$(512, 4, \varnothing)$	$(512, 4, \varnothing)$
RIS-CIM-RSM	$(8, 8, 4)$	$(8, 8, 4)$	$(32, 4, 4)$	$(16, 4, 8)$
RIS-CIM-RQSM	$(2, 8, 4)$	$(2, 8, 4)$	$(8, 4, 4)$	$(2, 4, 8)$

become computationally prohibitive, particularly in scenarios with large values of M, N_S, and N_r.

To address this limitation, we propose a low-complexity detector which offers significantly lower computational complexity compared to the ML detector. By counting the real multiplications required for the low-complexity detector, its computational complexity can be obtained as

$$\mathfrak{C}^{\mathrm{LC}}_{\text{RIS-CIM-QRSM}} = 2N_S N_r(N_S + 2) + 2N_r + M(4N + 6), \tag{4.28}$$

which is considerably more efficient than the ML detector, especially as M, N_S, and N_r grow.

In Fig. 4.2, the computational complexity of the ML and low-complexity detectors is compared in terms of real multiplications for various system parameters: number of RIS elements (N), modulation order (M), number of spreading codes (N_S), and number of receive antennas (N_r). As expected, for both detectors, the complexity increases as any of these parameters grows. However, the ML detector experiences a significantly steeper rise in complexity across all cases, making it computationally prohibitive for large values of N, M, N_S, and N_r. In contrast, the low-complexity detector consistently provides a much lower computational burden, making it more efficient and practical for real-world applications.

In Fig. 4.3, the computational complexities of the low-complexity detectors for RIS-CIM, RIS-CIM-RSM, and RIS-CIM-QRSM schemes is compared across four

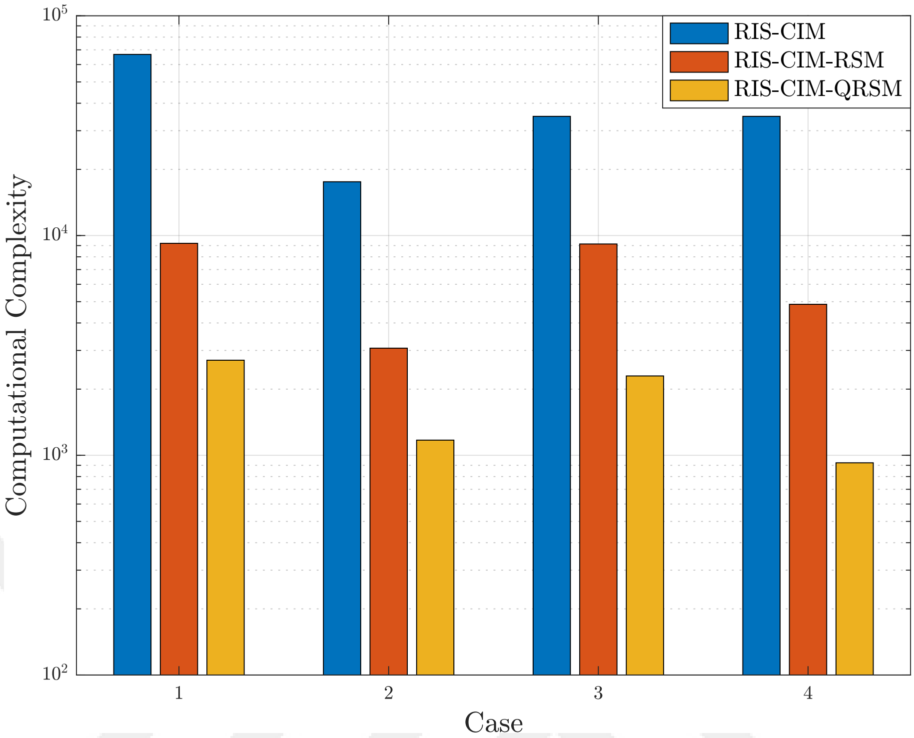

Figure 4.3: Computational complexity comparison of LC detectors for RIS-CIM, RIS-CIM-RSM, and RIS-CIM-QRSM schemes across four cases.

cases, with bpcu fixed at 11 for all schemes. The computational complexities of the low-complexity detectors for the RIS-CIM and RIS-CIM-RSM schemes, in terms of real multiplications, can be expressed as follows:

$$\mathfrak{C}_{\text{RIS-CIM}}^{\text{LC}} = 2N_S^2 + 4N_S + M(N+4), \tag{4.29}$$

$$\mathfrak{C}_{\text{RIS-CIM-RSM}}^{\text{LC}} = 2N_r N_S(N_S+2) + M(4N+6N_S), \tag{4.30}$$

respectively. Note that the low-complexity detector of RIS-CIM-RSM decodes the receive antenna index, spreading code indices, and the modulated symbol sequentially. The specific parameters for each scheme in each case are summarized in Table 4.3.

As seen in Fig. 4.3, the low-complexity detector for the proposed RIS-CIM-QRSM scheme provides the lowest computational complexity in terms of real multiplications across all cases. This is primarily due to the high modulation order used in RIS-CIM to achieve the same bpcu as RIS-CIM-QRSM, as RIS-CIM does not transmit information bits via the receive antenna index, which leads to a significant increase in complexity. Similar to RIS-CIM, RIS-CIM-RSM exhibits higher complexity than RIS-CIM-QRSM because the low-complexity detector for RIS-CIM-RSM needs higher modulation order than the proposed scheme to achieve the same spectral efficiency, resulting in a higher computational load.

When comparing Cases 1 and 2, we observe the effect of RIS size on the complexity of the low-complexity detectors across the schemes. The increase in complexity as the RIS size grows is nearly linear. Comparing Cases 3 and 4 highlights the impact of the number of receive antennas (N_r) and the modulation order (M) for the same bpcu. Increasing N_r while decreasing M effectively lowers the computational complexity. Lastly, comparing Cases 2 and 3 shows the combined effect of spreading codes (N_S) and modulation order. Increasing N_S and decreasing M further reduces the complexity.

In all cases, the low-complexity detector of RIS-CIM-QRSM consistently presents the lowest complexity, making it the most efficient choice among the schemes.

4.3.2 Spectral Efficiency Analysis

In this subsection, the spectral efficiency values of RIS-CIM, RIS-CIM-RSM, and RIS-CIM-QRSM are compared. The spectral efficiencies of RIS-CIM, RIS-CIM-RSM, and RIS-CIM-QRSM, in terms of bps/Hz, can be given as:

$$\eta_{\text{RIS-CIM}} = \frac{\log_2(M) + \log_2(N_S)}{N_S}, \tag{4.31}$$

$$\eta_{\text{RIS-CIM-RSM}} = \frac{\log_2(M) + 2\log_2(N_r) + \log_2(N_S)}{N_S}, \tag{4.32}$$

$$\eta_{\text{RIS-CIM-QRSM}} = \frac{\log_2(M) + 2\log_2(N_r) + 2\log_2(N_S)}{N_S}, \tag{4.33}$$

respectively.

Figs. 4.4 and 4.5 illustrate the spectral efficiency comparisons for RIS-CIM, RIS-CIM-RSM, and RIS-CIM-QRSM schemes under different N_S values (2 and 4, respectively) as a function of M and N_r. In each case, RIS-CIM-QRSM achieves the highest spectral efficiency due to its ability to encode additional information

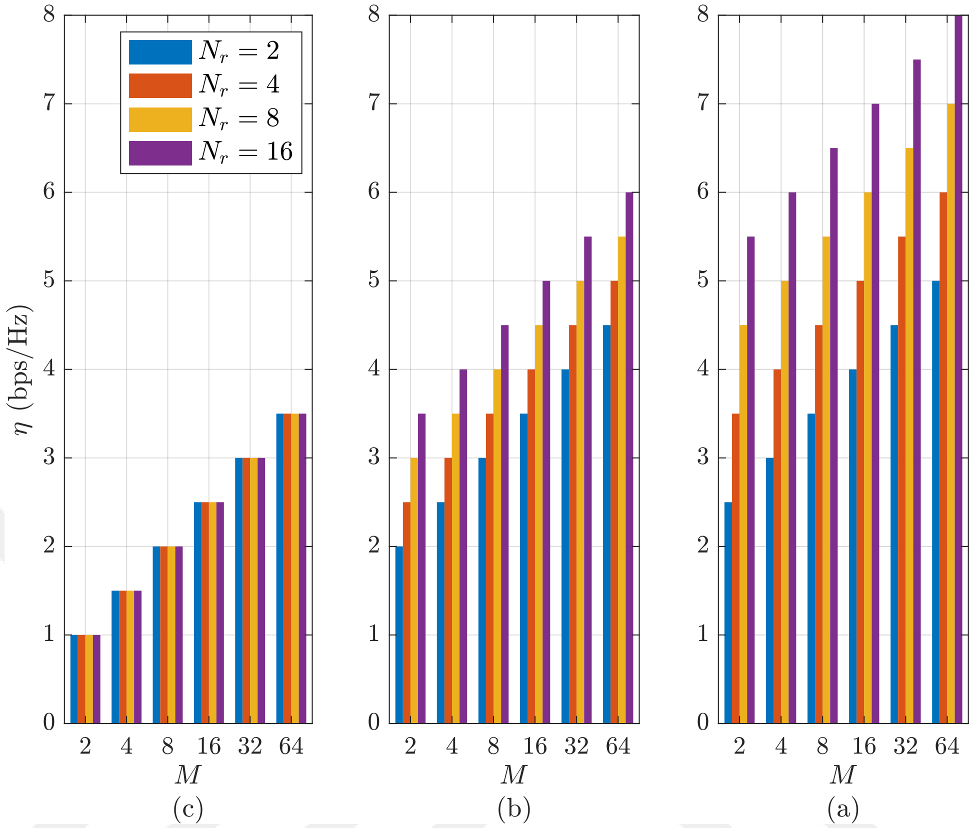

Figure 4.4: Spectral efficiency comparison of (a) RIS-CIM, (b) RIS-CIM-RSM, and (c) RIS-CIM-QRSM for $N_S = 2$, varying M and N_r values.

bits through both receive antenna indices, leveraging a higher number of IM bits compared to RIS-CIM and RIS-CIM-RSM. For RIS-CIM, the spectral efficiency remains unchanged as N_r increases since it does not use the receive antenna indices to convey information bits. Additionally, the increase in N_S from Fig. 4.4 to Fig. 4.5 causes a decline in spectral efficiency across all schemes. This is due to the larger spreading factor, which increases the required bandwidth and reduces spectral efficiency.

4.3.3 Energy Efficiency Analysis

Energy efficiency has become increasingly critical with the global expansion and evolution of wireless communication technologies. The importance of designing energy-efficient systems for wireless communication networks continues to grow. In

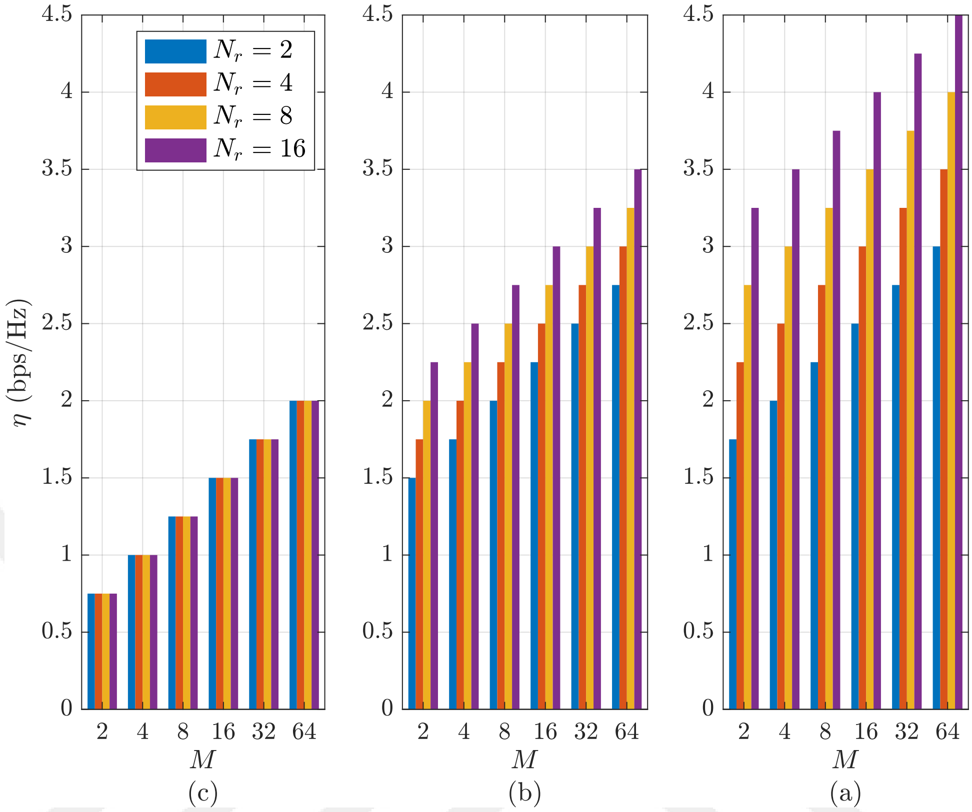

Figure 4.5: Spectral efficiency comparison of (a) RIS-CIM, (b) RIS-CIM-RSM, and (c) RIS-CIM-QRSM for $N_S = 4$, varying M and N_r values.

this subsection, we analyze the energy efficiency of the proposed RIS-CIM-QRSM scheme and compare it with benchmark schemes. Since RIS-CIM-QRSM conveys a higher number of IM bits compared to the benchmark schemes, it achieves superior energy efficiency. The energy-saving percentage of the proposed RIS-CIM-RSM scheme can be given as follows:

$$\mathcal{E}_{\text{saving}} = \left(1 - \frac{\eta_\iota}{\eta}\right) E_b\%, \tag{4.34}$$

where $E_b = 1/\log_2(M)$ is the bit energy, and η_ι is the spectral efficiency of the reference system with $\iota \in \{\text{RIS-CIM}, \text{RIS-CIM-RSM}\}$. The energy-saving percentage of RIS-CIM-QRSM is compared with that of RIS-CIM and RIS-CIM-RSM across multiple cases, as shown in Table 4.4. It can be seen from Fig. 4.6 that the proposed scheme consistently achieves higher energy efficiency than the benchmark schemes. The advantage becomes more pronounced when M is small, as the proportion of IM

Table 4.4: Parameters corresponding to the cases used for energy efficiency analysis.

Cases \ **Parameters**	M	N_r	N_S
1	2	2	2
2	2	2	4
3	2	4	2
4	2	4	4
5	4	2	2
6	4	2	4
7	4	4	2
8	4	4	4
9	8	2	2
10	8	2	4
11	8	4	2
12	8	4	4

bits in the total transmitted bits increases.

4.4 Simulation Results and Comparisons

In this section, the error performance of the proposed RIS-CIM-QRSM scheme is evaluated through extensive computer simulations for varying system parameters and bpcu values, and compared with benchmark schemes, including RIS-CIM and RIS-CIM-RSM.

In Fig. 4.7, the error performance of ML and low-complexity detectors is compared for $M = 2$, $N_S = 2$, $N_r = 2$, and varying N values. As N increases, both detectors show improved error performance due to enhanced SNR at the receive antennas. The ML detector achieves optimal performance by jointly detecting modulated symbol, spreading code indices, and receive antenna indices, whereas the

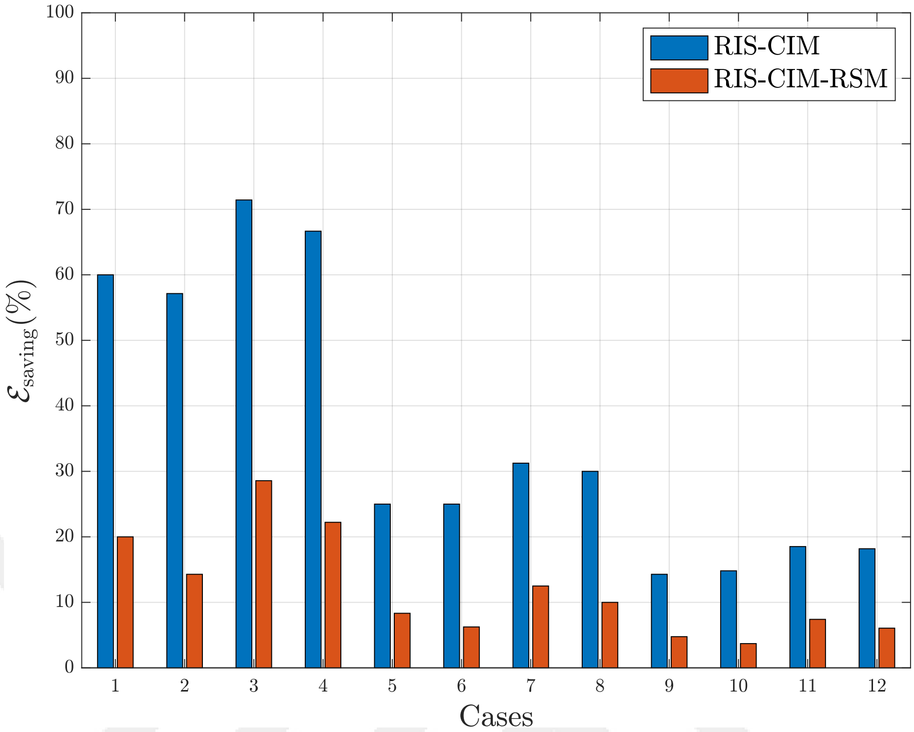

Figure 4.6: Comparison of energy-saving percentages for RIS-CIM, RIS-CIM-RSM, and RIS-CIM-QRSM across different cases.

low-complexity detector is a sub-optimal. The gap between the low-complexity and ML detectors widens as N decreases. However, as N increases, the low-complexity detector's error floor shifts to lower BER values, making it more competitive at higher SNR values. In terms of computational complexity, the ML detector requires 25856, 50432, and 99584 real multiplications for $N = 64$, 128, and 256, respectively, compared to 560, 1072, and 2096 multiplications for the low-complexity detector. Although the ML detector outperforms the low-complexity detector, its computational cost becomes prohibitive for larger values of M, N_S, and N_r, making the low-complexity detector a practical alternative in such scenarios.

In Fig. 4.8, the error performance of the RIS-CIM-QRSM scheme is compared for (a) varying numbers of spreading codes N_S and (b) varying numbers of receive antennas N_r. As seen in Fig. 4.8, as N increases, the error performance improves due to higher SNR at the receiver. For all values of N, increasing N_S results in better error performance, as a larger code length increases the minimum Euclidean

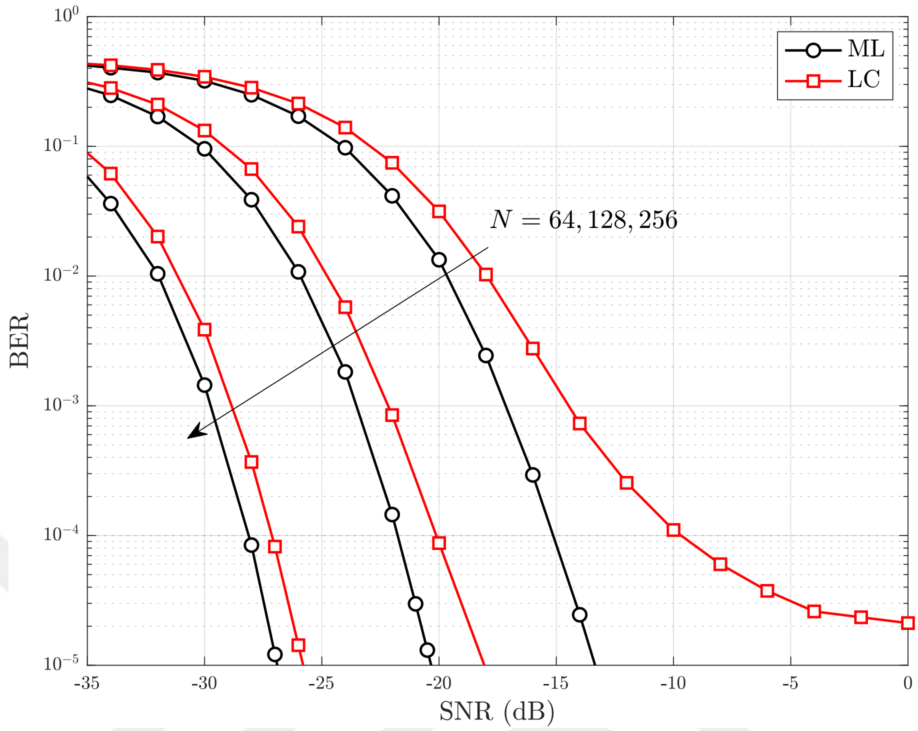

Figure 4.7: Error performance comparison of the ML and LC detectors for $M = 2$, $N_S = 2$, $N_r = 2$, and varying N values.

distance constellation points, reducing the probability of symbol errors. However, this improvement comes at the cost of increased bandwidth usage due to the spreading effect. The bpcu values are 4, 5, 6, and 7 for $N_S = 2$, 4, 8, and 16, respectively. In contrast, the spectral efficiency values decrease with higher spreading, with values of 2, 1.25, 0.75, and 0.4375 bps/Hz for $N_S = 2$, 4, 8, and 16, respectively, indicating a trade-off between error performance and spectral efficiency.

In Fig. 4.8(b), we observe that as N_r increases, the BER performance worsens across all values of N. This degradation occurs because the system may experience more interference or complexity in managing signals from multiple receive antennas, which affects the error performance negatively. Additionally, while increasing N_r can lead to higher bpcu values, contributing to improved throughput, it also increases hardware cost, as more receive antennas require additional components, impacting the feasibility of implementing the system in cost-sensitive environment

In Fig. 4.9, the error performance of the proposed RIS-CIM-QRSM scheme is

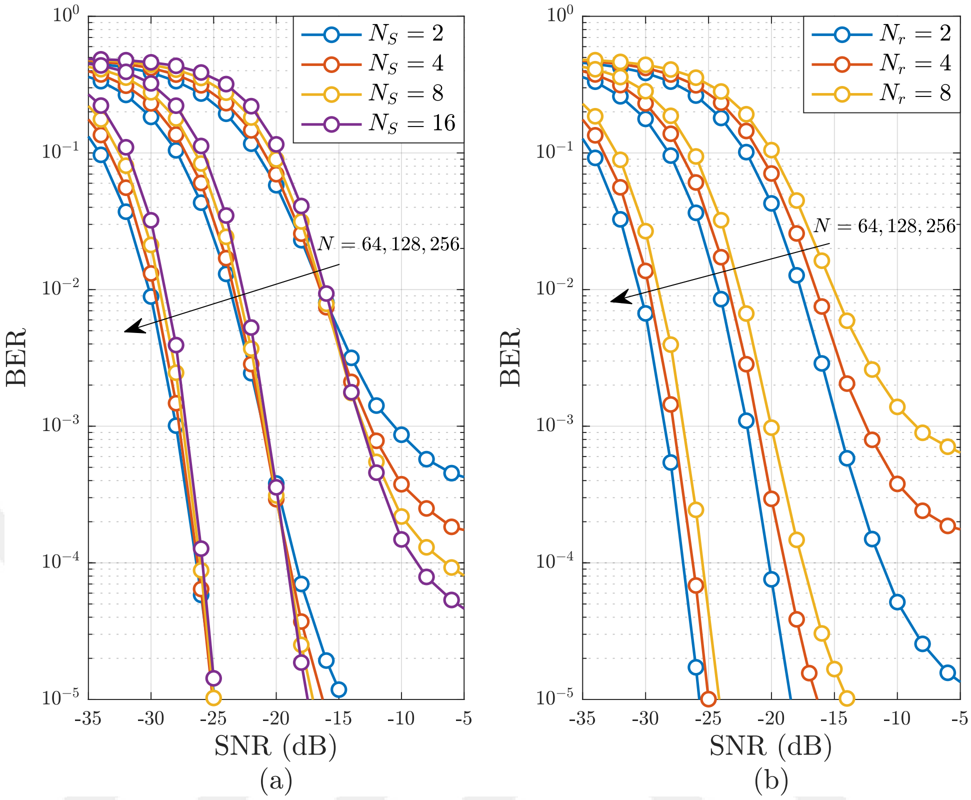

Figure 4.8: Error performance comparison of RIS-CIM-QRSM for (a) $N_r = 4$, $M = 2$, and varying N_S, and (b) $M = 2$, $N_S = 4$, and varying N_r.

compared with two benchmark schemes, RIS-CIM and RIS-CIM-RSM, for 11 bpcu and varying N values. The parameters for each scheme are as follows: for RIS-CIM, $N_S = 4$ and 512-QAM, for RIS-CIM-RSM, $N_S = 4$, $N_r = 8$, and 16-QAM; and for RIS-CIM-QRSM, $N_S = 4$, $N_r = 8$, and 2-PAM. As seen in Fig. 4.9, RIS-CIM-QRSM outperforms both RIS-CIM and RIS-CIM-RSM for $N = 256, 512$ in terms of error performance. This performance gain is attributed to the lower modulation order used in RIS-CIM-QRSM, compared to benchmark schemes, while still achieving the same bpcu value. The lower modulation order allows RIS-CIM-QRSM to maintain a greater minimum Euclidean distance between constellation points, thereby reducing the probability of symbol errors. The performance improvement of RIS-CIM-QRSM is particularly noticeable as N increases, showing a larger performance gap at higher N values.

In Fig. 4.10, the error performance of the RIS-CIM-QRSM scheme is compared

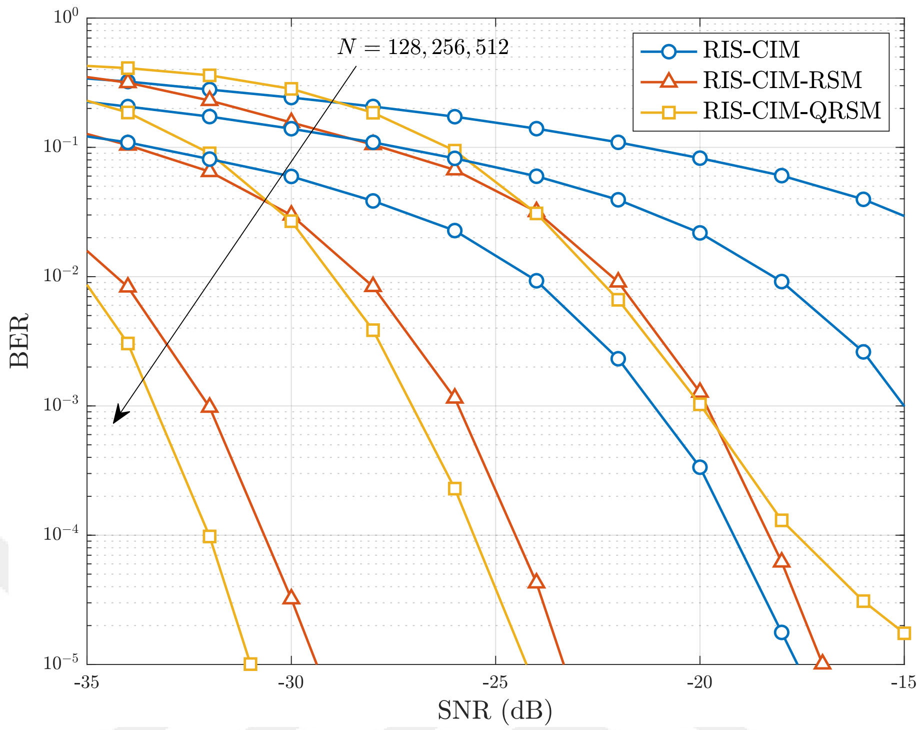

Figure 4.9: Error performance comparison of RIS-CIM-QRSM with benchmark schemes for 11 bpcu and varying N values.

to RIS-CIM-RSM for 13 bpcu and varying N values. The parameters for each scheme are as follows: for RIS-CIM-RSM, $N_S = 8$, $N_r = 8$ and 16-QAM; and for RIS-CIM-QRSM, $N_S = 8$, $N_r = 8$, and 2-PAM. As shown in Fig. 4.10, RIS-CIM-QRSM consistently achieves better error performance compared to RIS-CIM-RSM for $N = 192, 256$. This improvement is primarily due to the lower modulation order $M = 2$ used in RIS-CIM-QRSM, which allows for a greater minimum Euclidean distance between constellation points, reducing the probability of symbol errors. In contrast, RIS-CIM-RSM uses a much higher modulation order $M = 16$, which leads to a higher likelihood of error at comparable SNR levels. The performance gap between RIS-CIM-QRSM and RIS-CIM-RSM becomes even more pronounced as N increases.

In Fig. 4.11, the error performance of the RIS-CIM-QRSM scheme is compared with RIS-CIM-RSM for $N_r = 8$, $N_S = 16$, and 15 bpcu, with varying values of N. The modulation schemes used are 2-PAM for RIS-CIM-QRSM and 16-QAM for

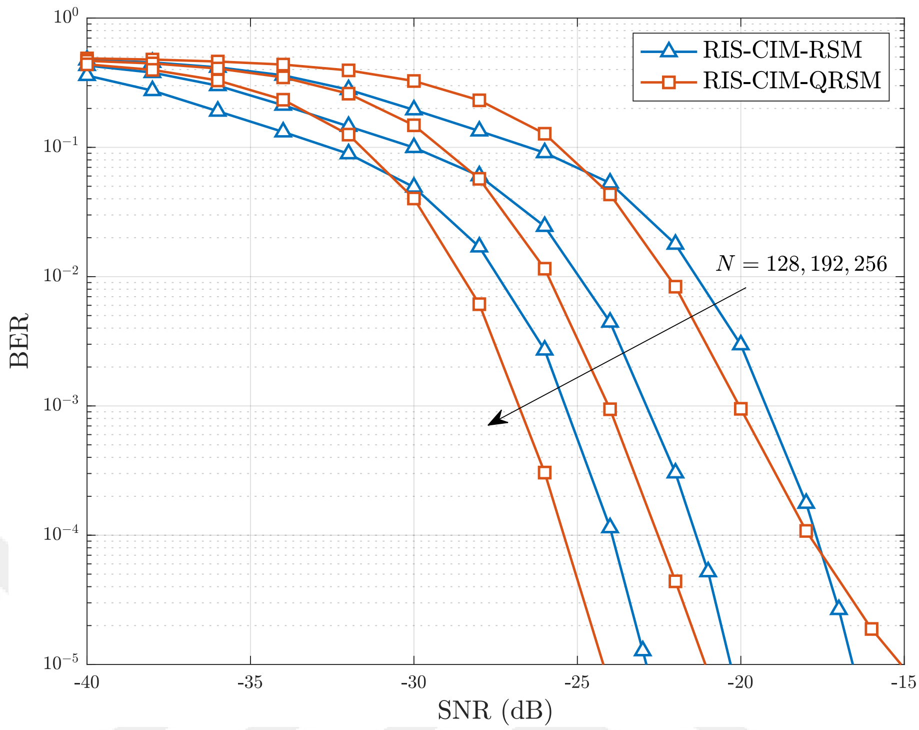

Figure 4.10: Error performance comparison of RIS-CIM-QRSM with RIS-CIM-RSM for 13 bpcu and varying N values.

RIS-CIM-RSM. As observed in Fig. 4.11, RIS-CIM-RSM outperforms the proposed RIS-CIM-QRSM scheme in the low SNR region. However, at higher SNR values, RIS-CIM-QRSM provides superior error performance compared to RIS-CIM-RSM. The error performance gap between the two schemes becomes more pronounced as N decreases.

4.5 Conclusion

In this chapter, we have presented RIS-CIM-QRSM, a new RIS-aided wireless communication scheme designed to improve the error performance, spectral efficiency, and energy efficiency of RIS-aided IM systems. The proposed scheme, which combines QRSM with CIM and uses RIS partitioning, uses in-phase and quadrature spreading codes to improve the minimum Euclidean distance, thereby improving system reliability. We have also introduced ML and low-complexity detectors, with the

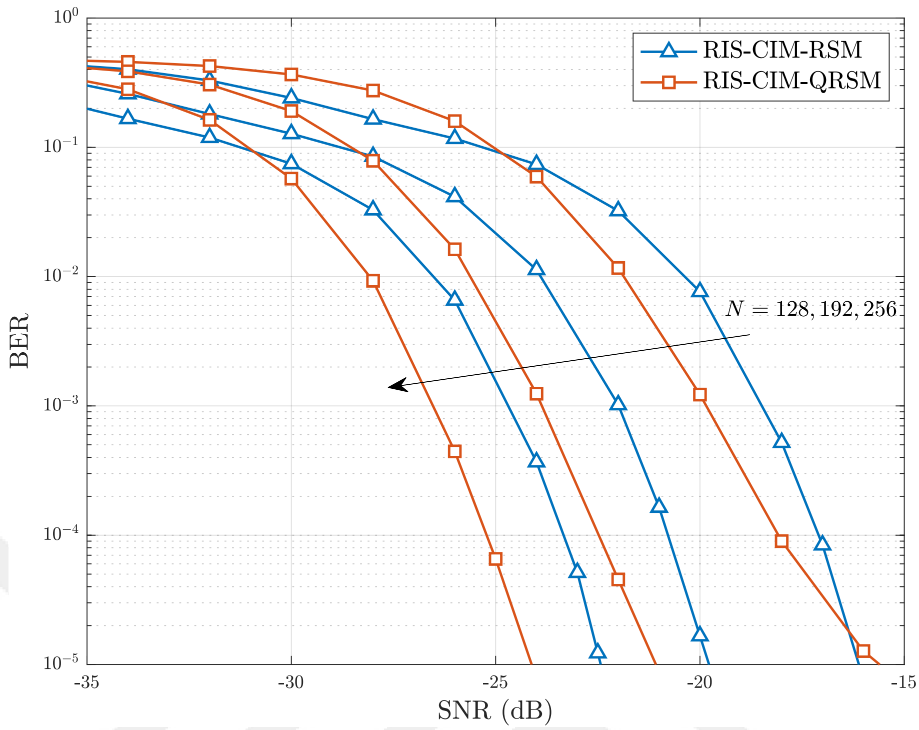

Figure 4.11: Error performance comparison of RIS-CIM-QRSM with RIS-CIM-RSM for $N_r = 8$, $N_S = 16$ and 15 bpcu, with varying N values.

latter offering a practical solution for reducing computational burden. Comparative analyses and extensive computer simulations have revealed that RIS-CIM-QRSM outperforms benchmark schemes RIS-CIM and RIS-CIM-RSM across a variety of scenarios in terms of error performance, spectral efficiency, and energy efficiency. Future research could focus on improving detector design, energy efficiency, and the RIS-CIM-QRSM framework's adaptability in dynamic wireless environments.

Chapter 5

HYBRID RECONFIGURABLE INTELLIGENT SURFACE-ENABLED ENHANCED REFLECTION MODULATION

5.1 Introduction

6G technology, representing the next evolutionary step in wireless communications, is poised to extend the capabilities of 5G networks with faster data speeds, reduced latency, and increased network density [Wang et al., 2023]. It aims to support a broad spectrum of applications, ranging from advanced artificial intelligence and machine learning integration to sophisticated sensing and URLLC [Jiang et al., 2021]. These enhancements are critical for powering future innovations like smart cities, autonomous systems, and immersive digital experiences. To meet these comprehensive demands, innovative technological solutions such as RISs are essential.

RIS-empowered communication is emerging as a promising technology that can contribute significantly to the efficiency and performance of 6G networks [Wu et al., 2023]. RISs offer a great potential to improve signal propagation and energy efficiency through dynamic manipulation of electromagnetic waves, thus complementing the diverse array of technologies required to realize the ambitious vision of 6G [Liu et al., 2021]. Characterized by their extensive reflective capabilities, RISs consist of numerous cost-effective metamaterial elements that can alter the properties of incoming signals. [ElMossallamy et al., 2020]. This capability allows RISs to not only reflect but also refract, absorb, and amplify signals without necessitating additional buffering or processing, effectively offering a virtual means of manipulating the wireless channel [Basar et al., 2019]. RISs are primarily considered for their potential to enhance coverage, improve signal quality, increase system capacity, and facilitate other performance enhancements. One of the key strengths of RIS technology lies in its versatility, allowing seamless integration with existing communication technologies [Basar et al., 2023]. Numerous studies highlight the significant advantages of incorporating RISs with well-established technologies, including NOMA [Dogukan et al., 2024a, Arslan et al., 2022a, Khaleel and Basar, 2021, Kilinc et al., 2023], OFDM [Yang et al., 2020], MIMO [Khaleel and Basar, 2020] and much more.

IM, as introduced in [Basar, 2016a], provides a straightforward yet efficient approach for information embedding and transmitting additional bits by utilizing the indices of transmit entities in communication systems. These entities, which can include subcarriers [Dogukan et al., 2022, Tugtekin et al., 2023], antennas [Kurt et al., 2023], constellations [Dogukan and Basar, 2020b], delay-Doppler bins [Tek and Basar, 2024], among others, serve as the foundation for this embedding process. IM has attracted significant attention and extensive research, proving its value and potential as a key instrument for future network designs [Basar et al., 2017]. Its advantages include improved error performance, enhanced energy and spectral efficiencies, and reduced complexity [Mao et al., 2018]. A defining feature of IM is its adaptability and compatibility, allowing for its seamless integration and coexistence with various methodologies within wireless communication systems, underlining its versatility and potential for future applications. Building on its inherent adaptability, IM can be effectively and seamlessly integrated with a variety of advanced technologies, such as NOMA [Arslan et al., 2020b], RIS [Basar, 2020], and deep learning [Ozpoyraz et al., 2022], among others, enhancing the overall performance and efficiency of communication systems and paving the way for innovative solutions in the wireless industry.

IM has demonstrated potential in enhancing the performance of RIS-assisted wireless systems. Thanks to the innovative application of IM, numerous compelling designs have been developed in RIS-assisted wireless communications, showcasing its potential to improve system efficiency and reliability. In [Basar, 2020], RIS-SSK and RIS-SM schemes are proposed, enhancing RIS-assisted communications by intelligently reflecting signals to improve reception and employing antenna indices for

IM, thus boosting spectral efficiency. In [Li et al., 2021b], the detailed comparison of RIS-aided SM schemes has been provided. To augment the number of bits transmitted through receive IM, multi-direction beamforming at the RIS is utilized to select multiple receive antennas, as explored in [Albinsaid et al., 2021]. By using the index of reflection states of RIS elements, passive beamforming and information transfer (PBIT) are performed in [Yan et al., 2019]. To address substantial variations in reflected signal power, RIS-based reflection pattern modulation (RIS-RPM) has been proposed in [Lin et al., 2020], enhancing the efficiency of PBIT and minimizing the communication outage probability. Additionally, another IM technique called RM has been introduced in [Guo et al., 2020], utilizing more advanced reflection patterns to improve PBIT. Inspired from [Jaradat et al., 2018], RIS-aided number modulation [Li et al., 2022], which can be considered as an another RM technique, has been proposed where the number of in-phase and quadrature RIS groups is used to apply IM. RM schemes in [Yan et al., 2019, Lin et al., 2020, Guo et al., 2020] activate only a subset of the available RIS elements; hence, the performance enhancement provided by an RIS is not fully utilized, leading to comparatively low levels of received signal power. To address this issue, a novel RM scheme, termed RIS-aided quadrature RM (RIS-QRM), is presented [Lin et al., 2021]. In RIS-QRM, an RIS is divided into two groups based on the information bits, with the elements in the first RIS group tuned to phase shift of $-\theta$ and those in the second RIS group to $-\theta+\pi/2$. In [Asmoro and Shin, 2022], RIS grouping based IM (RGB-IM) has been proposed, where information bits are transmitted by employing the indices of activated RIS groups. In [Feng and Li, 2023], an enhanced RIS APSK (E-RIS-APSK) scheme, which transmits information bits via the number of activated RIS groups and phase shifted PSK symbols, has been proposed.

The aforementioned studies predominantly focus on the passive RIS structures, which are advantageous because they introduce negligible additional noise and can significantly increase array gains, especially in SISO systems where the SNR gain is directly proportional to the square of the number of RIS elements [Wu and Zhang, 2019]. However, their effectiveness in enhancing capacity gains is mostly limited to scenarios with weak or blocked direct links, due to multiplicative fading effect which greatly increases path loss [Huang et al., 2019b]. To address these challenges in 6G networks, the use of active RIS structure has been introduced in [Zhang et al., 2022b, Long et al., 2021]. Unlike passive RISs, active RISs have the ability to amplify signals to mitigate the high path loss caused by multiplicative fading, thereby offering the potential for improved capacity gains, albeit with increased power consumption. Various studies in the literature have explored the active RIS structure. For instance, [Zhi et al., 2022] presents a theoretical comparison between active and passive RIS-aided systems, assuming the same overall power budgets for both setups. Furthermore, a novel active RIS design is proposed to improve secure wireless transmission, where RIS elements not only adjust the phase shift but also amplify the signal amplitude, effectively reducing the impact of multiplicative fading and significantly enhancing secrecy performance [Dong et al., 2021]. Meanwhile, [Chen et al., 2022] explores an active RIS-assisted IoT system aiming to maximize throughput by optimizing RIS beamforming and resource allocation for uplink transmissions from IoT devices to an AP.

Hybrid RIS, which combines active and passive elements, emerges as an interesting RIS structure [Schroeder et al., 2021]. In [Kang et al., 2023], a hybrid RIS design has been implemented in a multi-user wireless communication system, leveraging the advantages of both active and passive elements. Moreover, in [Yigit et al., 2022], a hybrid RIS-aided IM transmission technique called hybrid RM (HRM) has been proposed. HRM involves partitioning the RIS into groups, with information bits being transmitted through the index of the active RIS group number.

In this chapter, we introduce two novel IM techniques, named hybrid RIS-enabled enhanced RM scheme I (Hyb-ERM-I) and scheme II (Hyb-ERM-II), which aim to transmit information bits more reliably by exploiting a hybrid RIS partitioned into groups, thereby improving spectral efficiency and enhancing BER performance. Similar to the HRM scheme [Yigit et al., 2022], our proposed Hyb-ERM schemes I and II employ electronically controllable phase shifters and reflection-type amplifiers [Zhang et al., 2022b], allowing for simultaneous reflection and amplification of signals. These phase shifters can be dynamically adjusted to achieve appropriate phase shifts, while the power amplifiers can be switched ON or OFF based on the incoming information bits to control power usage. Consequently, an RIS element in the Hyb-ENM scheme can either passively reflect the incident signal without amplification or actively amplify it, increasing power consumption, depending on the information bits. By adopting the IM approach, in Hyb-ERM-I, an RIS is divided into groups, enabling the transmission of information through different channel realizations generated by the various active and passive reflecting elements within these RIS groups. In addition to IM, information bits are conveyed with M-ary modulated PSK signal constellation. Unlike HRM, Hyb-ENM scheme introduces an additional phase shift for an even number of the number of active RIS groups to improve the minimum Euclidean distance between constellation symbols. Moreover, in Hyb-ERM-I, Gray coding is used to map incoming bits to the number of active RIS subgroups, enhancing error performance by minimizing Euclidean distance shifts between successive signal constellations. Note that Hyb-ERM-I is an extension of E-RIS-APSK proposed in [Feng and Li, 2023] to a hybrid RIS structure. Since E-RIS-APSK exploits the number of active RIS groups to transmit information bits, the received SNR decreases dramatically due to use of passive RIS. However, Hyb-ERM-I uses hybrid RIS structure and it always activates the RIS elements leading to higher received SNR. To further improve the error performance of Hyb-ERM-I, Hyb-ERM-II is proposed. In Hyb-ERM-II, the RIS elements are ordered based on the corresponding channel coefficients and RIS groups are generated by using these ordered RIS elements.

5.2 System Model

In this section, we first provide the hybrid RIS structure that includes both active and passive elements. A SISO system with a hybrid RIS including N elements is considered where the BS and UE can communicate only by using the path through RIS since the direct link between the BS and UE is assumed to be blocked. As seen in Fig. 5.1, the RIS is separated into G groups, each including F elements, i.e.,

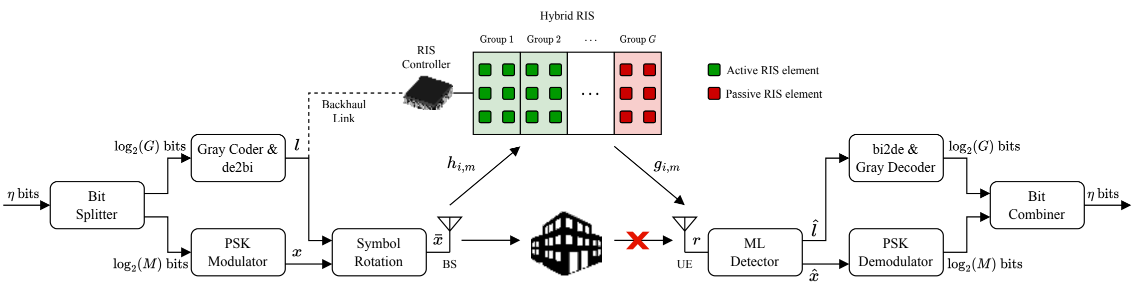

Figure 5.1: System model of Hyb-ERM-I.

$N = GF$. It is assumed that $L_h = L_0 d_h^{-\kappa_h}$ and $L_g = L_0 d_g^{-\kappa_g}$ denote the large-scale path losses for the BS to RIS and the RIS to UE links, respectively. Herein, L_0 represents the path loss encountered at a reference distance of one meter, while the parameters d_h and d_g represent the distances from the BS to the RIS and from the RIS to the UE, respectively. Additionally, κ_h and κ_g are denoted as the path loss exponents for the links between the BS and the RIS, and between the RIS and the UE, respectively. Moreover, the channel coefficients for the link from the BS to the (i,m)th element of the RIS and from this (i,m)th RIS element to the UE are defined as $h_{i,m} = \sqrt{L_h}\tilde{h}_{i,m}$ and $g_{i,m} = \sqrt{L_g}\tilde{g}_{i,m}$, respectively. The channel coefficients can be also represented as $h_{i,m} = |h_{i,m}|\, e^{j\phi_{i,m}}$ and $g_{i,m} = |g_{i,m}|\, e^{j\varphi_{i,m}}$. Here, the terms $\tilde{h}_{i,m}$ and $\tilde{g}_{i,m}$ denote independent Rician fading channel coefficients, characterized as follows:

$$\tilde{h}_{i,m} = \sqrt{\frac{K_h}{K_h+1}}\tilde{h}_{i,m}^{\text{LoS}} + \sqrt{\frac{1}{K_h+1}}\tilde{h}_{i,m}^{\text{NLoS}}, \tag{5.1}$$

$$\tilde{g}_{i,m} = \sqrt{\frac{K_g}{K_g+1}}\tilde{g}_{i,m}^{\text{LoS}} + \sqrt{\frac{1}{K_g+1}}\tilde{g}_{i,m}^{\text{NLoS}}, \tag{5.2}$$

where $\tilde{h}_{i,m}^{\text{LoS}} = \exp(-j2\pi d_h/\lambda)$ and $\tilde{g}_{i,m}^{\text{LoS}} = \exp(-j2\pi d_g/\lambda)$ correspond to the LOS components, while $\tilde{h}_{i,m}^{\text{NLoS}}$ and $\tilde{g}_{i,m}^{\text{NLoS}}$ indicate the NLOS components for $\tilde{h}_{i,m}$ and $\tilde{g}_{i,m}$, respectively. Furthermore, K_h and K_g are used to represent the Rician K factors associated with the links from the BS to the RIS and from the RIS to the UE, respectively. Note that the NLoS components of $\tilde{h}_{i,m}$ and $\tilde{g}_{i,m}$ ($\tilde{h}_{i,m}^{\text{NLoS}}$ and $\tilde{g}_{i,m}^{\text{NLoS}}$) are independent and identically distributed complex Gaussian RVs that follow $\mathcal{CN}(0,1)$.

Note that the proposed Hyb-ERM schemes can serve UE that is not within the coverage area of the BS.

5.2.1 Hybrid RIS Structure

The exploration of RIS in academic literature has predominantly concentrated on passive configurations, which intelligently manipulate the phase of incident signals without requiring any external power for signal amplification. Such passive elements, by design, do not alter the power of the signal, ensuring energy-efficient operation albeit with limitations in increasing signal strength [Huang et al., 2019b]. In contrast, the concept of active RIS emerges as a groundbreaking evolution in the field of wireless communications [Zhi et al., 2022]. Active RIS, unlike their passive counterparts, are endowed with the ability to not only redirect but also significantly amplify incoming signals. This amplification is achieved by integrating active components, including power amplifiers, which necessitate hardware such as tunnel diodes and low-noise amplifiers (LNAs) [Zhang et al., 2022b].

We assume that $\Gamma_{i,m} = \alpha_{i,m} e^{j\theta_{i,m}}$ is the reflection coefficient of the mth RIS element of the ith hybrid RIS group, respectively, $m = 1, \cdots, F$, $i = 1, \cdots, G$, where amplitudes and phase values for active and passive elements can be given as follows:

$$\alpha_{i,m} \leq 1,\ \theta_{i,m} \in [0, 2\pi)\,, \quad \text{if } (i,m)\text{th element is active,} \tag{5.3}$$

$$\alpha_{i,m} > 1,\ \theta_{i,m} \in [0, 2\pi)\,, \quad \text{if } (i,m)\text{th element is passive.} \tag{5.4}$$

5.2.2 Hyb-ERM-I

In this subsection, we introduce the system model of Hyb-ERM-I. In the proposed Hyb-ERM scheme I, information bits are conveyed via both the PSK modulated symbol and number of active RIS groups. Firstly, $\log_2(M)$ bits are mapped into the M-ary PSK modulated symbol (x), where M is the modulation order, $x \in \mathbb{X}$, and $\mathbb{X}$ is a set containing all M-PSK symbols. Secondly, $\log_2(G)$ bits are first Gray-coded and then is converted into its decimal value (l) by using bi2de operation,

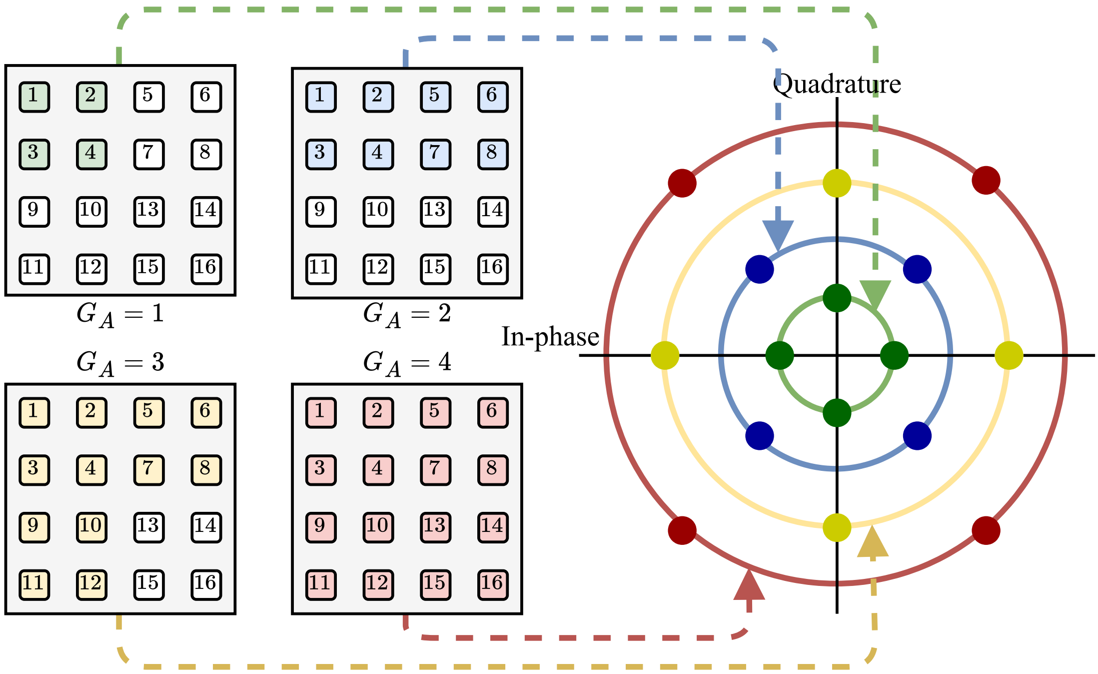

Figure 5.2: Illustration of hybrid-RIS impact on QPSK constellation for $G = 4$ according to incoming bits in Hyb-ERM-I scheme.

where $l + 1$ is equal to the number of active RIS groups (G_A), $l = 0, \cdots, G-1$. Note that the remaining $G_P = G - G_A$ RIS groups are passive. An example of obtaining the number of active RIS groups according to $\log_2(G)$ bits, is provided when $G = 4$ in Table I. Then, x is multiplied with $e^{j\bar{l}\pi/M}$, where $\bar{l} \equiv l \pmod 2$ and $\bar{x} = xe^{j\bar{l}\pi/M}$ is obtained. Then, $\bar{x}$ is transmitted from BS to UE through the BS-RIS-UE link. In Fig. 5.2, the impact of the number of active RIS groups on the symbols manipulated by hybrid RIS is shown as an illustration for $G = 4$ and QPSK signaling where $M = 4$. As seen from Fig. 5.2, if the number of active RIS groups is an even number, the QPSK constellation is rotated by $\pi/4$ to improve the minimum Euclidean distance. Additionally, the amplitude of the transmitted symbol from the BS to the RIS increases with the number of active RIS groups. Assuming $n^{\mathrm{a}}_{i,m}$ is a complex dynamic noise coefficient generated through the (i, m)th active RIS element and follows Gaussian distribution with $\mathcal{CN}(0, \sigma^2_{\mathrm{a}})$, and n is an AWGN sample with

Table 5.1: Selection of Number of Active And Passive RIS Groups For $G = 4$.

Incoming Bits	Gray-Coded Bits	l	G_A	G_P
$\{0,0\}$	$\{0,0\}$	0	1	3
$\{0,1\}$	$\{0,1\}$	1	2	2
$\{1,0\}$	$\{1,1\}$	3	4	0
$\{1,1\}$	$\{1,0\}$	2	3	1

$\mathcal{CN}(0,\sigma^2)$, the received signal at UE can be written as in follows:

$$r = \sqrt{P_t}\bar{x}\left(\sum_{i=1}^{G_A}\sum_{m=1}^{F} h_{i,m}\Gamma_{i,m}g_{i,m} + \sum_{i=G_A+1}^{G}\sum_{m=1}^{F} h_{i,m}\Gamma_{i,m}g_{i,m}\right) + \sum_{i=1}^{G_A}\sum_{m=1}^{F}\Gamma_{i,m}n^{\mathrm{a}}_{i,m}g_{i,m} + n \tag{5.5}$$

$$r = \underbrace{\sqrt{P_t}\bar{x}\left(\alpha\sum_{i=1}^{G_A}\sum_{m=1}^{F} h_{i,m}e^{j\theta_{i,m}}g_{i,m} + \sum_{i=G_A+1}^{G}\sum_{m=1}^{F} h_{i,m}e^{j\theta_{i,m}}g_{i,m}\right)}_{\text{Desired Signal}} + \underbrace{\alpha\sum_{i=1}^{G_A}\sum_{m=1}^{F} e^{j\theta_{i,m}}n^{\mathrm{a}}_{i,m}g_{i,m}}_{\text{Dynamic Noise}} + \underbrace{n}_{\text{Static Noise}} \tag{5.6}$$

where $\Gamma_{i,m}$ is defined as follows:

$$\Gamma_{i,m} = \begin{cases} \alpha_{i,m}e^{j\theta_{i,m}}, & i \in \{1,2,\cdots,G_A\}. \\ e^{j\theta_{i,m}}, & \text{otherwise.} \end{cases} \tag{5.7}$$

Note that an alternative approach permits the BS to transmit an unmodulated symbol; in this scenario, the RIS introduces an additional phase, effectively performing the modulation function similar to PSK, thus modulating the incoming unmodulated signal. Since an unmodulated signal is transmitted from the BS instead of an M-PSK symbol, this approach is more beneficial when a direct link exists between the BS and the UE. Consequently, the UE can easily remove the effect of the unmodulated signal conveyed through the direct link, assuming perfect CSI is known at the UE. In this case, $\Gamma_{i,m}$ can be given as:

$$\Gamma_{i,m} = \begin{cases} \alpha_{i,m} e^{j(\theta_{i,m}+\varpi)}, & i \in \{1, 2, \cdots, G_A\}. \\ e^{j(\theta_{i,m}+\varpi)}, & \text{otherwise,} \end{cases} \tag{5.8}$$

where $\varpi = \angle \bar{x}$ represents the phase of the symbol $\bar{x}$, which is determined by $\log_2(M)$ bits. Here, alongside l, $\bar{x}$ should also be provided from the BS to the RIS via the backhaul link.

The spectral efficiency of the proposed scheme can be obtained in terms of bpcu as $\eta = \log_2(M) + \log_2(G)$.

For simplification, the amplification factor of all active RIS elements is selected constant, i.e., $\alpha_{i,m} = \alpha$, $i \in \{1, 2, \cdots, G_A\}$, $\forall m$. By defining the following equations:

$$\mathbf{h}_\mathrm{a} = [\mathbf{h}_1^\mathrm{T}, \mathbf{h}_2^\mathrm{T}, \cdots, \mathbf{h}_{G_A}^\mathrm{T}]^\mathrm{T}, \tag{5.9}$$

$$\mathbf{h}_\mathrm{p} = [\mathbf{h}_{G_A+1}^\mathrm{T}, \mathbf{h}_{G_A+2}^\mathrm{T}, \cdots, \mathbf{h}_{G}^\mathrm{T}]^\mathrm{T}, \tag{5.10}$$

$$\mathbf{h}_i = [h_{i,1}, \cdots, h_{i,M}]^\mathrm{T}, \tag{5.11}$$

$$\mathbf{g}_\mathrm{a} = [\mathbf{g}_1^\mathrm{T}, \mathbf{g}_2^\mathrm{T}, \cdots, \mathbf{g}_{G_A}^\mathrm{T}]^\mathrm{T}, \tag{5.12}$$

$$\mathbf{g}_\mathrm{p} = [\mathbf{g}_{G_A+1}^\mathrm{T}, \mathbf{g}_{G_A+2}^\mathrm{T}, \cdots, \mathbf{g}_{G}^\mathrm{T}]^\mathrm{T}, \tag{5.13}$$

$$\mathbf{g}_\mathrm{p} = [\mathbf{g}_{G_A+1}^\mathrm{T}, \mathbf{g}_{G_A+2}^\mathrm{T}, \cdots, \mathbf{g}_{G}^\mathrm{T}]^\mathrm{T}, \tag{5.14}$$

$$\mathbf{g}_i = [g_{i,1}, \cdots, g_{i,M}]^\mathrm{T}, \tag{5.15}$$

$$\mathbf{\Theta}_\mathrm{a} = \mathrm{diag}([\boldsymbol{\gamma}_1^\mathrm{T}, \boldsymbol{\gamma}_2^\mathrm{T}, \cdots, \boldsymbol{\gamma}_{G_A}^\mathrm{T}]^\mathrm{T}), \tag{5.16}$$

$$\mathbf{\Theta}_\mathrm{p} = \mathrm{diag}([\boldsymbol{\gamma}_{G_A+1}^\mathrm{T}, \boldsymbol{\gamma}_{G_A+2}^\mathrm{T}, \cdots, \boldsymbol{\gamma}_{G}^\mathrm{T}]^\mathrm{T}), \tag{5.17}$$

$$\boldsymbol{\gamma}_i = [e^{j\theta_{i,1}}, e^{j\theta_{i,2}}, \cdots, e^{j\theta_{i,M}}]^\mathrm{T}, \tag{5.18}$$

(5.5) can be rewritten as:

$$r = P_t \bar{x} \left(\alpha \mathbf{g}_\mathrm{a}^\mathrm{T} \mathbf{\Theta}_\mathrm{a} \mathbf{h}_\mathrm{a} + \mathbf{g}_\mathrm{p}^\mathrm{T} \mathbf{\Theta}_\mathrm{p} \mathbf{h}_\mathrm{p} \right) + \alpha \mathbf{g}_\mathrm{a}^\mathrm{T} \mathbf{\Theta}_\mathrm{a} \mathbf{n}_\mathrm{a} + n, \tag{5.19}$$

where

$$\mathbf{n}_\mathrm{a} = [\mathbf{n}_1, \mathbf{n}_2, \cdots, \mathbf{n}_{G_A}]^\mathrm{T}, \tag{5.20}$$

$$\mathbf{n}_k = [n_{k,1}^\mathrm{a}, n_{k,2}^\mathrm{a}, \cdots, n_{k,M}^\mathrm{a}]^\mathrm{T}, \tag{5.21}$$

for $k = 1, 2, \cdots, G_A$. Hence, the SNR of the received signal can be given as:

$$\gamma = \frac{P_t \left\|\alpha \mathbf{g}_\mathrm{a}^\mathrm{T} \boldsymbol{\Theta}_\mathrm{a} \mathbf{h}_\mathrm{a} + \mathbf{g}_\mathrm{p}^\mathrm{T} \boldsymbol{\Theta}_\mathrm{p} \mathbf{h}_\mathrm{p}\right\|^2}{\alpha^2 \left\|\mathbf{g}_\mathrm{a}^\mathrm{T} \boldsymbol{\Theta}_\mathrm{a}\right\|^2 \sigma_\mathrm{a}^2 + \sigma^2}. \tag{5.22}$$

In Hyb-ERM, the reflection coefficients of all RIS elements are adjusted in such a way that the SNR is maximized. Then, considering P_A as the maximum amplification power at the RIS, which aligns with the power budget for active reflecting elements [Nguyen et al., 2022], the maximum instantaneous received SNR can be expressed as:

$$\max_{\alpha, \boldsymbol{\Theta}_\mathrm{a}, \boldsymbol{\Theta}_\mathrm{p}} \gamma, \tag{5.23}$$

$$\text{s.t. } \alpha^2 P_t \left\|\boldsymbol{\Theta}_\mathrm{a} \mathbf{h}_\mathrm{a}\right\|^2 + \alpha^2 \left\|\boldsymbol{\Theta}_\mathrm{a}\right\|^2 \sigma_\mathrm{a}^2 \leq P_A. \tag{5.24}$$

Utilizing the principles of the triangle and Cauchy-Schwarz inequalities [Moon and Stirling, 1999], given that $\alpha\|\mathbf{g}_\mathrm{a}\|\|\mathbf{h}_\mathrm{a}\| + \|\mathbf{g}_\mathrm{p}\|\|\mathbf{h}_\mathrm{p}\| \geq \|\alpha \mathbf{g}_\mathrm{a}^\mathrm{T} \boldsymbol{\Theta}_\mathrm{a} \mathbf{h}_\mathrm{a} + \mathbf{g}_\mathrm{p}^\mathrm{T} \boldsymbol{\Theta}_\mathrm{p} \mathbf{h}_\mathrm{p}\|^2$, the ideal phase shift ($\theta_{i,m}$) for the (i,m)th element of the RIS, which nullifies the phase of the corresponding channel coefficients, and the arbitrary reflection gain (α) under the given condition are defined as follows:

$$\theta_{i,m} = -(\phi_{i,m} + \varphi_{i,m}), \tag{5.25}$$

$$\alpha \leq \sqrt{\frac{P_A}{P_t \left\|\mathbf{h}_\mathrm{a}\right\|^2 + \sigma_\mathrm{a}^2}}. \tag{5.26}$$

By using (5.25) values for all RIS elements and an arbitrary amplification factor value (α), from (5.5), the received signal can be obtained as:

$$r = \sqrt{P_t} \bar{x} \left(\alpha \sum_{i=1}^{G_A} \zeta_i + \sum_{i=G_A+1}^{G} \zeta_i \right) + \alpha \sum_{i=1}^{G_A} \sum_{m=1}^{F} |g_{i,m}| \tilde{n}_{i,m}^\mathrm{a} + n, \tag{5.27}$$

where $\zeta_i = \sum_{m=1}^{F} |h_{i,m}||g_{i,m}|$, $\tilde{n}_{i,m}^\mathrm{a} = n_{i,m}^\mathrm{a} e^{-j\phi_{i,m}}$.

For simplicity, we can rewrite (5.27) as follows:

$$\begin{aligned} r &= \sqrt{P_t}\Delta_l \bar{x} + \bar{n}, \\ \Delta_l &= \alpha \sum_{i=1}^{G_A} \zeta_i + \sum_{i=G_A+1}^{G} \zeta_i, \\ \bar{n} &= \alpha \sum_{i=1}^{G_A} \sum_{m=1}^{F} |g_{i,m}| \tilde{n}_{i,m}^{\mathrm{a}} + n, \end{aligned} \tag{5.28}$$

where $\bar{n}$ is the overall noise term and follows complex Gaussian distribution due to CLT with $\mathcal{CN}(0, N_0)$, where $N_0 = \alpha^2 G_A F L_g \sigma_{\mathrm{a}}^2 + \sigma^2$. Note that l in Δ_l is associated with the number of active RIS groups (G_A), where $G_A = l + 1$. Moreover, the SNR in (5.22) reduces to $\gamma = P_t |\Delta_l|^2 / N_0$.

5.2.3 Hyb-ERM-II

In Hyb-ERM-II, all processes are the same as in in Hyb-ERM-I except for the generation of RIS groups. To generate RIS groups, firstly, the absolute values of channel coefficients corresponding to the ιth RIS element are multiplied as $c_\iota = |h_\iota||g_\iota|$, $\iota = 1, \cdots, N$. This forms the vector $\mathbf{c} = [c_1, \cdots, c_N]^{\mathrm{T}}$. Additionally, a vector for the indices of the RIS elements $\mathbf{k} = [1, \cdots, N]^{\mathrm{T}}$, is obtained. Then, the elements of $\mathbf{c}$ are sorted in descending order to produce $\bar{\mathbf{c}} = [\bar{c}_1, \cdots, \bar{c}_N]^{\mathrm{T}}$ with the corresponding indices $\bar{\mathbf{k}} = [\bar{k}_1, \cdots, \bar{k}_N]^{\mathrm{T}}$, where $\bar{c}_1 > \bar{c}_2 > \cdots > \bar{c}_N$ and $\bar{k}_\iota = 1, \cdots, N$. The index vector $\bar{\mathbf{k}}$ is separated into G groups as $\bar{\mathbf{k}} = [\bar{\mathbf{k}}_1^{\mathrm{T}}, \bar{\mathbf{k}}_2^{\mathrm{T}}, \cdots, \bar{\mathbf{k}}_G^{\mathrm{T}}]$, and the RIS elements indices of the ith RIS group is given as $\bar{\mathbf{k}}_i = [\bar{k}_{(i-1)F+1}, \cdots, \bar{k}_{iF}]^{\mathrm{T}}$, $i = 1, \cdots, G$, $F = N/G$. Hence, in Hyb-ERM-II, the RIS elements with higher channel gains are prioritized to be selected as active elements. A visual example on determination of RIS groups for Hyb-ERM-II is given in Fig. 5.3. Assume that the RIS elements with the highest channel gains are the ones with indices $5, 8, 10, 16$. Therefore, as seen in Fig. 5.3, when $G_A = 1$, RIS elements with indices $\{5, 8, 10, 16\}$ are selected as active elements instead of indices $\{1, 2, 3, 4\}$ as in Hyb-RIS-I.

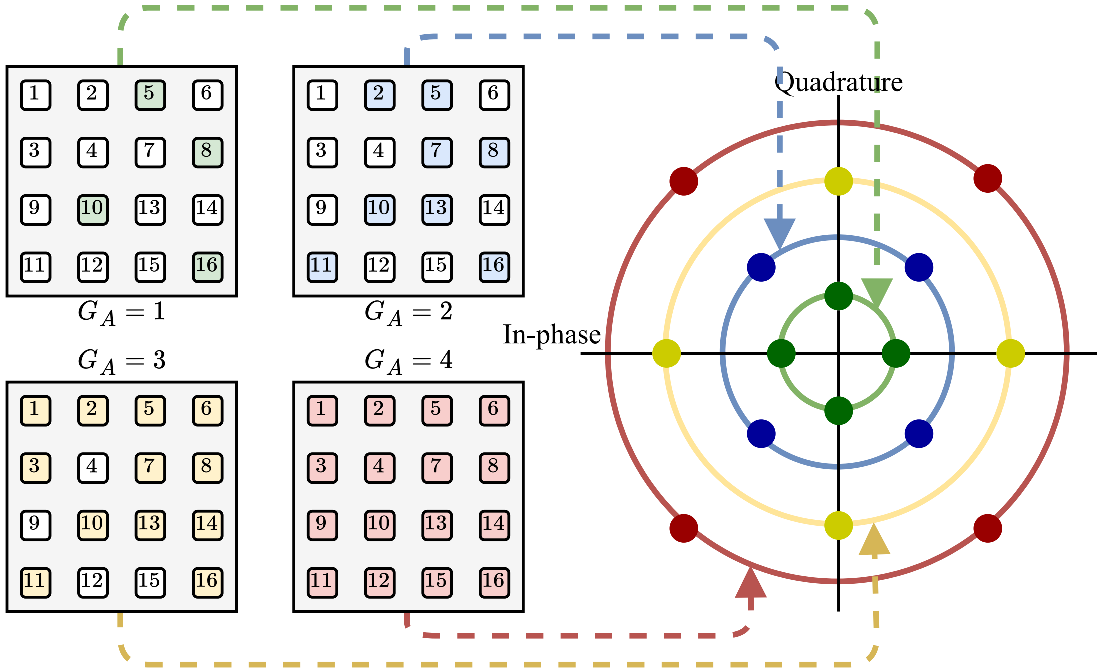

Figure 5.3: Illustration of hybrid-RIS impact on QPSK constellation for $G = 4$ according to incoming bits in Hyb-ERM-II scheme.

5.2.4 Hyb-ERM Detectors

Since the number of active RIS elements is not fixed in Hyb-ERM schemes, different signal levels are obtained at the receiver. With the perfect CSI, An ML detection algorithm can be exploited to determine the most likely estimate of x and l, given as:

$$\left(\hat{x}, \hat{l}\right) = \arg\max_{x,l} p(r|\Delta_l), \tag{5.29}$$

Where $p(r|\Delta_l)$ is the conditional probability density function of the received signal r given Δ_l, it can be expressed as follows:

$$p(r|\Delta_l) = \frac{1}{\pi N_0} e^{\frac{-\left|r-\sqrt{P_t}xe^{j\bar{l}\pi/M}\right|^2}{N_0}}. \tag{5.30}$$

Considering the noise generated by the active RIS groups is exposed of a significant path loss due to multiplicative fading of the path from BS-RIS-UE, the effect of N_A on the decision in (5.30) is negligible. Hence, the detection rule for Hyb-ERM scheme can be given as:

$$\left(\hat{x}, \hat{l}\right) = \arg \min_{x \in \mathbb{X}, l \in \{0, \cdots, G-1\}} \left| r - \sqrt{P_t} \Delta_l x e^{j \bar{l} \pi / M} \right|^2, \tag{5.31}$$

where $\hat{x}$ and $\hat{l}+1$ are the detected M-ary PSK modulated symbol and estimated number of active RIS groups, respectively, $\bar{l} \equiv l \pmod 2$. After obtaining $\hat{x}$ and $\hat{l}+1$, reverse process in the BS side is performed to obtain decoded information bits. Note that (5.31) provides an estimate nearly identical to that given by the ML algorithm described in (5.29). Here, all possible combinations of modulated symbols and number of active and passive RIS groups are taken into account and the computational complexity order of the ML detector can be given as $\mathcal{O}(GM)$ per channel use. Using an ML detector becomes challenging for high values of G and M; therefore, a detector that provides lower complexity than an ML detector is required. To reduce the decoding complexity order, we present two novel detectors, called low-complexity detector 1 (LC-1) and low-complexity detector 2 (LC-2).

Low-Complexity Detector 1 (LC-1)

In order to reduce the decoding complexity order of the ML detector, we also present a low-complexity detector. In this low-complexity detector, the number of active RIS groups (G_A) and the modulated symbol are decoded separately. Firstly, the number of active groups is detected as follows:

$$\hat{l} = \arg \min_{l \in \{0, \cdots, G-1\}} \left| |r| - \sqrt{P_t} \Delta_l \right|^2. \tag{5.32}$$

Then, $\hat{l}$ is used to detect the modulated symbol ($\hat{x}$) as follows:

$$\hat{x} = \arg \min_{x \in \mathbb{X}} \left| r - \sqrt{P_t} \Delta_{\hat{l}} x e^{j \nu \pi / M} \right|^2, \tag{5.33}$$

where $\nu \equiv \hat{l} \pmod 2$. Here, the number of complex multiplications (CMs) is reduced to $G+M$, whereas it is GM for the ML detection. Since the number of active RIS groups and the modulated symbol are detected separately, the computational complexity order can be obtained as $\mathcal{O}\left(\max\left(G, M\right)\right)$, where the greater of G and M values specifies the decoding complexity.

Table 5.2: Comparison of the Number of CMs for Proposed Detectors at 5 bpcu.

Detector	**Number of CMs**			
	$G=2$, $M=16$	$G=4$, $M=8$	$G=8$, $M=4$	$G=16$, $M=2$
ML	32	32	32	32
LC-1	18	12	12	18
LC-2	33	18	12	12

Low-Complexity Detector 2 (LC-2)

In contrast to LC-1, LC-2 first detects the modulated symbol as follows:

$$\left(\hat{x}, \hat{k}\right) = \arg \min_{x \in \mathbb{X}, k \in \{0,1\}} \left| r - |r| \, x e^{j\pi k/M} \right|^2, \tag{5.34}$$

where $\hat{x}$ and $\hat{k}$ are the estimated PSK modulated symbol and rotation factor, respectively. Then, depending on the value of $\hat{k}$, the following detection rule is exploited to detect (G_A) as follows:

$$\hat{l} = \arg \min_{l \in 2\mathbb{Z}, l < G} \left| r - \sqrt{P_t} \Delta_l \right|^2 \quad \text{if } \hat{k} = 0, \tag{5.35}$$

$$\hat{l} = \arg \min_{l \in 2\mathbb{Z}+1, l < G} \left| r - \sqrt{P_t} \Delta_l \right|^2 \quad \text{if } \hat{k} = 1. \tag{5.36}$$

where $\mathbb{Z}$ is the set of integer numbers. In LC-2, the number of CMs is equal to $2M + G/2$. As in LC-1, the computational complexity order can be obtained as $\mathcal{O}\left(\max\left(G, M\right)\right)$.

In Table II, we compare the number of CMs required by ML, LC-1, and LC-2 for various configurations of G and M when the spectral efficiency is 5 bpcu. As seen in Table II, LC-1 significantly reduces the required number of CMs compared to the ML detector when G and M are similar in value, while LC-2 achieves significant reductions when G is much greater than M.

5.3 Performance Analysis

In this subsection, we investigate the error performance of Hyb-ERM-I when using the ML detector. For simplicity, we first define the following vectors:

$$\boldsymbol{\xi} = [\zeta_1, \zeta_2, \cdots, \zeta_G]^{\mathrm{T}}, \tag{5.37}$$

$$\boldsymbol{\omega} = [\omega_1, \cdots, \omega_G]^{\mathrm{T}} = [\underbrace{\alpha, \cdots, \alpha}_{G_A}, \underbrace{1, \cdots, 1}_{G-G_A}]^{\mathrm{T}}, \tag{5.38}$$

where $\zeta_i = \sum_{m=1}^{F} |h_{i,m}|\, |g_{i,m}|$ can be considered as a Gaussian RV for $F >> 1$ due to CLT with the following mean and variance values:

$$\mu = F\left(\mathrm{E}\big[\, |h_{i,m}|\, \big]\mathrm{E}\big[\, |g_{i,m}|\, \big]\right), \tag{5.39}$$

$$\sigma^2 = F\left(\mathrm{E}[|h_{i,m}|^2]\mathrm{E}[|g_{i,m}|^2] - \mathrm{E}\big[|h_{i,m}|\big]^2\mathrm{E}\big[|g_{i,m}|\big]^2\right). \tag{5.40}$$

Note that $\boldsymbol{\omega}$ is a vector representing the states of RIS groups with $\omega_i = \{1, \alpha\}$, $i = 1, \cdots, G$. For example, if $G = 4$ and $G_A = 2$, then $\boldsymbol{\omega}$ is obtained as $[\alpha, \alpha, 1, 1]^{\mathrm{T}}$. Since the channel amplitudes ($|h_{i,m}|$, $|g_{i,m}|$) are independent Rician distributed RVs, their mean and variance values can be given as follows:

$$\mathrm{E}\big[\, |h_{i,m}|\, \big] = \mu_{|h|} = \frac{1}{2}\sqrt{\frac{L_h \pi}{K_h + 1}} L_{1/2}(-K_h), \tag{5.41}$$

$$\mathrm{E}\big[\, |g_{i,m}|\, \big] = \mu_{|g|} = \frac{1}{2}\sqrt{\frac{L_g \pi}{K_g + 1}} L_{1/2}(-K_g), \tag{5.42}$$

$$\mathrm{VAR}\big(\, |h_{i,m}|\, \big) = \sigma_{|h|}^2 = L_h - \frac{L_h \pi}{4(K_h + 1)} L_{1/2}^2(-K_h), \tag{5.43}$$

$$\mathrm{VAR}\big(\, |g_{i,m}|\, \big) = \sigma_{|g|}^2 = L_g - \frac{L_g \pi}{4(K_g + 1)} L_{1/2}^2(-K_g), \tag{5.44}$$

where $L_{1/2}(\cdot)$ is the Laguerre polynomial [Primak et al., 2004]. Hence, by exploiting the mean and variance values ($\mu_{|h|}$, $\mu_{|g|}$, $\sigma_{|h|}^2$, $\sigma_{|g|}^2$), μ and σ^2 can be obtained.

After defining $\boldsymbol{\xi}$ and $\boldsymbol{\omega}$, for ease of analysis, the received signal in (5.27) can be rewritten as follows:

$$r = \sqrt{P_t}\boldsymbol{\xi}^{\mathrm{T}}\boldsymbol{\omega}\bar{x} + \bar{n}. \tag{5.45}$$

The CPEP, indicating the probability that the transmitted pair $(\boldsymbol{\omega}, \bar{x})$ is incorrectly detected as $(\hat{\boldsymbol{\omega}}, \hat{\bar{x}})$ given the condition $\boldsymbol{\xi}$, is described by

$$P\left(\boldsymbol{\omega}, \bar{x} \rightarrow \hat{\boldsymbol{\omega}}, \hat{\bar{x}} | \boldsymbol{\xi}\right) = P\left(\left|r - \sqrt{P_t}\boldsymbol{\xi}^{\mathrm{T}}\boldsymbol{\omega}\bar{x}\right|^2 > \left|r - \sqrt{P_t}\boldsymbol{\xi}^{\mathrm{T}}\hat{\boldsymbol{\omega}}\hat{\bar{x}}\right|^2\right). \tag{5.46}$$

Note that the PEP quantifies the probability of an error occurring between two specific symbol pairs under given channel conditions, providing a measure of the system's detection performance. By substituting (5.45) into (5.46), we can obtain the following:

$$\begin{aligned} &P\left(\boldsymbol{\omega}, \bar{x} \rightarrow \hat{\boldsymbol{\omega}}, \hat{\bar{x}} | \boldsymbol{\xi}\right) = \\ &P\Bigg(P_t\left|\boldsymbol{\xi}^{\mathrm{T}}\boldsymbol{\omega}\bar{x}\right|^2 - 2\sqrt{P_t}\Re\left\{\left(\sqrt{P_t}\boldsymbol{\xi}^{\mathrm{T}}\boldsymbol{\omega}\bar{x} + \bar{n}\right)^{\mathrm{H}}\boldsymbol{\xi}^{\mathrm{T}}\boldsymbol{\omega}\bar{x}\right\} \\ &\quad > P_t\left|\boldsymbol{\xi}^{\mathrm{T}}\hat{\boldsymbol{\omega}}\hat{\bar{x}}\right|^2 - 2\sqrt{P_t}\Re\left\{\left(\sqrt{P_t}\boldsymbol{\xi}^{\mathrm{T}}\hat{\boldsymbol{\omega}}\hat{\bar{x}} + \bar{n}\right)^{\mathrm{H}}\boldsymbol{\xi}^{\mathrm{T}}\hat{\boldsymbol{\omega}}\hat{\bar{x}}\right\}\Bigg). \end{aligned} \tag{5.47}$$

Through various mathematical operations, the formula for the CPEP as shown in (5.47) can be restated as:

$$\begin{aligned} &P\left(\boldsymbol{\omega}, \bar{x} \rightarrow \hat{\boldsymbol{\omega}}, \hat{\bar{x}} | \boldsymbol{\xi}\right) = P(\chi > 0) = \\ &P\Bigg(-P_t\left|\boldsymbol{\xi}^{\mathrm{T}}\boldsymbol{\omega}\bar{x} - \boldsymbol{\xi}^{\mathrm{T}}\hat{\boldsymbol{\omega}}\hat{\bar{x}}\right|^2 - 2\Re\left\{\sqrt{P_t}\bar{n}^{\mathrm{H}}\left|\boldsymbol{\xi}^{\mathrm{T}}\boldsymbol{\omega}\bar{x} - \boldsymbol{\xi}^{\mathrm{T}}\hat{\boldsymbol{\omega}}\hat{\bar{x}}\right|\right\} > 0\Bigg). \end{aligned} \tag{5.48}$$

Hence, with χ defined as a Gaussian RV whose mean and variance values can be respectively obtained as $\mu_\chi = -P_t\left|\boldsymbol{\xi}^{\mathrm{T}}\boldsymbol{\omega}\bar{x} - \boldsymbol{\xi}^{\mathrm{T}}\hat{\boldsymbol{\omega}}\hat{\bar{x}}\right|^2$ and $\sigma_\chi^2 = 2P_t\left|\boldsymbol{\xi}^{\mathrm{T}}\boldsymbol{\omega}\bar{x} - \boldsymbol{\xi}^{\mathrm{T}}\hat{\boldsymbol{\omega}}\hat{\bar{x}}\right|^2$.

After obtaining μ_χ and σ_χ^2, the CPEP can be given by exploiting $\mathcal{Q}$-function as follows:

$$P\left(\boldsymbol{\omega}, \bar{x} \rightarrow \hat{\boldsymbol{\omega}}, \hat{\bar{x}} | \boldsymbol{\xi}\right) = \mathcal{Q}\left(\sqrt{\frac{\Upsilon\left|\boldsymbol{\xi}^{\mathrm{T}}\left(\boldsymbol{\omega}\bar{x} - \hat{\boldsymbol{\omega}}\hat{\bar{x}}\right)\right|^2}{2}}\right), \tag{5.49}$$

where $\Upsilon = P_t/N_0$. To derive the UPEP, (5.49) needs to be averaged further across $\boldsymbol{\xi}$. Under the assumption that the mean vector is defined as $\boldsymbol{\mu} = \mathbf{1}\mu$ and the covariance matrix as $\boldsymbol{\Sigma} = \mathrm{diag}(\mathbf{1}\sigma^2)$, and given that $\boldsymbol{\xi}$ is modeled as a Gaussian vector with the distribution $\mathcal{N}(\boldsymbol{\mu}, \boldsymbol{\Sigma})$, we obtain:

$$\Re\left\{\boldsymbol{\xi}^{\mathrm{T}}\left(\boldsymbol{\omega}\bar{x} - \hat{\boldsymbol{\omega}}\hat{\bar{x}}\right)\right\} \sim \mathcal{N}\left(\mu_{\Re}, \sigma_{\Re}^2\right), \tag{5.50}$$

$$\Im\left\{\boldsymbol{\xi}^{\mathrm{T}}\left(\boldsymbol{\omega}\bar{x} - \hat{\boldsymbol{\omega}}\hat{\bar{x}}\right)\right\} \sim \mathcal{N}\left(\mu_{\Im}, \sigma_{\Im}^2\right), \tag{5.51}$$

where

$$\mu_{\Re} = \mu \sum_{i=1}^{G} \Re\left\{\omega_i \bar{x} - \hat{\omega}_i \hat{\bar{x}}\right\}, \mu_{\Im} = \mu \sum_{i=1}^{G} \Im\left\{\omega_i \bar{x} - \hat{\omega}_i \hat{\bar{x}}\right\}, \tag{5.52}$$

$$\sigma_{\Re}^2 = \sigma^2 \sum_{i=1}^{G} \left(\Re\left\{\omega_i \bar{x} - \hat{\omega}_i \hat{\bar{x}}\right\}\right)^2, \sigma_{\Im}^2 = \sigma^2 \sum_{i=1}^{G} \left(\Im\left\{\omega_i \bar{x} - \hat{\omega}_i \hat{\bar{x}}\right\}\right)^2. \tag{5.53}$$

Based on (5.50) and (5.51), an approximated moment generating function of $\xi = \left|\boldsymbol{\xi}^{\mathrm{T}}\left(\boldsymbol{\omega}\bar{x} - \hat{\boldsymbol{\omega}}\hat{\bar{x}}\right)\right|^2$ is described as [Simon, 2002]:

$$M_{\xi}(s) = \sqrt{\frac{1}{1-2\sigma_{\Re}^2 s}} \sqrt{\frac{1}{1-2\sigma_{\Im}^2 s}} \exp\left(\frac{\mu_{\Re}^2 s}{1-2\sigma_{\Re}^2 s}\right) \exp\left(\frac{\mu_{\Im}^2 s}{1-2\sigma_{\Im}^2 s}\right). \tag{5.54}$$

The upper limit of the $\mathcal{Q}$-function can be given as [Chiani et al., 2003]:

$$\mathcal{Q}(x) \leq \frac{\exp(-2x^2)}{6} + \frac{\exp(-x^2)}{12} + \frac{\exp(-x^2/2)}{4}. \tag{5.55}$$

By utilizing the (5.55), the unconditional PEP can be formulated as:

$$\begin{aligned} P\left(\boldsymbol{\omega}, \bar{x} \to \hat{\boldsymbol{\omega}}, \hat{\bar{x}}\right) &= \mathrm{E}\left[P\left(\boldsymbol{\omega}, \bar{x} \to \hat{\boldsymbol{\omega}}, \hat{\bar{x}} | \boldsymbol{\xi}\right)\right] \\ &\leq \frac{2M_{\xi}\left(-\Upsilon\right) + M_{\xi}\left(-\frac{\Upsilon}{2}\right) + 3M_{\xi}\left(-\frac{\Upsilon}{4}\right)}{12}. \end{aligned} \tag{5.56}$$

By applying the union bound approach, the upper limits for the BERs with ML detection are described as:

$$P_{\bar{x}} \leq \sum_{\boldsymbol{\omega}, \bar{x}} \sum_{\hat{\boldsymbol{\omega}}, \hat{\bar{x}}} P\left(\boldsymbol{\omega}, \bar{x} \to \hat{\boldsymbol{\omega}}, \hat{\bar{x}}\right) e(\bar{x}, \hat{\bar{x}}), \tag{5.57}$$

$$P_{\boldsymbol{\omega}} \leq \sum_{\boldsymbol{\omega}, \bar{x}} \sum_{\hat{\boldsymbol{\omega}}, \hat{\bar{x}}} P\left(\boldsymbol{\omega}, \bar{x} \to \hat{\boldsymbol{\omega}}, \hat{\bar{x}}\right) e(\boldsymbol{\omega}, \hat{\boldsymbol{\omega}}), \tag{5.58}$$

where $e(\bar{x}, \hat{\bar{x}})$ and $e(\boldsymbol{\omega}, \hat{\boldsymbol{\omega}})$ are the number of erroneous bits for the pairwise error events when $\bar{x}$ and $\boldsymbol{\omega}$ are incorrectly detected as $\hat{\bar{x}}$ and $\hat{\boldsymbol{\omega}}$, respectively. Finally, the upper bound for the overall BER can be given as:

$$P_b = \frac{1}{MG}\left(\frac{P_{\bar{x}}}{\log_2 M} + \frac{P_{\boldsymbol{\omega}}}{\log_2 G}\right). \tag{5.59}$$

5.4 Simulation Results and Comparisons

In this section, extensive simulation results of the error performance of the proposed Hyb-ERM schemes are demonstrated. Furthermore, the error performance of Hyb-ERM is compared to various benchmark schemes: fully active RIS configuration

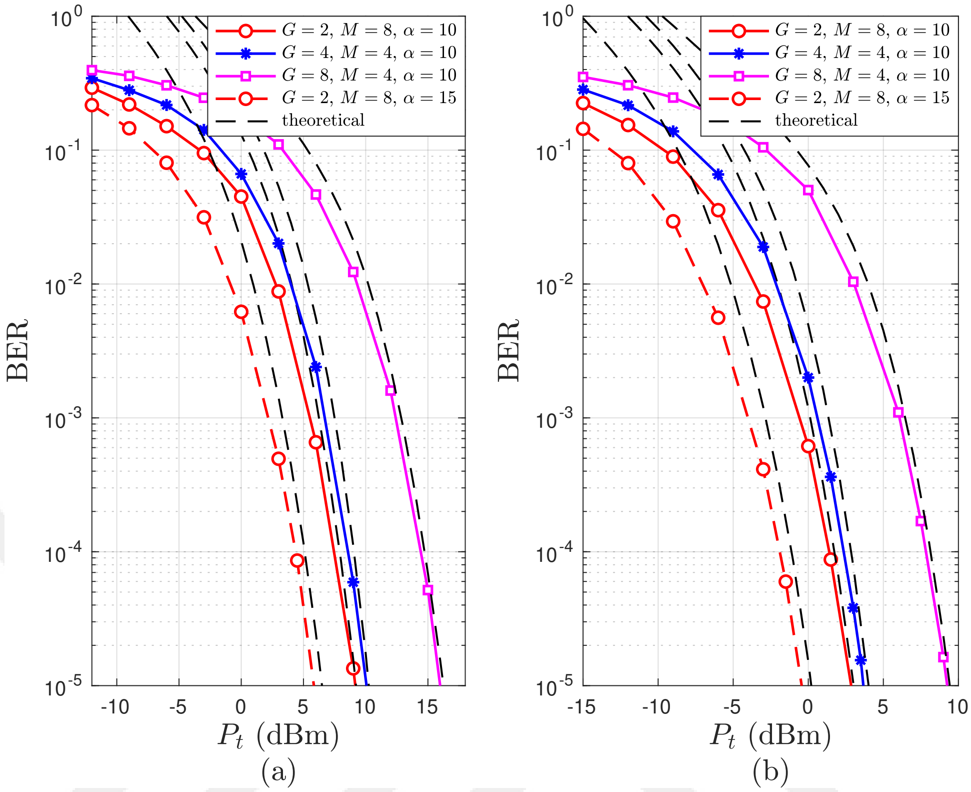

Figure 5.4: Simulation and theoretical error performance of Hyb-ERM for 4 bpcu, $\alpha = \{10, 15\}$, varying G and M where $N = 128$ (a) and $N = 256$ (b).

[Zhang et al., 2022b] and HRM [Yigit et al., 2022]. In fully active RIS configuration, all RIS elements are active and the information bits are transmitted by only M-QAM modulated symbols, where the spectral efficiency is defined as $\log_2(M)$. Note that Hyb-ERM-I and Hyb-ERM-II both utilize PSK modulation for their signal transmission. The simulation parameters are given as: the distances $d_h = 20$ m and $d_g = 50$ m, the wavelength $\lambda = 0.1$ m, the path loss exponents $\kappa_h = 2.2$ and $\kappa_g = 2.8$, the Rician shape factor $K = K_h = K_g \in \{0, 10\}$, noise variances $\sigma^2 = \sigma_{\mathrm{a}}^2 = -90$ dBm, the reference path loss value $L_0 = -30$ dB, and the amplification gain $\alpha = 10$.

5.4.1 Error Performance in Ideal Channel Conditions

In this subsection, the error performance of Hyb-ERM is shown where perfect CSI is assumed to be known at the BS side.

In Figs. 5.4(a) and 5.4(b), error performance of the proposed Hyb-ERM scheme

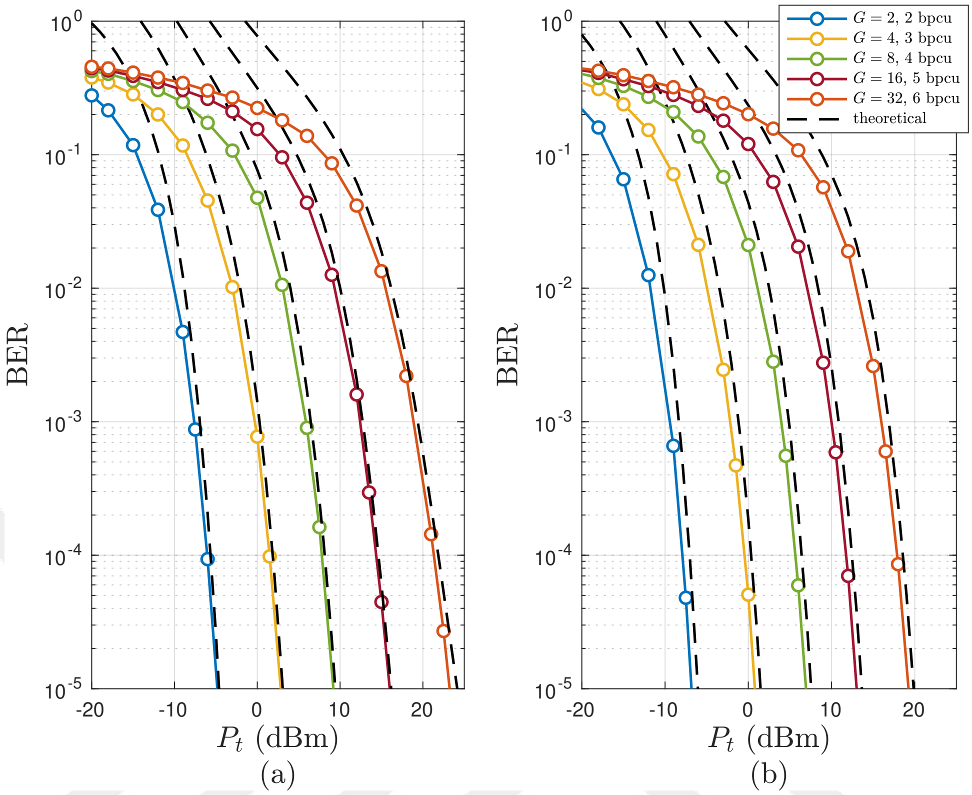

Figure 5.5: Simulation and theoretical error performance of Hyb-ERM for $M = 2$, $N = 256$, and varying G where $K = 0$ (a) and $K = 10$ (b).

is demonstrated for 4 bpcu, varying G and M, $\alpha = 10, 15$, and different RIS sizes $N = 128, 256$. As seen from Fig. 5.4, Hyb-ERM with $G = 2$ and $M = 8$ outperforms the configurations with $G = 4$, $M = 4$ and $G = 8$, $M = 2$ in terms of error performance. Additionally, it can be seen that theoretical BER curves in (5.59) behave as upper bounds for the curves obtained by computer simulations. When the configuration with $G = 2$ and $M = 8$ is investigated for different α values, it can be seen that as α increases, the error performance improves. This is because the signal reflected from the hybrid RIS is amplified more with a higher α, leading to an increase in the received SNR and an improvement in error performance. However, there is a trade-off between the improvement in error performance and the power consumption of the hybrid RIS. Note that since Hyb-ERM exploits the same RIS architecture with HRM, the energy efficiency and power consumption analyses are equivalent to that of HRM and can be found in [Yigit et al., 2022].

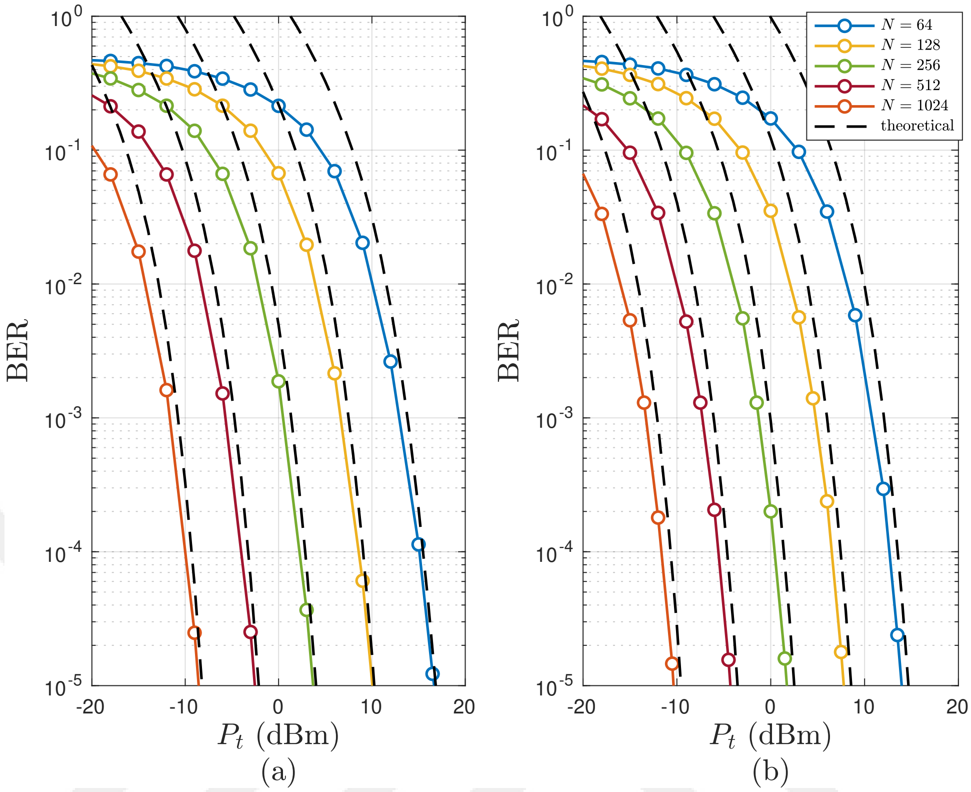

Figure 5.6: Simulation and theoretical error performance of Hyb-ERM for $M = 4$, $G = 4$, and varying N where $K = 0$ (a) and $K = 10(b)$.

The simulation and theoretical results for the error performance of Hyb-ERM are depicted in Fig. 5.5 for $M = 2$, $N = 256$, and varying number of RIS groups $G \in \{2, 4, 8, 16, 32\}$. The Rician shape factor K is selected as 0 and 10 for Figs. 5.5(a) and 5.5(b), respectively. As illustrated in Fig. 5.5, the error performance deteriorates with an increase in the number of RIS groups G. For a fixed N value, reducing G results in more elements being allocated to each RIS group, which in turn increases the distance between Hyb-ERM constellation points. This leads to a trade-off between error performance and spectral efficiency.

In Fig. 5.6, simulation and theoretical error performance results for the Hyb-ERM scheme are provided for parameters $M = 4$, $G = 4$, and varying RIS sizes $N \in \{64, 128, 256, 512, 1024\}$. The Rician factor K is selected as 0 and 10 for Figs. 5.6(a) and 5.6(b), respectively. As seen from Figs. 5.6(a) and 5.6(b), as N increases, the error performance improves. When the number of elements in each RIS groups

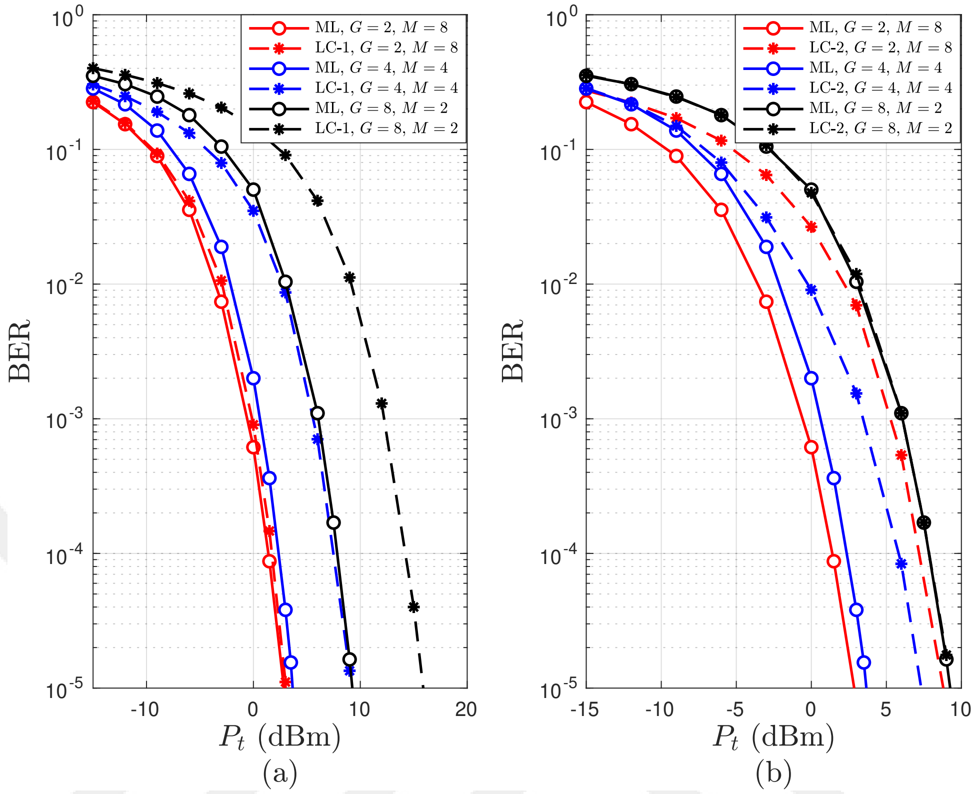

Figure 5.7: Error performance comparison of ML detector with LC-1 (a) and LC-2 (b) for 4 bpcu, $N = 256$, $K = 0$, and varying G and M.

increases, the probability of erroneously decoding the number of active RIS groups decreases. Hence, the BER performance improves with respect to N for a fixed G value. Furthermore, as N is doubled, approximately 6.5 dBm less transmit power P_t is required to achieve a BER value of 10^{-5} for $K = 0, 10$.

The ML detector, as defined in (5.31), is compared to low-complexity detectors 1 and 2 (LC-1 and LC-2) at a spectral efficiency of 4 bpcu with variations in G and M configurations presented in Fig. 5.7(a) and 5.7(b), respectively. As seen from Fig. 5.7(a), LC-1 detector achieves nearly identical error performance to ML detector when $G = 2$ and $M = 8$; however, as G increases, the performance gap between the ML and LC-1 detectors widens. As the number of RIS groups is increased for a fixed value of N, the distance between Hyb-ERM symbols decreases. Since the LC-1 detector initially decodes the active RIS groups, its error performance deteriorates with an increase in G. Therefore, LC-1 detector achieves better error performance

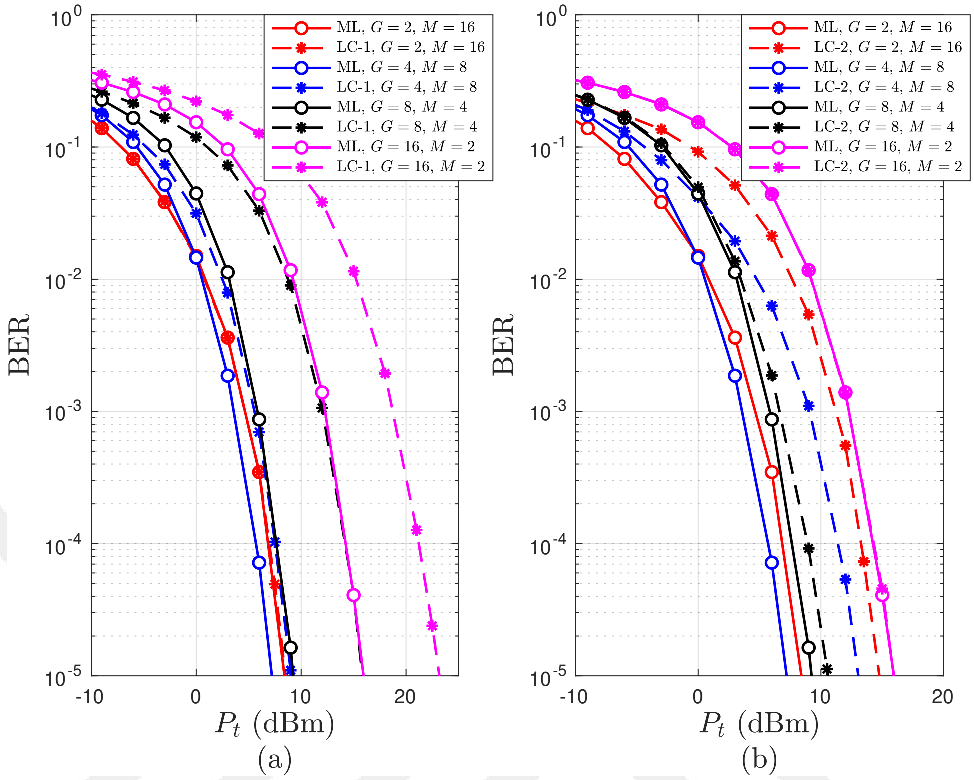

Figure 5.8: Error performance comparison of ML detector with LC-1 (a) and LC-2 (b) for 5 bpcu, $N = 256$, $K = 0$, and varying G and M.

when G is less than M. In contrast to LC-1 detector, the LC-2 detector performs better when G is higher than M. As shown in Fig. 5.7, the error performance of the LC-2 detector is comparable to that of the ML detector when $G = 8$ and $M = 2$. However, when G decreases and M increases, the performance gap between the ML and LC-2 detectors increases. Furthermore, in Fig. 5.8, the similar findings are obtained for a spectral efficiency of 5 bpcu.

In Fig. 5.9, the error performance of Hyb-ERM schemes is provided and compared to benchmark schemes for 5 bpcu, $N = 256$, and varying G and M. Note that K is selected as 0 and 10 in Figs. 5.9(a) and 5.9(b), respectively. Note that the best two configurations for HRM, Hyb-ERM-I, and Hyb-ERM-II, are included in Fig. 5.9. For $K = 0$, it can be seen that Hyb-ERM-I with $G = 4$ and $M = 8$ and Hyb-ERM-II with $G = 2$ and $M = 16$ provide better error performance than Hyb-ERM with other configurations and benchmark schemes. For $K = 10$, Hyb-

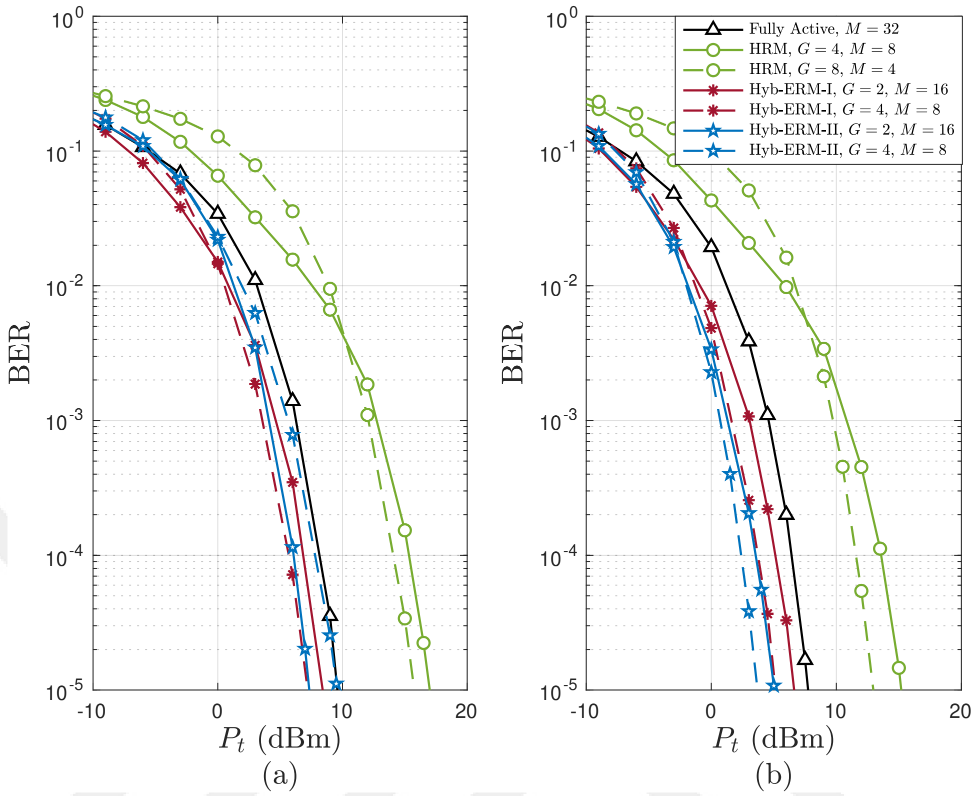

Figure 5.9: Error performance comparison of Hyb-ERM schemes with benchmark schemes for 5 bpcu, $N = 256$, and varying G and M where $K = 0$ (a) and $K = 10$ (b).

ERM-I with $G = 4$ and $M = 8$ and Hyb-ERM-II with $G = 4$ and $M = 8$ provide better error performance than Hyb-ERM with other configurations and benchmark schemes. When Hyb-ERM schemes are compared to HRM, it can be deduced that Hyb-ERM schemes always outperform HRM in terms of error performance for the same values of G and M.

Moreover, the error performance of Hyb-ERM schemes is presented and compared to benchmark schemes for 6 and 7 bpcu values in Figs. 5.10(a) and 5.10(b), respectively. In Fig. 5.10(a) and 5.10(b), Hyb-ERM-II with $G = 4$ and $M = 16$ and with $G = 4$ and $M = 32$ have superiority over other schemes, respectively. Since both Hyb-ERM-I and Hyb-ERM-II provide higher minimum Euclidean distance compared to HRM and fully-active RIS, Hyb-ERM schemes outperform HRM and fully-active RIS in terms of error performance. Moreover, Hyb-ERM-II out-

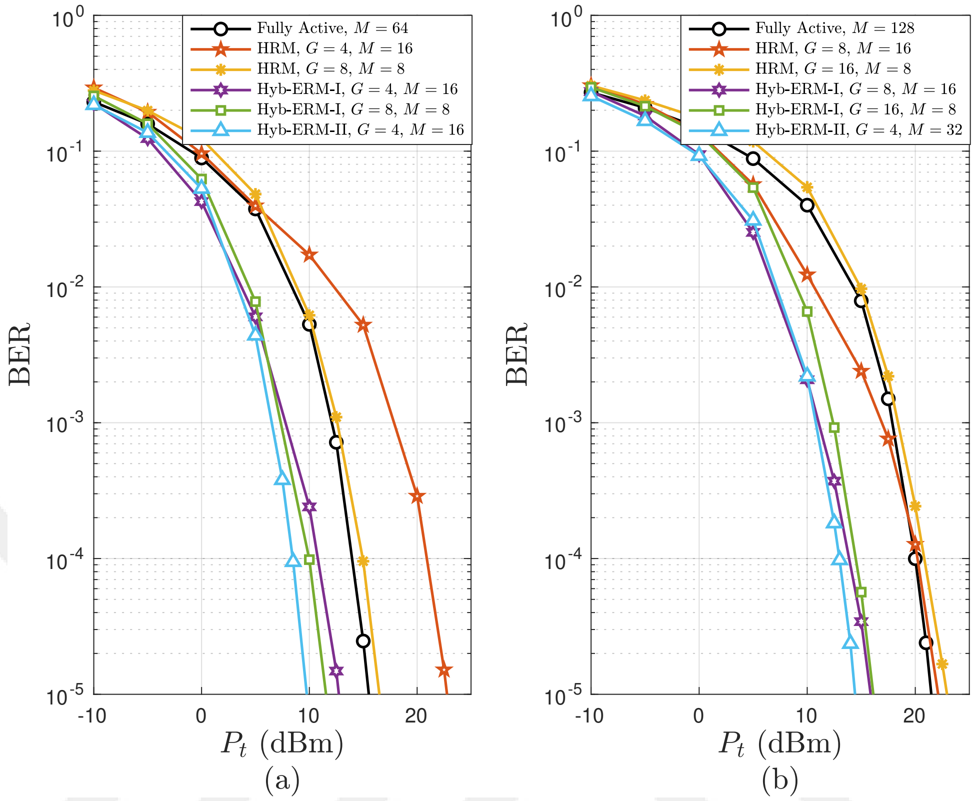

Figure 5.10: Error performance comparison of Hyb-ERM schemes with benchmark schemes for 6 bpcu (a), 7 bpcu (b), and $N = 256$.

performs Hyb-ERM-I by selecting RIS elements with higher channel gains as active elements, resulting in higher received SNR values.

5.4.2 Error Performance in Non-Ideal Channel Conditions

In this subsection, the error performance of Hyb-ERM-I is provided under non-ideal channel conditions.

In order to explore more practical scenarios, we examine the effectiveness of the Hyb-ERM-I approach when the RIS elements are spatially correlated, a factor whose influence on error performance is depicted in Fig. 5.11. Here, a square RIS is considered and ($\tilde{h}_{i,m} = \tilde{h}_{i,m}^{\text{NLoS}}$) and ($\tilde{g}_{i,m} = \tilde{g}_{i,m}^{\text{NLoS}}$) are assumed to be Rayleigh fading channel coefficients with $K_h = K_g = 0$. Hence, the spatially correlated channel vectors from the BS to RIS ($\mathbf{h}^{\text{Corr}}$) and from RIS to UE ($\mathbf{g}^{\text{Corr}}$) can be modeled as

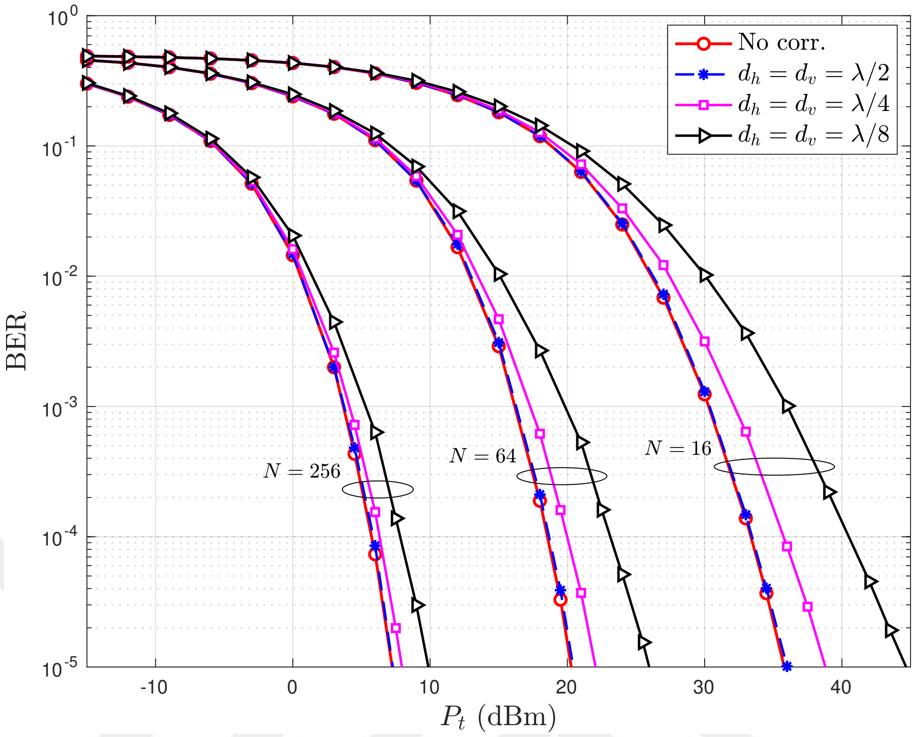

Figure 5.11: Error performance of Hyb-ERM-I under correlated channel conditions for $G = 4$, $M = 8$, $K = 0$ and varying N values.

$\mathbf{h}^{\text{Corr}} = \sqrt{L_h}\mathbf{h}\mathbf{R}^{1/2}$ and $\mathbf{g}^{\text{Corr}} = \sqrt{L_g}\mathbf{g}\mathbf{R}^{1/2}$, where $\mathbf{h} = \left[\mathbf{h}_{\text{a}}^{\text{T}}, \mathbf{h}_{\text{p}}^{\text{T}}\right]^{\text{T}}$, $\mathbf{g} = \left[\mathbf{g}_{\text{a}}^{\text{T}}, \mathbf{g}_{\text{p}}^{\text{T}}\right]^{\text{T}}$, and $\mathbf{R} \in \mathbb{R}^{N \times N}$ is the correlation matrix that models the spatially correlated RIS elements where the kth row and lth column of $\mathbf{R}$ can be given as $\mathbf{R}(k, l) = \text{sinc}(2\|\mathbf{z}_k - \mathbf{z}_l\|/\lambda)$ [Björnson and Sanguinetti, 2020], $k, l \in \{1, 2, \cdots, N\}$. Note that channel vectors, $\mathbf{h}^{\text{Corr}}$ and $\mathbf{g}^{\text{Corr}}$, are utilized instead of $\mathbf{h}$ and $\mathbf{g}$ to demonstrate the effect of spatially correlated channel model on the error performance of Hyb-ERM-I. Assuming d_h and d_v stand for the horizontal width and vertical height of a single RIS element, respectively, we obtain $\mathbf{z}_i = [0, \mod (i-1, \sqrt{N})d_h, \lfloor (i-1)/\sqrt{N} \rfloor d_v]^{\text{T}}$ for the square RIS, $i \in \{k, l\}$.

Fig. 5.11 illustrates the error performance of the Hyb-ERM scheme for the squared RIS elements under spatially correlated channel conditions, with $d_h = d_v \in \{\lambda/2, \lambda/4, \lambda/8\}$. Here, the simulation parameters are selected as: $G = 4$, $M = 8$, $K = 0$, and $N \in \{16, 64, 256\}$. It can be seen from Fig. 5.11 that for a given number of RIS elements (N), the error performance of the configuration with $d_h = d_v = \lambda/2$

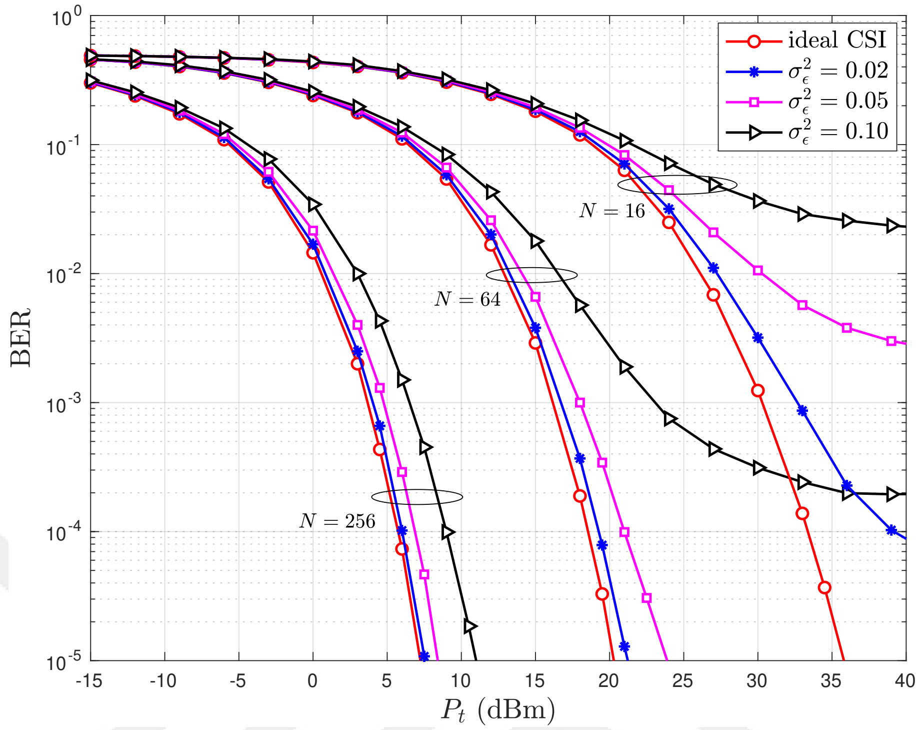

Figure 5.12: Error performance of Hyb-ERM-I under imperfect channel conditions for $G = 4$, $M = 8$, $K = 0$ and varying N values.

is almost the same as the ideal case. As d_h and d_v decrease, the impact of correlation over BER becomes more severe. Moreover, an increase in the number of RIS elements (N) enhances the system's resilience to correlated channel conditions due to higher received SNR associated with respect to RIS size.

Previous simulations presumed perfect CSI to configure RIS; however, in Fig. 5.12, the error performance of the Hyb-ERM scheme has also been evaluated under conditions of imperfect CSI. To model imperfect CSI, we assume that $\tilde{h}_{i,m}$ and $\tilde{g}_{i,m}$ are estimated as $\tilde{h}_{i,m} = \hat{h}_{i,m} + \epsilon_h$ and $\tilde{g}_{i,m} = \hat{g}_{i,m} + \epsilon_g$, where ϵ_h and ϵ_g represent channel estimation errors and follow complex Gaussian distributions with $\mathcal{CN}(0, \sigma_\epsilon^2)$. Hence, in (5.25), the imperfect channel coefficients ($\hat{h}_{i,m}$ and $\hat{g}_{i,m}$) are exploited to calculate the phase of RIS elements ($\theta_{i,m}$) instead of $h_{i,m}$ and $g_{i,m}$. In Fig. 5.12, the simulation parameters are selected as: $G = 4$, $M = 8$, $K = 0$, $N \in \{16, 64, 256\}$, and $\sigma_\epsilon^2 \in \{0.02, 0.05, 0.10\}$. As observed in Fig. 5.12, CSI errors critically degrade the error performance and it becomes more severe for lower N values. Similar to the correlated channel condition, as N increases, the system becomes more robust to CSI errors because increasing N results in obtaining a higher received SNR.

5.5 Conclusion

In this chapter, we have introduced two Hyb-ERM schemes, leveraging hybrid-RIS technology to enhance spectral efficiency and BER performance in RIS-aided communications. Hyb-ERM schemes utilize controllable phase shifters and amplifiers, mitigating multiplicative fading and improving transmission reliability. Its novel approach enhances the minimum Euclidean distance between constellation symbols, ensuring more reliable communication. Comparative analysis have shown that Hyb-ERM surpasses traditional HRM and fully-active RIS in error performance. Our findings establish a theoretical BER upper bound and introduce low-complexity detectors as efficient alternatives to the ML detector, demonstrating suitability of Hyb-ERM for 6G networks and highlighting its potential to advance RIS-assisted communication technologies. Future research could extend the Hyb-ERM schemes to MIMO models, analyze their performance under various channel models and impairments, and explore optimal allocation strategies for active and passive elements in Hybrid RIS to further improve error performance.

Chapter 6

HYBRID RECONFIGURABLE INTELLIGENT SURFACE ENABLED OVER-THE-AIR INDEX-MODULATION

6.1 Introduction

Wireless communication technologies are evolving rapidly as researchers move from 5G to 6G, aiming to meet the increasing demands driven by emerging vertical applications. While many novel solutions and technologies have been proposed, not all of them have been widely adopted due to challenges in practicality, performance, or complexity. However, as new trends and technologies emerge, researchers often revisit older solutions, considering their potential when combined with the latest advancements. This approach can lead to fresh insights, and previously overlooked technologies may emerge as valuable components of next-generation communication systems.

IM is an efficient, low-complexity technique that allows additional information bits to be transmitted by modulating the indices of resource blocks in communication systems [Basar, 2016a, Basar et al., 2017, Wen et al., 2017b, Tugtekin et al., 2023]. These resource blocks can include subcarriers, antennas, time slots, constellation points, activation orders, and more [Sugiura et al., 2017, Wen et al., 2017b]. IM has gained significant attention in research and has proven to be a valuable tool for future communication systems. It offers various advantages, such as improved error performance, enhanced energy and spectral efficiency, and low implementation complexity [Cheng et al., 2018]. One of IM's key strengths is its versatility and compatibility, allowing it to be integrated into communication systems in many different ways [Sugiura et al., 2017, Mao et al., 2018]. A prominent example is

OFDM-IM, where IM is applied to the subcarriers of an OFDM signal, enabling additional bits to be transmitted by selectively activating certain subcarriers [Başar et al., 2013, Wen et al., 2015]. Research has also explored combining IM with NOMA and joint radar-communication systems, proposing flexible OFDM-IM subcarrier activation schemes and innovative waveforms that support both communication and radar functions [Arslan et al., 2020b, Şahin et al., 2021]. Moreover, studies such as [Mao et al., 2016b] introduce novel methods, like splitting subcarriers into two groups with different constellation modes, and [Arslan et al., 2020c] presents a technique where multiple codebooks are indexed for sparse vector coding in ultra-reliable, low-latency communication networks.

RISs have gained significant attention in the wireless communication field and are considered a promising technology for next-generation 6G and beyond systems. RISs are large reflective surfaces composed of numerous small, cost-effective metamaterial elements that can manipulate the properties of incoming signals. By reflecting, refracting, absorbing, or even amplifying signals, RISs provide a form of virtual control over the wireless channel, all without the need for additional processing or buffering. RISs are typically envisioned to improve coverage, enhance signal quality, increase capacity, and contribute to other performance enhancements in communication systems [Subrt and Pechac, 2012, Huang et al., 2020, Kilinc et al., 2021, Su et al., 2020, Perović et al., 2020, Yigit et al., 2022]. One of the major advantages of RIS technology is its ability to seamlessly integrate with existing communication systems. Numerous studies have demonstrated the benefits of combining RIS with established technologies, such as NOMA [Arslan et al., 2022a], machine learning [Huang et al., 2019a], localization [Ma et al., 2020], OFDM [Pradhan et al., 2020], MIMO [Tang et al., 2020], and others [Alayasra and Arslan, 2022, Arslan et al., 2023, Arslan et al., 2022b].

Given the advantages and flexibility of both RIS and IM, researchers are exploring their integration to further enhance the performance of wireless communication systems. In [Dash et al., 2022], the authors introduce a greedy detector for an RIS-SSK system, where RIS phases are adjusted to optimize the instantaneous SNR

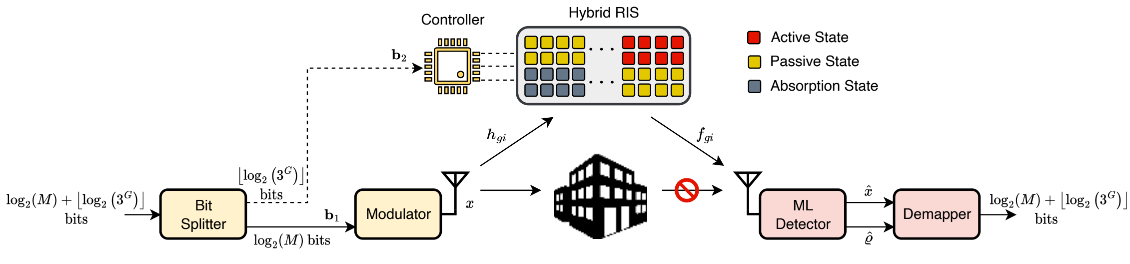

Figure 6.1: System model of E-OTA-RIS-IM.

at the target receiving antenna, with the antenna selection determined by IM bits. Additionally, an intelligent RIS grouping-based IM (RGB-IM) is proposed in [Asmoro and Shin, 2022] to improve the spectral efficiency and BER performance of traditional RIS systems.

In this chapter, we introduce a novel enhanced OTA RIS-IM (E-OTA-RIS-IM) technique that utilizes different modes for RIS groups to improve both spectral efficiency and BER performance. We propose a hybrid RIS configuration with multiple groups, where each group can switch between active, passive, and absorption modes based on the IM bits.

6.2 System Model

In this section, we present the system model of the proposed E-OTA-RIS-IM scheme. As illustrated in Fig. 6.1, the RIS consists of N elements, which are divided into G groups, each containing $\bar{N}$ elements, such that $N = G\bar{N}$. The reflection coefficient of the ith element in the gth group is denoted as $\theta_{gi} = e^{j\vartheta_{gi}}$ with unit amplitude, where $\vartheta_{gi} \in [0, 2\pi)$ represents the phase shift controlled by the RIS controller. The indices i and g range from 1 to $\bar{N}$ and 1 to G, respectively.

Assume that $L_h = \zeta_0 d_h^{-\varkappa_h}$ and $L_f = \zeta_0 d_f^{-\varkappa_f}$ represent the large-scale path loss of the BS-to-RIS and RIS-to-UE links, respectively. Here, ζ_0 is the path loss at the reference distance of 1 meter, while d_h and d_f represent the distances from the BS to the RIS and from the RIS to the UE, respectively. The parameters $\varkappa_h$ and $\varkappa_f$ are the path loss exponents for the BS-to-RIS and RIS-to-UE paths. The channel coefficients from the BS to the (g,i)th RIS element and from the (g,i)th RIS element to the UE are defined as $h_{gi} = |h_{gi}|\, e^{j\phi_{gi}} = \sqrt{L_h}\bar{h}_{gi}$ and $f_{gi} = |f_{gi}|\, e^{j\varphi_{gi}} = \sqrt{L_f}\bar{f}gi$, respectively. Additionally, $\bar{h}_{gi}$ and $\bar{f}_{gi}$ are independent Rician fading channel coefficients, defined as follows:

$$\bar{h}_{gi} = \sqrt{\frac{K_h}{K_h+1}}\bar{h}_{gi}^{\mathrm{LoS}} + \sqrt{\frac{1}{K_h+1}}\bar{h}_{gi}^{\mathrm{NLoS}}, \tag{6.1}$$

$$\bar{f}_{gi} = \sqrt{\frac{K_f}{K_f+1}}\bar{f}_{gi}^{\mathrm{LoS}} + \sqrt{\frac{1}{K_f+1}}\bar{f}_{gi}^{\mathrm{NLoS}}, \tag{6.2}$$

where $\bar{h}_{gi}^{\mathrm{LoS}}$ and $\bar{f}_{gi}^{\mathrm{LoS}}$ represent the LoS components, and $\bar{h}_{gi}^{\mathrm{NLoS}}$ and $\bar{f}_{gi}^{\mathrm{NLoS}}$ represent the NLoS components of $\bar{h}_{gi}$ and $\bar{f}_{gi}$, respectively. Additionally, K_h and K_f denote the Rician K factor for the BS-RIS and RIS-UE paths, respectively. Here, $\bar{h}_{gi}^{\mathrm{LoS}}$, $\bar{f}_{gi}^{\mathrm{LoS}}$, $\bar{h}_{gi}^{\mathrm{NLoS}}$, and $\bar{f}_{gi}^{\mathrm{NLoS}}$ are independent and identically distributed (i.i.d.) complex Gaussian RVs, with $\mathcal{CN}(0,1)$.

The system model of E-OTA-RIS-IM is illustrated in Fig. 6.1. Here, according to the incoming bits from the backhaul link, the hybrid RIS will determine whether the partitions will behave in the passive, active or absorption state. As in OTA-RIS-IM, firstly, $\mathbf{b}_1 = [b_{11}, b_{12}, \cdots, b_{1\kappa}]^{\mathrm{T}}$ bit vector is used to obtain the M-ary modulated symbol x, $\kappa = \log_2(M)$. Let us define a codebook $\mathcal{S}$ which includes all permutations with repetition of active/passive/absorption states of RIS groups, $\mathcal{S} = \{\mathbf{s}_1, \mathbf{s}_2, \cdots, \mathbf{s}_{2^\varpi}\}$, $\varpi = \left\lfloor \log_2\left(3^G\right)\right\rfloor$, where $\mathbf{s}_\varrho = [s_{\varrho 1}, s_{\varrho 2}, \cdots, s_{\varrho G}]^{\mathrm{T}}$ is the ϱth codeword of set $\mathcal{S}$ and $s_{\varrho\mu} \in \{\sqrt{\alpha}, 1, 0\}$, $\varrho = 1, 2, \cdots, 2^\varpi$, $\mu = 1, 2, \cdots, G$. Here, $s_{\varrho\mu}$ being α, 1, and 0 represent active, passive, and absorption states, respectively. Hence, $\mathbf{b}_2 = [b_{21}, b_{22}, \cdots, b_{2\varpi}]^{\mathrm{T}}$ bit vector is converted into its decimal value (ξ), and ξth codeword ($\mathbf{s}_\xi$) of $\mathcal{S}$ is selected. As seen in Table 6.2, an example of states of RIS groups selection is provided for $G = 2$. Here, a total number of 3^G permutations can be generated; however, only 2^ϖ can be used to transmit information. As can be seen in the table, for the same number of RIS partitions G, we can send an additional bit compared to the previous method. Hence, the spectral efficiency of E-OTA-RIS-IM in terms of bpcu can be given as:

$$\eta = \log_2(M) + \left\lfloor \log_2\left(3^G\right)\right\rfloor. \tag{6.3}$$

Table 6.1: E-OTA-RIS-IM Example of Bit Mapping For $G = 2$

Index Bits $[b_{21}, b_{22}, b_{23}]$	(ξ)	**Codeword**	**First RIS Group State**	**Second RIS Group State**
$[0,0,0]$	0	$\mathbf{s}_1 = [\sqrt{\alpha}, \sqrt{\alpha}]^{\mathrm{T}}$	Active	Active
$[0,0,1]$	1	$\mathbf{s}_2 = [\sqrt{\alpha}, 1]^{\mathrm{T}}$	Active	Passive
$[0,1,0]$	2	$\mathbf{s}_3 = [\sqrt{\alpha}, 0]^{\mathrm{T}}$	Active	Absorption
$[0,1,1]$	3	$\mathbf{s}_4 = [1, \sqrt{\alpha}]^{\mathrm{T}}$	Passive	Active
$[1,0,0]$	4	$\mathbf{s}_5 = [1, 1]^{\mathrm{T}}$	Passive	Passive
$[1,0,1]$	5	$\mathbf{s}_6 = [1, 0]^{\mathrm{T}}$	Passive	Absorption
$[1,1,0]$	6	$\mathbf{s}_7 = [0, 1]^{\mathrm{T}}$	Absorption	Active
$[1,1,1]$	7	$\mathbf{s}_8 = [0, 1]^{\mathrm{T}}$	Absorption	Passive
NaN	NaN	NaN	Absorption	Absorption

As in OTA-RIS-IM, the (g,i)th element of RIS is coherently aligned with the corresponding channel coefficients h_{gi} and f_{gi}, i.e., $\vartheta_{gi} = -(\phi_{gi} + \varphi_{gi})$. Hence, the received signal at UE can be written as:

$$y = \sqrt{P_t} x \left(\sum_{g=1}^{G} \left[\mathcal{H}_g s_{\xi g} + \sigma\left(s_{\xi g}\right) w_g^a \right] \right) + w, \tag{6.4}$$

where $\sigma(\beta)$ is a function which provides output as 1 if β equals to $\sqrt{\alpha}$, and 0 otherwise.

In order to decode the received signal, the ML detector can be used as follows:

$$(\hat{x}, \hat{\varrho}) = \underset{x \in \mathcal{M}, \varrho = 1, \cdots, 2^{\varpi}}{\arg\min} \left\| y - \sqrt{P_t} x \left[\sum_{g=1}^{G} \mathcal{H}_g s_{\varrho g} \right] \right\|^2 . \tag{6.5}$$

Moreover, the SNR of the received signal can be obtained as:

$$\gamma = \frac{P_t \left| \sum_{g=1}^{G} \mathcal{H}_g s_{\xi g} \right|^2}{\alpha V_0 \sum_{g=1}^{G} \sigma\left(s_{\xi g}\right) \sum_{i=1}^{\bar{N}} \left|\theta_{gi} f_{gi}\right|^2 + N_0}. \tag{6.6}$$

6.3 Simulation Results and Comparisons

In this section, we discuss the simulation results of the proposed E-OTA-RIS-IM scheme in terms of BER performance, comparing them to the OTA-RIS-IM and

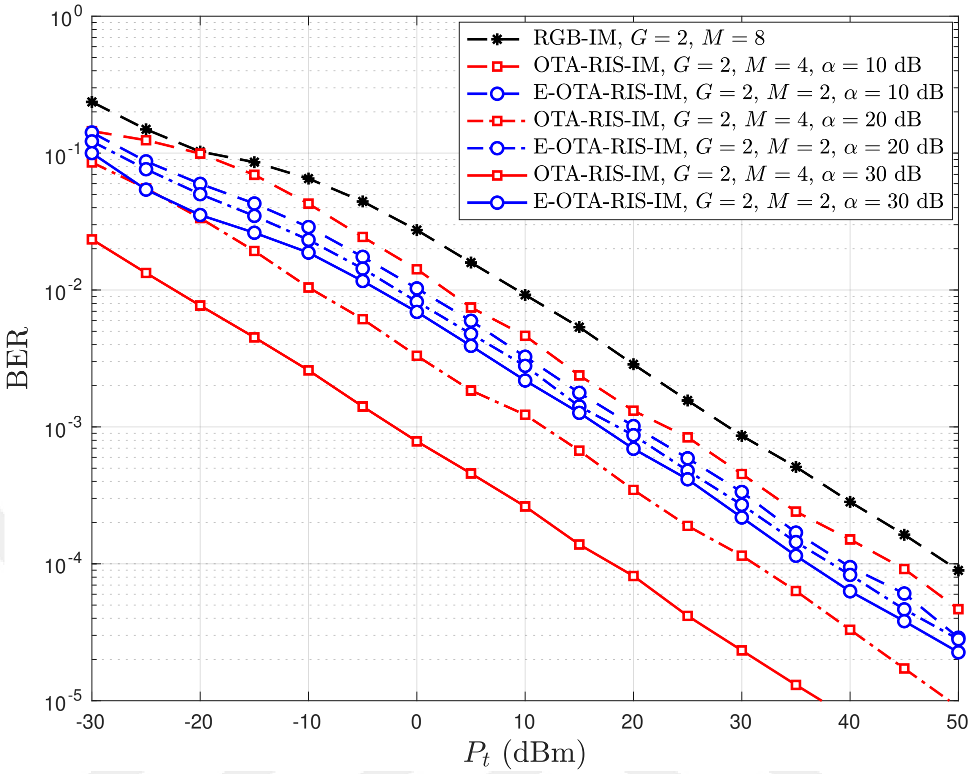

Figure 6.2: Error performance comparison of E-OTA-RIS-IM with OTA-RIS-IM and RGB-IM for varying α, $N = 256$, and 4 bpcu.

RGB-IM [Asmoro and Shin, 2022] benchmark schemes. For various values of G, M, N, and other parameters, we demonstrate the superior performance of the proposed schemes over the RGB-IM. Unless otherwise stated, the following system parameters are assumed in all simulations: distances $d_h = 20$ m and $d_f = 50$ m, path loss exponents $\varkappa_h = 2.2$ and $\varkappa_f = 2.8$, Rician K factors $K_h = K_f = 0$, noise variances, and reference path loss value $\zeta_0 = -30$ dB. For error performance analyses, the noise power N_0 and V_0 are fixed at -130 dBm, and the transmit power P_t is varied.

Fig. 6.2 presents the error performance of all schemes with $G = 2$, $N = 256$, and 4 bpcu for varying α. It is observed that E-OTA-RIS-IM requires the lowest modulation order of $M = 2$ since it can transmit additional bits via IM, making it the most spectral efficient. In contrast, OTA-RIS-IM requires $M = 4$, and the RGB-IM benchmark operates at $M = 8$ to maintain the same 4 bpcu. The results show that the proposed E-OTA-RIS-IM outperforms RGB-IM, while OTA-RIS-IM

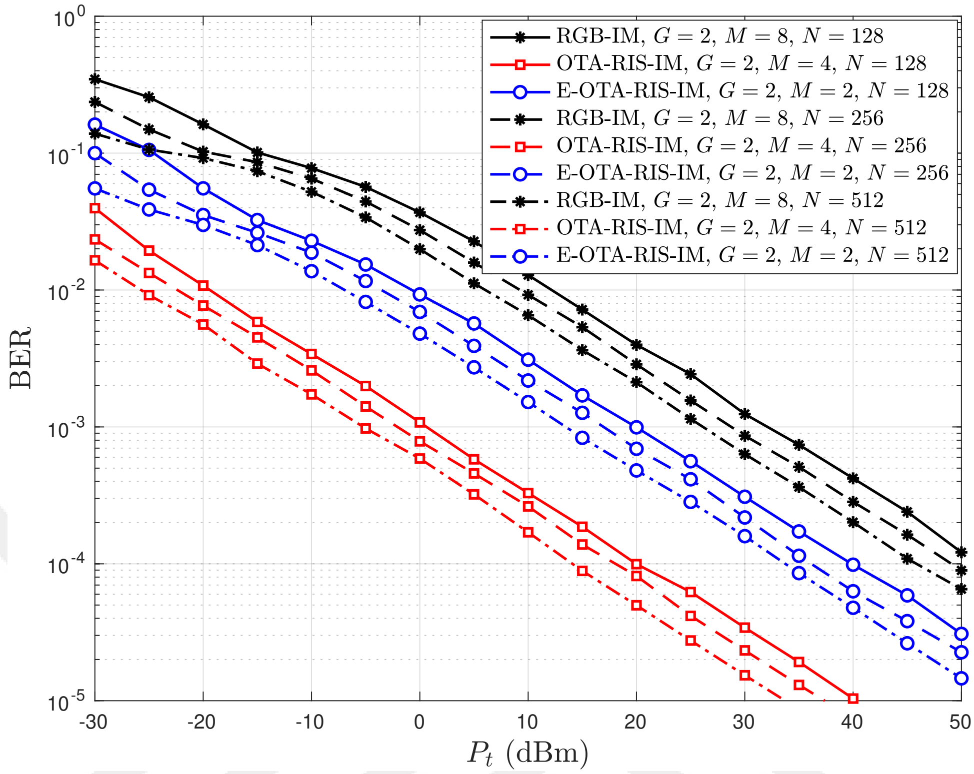

Figure 6.3: Error performance comparison of E-OTA-RIS-IM with OTA-RIS-IM and RGB-IM for varying N, $\alpha = 30$ dB, and 4 bpcu.

provides the best performance overall, as it utilizes the entire RIS at all times, unlike E-OTA-RIS-IM and RGB-IM, which have an absorption state. Additionally, the error performance of all schemes improves as α increases.

Fig. 6.3 illustrates the BER performance of the proposed scheme compared to OTA-RIS-IM and RGB-IM with $G = 2$ for varying N. To achieve the same bpcu values across all schemes, the modulation order is adjusted accordingly. It is observed that while E-OTA-RIS-IM requires only $M = 2$, OTA-RIS-IM operates at a higher modulation order of $M = 4$. Despite this higher modulation order, OTA-RIS-IM outperforms E-OTA-RIS-IM in terms of error performance, as it utilizes all RIS elements across all combinations. In contrast, RGB-IM requires $M = 8$ to maintain the same data rate. The results show that RGB-IM, even at the same bpcu, performs significantly worse than both proposed schemes.

Fig. 6.4 presents the BER performance of the proposed system compared to the

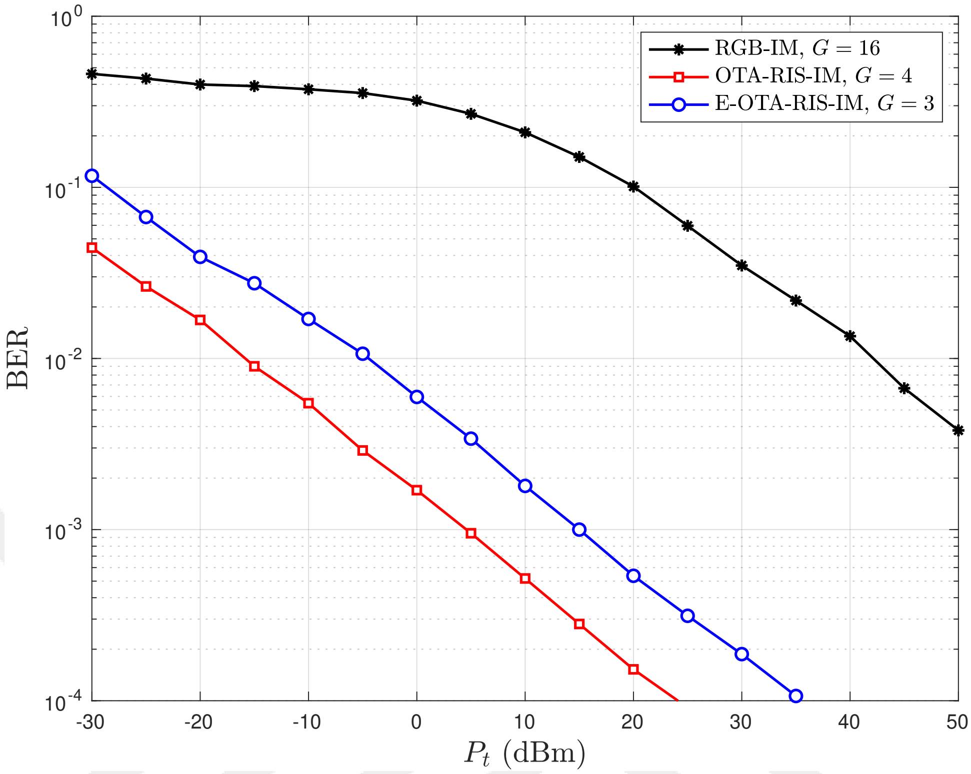

Figure 6.4: Error performance comparison of E-OTA-RIS-IM with OTA-RIS-IM and RGB-IM varying G, $M = 2$, $\alpha = 30$ dB, $N = 480$, and 5 bpcu.

benchmark schemes, all operating at the same bpcu and with $M = 2$. As seen in the figure, RGB-IM requires a large number of RIS groups, G, to transmit additional bits through IM in order to achieve the same bpcu. In contrast, OTA-RIS-IM achieves the same bpcu with only $G = 4$ RIS groups, and E-OTA-RIS-IM requires even fewer groups, $G = 3$, thanks to its ability to use an additional state enabled by the hybrid RIS. Furthermore, although the bpcu of OTA-RIS-IM is lower compared to E-OTA-RIS-IM, its BER performance is significantly superior because all RIS elements are fully utilized at all times, whereas E-OTA-RIS-IM has an absorption state that limits the RIS element usage.

Fig. 6.5 shows how the bpcu increases as the number of groups, G, increases for each scheme. It can be observed that, for the RGB-IM benchmark, the bpcu does not increase significantly as G grows. This is because only one group is activated at a time, with $\lfloor \log_2(G) \rfloor$ IM bits transmitted, while the rest of the RIS elements remain

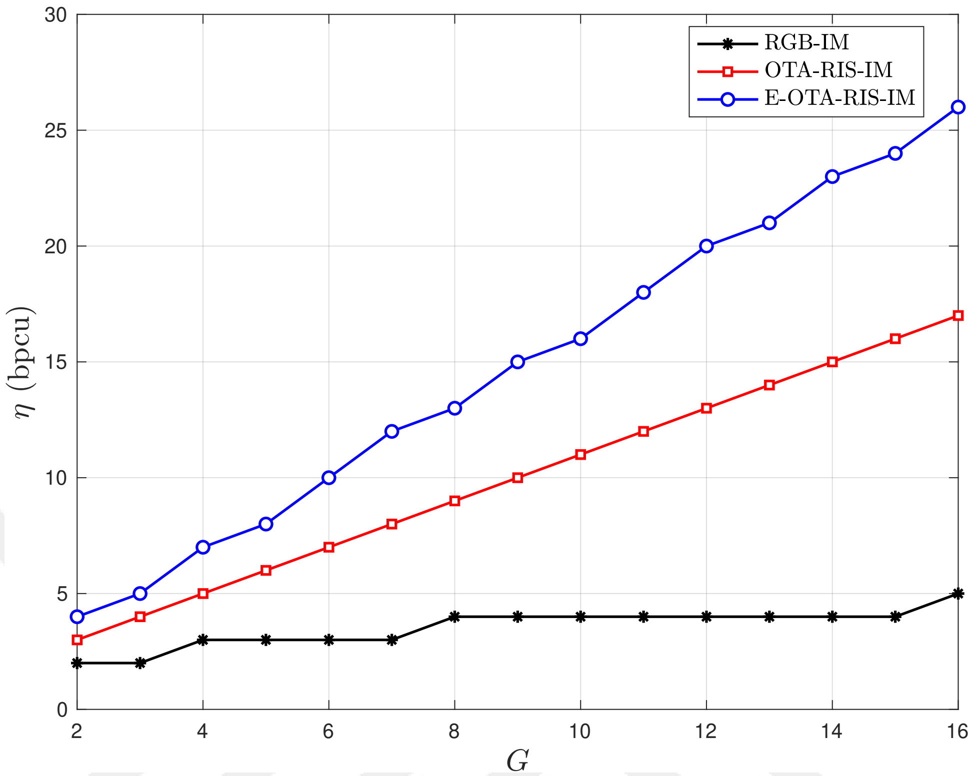

Figure 6.5: Spectrall efficiency comparison of all schemes for varying G and $M = 2$.

inactive. On the other hand, E-OTA-RIS-IM introduces an absorption state at the RIS, which enhances the bpcu at the cost of some reliability, as seen in the previous BER results. As a result, the bpcu increases drastically for the E-OTA-RIS-IM scheme, since the number of IM bits grows according to $\lfloor \log_2(3^G) \rfloor$.

6.4 Conclusion

In this chapter, a novel E-OTA-RIS-IM scheme is proposed, leveraging the combined advantages of IM and RIS technologies to significantly improve both spectral efficiency and BER performance in RIS-aided wireless communication systems. By partitioning the RIS and dynamically adjusting the states of its groups, the scheme enables additional IM bits to be transmitted OTA. Extensive computer simulations further highlight the performance benefits of the proposed system.

Chapter 7

RECONFIGURABLE INTELLIGENT SURFACE ENABLED DOWNLINK NOMA

7.1 Introduction

Globally, wireless communication technologies are in demand, and countries are striving to meet the strict expectations of 6G and beyond applications [Saad et al., 2019]. The advent of 6G technology is anticipated to facilitate the deployment of advanced applications, including but not limited to UAV networks, intelligent environments, autonomous systems, collaborative sensing and communication systems, eHealth solutions, VR experiences, and a myriad of other innovative applications [De Alwis et al., 2021]. In addition, many applications are envisioned to co-exist rather than function independently [Al-Ali and Yaacoub, 2023]. However, these applications require extremely high performance; for example, in autonomous systems, there is almost no room for error where reliability and latency are crucial since people's lives are at stake [Dang et al., 2020]. To meet these stringent requirements, innovative solutions are proposed to enhance the performance of wireless communication systems; nonetheless, it must be noted that one proposed solution alone cannot be sufficient to enhance wireless communication performance as needed. Hence, the co-existence and integration of multiple innovative technologies must be considered.

RISs have recently emerged as a preeminent technology that has captivated the interest of both academia and industry [Basar et al., 2019]. RISs are large surfaces with many elements that are made up of reflective meta-materials. These elements can contain PIN diodes, and when a voltage is applied, it allows the RIS to manipulate the electrical length and, hence, the phase of the impinging signal. Due to having intelligent control over its elements, one of the most significant advantages of RIS technology is its flexible structure [ElMossallamy et al., 2020]. It can easily be incorporated and integrated with existing wireless communication techniques such as IM [Basar et al., 2017], NOMA [Dai et al., 2018], different waveforms and much more. Furthermore, it is flexible in the modes it can operate in, which broadens the possible use cases of an RIS and makes it a desirable tool. An RIS can operate in reflect, refract, and absorb modes to the impinging signals for diverse intentions, allowing some degree of control over the channel with its reconfigurable elements [Tapio et al., 2021]. An RIS can operate in a hybrid manner and even be partitioned into multiple groups, with each group serving a different purpose.

NOMA is another technology that has great potential for future wireless communication systems. This approach has been contemplated as a subject of investigation within the context of 5G; nevertheless, empirical validation is required to establish the capacity of NOMA to yield substantial enhancements in the realm of post-5G communications [Vaezi et al., 2019]. NOMA allows multiple UEs to share valuable and scarce communication resources such as time, frequency, etc., by differentiating them in different domains, most popularly in code and power domains (PD) [Liu and Yang, 2021, Fu et al., 2021]. For example, through superposition coding and SIC methods, UEs can enjoy the benefits of NOMA in the power domain. NOMA also possesses flexibility in its applications and is an important tool that can be integrated into conventional communication systems such as IM, OFDM, RIS, and more [Arslan et al., 2020b].

7.1.1 Related Work

Studies on RIS

RISs have been used as a tool to enhance the performance of various methods in wireless communication systems. In [Zeng et al., 2021], the RIS orientation and horizontal distance have been investigated and optimized to maximize cell coverage. In [Ibrahim et al., 2021], the coverage probability of IRS-assisted communication networks have been evaluated with Nakagami-M fading channels. The DL coverage probability, ergodic capacity, and energy-efficiency performance for cellular networks in a multi-BS and multi-IRS configuration, accounting for both IRS-assisted and direct communication modes, have been examined in [Shafique et al., 2022]. RISs are able to provide energy efficiency and spectrum efficiency, but there exists a trade-off based on UE preference. The non-trivial trade-off between these for MIMO uplink (UL) communication is studied in [You et al., 2021]. While conventionally, the equalization process is performed at the transmitter (Tx) or receiver (Rx), [Arslan et al., 2022b] shows that the RIS can even virtually equalize a signal OTA in a frequency-selective scenario. RIS can be also used as a Tx by utilizing the OTA modulation concept. In OTA modulation, RIS manipulates the imcoming signal to encode the information [Basar et al., 2019]. In [Guo et al., 2020], reflection patterns have been used at the RIS to convey information, where reflection patterns can be generated by switching RIS elements to ON/OFF states. In [Tang et al., 2019b, Tang et al., 2019a], an RIS has been used as a Tx to realize OTA modulation and experimental results have been obtained by using a prototype system.

An RIS can be partitioned into different sections and groups where each partition can serve a different purpose. For a multi-UE scenario, the RIS elements are partitioned and allocated in an optimal manner to maximize UE fairness in [Khaleel and Basar, 2021]. On the other hand, an interesting study partitions the RIS for physical layer security in [Arzykulov et al., 2023]. While one part of the RIS serves to enhance communication at the legitimate UE, the other part of the RIS introduces artificial noise for the illegitimate UE. In addition, practical studies have been conducted for RIS-aided systems such as in [Arslan et al., 2023, Kayraklık et al., 2023], where the RIS enables coverage and efficient RIS codebook generation algorithms are proposed. Lastly, a comprehensive survey that summarizes the designs of the machine and deep learning-assisted RIS communication systems is presented in [Ozpoyraz et al., 2022].

Studies on NOMA

NOMA is a relatively older concept that has been and is still being investigated due to its large potential to enable multiple UEs to share valuable communication resources. Optimal power allocation for UEs is critical in NOMA and the authors in [Timotheou and Krikidis, 2015] and [Yang et al., 2016] address this issue by investigating power allocation and fairness for UEs. This is also considered for UE clusters in [Ali et al., 2016], which proposes a low-complexity and sub-optimal grouping scheme and then deriving a power allocation policy to maximize the overall system throughput considering both UL and DL. Furthermore, comprehensive error probability analyses with channel errors, BER performance investigations with SIC errors, and other detailed theoretical derivations have been conducted, giving NOMA studies a solid theoretical reference [Ferdi and Hakan, 2020, Kara and Kaya, 2018, Kara and Kaya, 2019]. The literature regarding NOMA is very rich due to its flexibility in means of coexisting with conventional technologies such as IM, machine learning, and even RIS [Arslan et al., 2020b, Arslan et al., 2022a].

Studies on RIS+NOMA

As stated previously, RIS and NOMA are both considerably flexible technologies that can be integrated with current wireless communication systems. The main motivation behind amalgamating RIS and NOMA is to fully embrace both flexible technologies potential and supplement each other while minimizing specific drawbacks either technology may have individually. For example, in conventional power domain NOMA systems, superposition coding and SIC is required to remove interference of other signals. However, the SIC process comes with unavoidable SIC errors which significantly degrade the practicality and performance of the system. RIS technology may provide alternative solutions to combat this issue. In addition, RIS technology is severely impacted by double fading path loss, hardware complexities, and other issues that the flexibility of NOMA may be able to alleviate. These two technologies have been further improved and merged to provide significant gains and new perspectives. For example, while the power difference required in power domain NOMA is generally conducted at the Tx or Rx, a hybrid RIS with active and passive partitions has been utilized to enable the power difference OTA in UL scenario [Arslan et al., 2022a]. In [Chauhan et al., 2022] and [Kumar et al., 2023], two RIS partitioned systems are introduced to maximize diversity order and improve signal quality, and an RIS assisted UE pairing THz-NOMA system has been proposed that pairs UEs based on the distance and power allocation between them to enhance their BER performance, respectively. Other works also investigate the physical layer security for RIS-NOMA systems, joint active and passive beamforming for MISO RIS-aided NOMA to maximize the sum rate [Mu et al., 2020], joint location and beamforming designs for STAR-RIS assisted NOMA systems, and attach an RIS to an UAV to assist in communication to other BS to UAV or UE communications [Song, 2021, Gao et al., 2023, Bariah et al., 2023]. In addition, an effective capacity analysis regarding an RIS and NOMA network is shown in [Li et al., 2021a]. In [Aldababsa et al., 2023], simultaneous transmitting and reflecting RIS (STAR-RIS)-aided NOMA scheme has been proposed.

7.1.2 Main Contributions

In this chapter, we propose a DL OTA NOMA scheme with the aid of an RIS to serve multiple UEs. It should be noted that in conventional DL PD-NOMA, the power difference is enabled at the BS through superposition coding. However, for the first time, DL-NOMA is enabled at the RIS using OTA modulation concept in the proposed scheme. To emphasize, the power difference required to enable power domain NOMA is not generated at the BS but rather we generate this power difference OTA with the help of the RIS as well as apply modulation to the impinging unmodulated signal. Here, the RIS elements are equally divided into multiple groups for enabling multiple-accessing where the number of groups is equal to the number of UEs. Note that each group serves one UE. An unmodulated carrier signal is transmitted from the BS to the RIS. Each partition of the RIS coherently aligns the phases of the impinging signal and modulates it using the information bits received by the BS through the backhaul link. Hence, a power level difference is generated at each UE since signals reflected by the elements of each RIS partition are constructively summed up. Even though there is interference of the reflected signals corresponding to the other UEs, since the intended signal is coherently aligned for the specified UE, this signal can be directly decoded without using SIC. In contrast to conventional NOMA schemes, since the proposed scheme does not require SIC to remove the interference of the other UEs, this leads to reducing the complexity and improving the efficiency of the system. It should be noted that SIC is a significant issue in conventional NOMA that dramatically increases the complexity and reduces the performance of wireless communications systems where the drawbacks exponentially increase with the increase of the number of UEs.

The major contributions of this chapter are listed as follows:

- We propose a novel communication system that uniquely enables DL NOMA utilizing a single passive RIS. Unlike conventional methods where NOMA is implemented at the BS or Rx, our approach leverages the RIS's flexibility to perform NOMA operations directly in the wireless medium, reducing system complexity and enhancing performance.

- A thorough end-to-end system model of the proposed scheme is provided and analyzed along with computer simulations.

- The outage probability is derived and calculated for different configurations and confirmed with simulations.

- A theoretical error probability analysis is provided along with computer simulation results for varying parameters and scenarios.

- Computer simulations have been performed with perfect and imperfect CSI conditions to assess the BER performance.

- Sum-rate has been presented for the proposed NOMA scheme.

- Comparisons for all of the above analysis have been conducted against conventional passive RIS OMA scenarios existing in the literature.

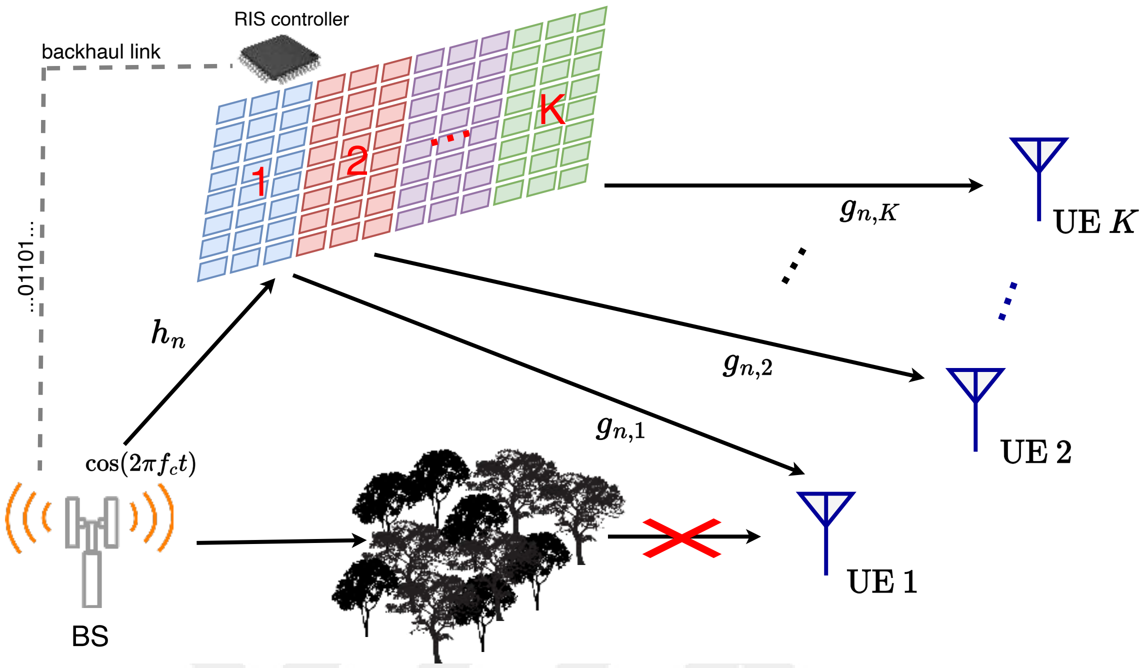

Figure 7.1: The system model of the proposed DL NOMA scheme that serves K UEs.

7.2 System Model

As seen in Fig. 7.1, a DL NOMA system is considered, where the BS and an RIS simultaneously serve K UEs under frequency-flat Rayleigh fading channels. Therefore, it is assumed that the LoS link between the BS and UEs is blocked via obstacles such as buildings or trees, and a backhaul link exists between the BS and RIS. As in [Araghi et al., 2022], the RIS can be used for coverage extension when LoS does not exist between the BS and UEs. Hence, this assumption is valid. To serve K UEs, the RIS with N elements is separated into K partitions, each including N_g number of elements, i.e., $N_g = N/K$. The BS transmits an unmodulated signal with a transmit power (P_t) and a carrier frequency (f_c). The k^{th} RIS partition modulates the incoming unmodulated signal according to the information bits of the k^{th} UE conveyed through the backhaul link between the BS and RIS by introducing an additional phase shift, $k = 1, \cdots, K$. At the k^{th} partition of the RIS, a total number of $\log_2(M_k)$ incoming bits introduce a phase shift ξ_k for the k^{th} UE, where

M_k and ξ_k are the modulation order and phase value of the determined symbol drawn from M_k-PSK constellation for the k^{th} UE, respectively. Hence, the RIS can be considered as a part of the BS which enables a low-cost Tx architecture as in[Basar et al., 2019, Basar, 2019]. Note that backhaul and wireless links between the BS and RIS play critical roles in configuring RIS elements and transmitting an actual RF signal from BS to RIS, respectively. Since RIS is a passive device and cannot configure itself, a feedback or backhaul link is necessary between the RIS and BS for BS to be able to configure RIS elements [Pan et al., 2021]. The received signal at the k^{th} UE can be obtained as:

$$y_k = \sqrt{P_t} \sum_{n=1}^{N} g_{n,k} e^{j\theta_n} h_n + w_k, \tag{7.1}$$

where $h_n = \alpha_n e^{j\phi_n}$ and $g_{n,k} = \beta_{n,k} e^{j\psi_{n,k}}$ are the independent and identically distributed (i.i.d.) Rayleigh fading channel coefficients between the BS and n^{th} RIS element and between the n^{th} RIS element and k^{th} UE, respectively, $n = 1, \cdots, N$. Moreover, w_k and θ_n stand for the AWGN sample, which follows the distributions $\mathcal{CN}(0, N_0)$ and adjustable phase introduced by the n^{th} RIS element, respectively. Since the k^{th} RIS partition serves the k^{th} UE, $\bar{n}^{\text{th}}$ RIS element is coherently aligned and modulated as $\theta_{\bar{n}} = \xi_k - \phi_{\bar{n}} - \psi_{\bar{n},k}$, $\bar{n} \in \mathbb{I}_k$, where $\mathbb{I}_k = \{N_g(k-1)+1, N_g(k-1)+2, \cdots, N_g k\}$, is a set of indices of the RIS elements allocated to serve the k^{th} UE, $k = 1, \cdots, K$, $|\mathbb{I}_k| = N_g$. Note that the distributions of h_n and $g_{n,k}$ follow $\mathcal{CN}(0, \sigma_h^2)$ and $\mathcal{CN}\left(0, \sigma_{g_k}^2\right)$, respectively. Assuming $\mathbb{I}_{k'} = \mathbb{I} - \mathbb{I}_k$, $\mathbb{I} = \{1, 2, \cdots, N\}$, $|\mathbb{I}_{k'}| = (K-1) N_g$, after determining the phase values of the RIS elements, (7.1) can be reexpressed as follows:

$$y_k = \sqrt{P_t} \Bigg[\underbrace{e^{j\xi_k} \sum_{n \in \mathbb{I}_k} \alpha_n \beta_{n,k}}_{\text{Useful term}} + \underbrace{\sum_{k' \neq k} \sum_{n \in \bar{\mathbb{I}}_k} \alpha_n \beta_{n,k} e^{\left(j\xi_{k'} - \psi_{n,k'} + \psi_{n,k}\right)}}_{\text{Interference of other RIS parts}} \Bigg] + w_k. \tag{7.2}$$

As we may know, the sum of real numbers increases monotonically, on the other hand, the sum of complex numbers is not monotonic due to phase terms resulting in fluctuations in their sum. The useful term in (7.2) is the sum of real numbers instead of complex numbers as in interference term. Hence, as mentioned previously, the useful term monotonically increases while the interference term does not grow and becomes negligible for a large value of $|\mathbb{I}_k|$.

At the k^{th} UE, the ML detection rule is used to decode y_k as below:

$$\hat{\mu}_k = \arg \min_{\mu=1,\cdots,M_k} \left\| y_k - e^{j\xi_k(\mu)}\Delta \right\|^2, \tag{7.3}$$

where $\Delta = \sqrt{P_t}\sum_{n\in\mathbb{I}_k} \alpha_n \beta_{n,k}$ and $\xi_k(\mu)$ is the phase value of the μ^{th} symbol drawn from M_k-ary PSK constellation. Finally, $\hat{\mu}_k$ is demapped into $\log_2(M_k)$ information bits. Note that SIC is not required to decode the received signal in the proposed scheme; however, it is a vital step in the power domain NOMA systems [Ding et al., 2020].

The SINR of the k^{th} UE can be derived from (7.2) as follows:

$$\gamma_k = \frac{P_t \left|\sum_{n\in\mathbb{I}_k} \alpha_n \beta_{n,k}\right|^2}{P_t \left|\sum_{k'\neq k}\sum_{n\in\mathbb{I}_{k'}} \alpha_n \beta_{n,k} e^{(j\xi_{k'} - \psi_{n,k'} + \psi_{n,k})}\right|^2 + N_0}. \tag{7.4}$$

It should be noted that when there exists a direct path between the BS and UE, the received signal at the k^{th} UE can be given as:

$$y_k = \sqrt{P_t}\left(f_k + \sum_{n=1}^{N} g_{n,k} e^{j\theta_n} h_n\right) + w_k, \tag{7.5}$$

where f_k is the Rayleigh fading coefficient between the BS and k^{th} UE. In this case, at the k^{th} UE, ML rule as in (7.3) can be used as follows:

$$\hat{\mu}_k = \arg \min_{\mu=1,\cdots,M_k} \left\| y_k - \sqrt{P_t} f_k - e^{j\xi_k(\mu)}\Delta \right\|^2, \tag{7.6}$$

Here, the unmodulated signal term $\sqrt{P_t} f_k$ arriving directly from the BS can easily be extracted to remove the interference effect of LoS path.

When compared to NOMA clustering studies where RIS partitions serve multiple users in a cluster rather than one user, in general, the proposed scheme is expected to provide enhanced performance since each group of the RIS focuses on serving a single UE. Whereas in a clustering approach, the RIS needs to optimize itself for numerous UEs at the same time in a cluster, which will inevitably come with significant trade-offs.

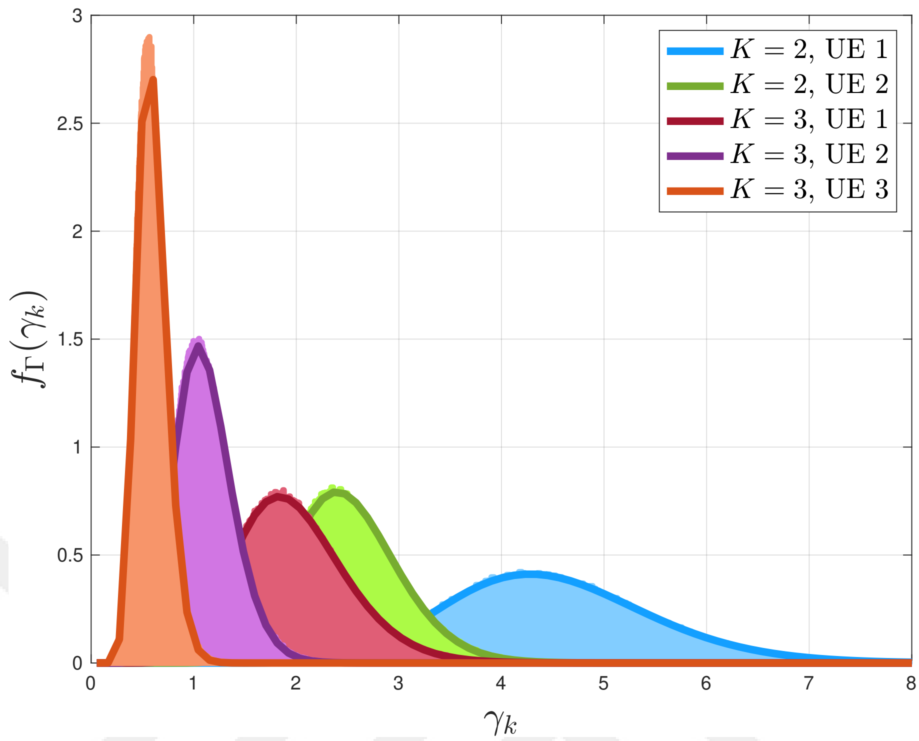

Figure 7.2: Distribution fit of SINR for varying UEs for $N = 256$.

While un-partitioned RIS-assisted NOMA [Yang et al., 2020, Mu et al., 2020] may offer better theoretical performance in terms of sum-rate, outage probability, and error probability, the partitioned RIS approach provides significant practical benefits. It reduces channel estimation overhead from $N \times K$ to only N coefficients to be estimated, easing RIS complexity. Additionally, it enables scalable and less complex phase shift design and resource allocation, independent optimization for each user, and simplifies the decoding process by obviating the need for SIC. These advantages highlight the partitioned RIS scheme's practicality, scalability, and efficiency, offering a nuanced view of its merits compared to conventional NOMA systems.

7.3 Performance Analysis

In this section, we provide a comprehensive theoretical outage probability and BER analysis for the proposed scheme. Using the SINR, we approach the outage probability analysis through the use of Gil-Pelaez's inversion formula to obtain the CDF for each user. The SINR distribution is confirmed theoretically along with the distribution fitter tool on MATLAB. Using the parameters of the fitted distribution, we obtain the BER analysis.

7.3.1 Theoretical Outage Probability Analysis

This subsection analyzes the theoretical outage probability of the RIS-DL-NOMA scheme. For convenience, the SINR of the k^{th} UE can be rewritten as:

$$\gamma_k = \frac{P_t \left|\mathcal{A}\right|^2}{P_t \left|\mathcal{B}\right|^2 + N_0}, \tag{7.7}$$

$$\mathcal{A} = \sum\nolimits_{n\in\mathbb{I}_k} \alpha_n \beta_{n,k}, \tag{7.8}$$

$$\mathcal{B} = \sum\nolimits_{k'\neq k} \sum\nolimits_{n\in\mathbb{I}_{k'}} \delta_{n,k,k'}, \tag{7.9}$$

where $\delta_{n,k,k'} = \alpha_n \beta_{n,k} e^{(j\xi_{k'} - \psi_{n,k'} + \psi_{n,k})}$ and the amplitudes of channel coefficients of h_n and $g_{n,k}$ (α_n and $\beta_{n,k}$) are assumed to be independently Rayleigh distributed RVs, and $\mathrm{E}[\alpha_n \beta_{n,k}] = \sigma_h \sigma_{g_k} \frac{\pi}{4}$ and $\mathrm{VAR}[\alpha_n \beta_{n,k}] = \sigma_h^2 \sigma_{g_k}^2 \left(1 - \frac{\pi^2}{16}\right)$. Due to the CLT, for a sufficiently large value of N_g, $\mathcal{A}$ follows Gaussian distribution as given:

$$\mathcal{A} \sim \mathcal{N}\left(N_g \sigma_h \sigma_{g_k} \frac{\pi}{4}, N_g \sigma_h^2 \sigma_{g_k}^2 \left(1 - \frac{\pi^2}{16}\right)\right), \tag{7.10}$$

Moreover, $|\mathcal{A}|^2$ becomes a non-central chi-square RV with one degree of freedom. In contrast, since complex terms exist in $\delta_{n,k,k'}$, $\mathcal{B}$ converges to complex Gaussian distribution with $\mathcal{B} \sim \mathcal{CN}\big(0, N_g(K-1)\sigma_h^2 \sigma_{g_k}^2\big)$ and $|\mathcal{B}|^2$ becomes a central chi-square RV with two degrees of freedom. Therefore, the SINR of the k^{th} UE (γ_k) is the ratio of two chi-square RVs.

Lemma 1 *The mean and variance values of $\mathcal{A}$ can be given as $\mu_{\mathcal{A}} = N_g \sigma_h \sigma_{g_k} (\pi/4)$ and $\sigma_{\mathcal{A}} = N_g \sigma_h^2 \sigma_{g_k}^2 (1 - \pi^2/16)$, respectively. The detailed derivation of these expressions is provided in Appendix A.*

Lemma 2 *The mean and variance values of $\mathcal{B}$ can be given as $\mu_{\mathcal{B}} = 0$ and $\sigma_{\mathcal{B}} = N_g(K-1)\sigma_h^2 \sigma_{g_k}^2$, respectively. The detailed derivation of these expressions is provided in Appendix B.*

Note that R_k and B are the minimum rate at which the QoS holds for the k^{th} UE and the bandwidth, respectively. The outage probability of the k^{th} UE can be found by using the following equation:

$$\begin{aligned} P_{\text{out}} &= \Pr\left[\gamma_k < 2^{R_k/B} - 1\right] = \Pr\left[\frac{|\mathcal{A}|^2}{|\mathcal{B}|^2 + N_0/P_t} < r_k\right] \\ &= \Pr\left[|\mathcal{A}|^2 - r_k\,|\mathcal{B}|^2 < \upsilon\right] = \Pr\left[\Upsilon < \upsilon\right] = F_{\Upsilon}(\upsilon), \end{aligned} \tag{7.11}$$

where $r_k = 2^{R_k/B} - 1$, $\upsilon = r_k(N_0/P_t)$, and $\Upsilon = |\mathcal{A}|^2 - r_k\,|\mathcal{B}|^2 = |\mathcal{A}|^2 - \left|\sqrt{r_k}\mathcal{B}\right|^2$ and $F_{\Upsilon}(\upsilon)$ are the difference of independent non-central and central chi-square RVs and the CDF of Υ, respectively. Moreover, the characteristic function of Υ can be given as [Simon, 2002]:

$$\Psi_{\Upsilon}(\omega) = \exp\left(\frac{j\omega\mu_{\mathcal{A}}^2}{1 - 2j\omega\sigma_{\mathcal{A}}^2}\right)\frac{1}{\left(1 - 2j\omega\sigma_{\mathcal{A}}^2\right)^{0.5}\left(1 + 2j\omega\sigma_{\mathcal{B}'}^2\right)}, \tag{7.12}$$

where $\sigma_{\mathcal{B}}^2 = 0.5 r_k N_g (K-1)\sigma_h^2\sigma_{g_k}^2$ is the variance of $\mathcal{B}' = \sqrt{r_k}\mathcal{B}$ and $\mu_{\mathcal{A}} = N_g\sigma_h\sigma_{g_k}\frac{\pi}{4}$ and $\sigma_{\mathcal{A}}^2 = N_g\sigma_h^2\sigma_{g_k}^2\left(1 - \frac{\pi^2}{16}\right)$ are the mean and variance values of $\mathcal{A}$, respectively. Since Υ is the difference of chi-square RVs, obtaining the pdf and cdf of Υ is not straightforward. Therefore, we exploit the Gil-Pelaez's inversion equation [Simon, 2002] to obtain the CDF of Υ through characteristic functions as follows:

$$F_{\Upsilon}(\upsilon) = \frac{1}{2} - \int_0^{\infty}\frac{\Im\left\{e^{-j\omega\upsilon}\Psi_{\Upsilon}(\omega)\right\}}{\omega\pi}d\omega. \tag{7.13}$$

Note that the outage probability can be found by using (7.13).

7.3.2 Theoretical Bit Error Rate Analysis

In this subsection, the theoretical BER of the proposed system is provided. As mentioned in Section III.A, the SINR of the k^{th} UE (γ_k) is the ratio of chi-square RVs; thus, one cannot exactly derive the γ_k and its closed form does not exist in the literature. Therefore, we exploit the Open Distribution Fitter app (dfittool) of the MATLAB program to create the distribution of γ_k as a semi-analytical method. Considering the impact of the interference term $|\mathcal{B}|^2$ on γ_k can be neglected, and the chi-square distribution $|\mathcal{A}|^2$ is a variant of the Gamma distribution, γ_k is foreseen to follow the Gamma distribution.

In the context of theoretical derivations, generating shape (κ) and scale (ρ) parameters for the gamma distribution corresponding to each configuration is imperative. These parameters are essential components in the analytical framework, facilitating the comprehensive exploration and analysis of the underlying theoretical constructs. As seen from Fig. 7.2, γ_k fits the Gamma distribution for different configurations. With these κ and ρ parameters, the PDF of γ_k can be given as [Lee et al., 1979]:

$$f_\Gamma(\gamma_k) = \frac{\gamma_k^{\kappa-1} e^{(-\gamma_k/\rho)}}{\rho^\kappa \Gamma(\kappa)}, \tag{7.14}$$

where $\Gamma(\cdot)$ is the Gamma function. Note that the parameters of the fitted Gamma distribution change for different configurations of UE and P_t.

Theoretical SEP is computed through the utilization of the MGF of the Gamma distribution in the following manner:

$$M_{\gamma_k}(s) = (1 - \rho s)^\kappa, \quad \text{for } s < \frac{1}{\rho}. \tag{7.15}$$

The average SEP pertaining to M-ary PSK modulation, employing the MGF as specified in (7.15), is presented as follows:

$$P_s = \frac{1}{\pi} \int_0^{(M-1)\pi/M} M_{\gamma_k} \left(\frac{-\sin^2(\pi/M)}{\sin^2 x} \right) dx. \tag{7.16}$$

A numerical computation of the SEP can be performed as defined in (7.16) by employing the parameters of the Gamma distribution. Additionally, BEP can be approximated as:

$$P_b \approx P_s / \log_2(M). \tag{7.17}$$

7.3.3 RIS Partitioning Optimization

In the proposed RIS-aided DL NOMA scheme, the RIS is partitioned into equal number of RIS elements. Hence, due to increased path loss, further UEs performs worse than near UEs in terms of many metrics such as error performance and outage probability. This is because when the RIS elements are distributed uniformly, more elements are assigned to near UEs than needed while necessary number of elements not allocated to the further UEs.

In this subsection, we define an optimization problem that considers the outage probability performance of all UEs. In this case, a UE is not assigned an unnecessary number of RIS elements when other users are more in need of those RIS elements hence, all users have a fair power disparity to enable power domain NOMA and make the interference negligible. Here, the optimization problem (P1) is defined in such a way that more RIS elements are allocated to further UEs in order to obtain outage probability performance in a more fair manner as follows:

$$\begin{aligned}(\mathrm{P1}) =&\min_{\mathbb{N}} \sum_{k=1}^{K} \sum_{k'=k+1}^{K} \left| P_{\mathrm{out}}^{(k)} - P_{\mathrm{out}}^{(k')} \right|, \\ &\text{s.t.} \sum_{k=1}^{K} N^{(k)} = N. \end{aligned} \tag{7.18}$$

where $\mathbb{N} = \{N^{(1)}, N^{(2)}, \cdots, N^{(K)}\}$ and $N^{(k)}$ is the number of RIS elements allocated to the k^{th} UE.

We utilize a simple search algorithm to solve (P1) for $K = 2$. Here, the value of $N^{(1)}$ is increased from 1 to N with an an increment of 1, while $N^{(2)}$ is equal $N - N^{(1)}$. When $K > 2$, this algorithm becomes significantly complex; therefore, a low-complexity algorithm to solve (P1) for $K > 2$ is left as a future study item.

7.4 Simulation Results And Comparisons

In this section, we provide the computer simulation results of the proposed scheme and compare them to the OMA benchmark. Furthermore, each figure for the proposed scheme and benchmark is confirmed with theoretical simulations. Performances of the outage probability, QoS, sum-rate, and BER are shown and discussed for varying parameters.

7.4.1 Benchmark Schemes

In this study, TDMA is considered as a benchmark scheme for performance comparison. To find the outage probability of the TDMA, its SNR expression for the k^{th}

UE is needed and can be given as $\gamma_k^{\mathrm{TDMA}} = P_t|\bar{\mathcal{A}}|^2/N_0$, where $\bar{\mathcal{A}} = \sum_{n\in\mathbb{I}} \alpha_n \beta_{n,k}$ and $\mathbb{I} = \{1, \cdots, N\}$ is a set of indices of all RIS elements. Since all elements of the RIS serve only one UE at a given time slot, there is no interference term in γ_k^{TDMA}. It should be noted that for a fair comparison, since the UEs do not share the same time resource and communicate simultaneously, the time allocated for each UE is divided into K; hence, the rate of data for each UE is multiplied by K. Finally, the outage probability of the k^{th} UE for TDMA is given as $P_{\mathrm{out},k}^{\mathrm{TDMA}} = \Pr[\gamma_k^{\mathrm{TDMA}} < 2^{(KR_k/B)} - 1]$. Additionally, the sum rate for TDMA can be expressed as $(\sum_k \gamma_k^{\mathrm{TDMA}})/K$.

7.4.2 Simulation Setup Parameters

In this subsection, the simulation setup parameters are provided. The k^{th} UE, an RIS, and a BS are located in 2D coordinate system with coordinate vectors $\mathbf{p}^{\mathrm{UE}_k} = [x^{\mathrm{UE}_k}, y^{\mathrm{UE}_k}]^{\mathrm{T}}$, $\mathbf{p}^{\mathrm{RIS}} = [x^{\mathrm{RIS}}, y^{\mathrm{RIS}}]^{\mathrm{T}}$, and $\mathbf{p}^{\mathrm{BS}} = [x^{\mathrm{BS}}, y^{\mathrm{BS}}]^{\mathrm{T}}$, respectively, $k = 1, \cdots, K$. Hence, the distance between the k^{th} UE and the RIS and the RIS and BS can be calculated as $d^{\mathrm{UE}_k-\mathrm{RIS}} = ||\mathbf{p}^{\mathrm{UE}_k} - \mathbf{p}^{\mathrm{RIS}}||$ and $d^{\mathrm{RIS-BS}} = ||\mathbf{p}^{\mathrm{RIS}} - \mathbf{p}^{\mathrm{BS}}||$, respectively. In order to calculate the path loss with the given distances, the 3GPP UMi path loss model for NLoS transmission defined within the 2-6 GHz frequency band and Tx-Rx range varying from 10-2000 m, can be given as:

$$L\left(d^i\right) \text{ [dB]} = 36.7\log_{10}\left(d^i\right) + 22.7 + 26\log_{10}\left(f_c\right), \tag{7.19}$$

where $i \in \{\mathrm{UE}_k\text{–}\mathrm{RIS}, \mathrm{RIS}-\mathrm{BS}\}$ and f_c is the operating frequency. The power of the channel between the k^{th} UE and RIS and the RIS and BS can be calculated as: $\sigma_{g_k}^2 = 1/10^{L(d^{\mathrm{UE}_k-\mathrm{RIS}})/10}$ and $\sigma_h^2 = 1/10^{L(d^{\mathrm{RIS-BS}})/10}$, respectively. The parameters considered in computer simulations are given in Table 7.1. Note that the transmit power of the BS (P_t) is in the range of -30 and 40 dBm, and and operating frequency (f_c) is 2.4 GHz as specified [38.104, 2019]. In addition, RIS element sizes are in the range of 64-1024 as can be confirmed in [Araghi et al., 2022].

Table 7.1: Computer Simulation Parameters

Carrier frequency (GHz)	f_c	2.4
Location of UE1	$\mathbf{p}^{\mathrm{UE}_1}$	$[15, 12]^{\mathrm{T}}$
Location of UE2	$\mathbf{p}^{\mathrm{UE}_2}$	$[10, 8]^{\mathrm{T}}$
Location of UE3	$\mathbf{p}^{\mathrm{UE}_3}$	$[5, 2]^{\mathrm{T}}$
Location of UE4	$\mathbf{p}^{\mathrm{UE}_4}$	$[2, 1]^{\mathrm{T}}$
Location of BS	$\mathbf{p}^{\mathrm{BS}}$	$[55, 10]^{\mathrm{T}}$
Location of RIS	$\mathbf{p}^{\mathrm{RIS}}$	$[35, 5]^{\mathrm{T}}$
Noise variance (dBm)	N_0	-130

7.4.3 Computer Simulations and Discussions

In this subsection, comprehensive simulation results are presented to investigate the performance of the proposed DL-NOMA scheme. We investigate the performance of outage probability (P_{out}), sum rate, QoS, and BER for varying parameters, cases and UEs. Additionally, the performance of the proposed DL-NOMA is compared to the TDMA-OMA benchmark scheme. As it can be seen in all simulation results, the theoretical results align and match exactly in performance and behaviour. For all simulations, the computer simulation set-up parameters in Table I are considered.

In Figs. 7.3 and 7.4, the outage probability performance of the proposed DL-NOMA scheme is presented and compared to TDMA OMA benchmark. In Fig. 7.3, the parameters are selected as $N = 512$ and $K = 2, 4$. As seen from Fig. 7.3, the performance of the proposed system is better in the case of $K = 2$. Since the interference effect is more severe for the scenario with more UEs, the outage probability performance is better when $K = 2$ compared to the case where $K = 4$. Since there is an increase interference in the case of $K = 4$, an error floor is observed at around $P_{out} = 10^{-4}$. When $K = 4$, the proposed DL-NOMA scheme outperforms our benchmark until it reaches a certain point of saturation in terms of outage

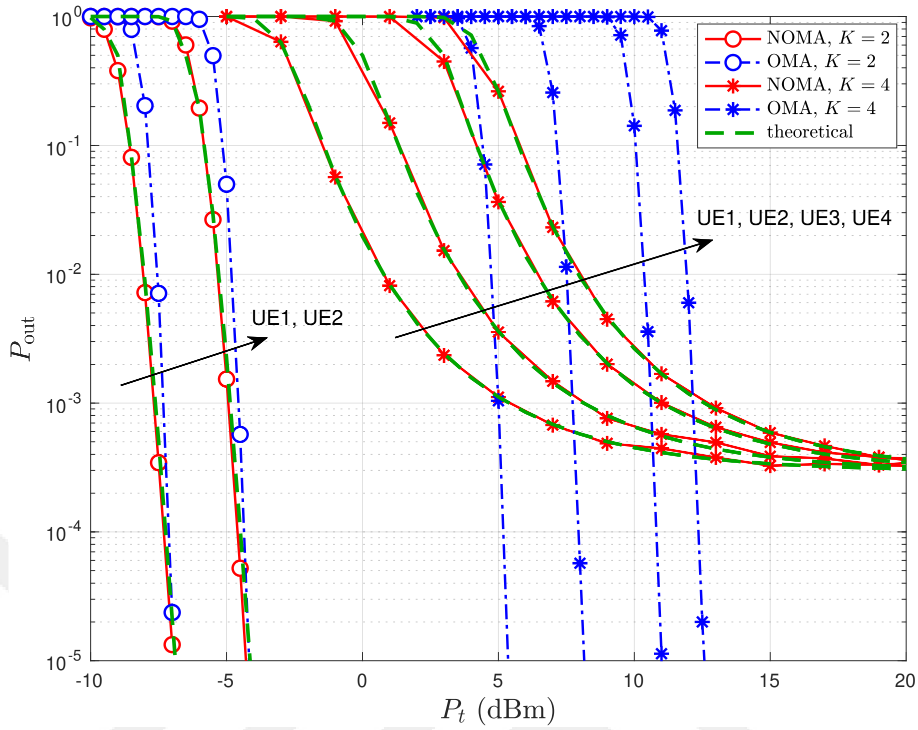

Figure 7.3: Comparison of the outage probability performance of the proposed DL-NOMA scheme and TDMA for $R_k = 2$ bps/Hz, $N = 512$ and $K = 2$, 4.

probability performance for all UEs; however, it becomes worse than the benchmark as P_t increases due to the interference effect of the UEs which can also be observed by the error floor. It can also be seen that the theoretical curves derived from (7.13) verify our simulation results.

In Fig. 7.4, the outage probability performance of the proposed DL-NOMA scheme is demonstrated and compared with TDMA for $K = 3$ and varying RIS sizes N. As seen from Fig. 7.4, as N increases, the outage probability performance of the proposed DL-NOMA scheme significantly improves due to the gains from the RIS elements. For small values of N, the interference of the UEs has a higher impact which can be seen by the error floors and the performance of the proposed scheme is less impactful. Therefore, the superiority of the proposed DL-NOMA scheme over the benchmark in terms of outage probability is more obvious when N is determined as a high value because the interference of the UEs becomes more negligible and the RIS can enable NOMA more effectively. Furthermore, it can

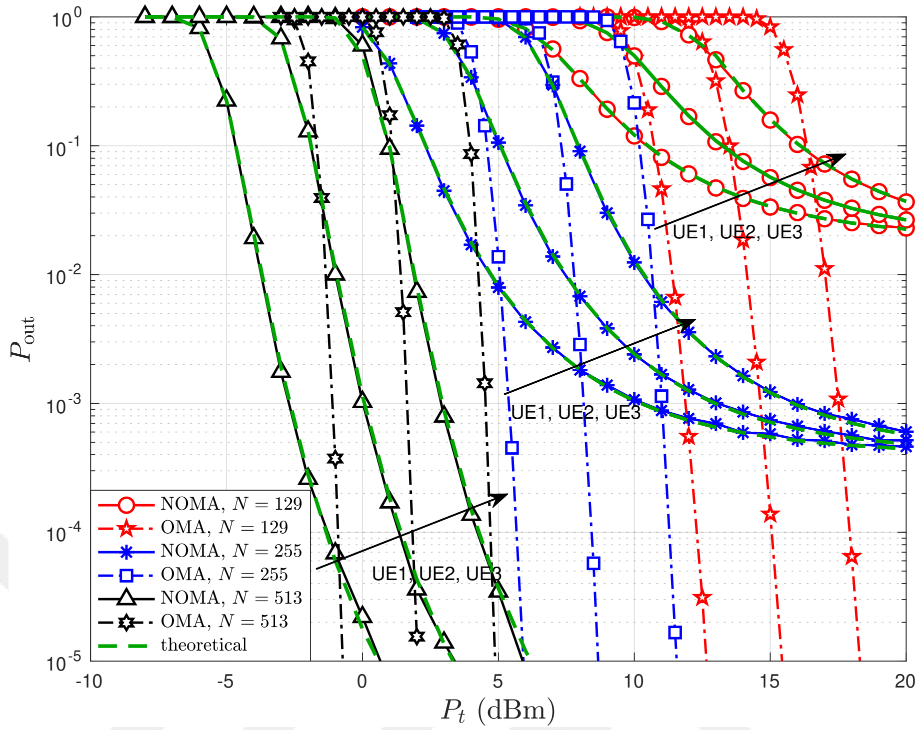

Figure 7.4: Comparison of the outage probability performance of the proposed DL-NOMA scheme and TDMA for $R_k = 2$ bps/Hz, varying N and $K = 3$.

be seen that the theoretical curves obtained by (7.13) coincide with the simulation results for different N values.

In Fig. 7.5, the performance superiority of the proposed scheme over the benchmark can be observed as the QoS requirement becomes more strict. As the QoS requirement for a UE's communication performance gets higher, the outage probability increases since it is harder to sustain that quality. This can be seen in Fig. 7.5 for both UEs and varying RIS size. It should be noted that, while the benchmark outperforms the proposed NOMA scheme for low QoS value, after a certain QoS value, the proposed scheme shows its superiority over OMA. Additionally, at higher QoS values, NOMA enables communication to the users whereas communication can not be longer sustained in the OMA case. It can be seen that as the RIS size increases, the outage probability performance improves for both UEs. It should be noted that in NOMA the UEs QoS performance is almost similar whereas there is a larger difference in performance in the OMA benchmark. Furthermore, it can

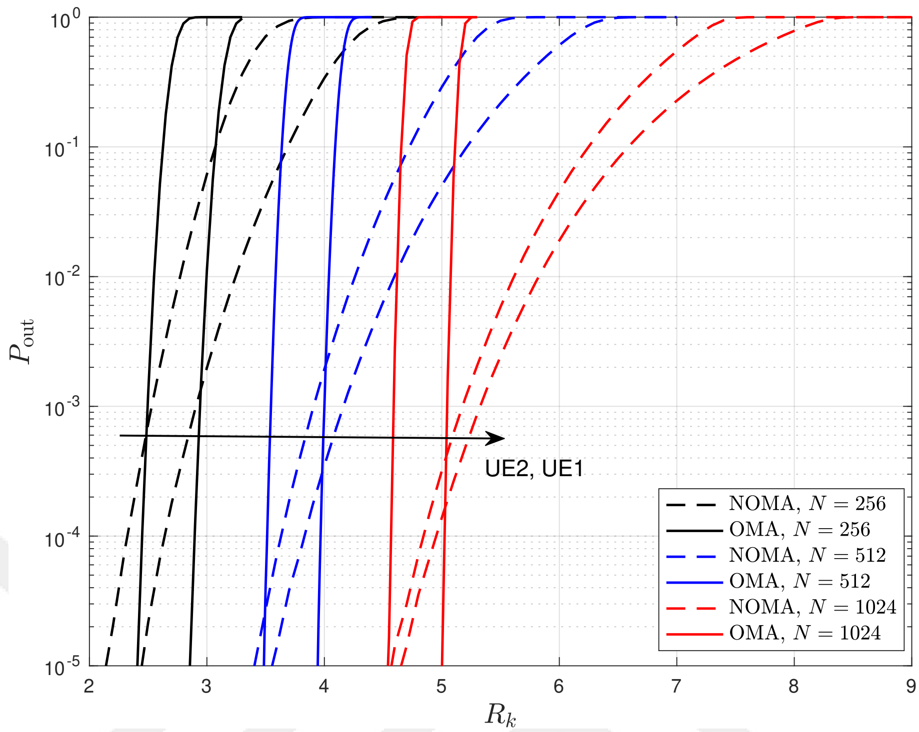

Figure 7.5: Outage probability vs QoS performance comparison of the proposed DL-NOMA and OMA schemes for $K = 2$, varying N, $P_t = 5$ dBm.

be analyzed that as the RIS size (N) increases, the system can sustain higher QoS requirement. Since UE1 is closer to the BS compared to UE2, its performance is better.

In Fig. 7.6, the outage probability performance of the proposed DL NOMA scheme is demonstrated with respect to varying QoS (R_k) values for $P_t = 7$ dBm and $B = 1$ where $N = 512$ and 513 for $K = 2$, 4, and 3, respectively. The reason why N is selected as 513 for $K = 3$ is to allocate the same integer number RIS elements to each UE. Additionally, the outage probability performance of DL NOMA scheme is compared to OMA. As seen from Fig. 7.6, as the number of UEs (K) decreases, higher QoS values can be provided because more RIS elements can be allocated to a specific UE for a given RIS size (N) in a system with fewer UEs. When the proposed DL NOMA scheme is compared to OMA, it can be seen that after a certain QoS value, the OMA scheme can no longer enable communication while the proposed scheme can for all values of K.

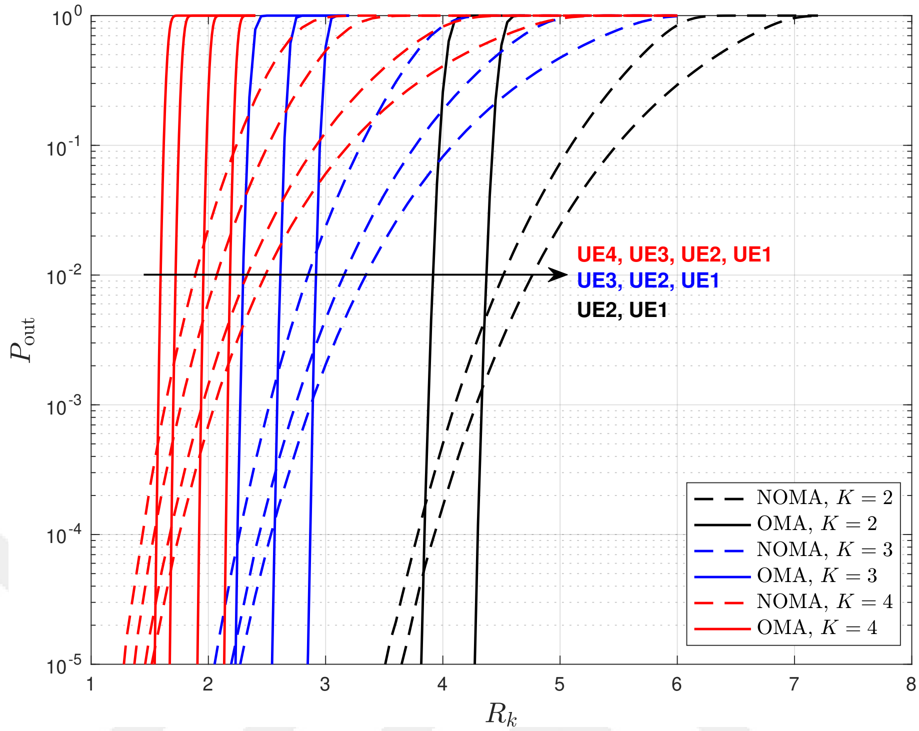

Figure 7.6: Outage probability vs. QoS performance comparison for the proposed DL-NOMA and OMA schemes at $P_t = 7$ dBm with $N = 512$ for $K = 2, 4$ and $N = 513$ for $K = 3$.

In Figs. 7.7 and 7.8, the sum rate superiority of the proposed scheme over the benchmark can be analyzed as the transmit power of the system increases for varying UEs. It can be visualized in Fig. 7.7 that as P_t increases the TDMA benchmark also increases linearly and an increase in the number of UEs does not introduce immense gains in the system. On the other hand, the proposed scheme's sum rate significantly increases and surpasses that of the benchmark. Furthermore, an increase in the number of UEs in the NOMA system has a notable positive impact on the systems sum rate. In Fig. 7.8, the sum rate performance is considered as the number of RIS elements N increases. It can be seen that as before, an increase in P_t has a great impact on improving the proposed system performance, while for the benchmark it only provides a linear gain. Additionally, it can also be observed that for a small N the proposed system still outperforms the benchmark however, the proposed system becomes much more effective and the performance gains are

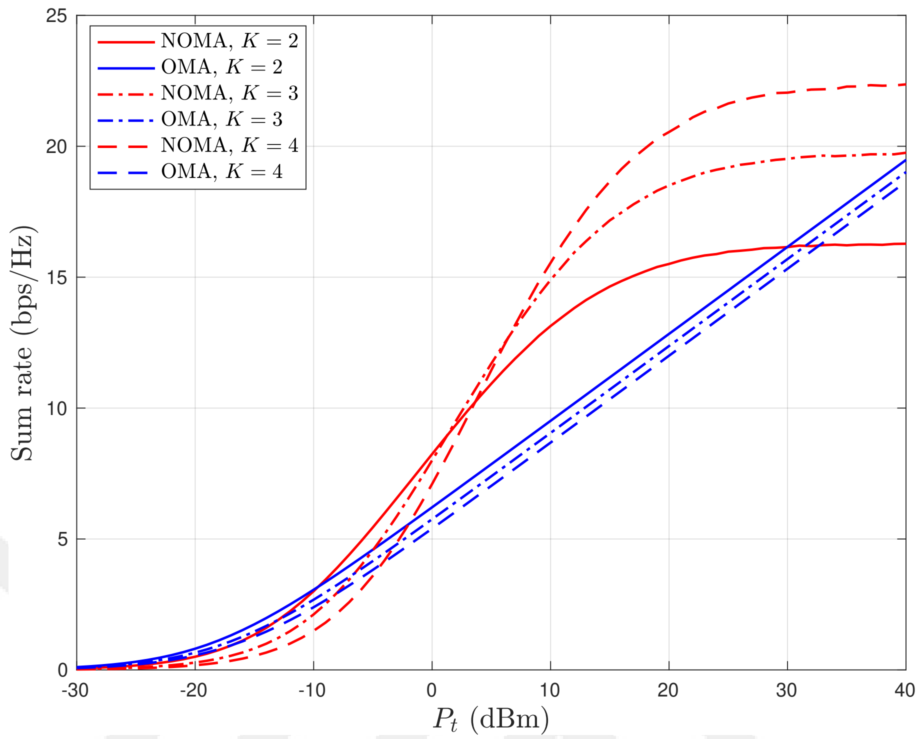

Figure 7.7: Sum rate comparison for the proposed DL-NOMA and OMA schemes when $N = 512$ for $K = 2, 4$ and $N = 513$ for $K = 3$.

significantly enhanced for a larger N.

Figs 7.9, 7.10 and 7.11 provide BER comparisons of the proposed system and TDMA benchmark for a varying P_t. In Fig. 7.9, BER performance of the proposed DL NOMA scheme is compared to OMA for $K = 4$, $N = 1024$, and 1 bps/Hz. Note that ML detection rule in (7.3) is used to decode the DL NOMA signal. In order to provide 1 bps/Hz, M is selected as 2 and 16 for NOMA and OMA schemes, respectively. It can be observed that the proposed NOMA outperforms the OMA benchmark for all UEs. Furthermore, the nearest UE to BS (UE1) provides the best error performance and the furthest UE to BS (UE4) has the worst as expected. Moreover, it can be seen that for low P_t values, the theoretical results obtained by using (7.17) and the parameters in Table 7.2 match the simulated BER results. However, after a certain P_t value, a gap between theoretical and simulation curves emerges and, this gap increases with respect to P_t since the SINR of the k^{th} UE (γ_k) no longer follows the Gamma distribution exactly due to the non-negligible

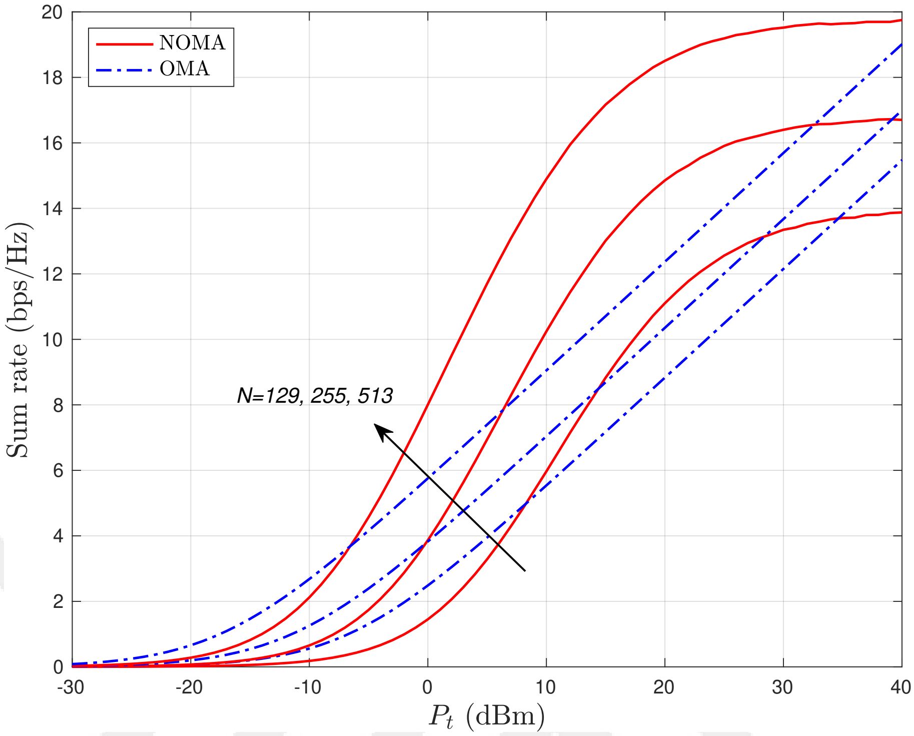

Figure 7.8: Sum rate comparison of the proposed DL-NOMA and OMA schemes for $K = 3$ and varying N values.

interference effect.

On the other hand, in Fig. 7.10, the BER performance vs transmit power (P_t) of the proposed scheme and benchmark is shown for a varying number of UEs (K), $N = 256$, and 2 bps/Hz. Here, M is chosen as 4 and 4^K for NOMA and OMA, respectively, to provide 2 bps/Hz spectral efficiency. Note that N is selected as 255 for $K = 3$ since 256/3 is not an integer. Similarly in the BER performance, the case of $K = 2$ provides the best performance and an increase in K introduces a degradation in the system performance for the proposed NOMA since interference between UEs becomes more dramatic. For $K = 2$ and 3, it can be seen that NOMA scheme outperforms OMA for all UEs. Additionally, for $K = 4$, NOMA outperforms OMA for P_t values less than 30 dBm due to lower modulation order. However, for P_t values greater than approximately 30 dBm, NOMA shows worse error performance than OMA since interference causes an error floor in BER curve.

In Fig. 7.11, the effect of imperfect channel knowledge at RIS over error perfor-

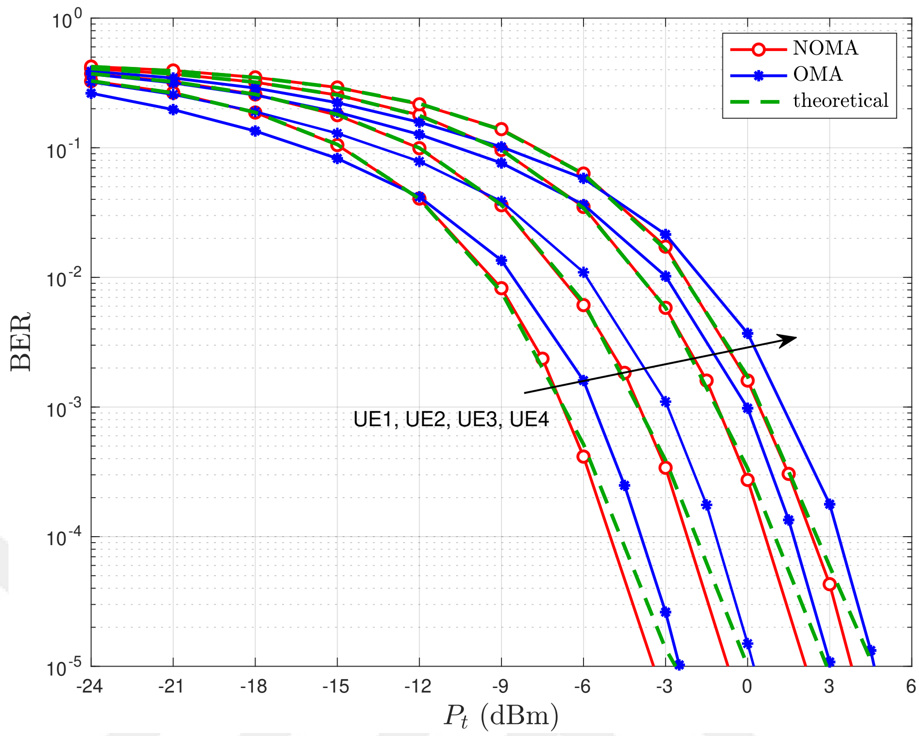

Figure 7.9: BER performance comparison of the proposed DL-NOMA and OMA schemes for $N = 1024$, $K = 4$, and 1 bps/Hz.

mance is investigated for DL NOMA scheme for 3 bps/Hz, $N = 256$ and $K = 2$. Note that M is selected as 8 and 8^K for NOMA and OMA, respectively. In order to model the imperfect channel estimation, θ_n is obtained by using $\hat{\phi}_n$ and $\hat{\psi}_{n,k}$ instead of ϕ_n and $\psi_{n,k}$, where $\hat{\phi}_n = \angle\hat{h}_n$, $\hat{\psi}_{n,k} = \angle\hat{g}_{n,k}$, $\hat{h}_n = h_n - \epsilon_h$, $\hat{g}_{n,k} = g_{n,k} - \epsilon_g$, $\epsilon_h \sim \mathcal{CN}\left(0, \zeta\sigma_h^2\right)$, and $\epsilon_g \sim \mathcal{CN}\left(0, \zeta\sigma_{g_k}^2\right)$. The BER simulations in Fig. 7.11 have been realized under $\zeta = 0.05$, $\zeta = 0.02$ and perfect CSI ($\zeta = 0$). It can seen from Fig. 7.11 that channel estimation errors impact the benchmark scheme more dramatically compared to the proposed scheme. Additionally, NOMA scheme outperforms OMA for all cases.

In Fig. 7.12, the outage probability performance is investigated for the two most distant UEs (UE1 and UE4) when $N^{(1)}$ is increased from 1 to $N-1$ with an increment of 1, where $N = 200$ and $P_t = 10$ dBm. As seen from Fig. 7.12, $N^{(1)}$ is obtained as 92 which minimizes $\left|P_{\text{out}}^{(1)} - P_{\text{out}}^{(4)}\right|$, where $N^{(4)} = N - N^{(1)} = 108$. From the fairness perspective, since UE1 is closer to the BS and has better channel conditions

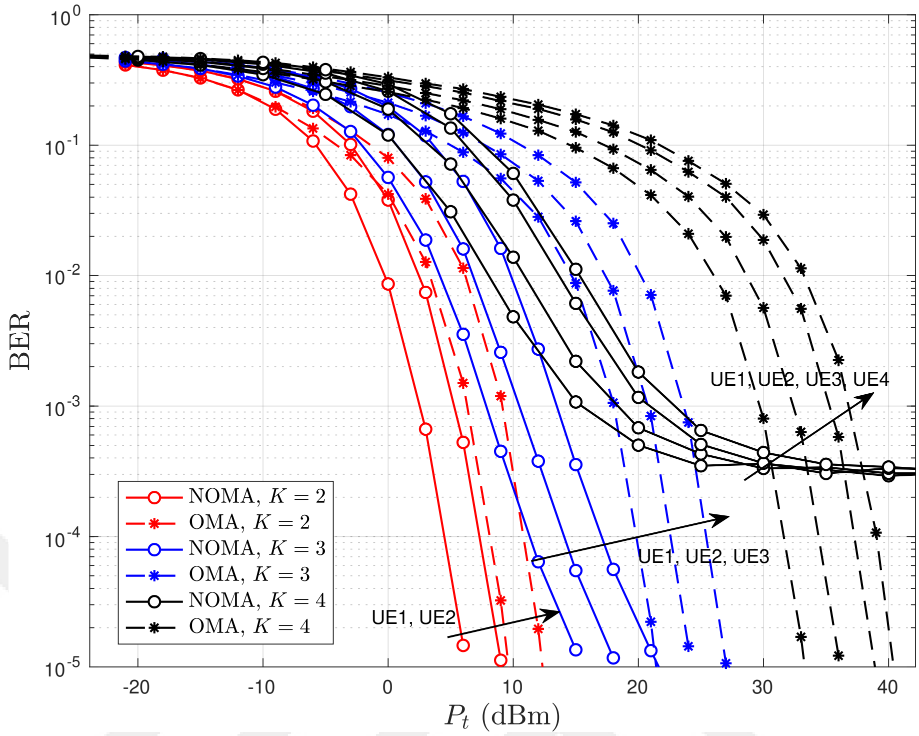

Figure 7.10: BER performance comparison of the proposed DL-NOMA and OMA schemes for $N = 256$, 2 bps/Hz, and varying number of UEs (K).

and UE4 is further to the BS with worse channel conditions, it makes sense to allocate more RIS elements to UE4. This is also confirmed with the proposed sub-optimal algorithm and we can see this in Fig. 7.13, where we present the the outage probability performance comparison for the scenarios where RIS has uniform and sub-optimal partitioning for $K = 2$, $N = 200$, and $R_k = 2$ bps/Hz. $N^{(1)}$ is selected as 92 as in 7.13. As we can observe, the performance of UE4 significantly improves which there is a trade-off from the performance of UE1. Most importantly, we can observe that the outage probability curves reach closer together for both UEs hence, providing a more fair system and RIS element partitioning.

7.5 Conclusion

In this chapter, we have proposed a novel OTA DL NOMA scheme with the aid of an passive RIS. In addition, a thorough theoretical analysis considering outage

Table 7.2: Fitted Gamma Distribution Parameters for Different UEs and Varying P_t.

UE	P_t (dB):	-24	-21	-18	-15	-12	-9	-6	-3	0
	κ	102.558	102.762	102.741	101.213	94.963	79.924	52.903	27.465	12.893
UE 1	ρ	0.0009746	0.001937	0.0038528	0.0077486	0.0162433	0.03749	0.107683	0.38155	1.42646
	κ	103.181	102.873	102.771	102.713	100.714	94.803	78.058	50.728	25.909
UE 2	ρ	0.00051472	0.00102934	0.00205164	0.00407926	0.00823733	0.0172064	0.0405408	0.118369	0.424852
	κ	103.448	103.288	103.323	102.947	102.796	100.473	95.084	77.188	49.051
UE 3	ρ	0.00026515	0.000529542	0.00105591	0.00210947	0.00419777	0.00850284	0.0176538	0.0421751	0.125799
	κ	103.151	103.293	102.924	103.789	103.372	101.781	98.843	87.664	64.441
UE 4	ρ	0.00018594	0.000370327	0.000740912	0.00146360	0.00292481	0.00589186	0.0119778	0.0263828	0.06889412

probability and BER is presented along with computer simulation results and each are discussed along with a benchmark comparison. Furthermore, additional analysis such as sum-rate and consideration of imperfect CSI conditions are included. While the NOMA process is conventionally conducted at the BS or UEs, the proposed system enables NOMA through the RIS and virtually enabling the NOMA process OTA. Furthermore, SIC is a major concern in most NOMA systems where errors in SIC reduce the system performance and the entire SIC process uses energy and increases complexity of the system. However, in the proposed system, SIC is not required hence reducing complexity at the UEs and BS and reduces the possibility of SIC errors in degrading the system performance. Future works may consider the incorporation of active RIS structure, RIS element optimization, use of deep learning models, further theoretical analysis regarding different channel models such as Rician fading and much more.

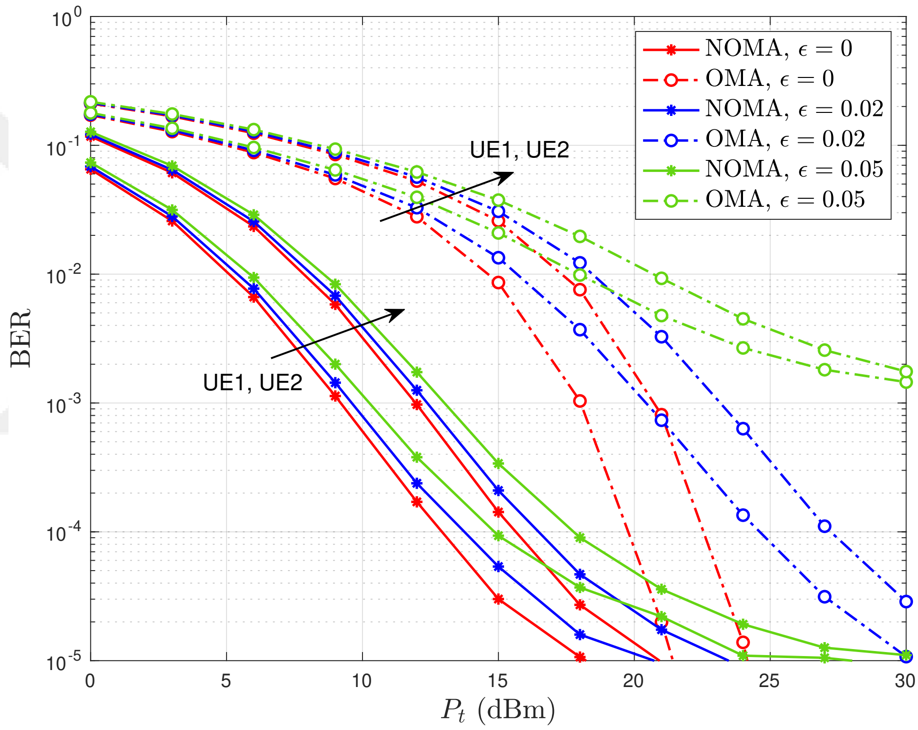

Figure 7.11: BER performance comparison of the proposed NOMA and OMA schemes under imperfect CSI knowledge for 3 bps/Hz, $N = 256$, $M = 4$, and $K = 2$.

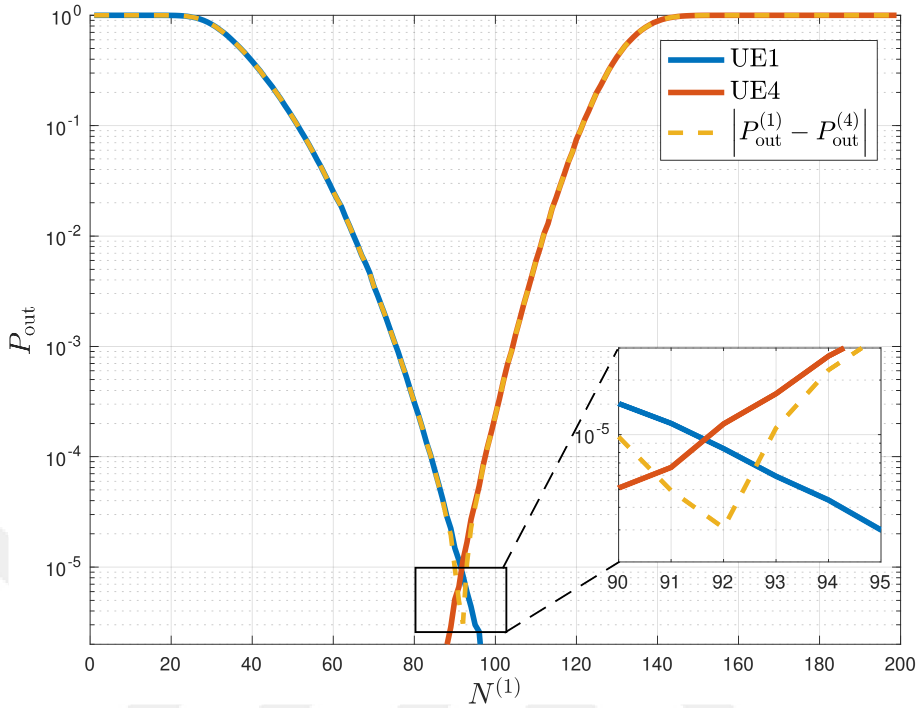

Figure 7.12: Determining the value of $N^{(1)}$ to solve (P1) for $K = 2$, $P_t = 10$ dBm, and $N = 200$.

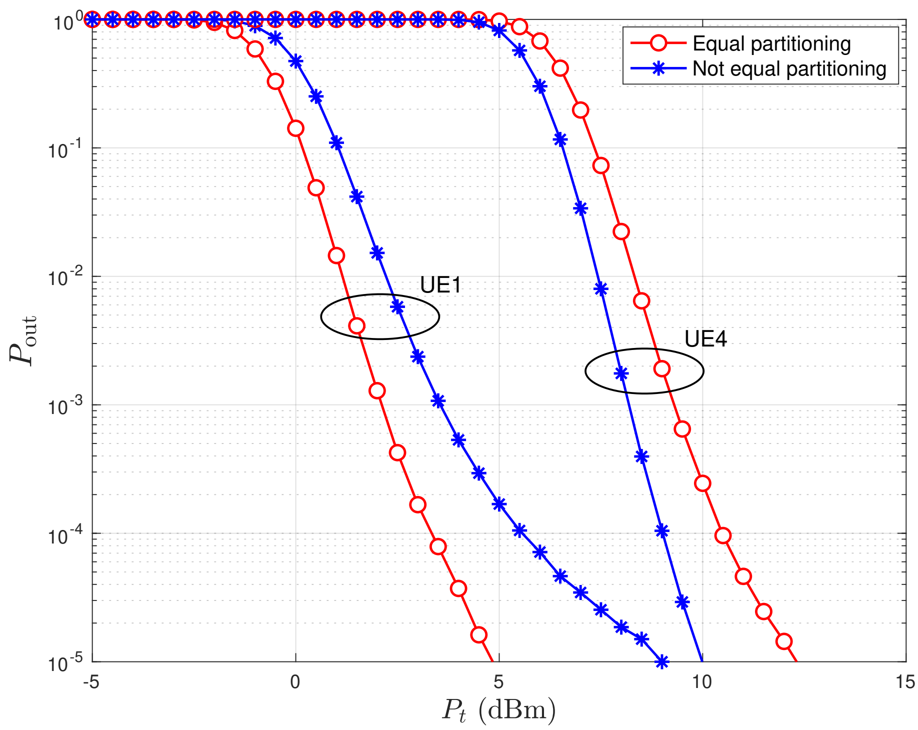

Figure 7.13: Outage probability performance comparison of equal partitioning and not equal partitioning with $N^{(1)} = 92$ for $K = 2$, $N = 200$, and $R_k = 2$ bps/Hz.

Chapter 8

CONCLUSION

This thesis explored sophisticated transmission schemes employing IM, RIS, and their integration with complementing technologies such as OFDM and NOMA to improve the efficiency of wireless communication networks. The main goal was to devise novel solutions that enhance spectral efficiency, bit error rate performance, and system reliability while ensuring low complexity, which are essential requirements for next-generation wireless networks, especially 6G. The presented methods tackle numerous aspects of IM, RIS, OFDM, and NOMA-based communication, highlighting innovative system designs, thorough performance evaluations, and practical viability for real-world application.

8.1 Summary of Contributions

In this thesis, we have made significant contributions across several key areas:

Chapter 2: A novel diversity-achieving OFDM-IM-based transmission scheme called CI-OFDM-IQIM was proposed. This scheme improves system reliability by dividing subblocks into clusters and transmitting real and imaginary parts of data symbols over active subcarriers, achieving superior error performance. The LLR-based detector was designed to reduce decoding complexity, making the scheme well-suited for high spectral efficiency communication systems.

Chapter 3: The RIS-ERSM scheme was introduced, leveraging RIS to enhance spectral efficiency and reliability. By exploiting flexible receive antenna combinations and M-ary modulation, RIS-ERSM outperforms benchmark systems in terms of error performance. This makes it a promising candidate for future wireless communication networks, particularly in scenarios demanding high reliability.

Chapter 4: The RIS-CIM-QRSM scheme was presented, combining quadrature

SM (QRSM) with CIM and RIS partitioning to enhance error performance and energy efficiency. The scheme improved the minimum Euclidean distance, significantly boosting system reliability. ML and low-complexity detectors were introduced, providing a practical solution for reducing computational burden. The simulation results confirmed that RIS-CIM-QRSM outperforms existing schemes.

Chapter 5: Two novel Hyb-ERM schemes were proposed, utilizing hybrid-RIS technology to improve spectral efficiency and BER performance. The use of controllable phase shifters and amplifiers mitigated fading and improved transmission reliability. Extensive analysis demonstrated that Hyb-ERM outperforms traditional hybrid RIS and fully-active RIS systems. The introduction of low-complexity detectors further enhanced the scheme's practicality for real-world applications, particularly for 6G systems.

Chapter 6: The E-OTA-RIS-IM scheme was proposed, which leverages RIS's dynamic capabilities to enhance both spectral efficiency and BER performance. By partitioning the RIS into groups with adjustable states, additional IM bits were transmitted OTA, further improving the system's performance in terms of both throughput and reliability.

Chapter 7: A novel DL OTA NOMA scheme using passive RIS was introduced, addressing key limitations in conventional NOMA systems. The scheme eliminated the need for SIC at UE and the BS, reducing complexity and improving system efficiency. Through thorough theoretical analysis and extensive simulations, the scheme demonstrated superior performance compared to conventional RIS-based OMA systems.

8.2 Key Findings

The key findings of this research include:

The proposed schemes, including CI-OFDM-IQIM, RIS-ERSM, RIS-CIM-QRSM, and others, consistently demonstrated improvements in spectral efficiency and BER performance, especially under high spectral efficiency values, without significantly increasing system complexity.

The integration of RIS with IM techniques, particularly in hybrid configurations and OTA modulation schemes, provided a substantial enhancement to system performance. This integration was particularly effective in scenarios involving high interference or complex channel conditions.

The introduction of low-complexity detectors for several schemes (such as in RIS-CIM-QRSM and Hyb-ERM) demonstrated that high-performance systems could be achieved without the computational overhead typically associated with ML detectors, making these schemes more suitable for practical implementation.

The passive RIS-based NOMA scheme in Chapter 7 successfully eliminated the need for SIC, reducing system complexity and minimizing interference errors. This highlights the potential of RIS to facilitate more efficient NOMA systems, particularly for 6G networks, where the number of users and interference levels are expected to be higher.

8.3 Implications for Future Wireless Communication Systems

This thesis's findings have important value for the design of forthcoming wireless communication systems, especially regarding 6G. The proposed approaches exhibit scalability, effectively managing the growing number of users as well as various service demands in 6G networks, ranging from low-power IoT devices to high-bandwidth applications such as VR and AR. The decrease in computational complexity, attained by employing low-complexity detectors and eliminating SIC in the NOMA framework, renders these solutions feasible for mobile settings with constrained processing capabilities. Moreover, the capacity to improve performance in fading, interference-constrained, and high-traffic conditions confirms their suitability for practical applications. RIS-based methodologies provide flexibility to diverse channel conditions and user distribution patterns, while their passive characteristics enhance energy efficiency, a crucial factor for sustainable 6G networks.

8.4 Future Directions

This thesis has introduced various innovative ideas and contributions; yet, many opportunities for further research exist. Expanding the proposed RIS-based systems to MIMO systems may improve performance in high data rate and extensive connectivity situations. Investigating dynamic channel models, including Rician fading, shadowing, and mobility-induced fluctuations, would yield insights into the adaptability of these systems in real-world settings. Integrating active RIS components may enhance performance by providing extra degrees of freedom in signal manipulation, facilitating improved beamforming and interference management. The utilization of deep learning for RIS optimization, encompassing power allocation and beamforming techniques, may result in adaptable, self-optimizing RIS systems capable of real-time modifications. Optimizing the deployment and segmentation of RIS in extensive networks, while accounting for mobility and user density, continues to be a significant problem at the network level. The collaboration between RIS and NOMA in intricate situations, like URLLC and vehicle-to-everything (V2X) networks, presents considerable promise for the progression of next-generation wireless systems.

8.5 Conclusion

This thesis has presented a series of innovative communication schemes that leverage the capabilities of IM, RIS, and their integration with complementary technologies such as OFDM and NOMA to enhance the performance of wireless communication systems. Through detailed theoretical analysis, extensive simulations, and performance comparisons, it has been demonstrated that the proposed schemes significantly improve spectral efficiency, BER performance, and system reliability. The exploration of RIS, IM, OFDM, and NOMA provides a promising pathway for the design of future wireless networks, particularly 6G, where scalability, energy efficiency, and robust performance are paramount. The findings of this research contribute to both the academic understanding of these advanced technologies and offer practical, implementable solutions for next-generation communication systems.

8.6 Publications Derived from This Thesis

The following research papers have been published or submitted for publication as a result of the work conducted in this thesis:

1. O. F. Tugtekin, A. T. Dogukan, E. Arslan, and E. Basar, ”Coordinate interleaved OFDM with repeated in-phase/quadrature index modulation,” IEEE Trans. Wireless Commun., vol. 23, no. 1, pp. 117–127, May 2024, doi: 10.1109/TWC.2023.3276178.

2. A. T. Dogukan, E. Arslan, M. E. Pihtili, and E. Basar, ”RIS-aided enhanced receive spatial modulation,” IEEE Wireless Commun. Lett., vol. –, no. –, pp. 1–1, Nov. 2024, doi: 10.1109/LWC.2024.3491999.

3. Ali Tugberk Dogukan, Emre Arslan, and Ertugrul Basar, ”Reconfigurable Intelligent Surface Code Index Modulation With Quadrature Receive Spatial Modulation,” Submitted to IEEE Trans. Green Commun. Netw.

4. A. T. Dogukan, E. Arslan, F. Kilinc, E. Demircioglu, and E. Basar, ”Hybrid reconfigurable intelligent surface-enabled enhanced reflection modulation,” IEEE Trans. Wireless Commun., vol. 23, no. 12, pp. 18929–18939, Sep. 2024, doi: 10.1109/TWC.2024.3462794.

5. E. Arslan, A. T. Dogukan, F. Kilinc, and E. Basar, ”Hybrid reconfigurable intelligent surface enabled over-the-air index-modulation,” in Proc. 2024 6th Int. Conf. Commun., Signal Process. Appl. (ICCSPA), Jul. 2024, pp. 1–6, doi: 10.1109/ICCSPA61559.2024.10794231.

6. A. T. Dogukan, E. Arslan, and E. Basar, ”Reconfigurable intelligent surface-enabled downlink NOMA,” IEEE Trans. Wireless Commun., vol. 23, no. 11, pp. 16950–16961, Aug. 2024, doi: 10.1109/TWC.2024.3448246.

BIBLIOGRAPHY

[38.104, 2019] 38.104, G. T. (2019). NR; base station (BS) radio transmission and reception.

[Al-Ali and Yaacoub, 2023] Al-Ali, M. and Yaacoub, E. (2023). Resource allocation scheme for eMBB and uRLLC coexistence in 6G networks. *Wireless Networks*, pages 1–20.

[Alayasra and Arslan, 2022] Alayasra, M. and Arslan, H. (2022). IRS-enabled beam-space channel. *IEEE Trans. Wireless Commun.*, 21(6):3822–3835.

[Albinsaid et al., 2021] Albinsaid, H., Singh, K., Bansal, A., Biswas, S., Li, C.-P., and Haas, Z. J. (2021). Multiple antenna selection and successive signal detection for SM-based IRS-aided communication. *IEEE Signal Process. Lett.*, 28:813–817.

[Aldababsa et al., 2023] Aldababsa, M., Khaleel, A., and Basar, E. (2023). Simultaneous transmitting and reflecting reconfigurable intelligent surfaces-empowered NOMA networks. *IEEE Syst. J.*

[Ali et al., 2016] Ali, M. S., Tabassum, H., and Hossain, E. (2016). Dynamic user clustering and power allocation for uplink and downlink non-orthogonal multiple access (NOMA) systems. *IEEE Access*, 4:6325–6343.

[Araghi et al., 2022] Araghi, A., Khalily, M., Safaei, M., Bagheri, A., Singh, V., Wang, F., and Tafazolli, R. (2022). Reconfigurable intelligent surface (RIS) in the sub-6 GHz band: Design, implementation, and real-world demonstration. *IEEE Access*, 10:2646–2655.

[Arslan et al., 2020b] Arslan, E., Dogukan, A. T., and Basar, E. (2020b). Index modulation-based flexible non-orthogonal multiple access. *IEEE Wireless Commun. Lett.*, 9(11):1942–1946.

[Arslan et al., 2020c] Arslan, E., Dogukan, A. T., and Basar, E. (2020c). Sparse-encoded codebook index modulation. *IEEE Trans. Veh. Technol.*, 69(8):9126–9130.

[Arslan et al., 2020a] Arslan, E., Dogukan, A. T., and Basar, E. (Nov. 2020a). Index modulation-based flexible non-orthogonal multiple access. *IEEE Wireless Commun. Lett.*, 9(11):1942–1946.

[Arslan et al., 2024] Arslan, E., Dogukan, A. T., Kilinc, F., and Basar, E. (2024). Hybrid reconfigurable intelligent surface enabled over the air index modulation. *arXiv preprint arXiv:2407.08985*.

[Arslan et al., 2022a] Arslan, E., Kilinc, F., Arzykulov, S., Dogukan, A. T., Celik, A., Basar, E., and Eltawil, A. M. (2022a). Reconfigurable intelligent surface enabled over-the-air uplink NOMA. *IEEE Trans. Green Commun. Netw.*

[Arslan et al., 2023] Arslan, E., Kilinc, F., Basar, E., and Arslan, H. (2023). Network-independent and user-controlled RIS: An experimental perspective. In *Proc. 26th Int. Symp. Wireless Pers. Multimedia Commun. (WPMC)*, pages 1–6. IEEE.

[Arslan et al., 2022b] Arslan, E., Yildirim, I., Kilinc, F., and Basar, E. (2022b). Over-the-air equalization with reconfigurable intelligent surfaces. *IET Commun.*, 16(13):1486–1497.

[Arzykulov et al., 2023] Arzykulov, S., Celik, A., Nauryzbayev, G., and Eltawil, A. M. (2023). Artificial noise and RIS-aided physical layer security: Optimal RIS partitioning and power control. *IEEE Wireless Commun. Lett.*

[Asmoro and Shin, 2022] Asmoro, K. and Shin, S. Y. (2022). RIS grouping based index modulation for 6G telecommunications. *IEEE Wireless Commun. Lett.*, 11(11):2410–2414.

[Azim et al., 2020] Azim, A. W., Le Guennec, Y., Chafii, M., and Ros, L. (July 2020). Enhanced optical-OFDM with index and dual-mode modulation for optical wireless systems. *IEEE Access*, 8:128646–128664.

[Bariah et al., 2023] Bariah, L., Boukhalfa, F., Jaafar, W., Muhaidat, S., and Yanikomeroglu, H. (2023). On the performance of RIS-enabled NOMA for aerial networks. In *Proc. 2023 IEEE Wireless Commun. Netw. Conf. (WCNC)*, pages 1–6. IEEE.

[Basar, 2016a] Basar, E. (2016a). Index modulation techniques for 5G wireless networks. *IEEE Commun. Mag.*, 54(7):168–175.

[Basar, 2019] Basar, E. (2019). Transmission through large intelligent surfaces: A new frontier in wireless communications. In *2019 European Conference on Networks and Communications (EuCNC)*, pages 112–117. IEEE.

[Basar, 2020] Basar, E. (2020). Reconfigurable intelligent surface-based index modulation: A new beyond MIMO paradigm for 6G. *IEEE Trans. Commun.*, 68(5):3187–3196.

[Başar, 2015] Başar, E. (Aug. 2015). OFDM with index modulation using coordinate interleaving. *IEEE Wireless Commun. Lett.*, 4(4):381–384.

[Basar, 2016b] Basar, E. (Aug. 2016b). On multiple-input multiple-output OFDM with index modulation for next generation wireless networks. *IEEE Trans. Signal Process.*, 64(15):3868–3878.

[Basar et al., 2023] Basar, E., Alexandropoulos, G. C., Liu, Y., Wu, Q., Jin, S., Yuen, C., Dobre, O. A., and Schober, R. (2023). Reconfigurable intelligent surfaces for 6G: Emerging hardware architectures, applications, and open challenges. *arXiv preprint arXiv:2312.16874*. (to appear in IEEE Veh. Technol. Mag.).

[Başar et al., 2013] Başar, E., Aygölü, Ü., Panayırcı, E., and Poor, H. V. (2013). Orthogonal frequency division multiplexing with index modulation. *IEEE Trans. Signal Process.*, 61(22):5536–5549.

[Basar et al., 2019] Basar, E., Di Renzo, M., De Rosny, J., Debbah, M., Alouini, M.-S., and Zhang, R. (2019). Wireless communications through reconfigurable intelligent surfaces. *IEEE access*, 7:116753–116773.

[Başar and Panayırcı, 2015] Başar, E. and Panayırcı, E. (Sep. 2015). Optical OFDM with index modulation for visible light communications. In *Proc. IEEE Int. Workshops Opt. Wireless Commun.*, pages 11–15. IEEE.

[Basar et al., 2017] Basar, E., Wen, M., Mesleh, R., Di Renzo, M., Xiao, Y., and Haas, H. (2017). Index modulation techniques for next-generation wireless networks. *IEEE access*, 5:16693–16746.

[Björnson and Sanguinetti, 2020] Björnson, E. and Sanguinetti, L. (2020). Rayleigh fading modeling and channel hardening for reconfigurable intelligent surfaces. *IEEE Wireless Commun. Lett.*, 10(4):830–834.

[Chauhan et al., 2022] Chauhan, A., Ghosh, S., and Jaiswal, A. (2022). RIS partition-assisted non-orthogonal multiple access (NOMA) and quadrature-NOMA with imperfect SIC. *IEEE Trans. Wireless Commun.*

[Chen et al., 2022] Chen, G., Wu, Q., He, C., Chen, W., Tang, J., and Jin, S. (2022). Active IRS aided multiple access for energy-constrained IoT systems. *IEEE Trans. Wireless Commun.*, 22(3):1677–1694.

[Chen and Zheng, 2018] Chen, R. and Zheng, J. (Oct. 2018). Index-modulated MIMO-OFDM: Joint space-frequency signal design and linear precoding in rapidly time-varying channels. *IEEE Trans. Wireless Commun.*, 17(10):7067–7079.

[Chen et al., 2020] Chen, X., Wen, M., and Dang, S. (Sept. 2020). On the performance of cooperative OFDM-NOMA system with index modulation. *IEEE Wireless Commun. Lett.*, 9(9):1346–1350.

[Cheng et al., 2018] Cheng, X., Zhang, M., Wen, M., and Yang, L. (2018). Index modulation for 5G: Striving to do more with less. *IEEE Wirel. Commun.*, 25(2):126–132.

[Chiani et al., 2003] Chiani, M., Dardari, D., and Simon, M. K. (2003). New exponential bounds and approximations for the computation of error probability in fading channels. *IEEE Trans. Wireless Commun.*, 2(4):840–845.

[Choi, 2017] Choi, J. (July 2017). Coded OFDM-IM with transmit diversity. *IEEE Trans. Commun.*, 65(7):3164–3171.

[Cogen et al., 2024] Cogen, F., Ozden, B. A., Aydin, E., and Kabaoglu, N. (2024). Reconfigurable intelligent surface-empowered code index modulation for high-rate SISO systems. *Trans. on Cogn. Commun. Netw.*

[Dai et al., 2018] Dai, L., Wang, B., Ding, Z., Wang, Z., Chen, S., and Hanzo, L. (2018). A survey of non-orthogonal multiple access for 5G. *IEEE commun. surveys & tutorials*, 20(3):2294–2323.

[Dang et al., 2020] Dang, S., Amin, O., Shihada, B., and Alouini, M.-S. (2020). What should 6G be? *Nature Electron.*, 3(1):20–29.

[Dash et al., 2022] Dash, S. P., Mallik, R. K., and Pandey, N. (2022). Performance analysis of an index modulation-based receive diversity RIS-assisted wireless communication system. *IEEE Commun. Lett.*, 26(4):768–772.

[De Alwis et al., 2021] De Alwis, C., Kalla, A., Pham, Q.-V., Kumar, P., Dev, K., Hwang, W.-J., and Liyanage, M. (2021). Survey on 6G frontiers: Trends, applications, requirements, technologies and future research. *IEEE Open J. Commun. Soc.*, 2:836–886.

[Department, 2023] Department, S. R. (2023). Global mobile subscriptions since 1993. Accessed: 2023-12-20.

[Dinan et al., 2022] Dinan, M. H., Perović, N. S., and Flanagan, M. F. (2022). RIS-assisted receive quadrature space-shift keying: A new paradigm and performance analysis. *IEEE Trans. Commun.*, 70(10):6874–6889.

[Ding et al., 2020] Ding, Z., Schober, R., and Poor, H. V. (2020). Unveiling the importance of SIC in NOMA systems—part 1: State of the art and recent findings. *IEEE Commun. Lett.*, 24(11):2373–2377.

[Doğan et al., 2019] Doğan, S., Tusha, A., and Arslan, H. (Oct. 2019). NOMA with index modulation for uplink URLLC through grant-free access. *IEEE J. Sel. Topics Signal Process.*, 13(6):1249–1257.

[Dogukan and Basar, 2020a] Dogukan, A. and Basar, E. (Oct. 2020a). Orthogonal frequency division multiplexing with power distribution index modulation. *Electron. Lett*, 56(21):1156–1159.

[Dogukan et al., 2024a] Dogukan, A. T., Arslan, E., and Basar, E. (2024a). Reconfigurable intelligent surface-enabled downlink NOMA. *arXiv preprint arXiv:2401.04430*.

[Dogukan et al., 2024b] Dogukan, A. T., Arslan, E., Kilinc, F., Demircioglu, E., and Basar, E. (2024b). Hybrid reconfigurable intelligent surface-enabled enhanced reflection modulation. *IEEE Trans. Wireless Commun.*, pages 1–1.

[Dogukan et al., 2024c] Dogukan, A. T., Arslan, E., Pihtili, M. E., and Basar, E. (2024c). RIS-aided enhanced receive spatial modulation. *IEEE Wireless Commun. Lett.*

[Dogukan and Basar, 2020b] Dogukan, A. T. and Basar, E. (2020b). Super-mode OFDM with index modulation. *IEEE Trans. Wireless Commun.*, 19(11):7353–7362.

[Dogukan et al., 2022] Dogukan, A. T., Tugtekin, O. F., and Basar, E. (2022). Coordinate interleaved OFDM with power distribution index modulation. *IEEE Commun. Lett.*, 26(8):1908–1912.

[Dong et al., 2021] Dong, L., Wang, H.-M., and Bai, J. (2021). Active reconfigurable intelligent surface aided secure transmission. *IEEE Trans. Veh. Technol.*, 71(2):2181–2186.

[Electronics, 2015] Electronics, S. (2015). Samsung 5g vision. Technical report, Samsung Electronics. Accessed: 2023-12-20.

[ElMossallamy et al., 2020] ElMossallamy, M. A., Zhang, H., Song, L., Seddik, K. G., Han, Z., and Li, G. Y. (2020). Reconfigurable intelligent surfaces for wireless communications: Principles, challenges, and opportunities. *Trans. on Cogn. Commun. Netw.*, 6(3):990–1002.

[Elzanaty et al., 2021] Elzanaty, A., Guerra, A., Guidi, F., and Alouini, M.-S. (2021). Reconfigurable intelligent surfaces for localization: Position and orientation error bounds. *IEEE Trans. Signal Process.*, 69:5386–5402.

[Fan et al., 2014] Fan, R., Yu, Y. J., and Guan, Y. L. (Dec. 2014). Orthogonal frequency division multiplexing with generalized index modulation. In *Proc. IEEE Glob. Commun. Conf.*, pages 3880–3885. IEEE.

[Feng and Li, 2023] Feng, Y. and Li, Q. (2023). Enhanced reconfigurable intelligent surface-aided amplitude phase shift keying. In *2023 Int. Conf. Wireless Commun. Signal Process. (WCSP)*, pages 1197–1202. IEEE.

[Ferdi and Hakan, 2020] Ferdi, K. and Hakan, K. (2020). Error probability analysis of non-orthogonal multiple access with channel estimation errors. In *2020 Proc. IEEE Int. Black Sea Conf. Commun. Netw. (BlackSeaCom)*, pages 1–5. IEEE.

[Fu et al., 2021] Fu, M., Zhou, Y., Shi, Y., and Letaief, K. B. (2021). Reconfigurable intelligent surface empowered downlink non-orthogonal multiple access. *IEEE Trans. on Commun.*, 69(6):3802–3817.

[Gao et al., 2023] Gao, Q., Liu, Y., Mu, X., Jia, M., Li, D., and Hanzo, L. (2023). Joint location and beamforming design for STAR-RIS assisted NOMA systems. *IEEE Trans. Commun.*, 71(4):2532–2546.

[Giordani et al., 2020] Giordani, M., Polese, M., Mezzavilla, M., Rangan, S., and Zorzi, M. (2020). Toward 6G networks: Use cases and technologies. *IEEE Commun. Mag.*, 58(3):55–61.

[Guo et al., 2020] Guo, S., Lv, S., Zhang, H., Ye, J., and Zhang, P. (2020). Reflecting modulation. *IEEE J. Sel. Areas Commun.*, 38(11):2548–2561.

[Hakak et al., 2023] Hakak, S., Gadekallu, T. R., Maddikunta, P. K. R., Ramu, S. P., Parimala, M., De Alwis, C., and Liyanage, M. (2023). Autonomous vehicles in 5g and beyond: A survey. *Vehicular Communications*, 39:100551.

[Huang et al., 2019a] Huang, C., Alexandropoulos, G. C., Yuen, C., and Debbah, M. (2019a). Indoor signal focusing with deep learning designed reconfigurable intelligent surfaces. In *IEEE Workshop Signal Process. Adv. Wirel. Commun. (SPAWC).*, pages 1–5. IEEE.

[Huang et al., 2020] Huang, C., Hu, S., Alexandropoulos, G. C., Zappone, A., Yuen, C., Zhang, R., Di Renzo, M., and Debbah, M. (2020). Holographic MIMO surfaces for 6G wireless networks: Opportunities, challenges, and trends. *IEEE Wireless Commun.*, 27(5):118–125.

[Huang et al., 2019b] Huang, C., Zappone, A., Alexandropoulos, G. C., Debbah, M., and Yuen, C. (2019b). Reconfigurable intelligent surfaces for energy efficiency in wireless communication. *IEEE Trans. Wireless Commun.*, 18(8):4157–4170.

[Ibrahim et al., 2021] Ibrahim, H., Tabassum, H., and Nguyen, U. T. (2021). Exact coverage analysis of intelligent reflecting surfaces with nakagami-m channels. *IEEE Trans. Veh. Technol.*, 70(1):1072–1076.

[Jaradat et al., 2018] Jaradat, A. M., Hamamreh, J. M., and Arslan, H. (2018). OFDM with subcarrier number modulation. *IEEE Wireless Commun. Lett.*, 7(6):914–917.

[Jaradat et al., 2020] Jaradat, A. M., Hamamreh, J. M., and Arslan, H. (Mar. 2020). OFDM with hybrid number and index modulation. *IEEE Access*, 8:55042–55053.

[Jiang et al., 2021] Jiang, W., Han, B., Habibi, M. A., and Schotten, H. D. (2021). The road towards 6G: A comprehensive survey. *IEEE Open J. Commun. Soc.*, 2:334–366.

[Jin et al., 2024] Jin, J., Jin, X., Wen, M., Song, M., Huang, C., and Yao, Y. (2024). Active fully-connected RIS based on index modulation for high rate and energy-efficient systems. *IEEE Trans. Commun.*

[Jin et al., 2023] Jin, X., Bian, L., Li, Z., Xing, S., and Wen, M. (2023). A novel RIS-aided code index modulation scheme with low-complexity detection. *IEEE Trans. Veh. Technol.*, 72(11):14279–14288.

[Kaddoum et al., 2014] Kaddoum, G., Ahmed, M. F., and Nijsure, Y. (2014). Code index modulation: A high data rate and energy efficient communication system. *IEEE Commun. Lett.*, 19(2):175–178.

[Kang et al., 2023] Kang, Z., You, C., and Zhang, R. (2023). Active-passive IRS aided wireless communication: New hybrid architecture and elements allocation optimization. *IEEE Trans. Wireless Commun.*

[Kara and Kaya, 2018] Kara, F. and Kaya, H. (2018). BER performances of downlink and uplink NOMA in the presence of SIC errors over fading channels. *IET Commun.*, 12(15):1834–1844.

[Kara and Kaya, 2019] Kara, F. and Kaya, H. (2019). Performance analysis of SSK-NOMA. *IEEE Trans. Veh. Technol.*, 68(7):6231–6242.

[Kayraklık et al., 2023] Kayraklık, S., Yildirim, I., Gevez, Y., Basar, E., and Görçin, A. (2023). Indoor coverage enhancement for RIS-assisted communication systems: Practical measurements and efficient grouping. In *Proc. 2023 Int. Conf. Commun. (ICC)*. IEEE.

[Khaleel and Basar, 2020] Khaleel, A. and Basar, E. (2020). Reconfigurable intelligent surface-empowered MIMO systems. *IEEE Syst. J.*, 15(3):4358–4366.

[Khaleel and Basar, 2021] Khaleel, A. and Basar, E. (2021). A novel NOMA solution with RIS partitioning. *IEEE J. Sel. Topics Signal Process.*, 16(1):70–81.

[Khan and Rajan, 2006] Khan, M. Z. and Rajan, B. S. (May 2006). Single-symbol maximum likelihood decodable linear STBCs. *IEEE Trans. Inf. Theory*, 52(5):2062–2091.

[Khoshafa et al., 2024] Khoshafa, M. H., Maraqa, O., Moualeu, J. M., Aboagye, S., Ngatched, T. M., Ahmed, M. H., Gadallah, Y., and Di Renzo, M. (2024). RIS-assisted physical layer security in emerging RF and optical wireless communication systems: A comprehensive survey. *IEEE Commun. Surveys Tuts.*

[Kilinc et al., 2023] Kilinc, F., Tasci, R. A., Celik, A., Abdallah, A., Eltawil, A. M., and Basar, E. (2023). RIS-assisted grant-free NOMA: User pairing, RIS assignment, and phase shift alignment. *Trans. on Cogn. Commun. Netw.*, 9(5):1257–1270.

[Kilinc et al., 2021] Kilinc, F., Yildirim, I., and Basar, E. (2021). Physical channel modeling for RIS-empowered wireless networks in sub-6 GHz bands. In *Proc. 55th Asilomar Conf. Signals, Syst., Comput.*, pages 704–708.

[Kumar et al., 2023] Kumar, M. H., Sharma, S., Deka, K., and Sharma, M. K. (2023). RIS-assisted user pairing NOMA system for THz communications. In *Proc. 2023 Nat. Conf. Commun. (NCC)*, pages 1–6. IEEE.

[Kurt et al., 2023] Kurt, M. A., Dogukan, A. T., and Basar, E. (2023). Spatial modulation using signal space diversity. *IEEE Commun. Lett.*, 27(3):1020–1024.

[Le et al., 2021] Le, T. T. H., Tran, X. N., Ngo, V.-D., and Le, M.-T. (Sept. 2021). Repeated index modulation-OFDM with coordinate interleaving: Performance optimization and low-complexity detectors. *IEEE Syst. J.*, 15(3):3673–3681.

[Lee et al., 1979] Lee, R.-Y., Holland, B. S., and Flueck, J. A. (1979). Distribution of a ratio of correlated gamma random variables. *SIAM J. Appl. Math*, 36(2):304–320.

[Li et al., 2021a] Li, G., Liu, H., Huang, G., Li, X., Raj, B., and Kara, F. (2021a). Effective capacity analysis of reconfigurable intelligent surfaces aided NOMA network. *EURASIP J. Wireless Commun. Netw.*, 2021:1–16.

[Li et al., 2019] Li, J., Dang, S., Wen, M., Jiang, X.-Q., Peng, Y., and Hai, H. (2019). Layered orthogonal frequency division multiplexing with index modulation. *IEEE Syst. J.*, 13(4):3793–3802.

[Li et al., 2023] Li, Q., Bai, S., Wen, M., and Huang, D. (2023). RIS-based code index modulation for joint active/passive transmission. *IEEE Trans. Veh. Technol.*

[Li et al., 2018] Li, Q., Wen, M., Basar, E., and Chen, F. (2018). Index modulated OFDM spread spectrum. *IEEE Trans. Wireless Commun.*, 17(4):2360–2374.

[Li et al., 2021b] Li, Q., Wen, M., and Di Renzo, M. (2021b). Single-RF MIMO: From spatial modulation to metasurface-based modulation. *IEEE Wirel. Commun.*, 28(4):88–95.

[Li et al., 2022] Li, Q., Wen, M., Xu, L., and Li, K. (2022). Reconfigurable intelligent surface-aided number modulation for symbiotic active/passive transmission. *IEEE Internet Things J.*

[Lin et al., 2021] Lin, S., Chen, F., Wen, M., Feng, Y., and Di Renzo, M. (2021). Reconfigurable intelligent surface-aided quadrature reflection modulation for simultaneous passive beamforming and information transfer. *IEEE Trans. Wireless Commun.*, 21(3):1469–1481.

[Lin et al., 2020] Lin, S., Zheng, B., Alexandropoulos, G. C., Wen, M., Di Renzo, M., and Chen, F. (2020). Reconfigurable intelligent surfaces with reflection pattern modulation: Beamforming design and performance analysis. *IEEE Trans. Wireless Commun.*, 20(2):741–754.

[Liu et al., 2023] Liu, R., Li, M., Luo, H., Liu, Q., and Swindlehurst, A. L. (2023). Integrated sensing and communication with reconfigurable intelligent surfaces: Opportunities, applications, and future directions. *IEEE Wireless Commun.*, 30(1):50–57.

[Liu et al., 2021] Liu, Y., Liu, X., Mu, X., Hou, T., Xu, J., Di Renzo, M., and Al-Dhahir, N. (2021). Reconfigurable intelligent surfaces: Principles and opportunities. *IEEE Commun. Surveys Tuts.*, 23(3):1546–1577.

[Liu and Yang, 2021] Liu, Z. and Yang, L.-L. (2021). Sparse or dense: A comparative study of code-domain NOMA systems. *IEEE Trans. Wireless Commun.*, 20(8):4768–4780.

[Long et al., 2021] Long, R., Liang, Y.-C., Pei, Y., and Larsson, E. G. (2021). Active reconfigurable intelligent surface-aided wireless communications. *IEEE Trans. Wireless Commun.*, 20(8):4962–4975.

[Lu et al., 2018] Lu, S., Hemadeh, I. A., El-Hajjar, M., and Hanzo, L. (July 2018).

Compressed-sensing-aided space-time frequency index modulation. *IEEE Trans. Veh. Technol.*, 67(7):6259–6271.

[Ma et al., 2020] Ma, T., Xiao, Y., Lei, X., Xiong, W., and Ding, Y. (2020). Indoor localization with reconfigurable intelligent surface. *IEEE Commun. Lett.*, 25(1):161–165.

[Mao et al., 2016a] Mao, T., Wang, Q., and Wang, Z. (Apr. 2016a). Generalized dual-mode index modulation aided OFDM. *IEEE Commun. Lett.*, 21(4):761–764.

[Mao et al., 2018] Mao, T., Wang, Q., Wang, Z., and Chen, S. (2018). Novel index modulation techniques: A survey. *IEEE Commun. Surveys Tuts.*, 21(1):315–348.

[Mao et al., 2016b] Mao, T., Wang, Z., Wang, Q., Chen, S., and Hanzo, L. (2016b). Dual-mode index modulation aided OFDM. *IEEE Access*, 5:50–60.

[Moon and Stirling, 1999] Moon, T. K. and Stirling, W. C. (1999). Mathematical methods and algorithms for signal processing. *New Jersey: Prentice Hall*.

[Mu et al., 2020] Mu, X., Liu, Y., Guo, L., Lin, J., and Al-Dhahir, N. (2020). Exploiting intelligent reflecting surfaces in NOMA networks: Joint beamforming optimization. *IEEE Trans. Wireless Commun.*, 19(10):6884–6898.

[Nguyen et al., 2022] Nguyen, N. T., Vu, Q.-D., Lee, K., and Juntti, M. (2022). Hybrid relay-reflecting intelligent surface-assisted wireless communications. *IEEE Trans. Veh. Technol.*, 71(6):6228–6244.

[Ozden et al., 2024] Ozden, B. A., Cogen, F., Aydin, E., Ilhan, H., Basar, E., and Wen, M. (2024). A novel reconfigurable intelligent surface-supported code index modulation-based receive spatial modulation system. In *2024 IEEE Wireless Commun. Netw. Conf. (WCNC)*, pages 1–6. IEEE.

[Ozpoyraz et al., 2022] Ozpoyraz, B., Dogukan, A. T., Gevez, Y., Altun, U., and Basar, E. (2022). Deep learning-aided 6G wireless networks: A comprehensive survey of revolutionary PHY architectures. *IEEE Open J. Commun. Soc.*, 3:1749–1809.

[Pan et al., 2021] Pan, C., Ren, H., Wang, K., Kolb, J. F., Elkashlan, M., Chen, M., Di Renzo, M., Hao, Y., Wang, J., Swindlehurst, A. L., et al. (2021). Reconfigurable intelligent surfaces for 6G systems: Principles, applications, and research directions. *IEEE Commun. Mag.*, 59(6):14–20.

[Perović et al., 2020] Perović, N. S., Di Renzo, M., and Flanagan, M. F. (2020). Channel capacity optimization using reconfigurable intelligent surfaces in indoor mmwave environments. In *Proc. IEEE Int. Conf. Commun. (ICC)*, pages 1–7. IEEE.

[Pradhan et al., 2020] Pradhan, C., Li, A., Song, L., Li, J., Vucetic, B., and Li, Y. (2020). Reconfigurable intelligent surface (RIS)-enhanced two-way OFDM communications. *IEEE Trans. Veh. Technol.*, 69(12):16270–16275.

[Primak et al., 2004] Primak, S., Kontorovich, V., and Lyandres, V. (2004). *Stochastic methods and their applications to communications: stochastic differential equations approach.* John Wiley & Sons.

[Saad et al., 2019] Saad, W., Bennis, M., and Chen, M. (2019). A vision of 6G wireless systems: Applications, trends, technologies, and open research problems. *IEEE Network*, 34(3):134–142.

[Şahin and Arslan, 2020] Şahin, M. M. and Arslan, H. (2020). Waveform-domain NOMA: The future of multiple access. In *Proc. IEEE Int. Conf. Commun. Workshops (ICC Workshops)*, pages 1–6. IEEE.

[Şahin et al., 2021] Şahin, M. M., Gurol, I. E., Arslan, E., Basar, E., and Arslan, H. (2021). OFDM-IM for joint communication and radar-sensing: a promising waveform for dual functionality. *Front. Commun. Netw.*, 2:715944.

[Sarkar et al., 2006] Sarkar, T. K., Mailloux, R., Oliner, A. A., Salazar-Palma, M., and Sengupta, D. L. (2006). *History of Wireless*. John Wiley & Sons.

[Schroeder et al., 2021] Schroeder, R., He, J., and Juntti, M. (2021). Passive RIS vs. hybrid RIS: A comparative study on channel estimation. In *2021 IEEE 93rd Veh. Technol. Conf. (VTC-Spring)*, pages 1–7. IEEE.

[Shafique et al., 2022] Shafique, T., Tabassum, H., and Hossain, E. (2022). Stochastic geometry analysis of IRS-assisted downlink cellular networks. *IEEE Trans. Commun.*, 70(2):1442–1456.

[Sharma, 2013] Sharma, P. (2013). Evolution of mobile wireless communication networks-1G to 5G as well as future prospective of next generation communication network. *International Journal of Computer Science and Mobile Computing*, 2(8):47–53.

[Simon, 2002] Simon, M. K. (2002). *Probability distributions involving Gaussian random variables: A handbook for engineers and scientists*. Springer.

[Song, 2021] Song, C. (2021). Physical layer security of RIS-assisted NOMA networks over fisher-snedecor composite fading channel. In *Proc. 2021 Int. Conf. Commun. Comput. Cybersecur. Informatics (CCCI)*, pages 1–6. IEEE.

[Su et al., 2020] Su, R., Dai, L., Tan, J., Hao, M., and MacKenzie, R. (2020). Capacity enhancement for irregular reconfigurable intelligent surface-aided wireless communications. In *Proc. IEEE Global Commun. Conf.*, pages 1–6. IEEE.

[Subrt and Pechac, 2012] Subrt, L. and Pechac, P. (2012). Controlling propagation environments using intelligent walls. In *Proc. Eur. Conf. Antennas Propag. (EUCAP)*, pages 1–5. IEEE.

[Sugiura et al., 2017] Sugiura, S., Ishihara, T., and Nakao, M. (2017). State-of-the-art design of index modulation in the space, time, and frequency domains: Benefits and fundamental limitations. *IEEE Access*, 5:21774–21790.

[Tang et al., 2019a] Tang, W., Dai, J. Y., Chen, M., Li, X., Cheng, Q., Jin, S., Wong, K.-K., and Cui, T. J. (2019a). Programmable metasurface-based RF chain-free 8PSK wireless transmitter. *Electron. Lett.*, 55(7):417–420.

[Tang et al., 2020] Tang, W., Dai, J. Y., Chen, M. Z., Wong, K.-K., Li, X., Zhao, X., Jin, S., Cheng, Q., and Cui, T. J. (2020). MIMO transmission through reconfigurable intelligent surface: System design, analysis, and implementation. *IEEE J. Sel. Areas Commun.*, 38(11):2683–2699.

[Tang et al., 2019b] Tang, W., Li, X., Dai, J. Y., Jin, S., Zeng, Y., Cheng, Q., and Cui, T. J. (2019b). Wireless communications with programmable metasurface: Transceiver design and experimental results. *China Commun.*, 16(5):46–61.

[Tapio et al., 2021] Tapio, V., Hemadeh, I., Mourad, A., Shojaeifard, A., and Juntti, M. (2021). Survey on reconfigurable intelligent surfaces below 10 GHz. *EURASIP J. Wireless Commun. Netw.*, 2021:1–18.

[Technologies, 2023] Technologies, H. (2023). Terahertz sensing and communication: Exploring the future of RIS. Accessed: 2023-12-20.

[Tek and Basar, 2024] Tek, Y. I. and Basar, E. (2024). Joint delay-doppler index modulation for orthogonal time frequency space modulation. *IEEE Trans. Commun.*

[Thanh et al., 2018] Thanh, H. L. T., Ngo, V.-D., Le, M.-T., and Tran, X. N. (2018). Repeated index modulation with coordinate interleaved OFDM. In *Proc. 5th NAFOSTED Conf. Infor. and Comput. Sci.*, pages 114–118. IEEE.

[Timotheou and Krikidis, 2015] Timotheou, S. and Krikidis, I. (2015). Fairness for non-orthogonal multiple access in 5G systems. *IEEE Signal Process. Lett.*, 22(10):1647–1651.

[Topics, 2023] Topics, E. (2023). Mobile internet traffic. Accessed: 2023-12-20.

[Tugtekin et al., 2023] Tugtekin, O. F., Dogukan, A. T., Arslan, E., and Basar, E. (2023). Coordinate interleaved OFDM with repeated in-phase/quadrature index modulation. *IEEE Trans. Wireless Commun.*

[Tusha et al., 2020a] Tusha, A., Doğan, S., and Arslan, H. (Mar. 2020a). A hybrid downlink NOMA with OFDM and OFDM-IM for beyond 5G wireless networks. *IEEE Signal Process. Lett.*, 27:491–495.

[Tusha et al., 2020b] Tusha, S. D., Tusha, A., Basar, E., and Arslan, H. (2020b). Multidimensional index modulation for 5G and beyond wireless networks. *Proc. IEEE*, 109(2):170–199.

[Vaezi et al., 2019] Vaezi, M., Schober, R., Ding, Z., and Poor, H. V. (2019). Non-orthogonal multiple access: Common myths and critical questions. *IEEE Wireless Commun.*, 26(5):174–180.

[Valdez et al., 2021] Valdez, L. B., Datta, R. R., Babic, B., Müller, D. T., Bruns, C. J., and Fuchs, H. F. (2021). 5G mobile communication applications for surgery: An overview of the latest literature. *Artificial Intelligence in Gastrointestinal Endoscopy*, 2(1):1–11.

[Van Luong et al., 2018] Van Luong, T., Ko, Y., and Choi, J. (June 2018). Repeated MCIK-OFDM with enhanced transmit diversity under CSI uncertainty. *IEEE Trans. Wireless Commun.*, 17(6):4079–4088.

[Vannithamby and Talwar, 2017] Vannithamby, R. and Talwar, S. (2017). *Towards 5G: Applications, requirements and candidate technologies*. John Wiley & Sons.

[Viswanathan and Mogensen, 2020] Viswanathan, H. and Mogensen, P. E. (2020). Communications in the 6G era. *IEEE access*, 8:57063–57074.

[Wang et al., 2023] Wang, C.-X., You, X., Gao, X., Zhu, X., Li, Z., Zhang, C., Wang, H., Huang, Y., Chen, Y., Haas, H., et al. (2023). On the road to 6G:

Visions, requirements, key technologies and testbeds. *IEEE Commun. Surveys Tuts.*

[Wang et al., 2024a] Wang, J., Tang, W., Liang, J. C., Zhang, L., Dai, J. Y., Li, X., Jin, S., Cheng, Q., and Cui, T. J. (2024a). Reconfigurable intelligent surface: Power consumption modeling and practical measurement validation. *IEEE Trans. Commun.*

[Wang, 2021] Wang, L. (Sept. 2021). Generalized quadrature space-frequency index modulation for MIMO-OFDM systems. *IEEE Trans. Commun.*, 69(9):6375–6389.

[Wang et al., 2024b] Wang, R., Yang, Y., Makki, B., and Shamim, A. (2024b). A wideband reconfigurable intelligent surface for 5G millimeter-wave applications. *IEEE Trans. Antennas Propag.*

[Wen et al., 2017a] Wen, M., Basar, E., Li, Q., Zheng, B., and Zhang, M. (Sept. 2017a). Multiple-mode orthogonal frequency division multiplexing with index modulation. *IEEE Trans. Commun.*, 65(9):3892–3906.

[Wen et al., 2015] Wen, M., Cheng, X., Ma, M., Jiao, B., and Poor, H. V. (2015). On the achievable rate of OFDM with index modulation. *IEEE Trans. Signal Process.*, 64(8):1919–1932.

[Wen et al., 2017b] Wen, M., Cheng, X., and Yang, L. (2017b). *Index modulation for 5G wireless communications*, volume 52. Springer.

[Wen et al., 2018] Wen, M., Li, Q., Basar, E., and Zhang, W. (Oct. 2018). Generalized multiple-mode OFDM with index modulation. *IEEE Trans. Wireless Commun.*, 17(10):6531–6543.

[Wen et al., 2017c] Wen, M., Ye, B., Basar, E., Li, Q., and Ji, F. (2017c). Enhanced orthogonal frequency division multiplexing with index modulation. *IEEE Trans. Wireless Commun.*, 16(7):4786–4801.

[Wu and Zhang, 2019] Wu, Q. and Zhang, R. (2019). Intelligent reflecting surface enhanced wireless network via joint active and passive beamforming. *IEEE Trans. Wireless Commun.*, 18(11):5394–5409.

[Wu et al., 2023] Wu, Q., Zheng, B., You, C., Zhu, L., Shen, K., Shao, X., Mei, W., Di, B., Zhang, H., Basar, E., et al. (2023). Intelligent surfaces empowered wireless network: Recent advances and the road to 6G. *arXiv preprint arXiv:2312.16918*.

[Xiao et al., 2021] Xiao, L., Liu, G., Xiao, P., and Jiang, T. (2021). Error probability analysis for rectangular differential OFDM with index modulation over dispersive channels. *IEEE Wireless Commun. Lett.*, 10(12):2795–2799.

[Xiao et al., 2014] Xiao, Y., Wang, S., Dan, L., Lei, X., Yang, P., and Xiang, W. (Aug. 2014). OFDM with interleaved subcarrier-index modulation. *IEEE Commun. Lett.*, 18(8):1447–1450.

[Yan et al., 2019] Yan, W., Yuan, X., and Kuai, X. (2019). Passive beamforming and information transfer via large intelligent surface. *IEEE Wireless Commun. Lett.*, 9(4):533–537.

[Yang et al., 2020] Yang, Y., Zheng, B., Zhang, S., and Zhang, R. (2020). Intelligent reflecting surface meets OFDM: Protocol design and rate maximization. *IEEE Trans. Commun.*, 68(7):4522–4535.

[Yang et al., 2016] Yang, Z., Ding, Z., Fan, P., and Al-Dhahir, N. (2016). A general power allocation scheme to guarantee quality of service in downlink and uplink NOMA systems. *IEEE Trans. Wireless Commun.*, 15(11):7244–7257.

[Yarkin and Coon, 2022] Yarkin, F. and Coon, J. P. (Jan 2022). Modulation based on a simple MDS code: Achieving better error performance than index modulation and related schemes. *IEEE Trans. Commun.*, 70(1):118–131.

[Yarkin and Coon, 2020a] Yarkin, F. and Coon, J. P. (July 2020a). Q-ary multi-mode OFDM with index modulation. *IEEE Wireless Commun. Lett.*, 9(7):1110–1114.

[Yarkin and Coon, 2020b] Yarkin, F. and Coon, J. P. (Nov. 2020b). Set partition modulation. *IEEE Trans. Wireless Commun.*, 19(11):7557–7570.

[Yigit et al., 2022] Yigit, Z., Basar, E., Wen, M., and Altunbas, I. (2022). Hybrid reflection modulation. *IEEE Trans. Wireless Commun.*

[You et al., 2021] You, L., Xiong, J., Ng, D. W. K., Yuen, C., Wang, W., and Gao, X. (2021). Energy efficiency and spectral efficiency tradeoff in RIS-aided multiuser MIMO uplink transmission. *IEEE Trans. Signal Process.*, 69:1407–1421.

[Yuan et al., 2021] Yuan, J., Wen, M., Li, Q., Basar, E., Alexandropoulos, G. C., and Chen, G. (2021). Receive quadrature reflecting modulation for RIS-empowered wireless communications. *IEEE Trans. Veh. Technol.*, 70(5):5121–5125.

[Yue et al., 2024] Yue, M., Peng, Y., Ye, R., Hai, H., Al-Hazemi, F., and Lee, J. (2024). IRS-assisted extended variable spatial modulation: A high spectral efficiency scheme. *IEEE Wireless Commun. Lett.*

[Zeng et al., 2021] Zeng, S., Zhang, H., Di, B., Han, Z., and Song, L. (2021). Reconfigurable intelligent surface (RIS) assisted wireless coverage extension: RIS orientation and location optimization. *IEEE Commun. Lett.*, 25(1):269–273.

[Zhang et al., 2022a] Zhang, C., Peng, Y., Li, J., and Tong, F. (2022a). An IRS-aided GSSK scheme for wireless communication system. *IEEE Commun. Lett.*, 26(6):1398–1402.

[Zhang et al., 2021] Zhang, L., Lei, X., Xiao, Y., and Ma, T. (2021). Large intelligent surface-based generalized index modulation. *IEEE Commun. Lett.*, 25(12):3965–3969.

[Zhang et al., 2022b] Zhang, Z., Dai, L., Chen, X., Liu, C., Yang, F., Schober, R., and Poor, H. V. (2022b). Active RIS vs. passive RIS: Which will prevail in 6G? *IEEE Trans. Commun.*, 71(3):1707–1725.

[Zheng et al., 2015] Zheng, B., Chen, F., Wen, M., Ji, F., Yu, H., and Liu, Y. (Nov. 2015). Low-complexity ML detector and performance analysis for OFDM with in-phase/quadrature index modulation. *IEEE Commun. Lett.*, 19(11):1893–1896.

[Zheng and Chen, 2017] Zheng, J. and Chen, R. (May 2017). Achieving transmit diversity in OFDM-IM by utilizing multiple signal constellations. *IEEE Access*, 5:8978–8988.

[Zhi et al., 2022] Zhi, K., Pan, C., Ren, H., Chai, K. K., and Elkashlan, M. (2022). Active RIS versus passive RIS: Which is superior with the same power budget? *IEEE Commun. Lett.*, 26(5):1150–1154.

Appendix A

PROOF OF LEMMA 1

Let us define

$$\mathcal{A} = \sum_{n \in \mathbb{I}_k} |h_n| \, |g_{n,k}| = \sum_{n \in \mathbb{I}_k} \alpha_n \beta_{n,k}, \tag{A.1}$$

where $\mathbb{I}_k = \{(k-1)N_g + 1, (k-1)N_g + 2, \cdots, kN_g\}$ is a set of RIS elements indices allocated for the k^{th} UE. Since the phase value of n^{th} RIS element is determined to provide coherent alignment with the corresponding channel coefficients h_n and $g_{n,k}$ for $n \in \mathbb{I}_k$, the phase values of these coefficients are removed, causing the multiplication of amplitudes only as in (A.1). Note that α_n and $\beta_{n,k}$ are i.i.d. Rayleigh distributed RVs, and the mean of the multiplication of them can be given as:

$$\mathrm{E}\left[\alpha_n \beta_{n,k}\right] = \mathrm{E}\left[\alpha_n\right] \mathrm{E}\left[\beta_{n,k}\right] = \frac{\sigma_h \sigma_{g_k} \pi}{4}, \tag{A.2}$$

where $\mathrm{E}\left[\alpha_n\right] = \sigma_h \sqrt{\pi/4}$ and $\mathrm{E}\left[\beta_{n,k}\right] = \sigma_{g_k} \sqrt{\pi/4}$.

Additionally, the variance can be given as:

$$\mathrm{Var}\left[\alpha_n \beta_{n,k}\right] = \mathrm{E}\left[\left[\alpha_n \beta_{n,k}\right]^2\right] - \left(\mathrm{E}\left[\alpha_n \beta_{n,k}\right]\right)^2. \tag{A.3}$$

By taking square of (A.2), $\left(\mathrm{E}\left[\alpha_n \beta_{n,k}\right]\right)^2$ can be calculated as $\sigma_h^2 \sigma_{g_k}^2 \pi^2/16$.

Since α_n and $\beta_{n,k}$ are i.i.d. RVs, we have the following derivations: $\mathrm{E}[[\alpha_n \beta_{n,k}]^2] = \mathrm{E}[[\alpha_n^2 \beta_{n,k}^2]] = \mathrm{E}[\alpha_n^2]\mathrm{E}[\beta_{n,k}^2]$.

In order to find $\mathrm{E}\left[\alpha_n^2\right]$, the variance value of α_n can be exploited as follows:

$$\mathrm{Var}\left[\alpha_n\right] = \mathrm{E}\left[\alpha_n^2\right] - \left(\mathrm{E}\left[\alpha_n\right]\right)^2, \tag{A.4}$$

$$\mathrm{E}\left[\alpha_n^2\right] = \mathrm{Var}\left[\alpha_n\right] + \left(\mathrm{E}\left[\alpha_n\right]\right)^2 = \frac{\sigma_h^2}{2}\left(2 - \frac{\pi}{2}\right) + \frac{\sigma_h^2 \pi}{4} = \sigma_h^2. \tag{A.5}$$

The same derivations are also valid for $\mathrm{E}\left[\beta_{n,k}^2\right]$, and its value can be obtained as $\sigma_{g_k}^2$. Therefore, we can obtain the following result:

$$\mathrm{E}\left[\left[\alpha_n \beta_{n,k}\right]^2\right] = \mathrm{E}\left[\alpha_n^2\right] \mathrm{E}\left[\beta_{n,k}^2\right] = \sigma_h^2 \sigma_{g_k}^2. \tag{A.6}$$

Lastly, by substituting $\left(\mathrm{E}\left[\alpha_n \beta_{n,k}\right]\right)^2$ and (A.6) into (A.3), the variance of the multiplication of α_n and $\beta_{n,k}$ can be found as follows:

$$\mathrm{Var}\left[\alpha_n \beta_{n,k}\right] = \sigma_h^2 \sigma_{g_k}^2 - \sigma_h^2 \sigma_{g_k}^2 \pi^2/16 = \sigma_h^2 \sigma_{g_k}^2 (1 - \pi^2/16). \tag{A.7}$$

When the number of RIS elements allocated to the each UE (N_g) is sufficiently large, $\mathcal{A}$ becomes a real Gaussian distributed RV due to CLT with mean $\left(N_g \sigma_h \sigma_{g_k} \pi\right)/4$ and variance $N_g \sigma_h \sigma_{g_k} (1 - \pi^2/16)$.

Appendix B

PROOF OF LEMMA 2

The interference term in the received signal for the k^{th} UE is given as:

$$\mathcal{B} = \sum_{k'\neq k}\sum_{n\in\mathbb{I}_{k'}} \alpha_n e^{j\theta_n}\beta_{n,k}e^{j\psi_{n,k}}e^{j\left(\xi_{k'}-\theta_n-\psi_{n,k'}\right)}, \tag{B.1}$$

$$= \sum_{k'\neq k}\sum_{n\in\mathbb{I}_{k'}} \alpha_n \beta_{n,k}e^{j\psi_{n,k}}e^{j\left(\xi_{k'}-\psi_{n,k'}\right)}, \tag{B.2}$$

$$= \sum_{k'\neq k}\sum_{n\in\mathbb{I}_{k'}} \alpha_n g_{n,k}e^{j\left(\xi_{k'}-\psi_{n,k'}\right)} = \sum_{k'\neq k}\sum_{n\in\mathbb{I}_{k'}} \delta_{n,k,k'}, \tag{B.3}$$

where $g_{n,k} = \beta_{n,k}e^{j\psi_{n,k}}$ is a RV which follows $\mathcal{CN}\left(0,\sigma_{g_k}^2\right)$. Since there is no coherent alignment, phase terms in $\mathcal{B}$ are not canceled out and the term $e^{j\left(\xi_{k'}+\psi_{n,k}-\psi_{n,k'}\right)}$ remains. Considering $\mathrm{E}\left[g_{n,k}\right]=0$, the expected value of $\delta_{n,k,k'}$ is found as

$$\mathrm{E}\left[\delta_{n,k,k'}\right] = \mathrm{E}\left[\alpha_n\right]\mathrm{E}\left[g_{n,k}\right]\mathrm{E}\left[e^{j\left(\xi_{k'}-\psi_{n,k'}\right)}\right] = 0. \tag{B.4}$$

Moreover, the variance of $\delta_{n,k,k'}$ is given as:

$$\mathrm{Var}\left[\delta_{n,k,k'}\right] = \mathrm{E}\left[\left[\alpha_n g_{n,k}e^{j(\xi_{k'}-\psi_{n,k'})}\right]^2\right] - \left(\mathrm{E}\left[\alpha_n g_{n,k}e^{j\left(\xi_{k'}-\psi_{n,k'}\right)}\right]\right)^2, \tag{B.5}$$

$$= \mathrm{E}\left[\alpha_n^2\right]\mathrm{E}\left[g_{n,k}^2\right]\mathrm{E}\left[e^{2j(\xi_{k'}-\psi_{n,k'})}\right], \tag{B.6}$$

$$= \sigma_h^2\sigma_{g_k}^2. \tag{B.7}$$

Based on the CLT, the summation of a total number of $(K-1)\,N_g$ complex terms results in $\mathcal{B}$ converging to a complex Gaussian distribution with zero mean and variance $N_g\,(K-1)\,\sigma_h^2\sigma_{g_k}^2$.